DEVELOPMENT OF EFFICIENT COLOR TUNABLE RARE EARTH DOPED TUNGSTATE PHOSPHOR FOR SOLID STATE LIGHTING AND ANTI-COUNTERFEITING APPLICATIONS

A Thesis Submitted
in Partial Fulfillment of the Requirements

for the Degree of

DOCTOR OF PHILOSOPHY

in

PHYSICS

by

INDRAJEET MAURYA
(Roll No. 2K20/PhD/AP/503)

Under the Supervision of

DR. M. JAYASIMHADRI
Associate Professor

DEPARTMENT OF APPLIED PHYSICS

DELHI TECHNOLOGICAL UNIVERSITY

BAWANA ROAD, DELHI-110 042, INDIA

November, 2025

Dedicated to…..

My beloved family….

DELHI TECHNOLOGICAL UNIVERSITY

(Formerly Delhi college of Engineering)
Shahabad Daulatpur, Main Bawana Road, Delhi-110 042

CANDIDATE'S DECLARATION

I ***Mr. Indrajeet Maurya*** (***2K20/PhD/AP/503)*** hereby certify that the work which is being presented in the thesis entitled "***Development of Efficient Color Tunable Rare Earth Doped Tungstate Phosphor for Solid State Lighting and Anti-Counterfeiting Applications***" in partial fulfillment of the requirements for the award of the Degree of Doctor of Philosophy, submitted in the Department of ***Applied Physics***, Delhi Technological University, is an authentic record of my own work carried out during the period from ***12-01-2021*** to ***24-11-2025*****,** under the supervision of ***Dr. M. Jayasimhadri***.

The matter presented in the thesis has not been submitted by me for the award of any degree of this or any other Institute.

Indrajeet Maurya
Roll No. 2K20/Ph.D./AP/503

This is to certify that the students has incorporated all the corrections suggested by the examiners in the thesis and statement made by the candidate is correct to the best of our knowledge.

Dr. M. Jayasimhadri
Supervisor & Associate Professor
Department of Applied Physics
Delhi Technological University
Shahbad Daulatpur, Bawana road
Delhi-110042, India

Signature of the External Examiner

DELHI TECHNOLOGICAL UNIVERSITY

(Formerly Delhi college of Engineering)
Shahabad Daulatpur, Bawana Road, Delhi-110 042

CERTIFICATE BY THE SUPERVISOR

Certified that ***Mr. Indrajeet Maurya (Reg. No.: 2K20/Ph.D./AP/503)*** has carried out their research work presented in this thesis entitled "***Development of Efficient Color Tunable Rare Earth Doped Tungstate Phosphor for Solid State Lighting and Anti-Counterfeiting Applications***" for the award of the ***Doctor of Philosophy*** in Physics from the Department of Applied Physics, Delhi Technological University, Delhi, under my supervision. The thesis embodies results of original work, and studies are carried out by the candidate himself and the contents of the thesis do not form the basis for the award of any other degree to the candidate or to anybody else from this or any other University/Institution.

Dr. M. Jayasimhadri
Supervisor & Associate Professor
Department of Applied Physics
Delhi Technological University
Shahbad Daulatpur, Bawana road
Delhi-110 042, India

Prof. Vinod Singh
Head,
Department of Applied Physics
Delhi Technological University
Shahbad Daulatpur, Bawana road
Delhi-110 042, India

ACKNOWLEDGEMENTS

The successful completion of my research journey has been made possible by the valuable support of many individuals. It is a gratifying moment to have the opportunity to express my sincere gratitude to all of them.

First and foremost, I wish to express my profound sense of gratitude, indebtedness, and reverence to my supervisor, ***Dr. M. Jayasimhadri****, Department of Applied Physics, Delhi Technological University (DTU), Delhi, who has played a pivotal role in shaping my research abilities and guiding me toward a successful scientific career. It has been a great honor to work under such an excellent, enthusiastic, and distinguished mentor. His unwavering encouragement, continuous support, meticulous supervision, and constructive feedback have been instrumental throughout the course of my study, marking a significant milestone in my academic journey. His extensive subject knowledge, analytical insight, and perseverance served as a constant source of inspiration during the preparation of this thesis.*

I further stand ovate to ***Prof. Vinod Singh****, Head & DRC chairman Department of Applied Physics, DTU, for his timely advice, valuable help, suggestions, and support. My deepest recognitions for* ***Prof. S.C. Sharma****, former DRC Chairman,* ***Prof. Rinku Sharma,*** *Dean (Academic PG) DTU, and my SRC & DRC committee members for their enduring support. My deepest regards to* ***Prof. A. Srinivasa Rao*** (Vice-Chancellor, Vikram Simhapuri University, Nellore & former HOD & DRC chairman, Department of Applied Physics, DTU) *for his enduring support. It is my pleasure to express my sincere thanks to all the faculty members of DTU. I am also grateful to the* ***Advanced Instrumentation Centre****, technical and staff, for their timely support and cooperation whenever required.*

I express my sincere gratitude to ***Prof. O. P. Thakur****, Netaji Subhash University of Technology,* ***Dr. S. Shankar Subramaniam****, ARSD College, University of Delhi,* ***Dr. P. Koteswara Rao****, University of Delhi, South campus,* ***Dr. Arvind Kumar,*** *Jawaharlal Nehru*

University, ***Dr. Raghvendra Pandey,*** *ARSD College, University of Delhi****, Dr. Upendra Singh Kushwaha,*** *University of Allahabad,* ***Dr. G. Swati,*** *VIT Vellore, for providing the lab equipment and their continuous support.*

I sincerely thank my dear former and present labmates whose support helped in accomplishing my work. It is my pleasure to thank seniors in ***LMRL****,* ***Dr. Amit K. Vishwakarma, Dr. Kaushal Jha, Dr. Sumandeep Kaur, Dr. Mukesh Kumar Sahu, Dr. Harpreet Kaur, Dr. Deepali, Dr. Vikas Sangwan,*** *and present labmates* ***Ms. Vertika Siwach, Mr. Anupam, Mr. Vishvendra, Ms. Anisha,*** *for their support. It's my pleasure to thank my seniors,* ***Mr. Rajat Bajaj, Ms. Sheetal, Dr. Anu Mor, Dr. Richa Gautam, Dr. Mrityunjay, Dr. Vishal Singh, Dr. Ankit, Mr. Rahul Kundra, Mr. Jasveer Singh, Dr. Gaurav, Dr. Lakhan, Dr. Shadab.*** *Special thanks to my dear friends,* ***Dr. Vivek Prajapati, Dr. Sanjeev Kumar, Dr. Prashant Kumar, Dr. Rohit Surya Gupta, Dr. Ankur Sandilya, Mr. Pravesh Bansal, Mr. Arvind Kumar, Mr. Sharad Singh, Mr. Vinay Kumar, and Ms. Shivani,*** *for their enjoyable company and support during this tenure. I would also like to thank all the other research scholars of DTU, Delhi for their help and advice.*

I extend my heartfelt gratitude to my family for their unwavering support and motivation throughout every stage of my research journey. With deep love and appreciation, I express my sincere thanks to my father, ***Shri Vishwanath Maurya****, and my mother, Late* ***Smt. Hirawati Devi****, for their constant encouragement and boundless affection throughout my life. I am equally grateful to my dear brothers and sisters for their invaluable advice, care, and enduring faith in me. I am especially thankful to my elder brother,* ***Mr. Samarjeet Maurya****, and his wife,* ***Mrs. Sweta Maurya****, for their financial assistance and continuous support, which helped me maintain a positive outlook during my studies. I also wish to express my lasting gratitude to all my cherished friends across the globe for standing by me and sharing in both my joys and challenges.*

I sincerely acknowledge Delhi Technological University (DTU), Delhi, for providing all the necessary facilities and for extending financial support in the form of the ***Junior Research Fellowship (JRF)*** *and* ***Senior Research Fellowship (SRF)*** *during the course of my research. I also extend my heartfelt thanks to DTU and the staff of the Administration, Accounts, Store & Purchase, Library, and Computer Centre for their invaluable assistance and services.*

I am truly grateful to everyone who contributed to the successful completion of this thesis.

Thank you all!

(Indrajeet Maurya)

LIST OF RESEARCH PUBLICATIONS INCLUDED IN THESIS

1. **Indrajeet Maurya,** M. Jayasimhadri "*Comprehensive study on thermal, structural, and luminescent properties of $BiYWO_6$: Eu^{3+} phosphors synthesized by various methods*" ***Journal of Materials Science: Materials in Electronics*** 35 (2024) 2106. ***(IF: 2.8)***
2. **Indrajeet Maurya,** M. Jayasimhadri "*Structural and spectroscopic features of single-phase Dy^{3+} activated $BiYWO_6$ phosphor for luminescent device applications*" ***Applied Physics A*** 130 (2024) 748. ***(IF: 2.5)***
3. **Indrajeet Maurya,** Vikas Sangwan, Amit K. Vishwakarma, M. Jayasimhadri "*Red light emitting Eu^{3+} doped bismuth yttrium tungstate phosphor for solid state lighting applications*" ***ChemistrySelect*** (Under review). ***(IF:2.0)***
4. **Indrajeet Maurya,** Vikas Sangwan, K. Pavani, M. Jayasimhadri "*Development of wavelength-dependent multicolor emitting $BiYWO_6$: Sm^{3+} phosphor for w-LEDs and anti-counterfeiting applications*" ***Journal of Molecular Structure*** (Under review). ***(IF: 4.7)***
5. **Indrajeet Maurya,** M. Jayasimhadri "*Color tunable emission in Dy^{3+}/Eu^{3+} co-doped $BiYWO_6$ phosphor for w-LEDs and ant-counterfeiting applications*" will be submitted to ***Journal of Luminescence (IF: 3.6)***

Not Included in thesis

1. Vedika Dubey, Vikas Sangwan, **Indrajeet Maurya**, Tannavi, M. Jayasimhadri, "*Investigation of structural and luminescent aspects of Sm^{3+} activated yttrium niobium titanate phosphor for optoelectronic applications*" ***Journal of Electronic Materials*** 53 (2024) 7967-7978. (***IF:2.1***)
2. Vikas Sangwan, Vertika Siwach, Mukesh K. Sahu, **Indrajeet Maurya,** M. Jayasimhadri, D. Haranath, "*Influence of Dy^{3+} ions on spectroscopic studies of thermally stable telluro zinc phosphate glasses for white light emitting devices*" ***Materials Today: Proceedings*** 2024 (In Press: Online Published).

RESEARCH WORK PRESENTED AT INTERNATIONAL CONFERENCES

1. **Indrajeet Maurya**, Amit K. Vishwakarma, M. Jayasimhadri, "*Red light emitting Eu^{3+} doped bismuth yttrium tungstate phosphor for photonic device applications*" 3rd International Conference on Advanced Functional Materials and Devices for Sustainable Development (AFMD-2025), at Department of Physics, ARSD College, University of Delhi, during 3-5th March, 2025.

2. **Indrajeet Maurya**, Vikas Sangwan, A. K. Vishwakarma, M. Jayasimhadri "*Red light emitting Eu^{3+} doped lithium bismuth tungstate, $LiBi(WO_4)_2$, phosphor for photonic device applications*" 2nd International Conference on Spectroscopy in Materials Science (ICOSIMS-2024), organized by Department of Physics, University of Aveiro, Portugal, during 5-7th June 2024.

3. **Indrajeet Maurya**, M. Jayasimhadri "*Thermally stable spectroscopic studies of Sm^{3+} doped bismuth lithium tungstate phosphor for w-LEDs*" 2nd International Conference on Recent Advances in Functional Materials (RAFM-2024), at Department of Physics, ARSD College, University of Delhi, during 14-16th March, 2024.

4. **Indrajeet Maurya**, M. Jayasimhadri "*Multifunctional Sm^{3+} induced bismuth lithium tungstate phosphor for flexible anti-counterfeiting and encryption*" 1st International Conference on Spectroscopy in Materials Science (ICOSIMS-2023), organized by Department of Physics, University of Aveiro, Portugal, during 20-22nd June, 2023.

ABSTRACT

DEVELOPMENT OF EFFICIENT COLOR TUNABLE RARE EARTH DOPED TUNGSTATE PHOSPHOR FOR SOLID STATE LIGHTING AND ANTI-COUNTERFEITING APPLICATIONS

The substantial growth of industrial production and economic sectors has exacerbated the global energy crisis and environmental pollution, attracting significant attention from researchers worldwide. The rising global electricity demand, growing energy consumption, and the urgent need for energy conservation have emerged as critical concerns. One promising solution to address these challenges lies in the adoption of the solid state lighting (SSL) technology. The SSL technology has demonstrated widespread applicability across various domains, particularly through the implementation of phosphor converted light emitting diodes (pc-LEDs), which represent a viable alternative to conventional incandescent and fluorescent lighting systems. This is attributed due to their remarkable luminous efficiency, compact design, reduced energy consumption, high brightness, less emission of harmful gases, extended operational lifetimes, and rapid switching capabilities. In pc-LEDs, phosphor materials are integrated with LED chips and emit light in specific spectral regions upon appropriate excitation. Given these advantageous properties, pc-LEDs are regarded as the next generation of SSL technology, poised to revolutionize the lighting industry. Notably, white pc-LEDs have emerged as the preferred solution for general illumination applications due to their superior energy efficiency, longevity, environmental safety, and overall performance.

The realization of phosphor based w-LEDs can be accomplished through two primary approaches: (i) employing a suitable combination of red, green, and blue (RGB) phosphors excited by a UV LED chip, or (ii) utilizing a single yellow emitting phosphor in conjunction with a blue LED chip. However, the first approach may suffer from issues such as the

reabsorption of blue light by red and green phosphors, while the second approach often lacks a red spectral component. These limitations can lead to deteriorate color rendering index (CRI), compromised color saturation, and instability in color temperature. To overcome these challenges, it is imperative to develop single phase phosphor materials doped with an optimized combination of rare earth (RE) ions capable of generating white light emission via efficient energy transfer mechanism. Alternatively, the design and synthesis of novel red emitting phosphors with enhanced luminescent performance are crucial to improve key optical parameters, including luminous efficacy, CRI, and CCT stability in w-LED applications. In addition, the phosphor enables a wide range of applications, including solar cells, biosensing, and other photonic devices, owing to its adaptable chemical, physical, and luminescent features. Further, phosphor based material can be used, especially in anti-counterfeiting applications. The counterfeiting of currency and consumer goods poses significant challenges, leading to economic losses and health risks that adversely impact both fundamental research and industrial applications. Consequently, advanced anti-counterfeiting technologies are imperative to safeguard the economy and ensure the authenticity of consumer products in the face of a promptly expanding counterfeit market. Effective anti-counterfeiting techniques must be inherently resistant to duplication and straightforward to authenticate. In recent years, photo responsive materials, including rare earth (RE) activated fluorescent materials and quantum dots, have emerged as innovative solutions for anti-counterfeiting applications. Among these, RE-activated fluorescent nanomaterials have garnered particular attention for their critical and strong emission bands, exceptional stability, and environmentally friendly properties, making them highly promising candidates for next generation anti-counterfeiting technologies. Phosphor materials composed of a suitable host matrix and an activator element have emerged as key components in the advancement of technologies such as w-LEDs and anti-counterfeiting applications. Over recent decades, inorganic phosphors activated by RE ions have dominated

the fabrication of pc-LEDs, primarily due to the unique luminescent properties intrinsic to RE ions. Among various inorganic oxide hosts, tungstate-based materials have gained considerable interest for use in luminescent devices, attributed to their broad excitation spectra, wide range of emission colors, and superior thermal and chemical stability. Additionally, tungstates offer cost effectiveness and energy efficient synthesis processes.

The current research work deeply focused on the development of environmental friendly new perovskite tungstate ($BiYWO_6$) phosphor doped with appropriate rare earth ions, for applications in pc-w-LEDs and anti-counterfeiting applications. In the present thesis work, efforts have been made to synthesize various rare earth doped $BiYWO_6$ phosphors, to investigate their structural, morphological, optical, luminescent properties, and also to evaluate their potential utility for solid state lighting and anti-counterfeiting applications. The present thesis comprises eight chapters, and a brief summary of each chapter is presented as follows:

Chapter 1 starts with a brief introduction outlining the origin of the problem, the motivation of the research work, and an overview of the current literature on the development of efficient solid state lighting and anti-counterfeiting applications. It includes the fundamental concepts of photoluminescence, energy transfer processes, and the utility of rare earth doped inorganic crystalline materials for lighting and display devices. The shortfalls and limitations of the existing lighting technology and how to overcome these problems have been discussed. This chapter also highlights the importance of the selected host material ($BiYWO_6$) and outlines the objectives of the thesis work at the end of the chapter.

Chapter 2 included the experimental methods used to synthesize and characterize rare earth doped $BiYWO_6$ phosphors. It describes in detail the various methods employed to synthesize the desired phosphors, followed by the different analytical techniques used to assess their suitability for solid state lighting and anti-counterfeiting applications. The thermal, structural, morphological, compositional, optical, and photoluminescent properties of the

synthesized phosphors were investigated using thermogravimetric analysis (TGA)-differential scanning calorimetry (DSC), X-ray diffraction (XRD), field emission scanning electron microscopy (FE-SEM), along with energy dispersive spectroscopy (EDS), X-ray photoelectron spectroscopy (XPS), diffuse reflectance spectroscopy (DRS), and spectrofluorophotometer, respectively. A brief introduction to each of these characterization techniques has been discussed in this chapter.

Chapter 3 describes the synthesis of the crystalline monoclinic phase of Eu^{3+} doped bismuth yttrium tungstate (BYW: Eu^{3+}) phosphors via the sol-gel combustion (SGC) procedure. X-ray diffraction (XRD) outcomes indicate the pure monoclinic crystalline phase formation of the BYW: Eu^{3+} phosphors. The irregular shape and agglomerated dense packaging of the particles of BYW: Eu^{3+} phosphors have been revealed with the help of field emission scanning electron microscopy (FE-SEM) analysis. Defuse reflectance spectra (DRS) revealed the numerous absorption peaks in the UV/n-UV and visible regions. When excited with blue light, the BYW: Eu^{3+} phosphors radiate several emission peaks, and an intense emission peak has been observed at 613 nm (red region). CIE coordinates of the BYW: Eu^{3+} phosphors are positioned in the red section of the chromaticity diagram. The aforementioned results of the BYW: Eu^{3+} phosphors indicate their promising properties for usage in the field of white light emitting diodes (wLEDs) and other photonic device applications. [Part of this work has been communicated to ***ChemistrySelect*** *(Under review)*] **(IF: 2.0)**

Chapter 4 presents the optimization of synthesis method as well calcination temperature of the europium activated bismuth yttrium tungstate (BYW: Eu^{3+}) phosphors, synthesized using four different techniques, namely solid state reaction (SSR), sol-gel combustion (SGC), co-precipitation (CP), and hydrothermal (HT) methods. Relative investigations such as thermal, structural, morphological, and luminescence characterizations, have been carried out to optimize the synthesis process of BYW: Eu^{3+} phosphor. The

luminescent spectral profiles indicate the strong absorption in the blue region (λ_{ex}=465 nm) and intense emission in the red region (λ_{em}=613 nm) ascribed to the $^5D_0 \rightarrow {}^7F_2$ transition. The comparative photoluminescence (PL) results signify that the phosphor synthesized by the CP method at a calcination temperature 900 °C exhibits the strongest emission compared to the phosphor synthesized via other methods (SGC, SSR, and HT) and shows an emission intensity nearly twice that of the phosphor synthesized via the SSR method. Further, the PL intensity was enhanced with the activator concentration of Eu^{3+} ions up to 20 mol%. The calculated CIE chromaticity coordinates (0.654, 0.345) of 20.0 mol% Eu^{3+} doped BYW sample were located in the red region, which is comparable with the commercially available red emitting phosphors Y_2O_3: Eu^{3+} (0.645, 0.347) and Y_2O_2S: Eu^{3+} (0.647, 0.343). The average PL decay time of the synthesized phosphor was found to be in the microseconds range. The obtained results suggest that the BYW: Eu^{3+} phosphor synthesized by the CP method exhibits distinctive PL characteristics with good morphology, which can be employed as an intense red emitting component in photonics devices. [Part of this work has been published in the ***Journal of Materials Science: Materials in Electronics*** 35 (2024) 2106] **(IF: 2.8)**

Chapter 5 explains the structural and spectroscopic features of single phase Dy^{3+} activated $BiYWO_6$ phosphors synthesized using co-precipitation method. X-ray diffraction (XRD), field emission scanning electron microscope (FE-SEM) with energy dispersive X-ray (EDX), X-ray photoelectron spectroscopy (XPS), and photoluminescence (PL) measurement techniques were employed to examine the structural, morphological, compositional, elemental composition as well as their oxidation states, and photoluminescent characteristics of the Dy^{3+}: $BiYWO_6$ phosphors, respectively. Photoluminescence studies of the Dy^{3+} activated $BiYWO_6$ phosphor reveal that the CIE color coordinates phosphor falls in near white region under 290 nm wavelength. The average decay time (τ_{avg}) for the $^4F_{9/2}$ energy state of Dy^{3+} ions has been found to be in microseconds. The PL spectra measured from room temperature to 448 K

ensure good thermal stability of the phosphor of the as-synthesized phosphor. Therefore, the synthesized phosphor might be a considered as a promising candidate for UV excited phosphor-converted white LEDs (pc-wLEDs). [Part of this work has been published in the ***Applied Physics A*** 130 (2024) 748] **(IF: 2.5)**

Chapter 6 describes the studies of energy transfer and color tunable luminescent properties of Dy^{3+}/Eu^{3+} co-activated $BiYWO_6$ phosphors synthesized by the co-precipitation route. The Dy^{3+}/Eu^{3+} co-activated BYW phosphor demonstrates intense emission peaks in the blue, yellow, and red regions of the PL spectrum. Application of Dexter's energy transfer formulation with Reisfeld's approximation revealed that the energy transfer mechanism encompasses a non-radiative dipole-dipole (d-d) interaction between Dy^{3+} and Eu^{3+} ions. The CIE chromaticity coordinates (x, y) and the correlated color temperature (CCT) values of the synthesized BYW: Dy^{3+}/Eu^{3+} phosphors were estimated. Based on these values, it was observed that the emission color of the synthesized phosphors can be tuned from the warm white light to the red region by precisely adjusting the concentration of Eu^{3+} ions and excitation wavelengths, respectively. These findings confirm that the synthesized Dy^{3+}/Eu^{3+} co-activated $BiYWO_6$ phosphors can be a promising candidate for white light and anti-counterfeiting applications. [Part of this work will be communicated to ***Journal of Luminescence***] **(I.F.: 3.6)**

Chapter 7 focused on the development of wavelength dependent multicolour emitting $BiYWO_6$: Sm^{3+} phosphors using the co-precipitation technique. The single phase formation with a monoclinic structure of the as-synthesized $BiYWO_6$: Sm^{3+} (BYW: Sm^{3+}) phosphors was confirmed by the X-ray diffraction (XRD) patterns. The FE-SEM micrograph of the BYW: $x$$Sm^{3+}$, x = 3.0 mol% phosphor, illustrates the irregular and uniform distribution of closely spaced particles. The EDX result fully discloses the compositional behaviour of the synthesized BYW: $x$$Sm^{3+}$, x = 3.0 mol% phosphor. The Sm^{3+} activated BYW phosphor exhibits a strong deep red emission centered at 646 nm ($^4G_{5/2} \rightarrow {}^6H_{9/2}$), when excited with 290 nm, whereas an

intense red emission around 600 nm ($^4G_{5/2} \rightarrow {}^6H_{7/2}$) is observed under blue excitations at 406 and 465 nm. The CIE chromaticity characteristics for the synthesized BYW: Sm^{3+} phosphor have been computed under selected excitations. The estimated average decay time was found in the microseconds range for BYW: Sm^{3+} phosphor under UVn-UV/blue excitations. All the findings mentioned above validate the potential of the synthesized BYW: Sm^{3+} phosphor for solid-state lighting (SSL), and anti-counterfeiting applications. [Part of this work has been communicated to *the* ***Journal of Molecular Structure*** *(Minor revision)*] **(I.F.: 4.7)**

Chapter 8 summarizes the relevant conclusions based on the results obtained in the previous chapters, outlines the future scope of the work and highlights the social impact of this research work.

LIST OF FIGURES

LIST OF TABLES

TABLE OF CONTENTS

Page No.

CHAPTER 1

Introduction

The foundational framework of the research begins with the underlying motivation driven by self initiative and the identification of contemporary scientific challenges. It proceeds to outline a systematic approach for addressing the issue through well defined research strategies. This chapter presents a detailed overview of the problem statement, followed by a comprehensive literature review that contextualizes the research within existing developments of light emitting phosphors. It introduces the fundamental principle of photoluminescence and provides an in-depth discussion on luminescent materials (phosphors), emphasizing their structural and compositional characteristics. Furthermore, the role of phosphor in the advancement of SSL lighting technology and anti-counterfeiting applications has been discussed. This chapter particularly focused on the selection of host material, highlighting its relevance and potential in the development of efficient visible light emitting phosphors for solid state lighting, and anti-counterfeiting applications.

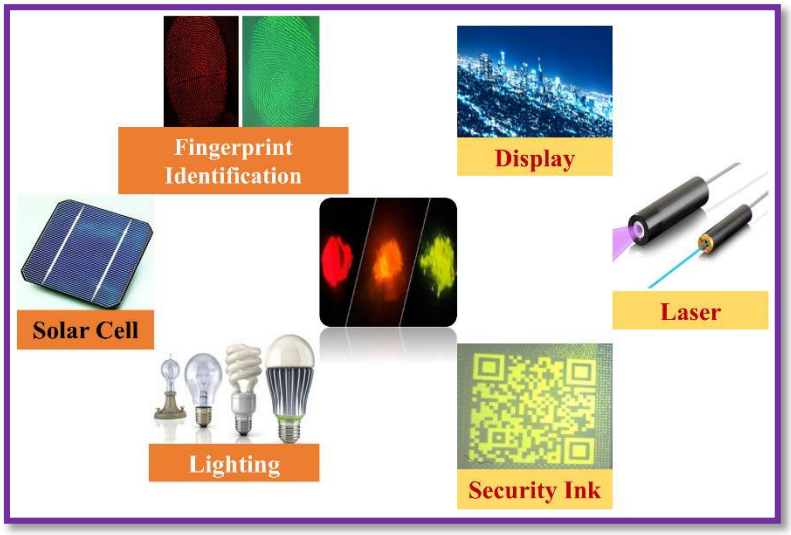

1.1. General Introduction and Motivation of the Research work

In recent years, energy demands rapidly increase worldwide to keep pace with the current technological advancements and the economic growth, which is also associated with a population expansion and the adoption of modern lifestyle. Reducing power consumption has become essential for mitigating climate change, as carbon emissions from the fossil fuel based electricity generation contribute significantly to global warming, leading to both financial and environmental costs [1–3]. The combustion of fossil fuels releases large amount of CO_2, a major greenhouse gas that significantly contributes to the rise in global temperature [4,5]. This rise in temperature accelerates climate change, which has become a serious global concern, threatening human life, disrupting biological and physical ecosystems, driving species extinction, and adversely affecting public health [1,6,7]. Nearly all power generation methods can have environmental impact, and the extent of these effects depends on the methods and locations of energy generation and distribution. Consequently, numerous scientists and researchers focus on energy efficient technologies that can reduce reliance on fossil fuels and lower energy consumption through the use of green technology for energy generation and energy savings.

The surging demand for energy and consumption can be addressed by implementing two effective strategies: an energy saving approach and the maintenance of green, renewable power producing methods. A significant reduction in global energy use will be essential for a sustainable and manageable transition to a clean energy future. Conversely, several energy saving technologies have been implemented to achieve comparable performance while minimizing energy consumption. Enhancing energy efficiency is one of the most rapid and cost effective methods to reduce greenhouse gas emissions, conserve financial resources, and meet rising energy costs, particularly in lighting, which accounts for approximately 20% of overall energy use [8]. Recently, SSL production has experienced significant advancement due to the

technology's potential to reduce electricity consumption for lighting purposes by 33% in the approaching decades [9].

On the other hand, duplicated and counterfeit goods have become a serious global issue in front of human beings, which obstructs the healthy development of the national economy and affects the image of the country as well as the worldwide industry sector [10,11]. The proliferation of counterfeit products, currency, pharmaceuticals, electronic devices, and information security measures has emerged as a significant global challenge [12]. The counterfeiting data indicate that the annual output value of counterfeit products has surpassed $500 worldwide, resulting in significant detriment to the interests of consumers and copyright holders [13]. Counterfeit is a significant concern for any government due to (i) its detrimental effects on innovation, (ii) the threats that affect consumer welfare and health. A considerable number of resources is diverted to criminal networks, organized crime, and other entities that undermine and corrupt societal structures. The implications for business, particularly in terms of their influence on sales and licensing, brand value, and corporate reputation, are significant, as well as the capacity of firms to capitalize on breakthroughs achieved in the development of new products. The significant health and safety risks posed by substandard counterfeit and pirated products are a matter of concern for consumers, as these items can have adverse effects on those who use them [12]. To prevent counterfeiting, several anti-counterfeiting solutions have been investigated, such as watermarks, barcodes, and two-dimensional codes. The said traditional anti-counterfeiting solutions are easily replicable and ineffective in preventing counterfeiting [14]. They offer to save huge amounts of economic loss and reduce black market activity globally. Hence, many scientists and researchers work on the new type of anti-counterfeiting technologies, which can minimize counterfeiting and decrease the black market by applying the efficient multicolor emitting anti-counterfeiting technology.

In light of the above facts, luminescent materials have emerged as an alternative to traditional energy sources. They provide substantial reductions in electrical energy consumption and decrease carbon emissions on a worldwide scale [15,16]. Consequently, it is imperative to manufacture an efficient n-UV/blue light excitable, visible light emitting, chemically stable, and environmental friendly phosphor suitable for white LEDs and advanced anticounterfeiting applications [17,18].

Phosphor is a mainly crystalline luminescent material that emits light preferably in the visible region when excited by some kinds of external energy. Additionally, phosphors have been found in an extensive range of applications in our daily life, including solid state lighting (SSL), advanced optical displays, optical waveguides, solar cells, finger print sensing, security ink, and many more [19–22]. The remarkable attributes of phosphor converted white light emitting diodes (w-LEDs) include significant energy savings, environmental friendliness, extended lifespan, excellent reliability, and reduced production costs in comparison to fluorescent and incandescent lamps [2,15,23,24]. At present, there are various methods to obtain white light. The prevalent and widely employed method utilizes a blue emitting InGaN chip as the source, covered with a mixture of YAG: Ce^{3+} yellow emitting phosphor and epoxy glue [25–27]. However, the aforementioned techniques exhibit deficiencies such as a low color rendering index, halo effect, and elevated associated color temperature due to the inadequacy of the red emitting component [28–30]. Another method to produce white light involves the amalgamation of ultraviolet (UV) / near-ultraviolet (n-UV) chips with red, green, and blue luminescent materials [15,31]. This method enhances CRI and provides suitable CCT, but increases the preparation process, duration, and expenditure. This technique also suffers from several drawbacks, including phase separation, reabsorption of blue light by green and red emitting luminescent materials, inadequate RGB color mixing, and low color stability due to the disparate emitting centers of luminescent materials [16,32,33]. These shortcomings were

overcome by a prepared UV/near-UV/blue pumped efficient red component in single phase phosphor, which produces proper white light [34–36]. Consequently, white light emission from a single phase phosphor has garnered significant attention in comparison to RGB emitting luminescent materials [37–39].

Furthermore, phosphor based luminescent materials are increasingly recognized for their potential in advanced anticounterfeiting applications. Technologies designed to combat counterfeiting enhance the difficulty of replicating genuine items while simplifying their authentication, playing a crucial role in safeguarding brands and important documents, such as banknotes, diplomas, and certificates. The use of phosphor based luminescence for anti-counterfeiting has garnered increasing interest due to the remarkable optical properties of phosphor materials, including high emission intensity, a range of emission colors, extended emission lifetimes, and diverse emission modes. Currently, the realization of inorganic luminescent materials doped with rare earth or transition metal ions is primarily achieved through single mode excitation, making them susceptible to counterfeiting by any alternative. The development of multi excitation and multi emission based anti-counterfeiting materials has emerged as a significant challenge within the realm of single phase phosphors. The increasing demand for innovative phosphor materials has driven scientific and technological initiatives aimed to enhance the current properties of luminescent materials [17]. Phosphors, typically comprise an inorganic matrix, referred to as the host lattice, along with dopant ions that serve as activators. The inorganic matrix serves a dual purpose: it functions as a host crystal that securely encapsulates the activator ions, while also enhancing their luminescent properties [40]. Various factors affect the luminescence characteristics of the phosphor, including synthesis technique, activator concentration, host material, and environmental conditions.

1.2. Luminescence

Light is a fundamental form of energy that enables the perception of visual stimuli. While natural sunlight serves as an abundant and readily accessible source of illumination, it can be harnessed and converted into electrical energy. The reliance on natural light is insufficient to meet the demands of modern technological applications. This limitation necessitates the development and utilization of artificial light sources to ensure consistent and controllable illumination across diverse environments and operational conditions. Artificial lighting systems have consistently served as a fundamental element in enhancing visibility in both indoor and outdoor environments, extending functionality beyond daylight hours. Initially, incandescent bulbs were employed for lighting, but they are now being replaced by light emitting diodes (LEDs). The Latin word "lumen," which means light, is where the word "luminescence" comes from [41]. Luminescence is the process by which electromagnetic radiation can be absorbed by a particular type of substance, which then emits light, preferably in the visible to near-infrared red (NIR) region is called luminescent material. Since luminescence is a cold light process rather than a hot one, it differs from incandescence. The luminescence can be excited in a variety of ways and classified into various categories based on the excitation source, as discussed below:

(i) ***Photoluminescence:*** The photoluminescence (PL) occurs when electrons in a material are excited by photon absorption and subsequently relax to their ground state, emitting energy in the form of visible light. This mechanism is widely employed in the lighting technology (phosphor based LEDs) and anti-counterfeiting applications.

(ii) ***Radioluminescence:*** Radioluminescence is induced by ionizing radiation, such as X-rays, β-rays, γ-rays, and cosmic rays, which interact with specific polymeric or organic molecules, leading to visible light emission. This phenomenon is used in the applications of X-ray imaging screens and scintillation detectors.

(iii) ***Cathodoluminescence:*** In this process, high energy electrons (cathode rays) interact with a luminescent material, exciting its electrons to higher energy states. Upon relaxation to the ground state, the electrons emit photons. Cathodoluminescence is commonly observed in cathode ray tubes, field emission display, and television screens.

(iv) ***Chemiluminescence:*** Chemiluminescence refers to light emission resulting from a chemical reaction. In this process, an intermediate reaction product reaches an excited state and emits light as it returns to the ground state. A specific subtype, bioluminescence, involves oxidation reduction reactions occurring in biological systems, often associated with the decomposition of organic materials.

(v) ***Electroluminescence:*** Electroluminescence is the phenomenon whereby photon emission is induced by the application of an electric field or current, which generates excess electron hole pairs in the material. This mechanism underpins the operation of devices such as LEDs, electroluminescent displays, sensors, and laser diodes.

(vi) ***Mechanoluminescence:*** When a certain amount of external mechanical energy is supplied to solid substances in order to grind, rub, cut, and compress the material or deformed solids by an impulse response, light emission takes place.

(vii) ***Thermoluminescence:*** This refers to the phenomenon of thermally stimulated luminescence, wherein the luminescent material is initially subjected to irradiation from ultraviolet rays, X-rays, gamma (γ) rays, or beta (β) rays. The absorbed radiation within the material generates defects, which subsequently emit energy in the visible spectrum upon thermal stimulation.

Among these various luminescence mechanisms, the present thesis work primarily focuses on photoluminescence and its associated materials, with an emphasis on their potential integration into advanced photonic devices.

1.2.1. Basic concepts of photoluminescence

Photoluminescence refers to the process by which activator ions absorb energy in the form of photons and subsequently emit light, typically within the visible spectral region. These activator ions, serving as luminescence centres, possess discrete energy levels that can be excited through photon absorption. The photoluminescence process generally follows a three step sequence: -

- ✓ The activator absorbs incident photons, resulting in excitation to a higher electronic energy state.
- ✓ The excited activator undergoes relaxation to a lower energy emissive state through non-radiative processes.
- ✓ Radiative de-excitation from the emissive state to the ground state occurs, emitting photons as visible light.

Initially, incident photons are absorbed by the activator ions, promoting electrons to excited states. Due to the closely spaced energy levels above the emissive state, transition to this state from higher excited levels typically occurs via non-radiative relaxation, mediated by phonon interaction (i.e., thermal or lattice vibrations), as radiative transitions in this region are improbable. The excited state lifetime prior to radiative emission is generally short. The subsequent radiative transition from the emissive state to the ground state leads to the emission of photons, constituting photoluminescence. The relatively large energy gap between the emissive and adjacent lower non-emissive states minimizes the probability of further non-radiative relaxation, thereby favouring photon emission, and this radiative emission results in photoluminescence [42]. Photoluminescence (PL) is classified into fluorescence and phosphorescence based on the immediate and delayed emission processes [43].

(a) Fluorescence

Fluorescence is defined as the prompt emission of light from a material upon excitation by an external radiation source. In this type of PL, emission occurs within a very short time frame (within 10^{-8} s) following the cessation of the excitation source. Emission of visible light occurs rapidly when excited electrons transition from the lowest excited states to designated ground states.

(b) Phosphorescence

Phosphorescence refers to the delayed light emission that persists even after the excitation source has been withdrawn. In this type of photoluminescence phenomenon, delayed emission occurs subsequent to the removal of the excitation source. Afterglow luminescence refers to the extended emission, in which the decay time of the excited state is higher than milliseconds that may be for few hours or days [43]. The phosphorescent materials emit light for a longer duration as the excited electrons slowly revert to their ground state.

Fluorescence is generally considered as temperature independent, while the decay dynamics of phosphorescence exhibit pronounced sensitivity to temperature variations [44]. The relaxation of excited electrons back to the ground state may proceed via two distinct pathways: radiative or non-radiative. Radiative relaxation results in the emission of photons (observable luminescence), whereas non-radiative relaxation involves the dissipation of excitation energy without photon emission [45]. For efficient luminescence, it is imperative to suppress non-radiative processes, which can occur either through phonon generation manifested as lattice vibrations or via electronic energy transfer (ET) mechanism between ions or defects within the material. The energy transfer processes will be discussed in detail in subsequent sections. As previously described, in a typical photoluminescence process, the absorption of high energy photons (typically in the UV or n-UV range) results in the excitation of electrons. A portion of this absorbed energy is subsequently re-emitted as lower energy

photons in the visible or near-infrared spectral region, which is illustrated by Stokes emission. This process is also called as down-conversion.

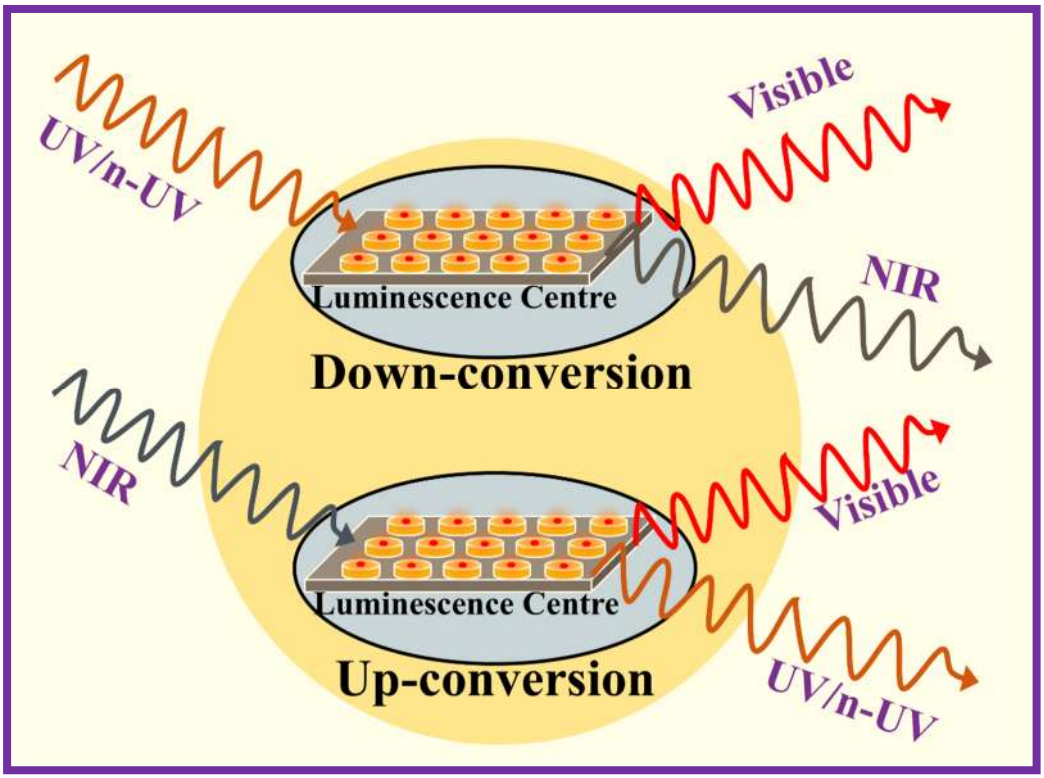

Fig. 1.01: *Down-conversion and Up-conversion processes.*

The energy loss incurred due to non-radiative relaxation prior to photon emission results in a shift between the excitation and emission wavelengths, known as the Stokes shift. Conversely, in certain materials, the sequential or simultaneous absorption of two or more low energy photons (typically in the near infrared region) can lead to the emission of a single higher energy photon in the visible or ultraviolet region. This process is known as up conversion or anti-Stokes emission [46,47]. The down-conversion and up-conversion processes are illustrated in Fig. 1.01.

1.2.2. Phosphors

Phosphors are a unique class of luminescent materials, when activated by certain types of external energy sources or radiation, produce light, ideally in the UV, visible, or infrared

region. Micro/nanocrystalline luminescent materials recognized as phosphor and amorphous solid materials, usually come under the luminescent glass/glass ceramics. Phosphors basically consist of a host lattice into which certain impurity ions, referred to as dopants (activator and sensitizer ions), are intentionally integrated [24,48,49].

(i) ***Host:*** Typically, a crystalline material serves as the host matrix for phosphors. The inorganic host matrix firmly retains both the activator and sensitizer ions to enhance their luminescent properties. Sometimes, an optically active host material efficiently absorbs the high energy $(h\nu_1)$ photons and gives the visible emission with less energy $(h\nu_2)$ as represented in Fig. 1.02(a), known as self luminescent material. The absorbed energy is emitted as phonons via molecular vibrations or atomic collisions, as depicted in Fig. 1.02(b).

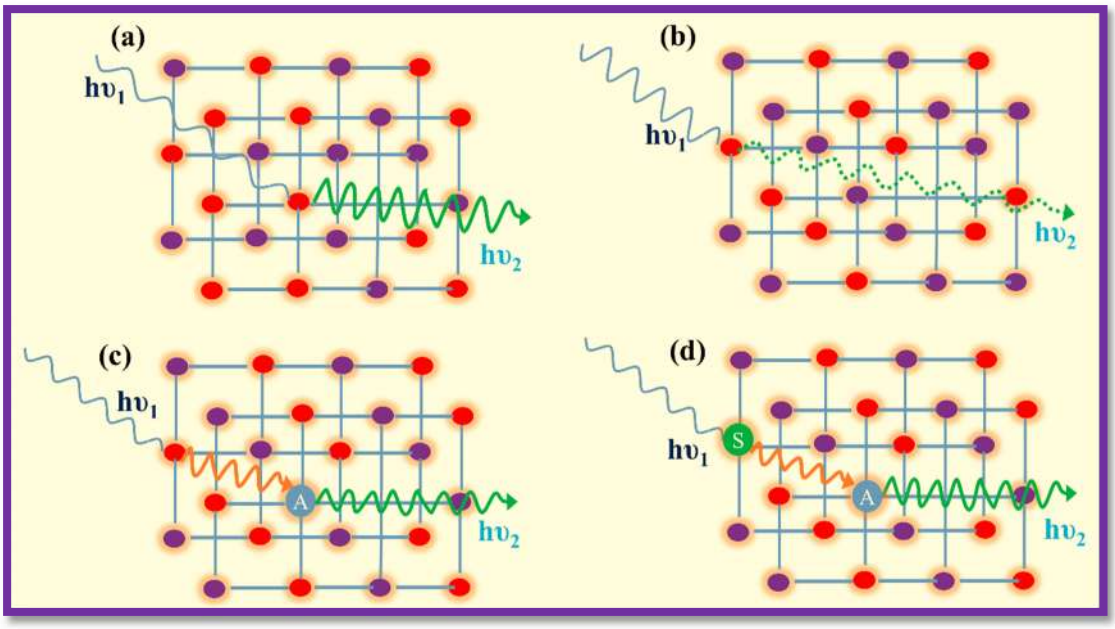

Fig.1.02: *Luminescence mechanism connecting host, sensitizer, and activator.*

(ii) ***Activators:*** When specific ions in minimal amounts replace a similar ion in the host lattice and possess the capacity to emit directly upon excitation with appropriate radiation/light sources, they are referred to as activator or dopant ions. Upon absorption of excitation energy, an ion from the activator jumps to the excited state and

subsequently emits energy as radiation while reverting to the ground state [42,50]. As displayed in Fig. 1.02(c), the high energy ($h\nu_1$) radiation is absorbed by the host lattice, subsequently transfers the energy to activator ions, and emission takes place from the activator ions. The activator ions exhibit varied roles in distinct host lattices, based upon their electronic configuration, structure, and solubility of the phosphor host lattices.

(iii) ***Sensitizers:*** Activator ions exhibit minimal absorption in some cases, hence, an alternative type of impurity, referred to as sensitizer ions, may be introduced. It enhances the absorption capacity and then transfers the absorbed energy to the activator ions. Fig. 1.02(d) illustrates the mechanism of luminescence, specifically the energy absorption by the sensitizer and the transfer of part of the absorbed energy to the activator ions. The sensitizer ions act in various ways inside distinct host matrices, based on their electronic configuration, structure, and surrounding atoms in host lattices [42].

Typically, there exists an optimal concentration of activator ions beyond which emission intensity declines owing to concentration quenching. This quenching is due to cross relaxation or energy transfer between closest ions [40]. Apart from the optimum activator ions concentration, there are so many various factors that affect luminescent characteristics. Additional factors, including the synthesis process, host material, sensitizer ions, and ambient conditions, influence the luminescent properties of the phosphor.

1.2.3. Important definitions of PL processes

(i) ***Absorption:*** When specific radiation interacts with materials and is partially absorbed by the ions within, this phenomenon is referred to as absorption, as seen in Fig. 1.03. Absorption is a process wherein ions assimilate a portion of radiation at the ground energy level to attain a higher energy level. Due to absorption, the incident radiation is diminished after traversing a substance [43].

(ii) ***Excitation:*** A portion of the received radiation by ions can induce their transition from the ground energy levels to elevated energy levels, named as excitation in Fig. 1.03. Excitation refers to the addition of energy to ions, resulting in their transformation, often from the ground state to an excited state [51].

(iii) ***Non-radiative relaxation:*** The transition of a stimulated ions from a higher excited state to a lower excited state, accompanied by the release of minimal energy by molecular vibrations or atomic collisions, is recognized as a non-radiative relaxation process, as seen in Fig. 1.03. The relaxation process to the ground state may transpire by non-radiative mechanisms, radiative mechanisms, or a combination of both. The non-radiative process results in non-visible emission [43].

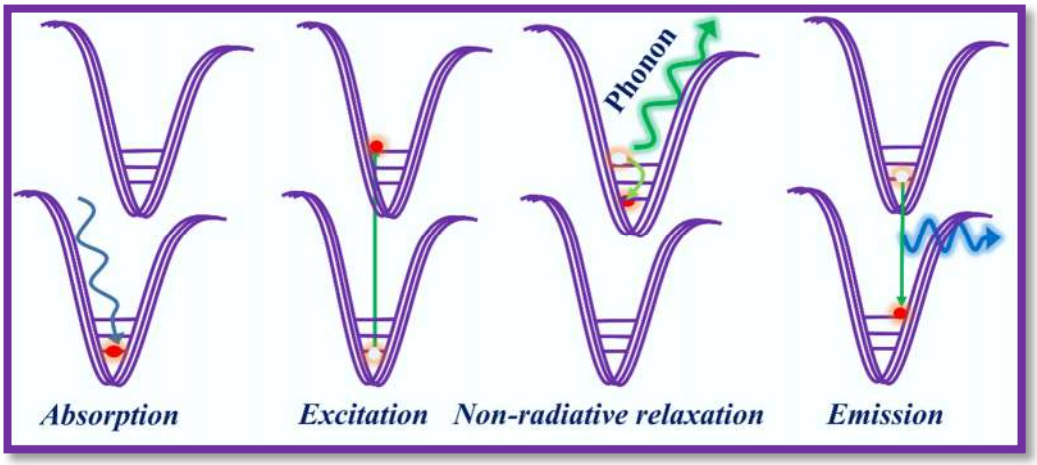

Fig.1.03: *PL processes: absorption, excitation, non-radiative relaxation, and emission.*

(iv) ***Emission:*** The spontaneous transition of a stimulated ions from the lowest excited state to specific lower energy levels results in the emission of photons corresponding to the energy difference between the involved energy levels. This process is referred to as emission or radiative transitions, as illustrated in Fig. 1.03 [42].

1.2.4. Energy Transfer Mechanism

Energy transmission between proximate ions (activator/sensitizer) occurs only when resonance exists in the energy difference between their ground and excited states. Either the phosphor host material or the sensitizer ions absorb the specific excitation source, but the

radiative emission occurs only due to existence of an activator ions [52]. As a result, the sensitizer ions have absorbed the incoming invisible excitation source and transferred a portion of the energy to the activator, which generates light, ideally in the visible spectrum. In some cases, a small portion of the excitation energy from the activator may be transferred to neighbouring activator ions. In luminescent materials, the energy in excited states can be released by several mechanisms [51,53]:

1. Visible light emission via direct excitation of the activator as revealed in Fig. 1.04(a)
2. Visible light emission from the activator ions via absorbed energy transfer from the sensitizer to the activator, as showing in Fig. 1.04(b).

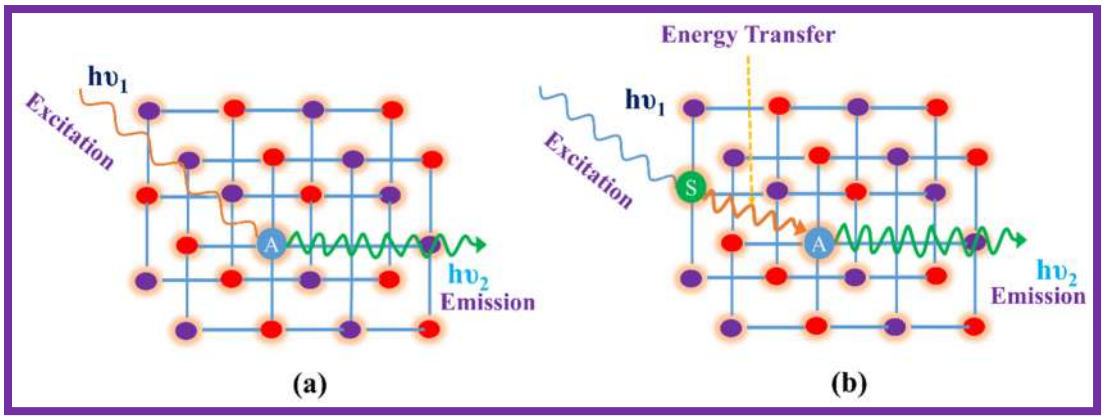

Fig. 1.04: *Schematic illustration of (a) excitation and emission by activator ions; (b) excitation, emission, and energy transfer processes among the sensitizer and activator ions in luminescent materials*.

In luminescent materials, mostly Stokes emission takes place in down conversion luminescence process. The energy difference between the absorbed photon and emitted photon is termed as Stokes shift. Lattice relaxation results in energy loss due to a modification in the strength of the chemical bond.

Following the absorption of photons or radiation, four fundamental mechanisms are involved in energy transfer (ET) activities among RE ions:

(i) Resonant radiative ET from sensitizer emission to activator ions reabsorption.

(ii) Energy transfer that occurs without radiation is associated with the resonance between the sensitizer and activator.

(iii) Multi phonon assisted energy transfer.

(iv) Cross relaxation in intermediate energy levels of two identical ions.

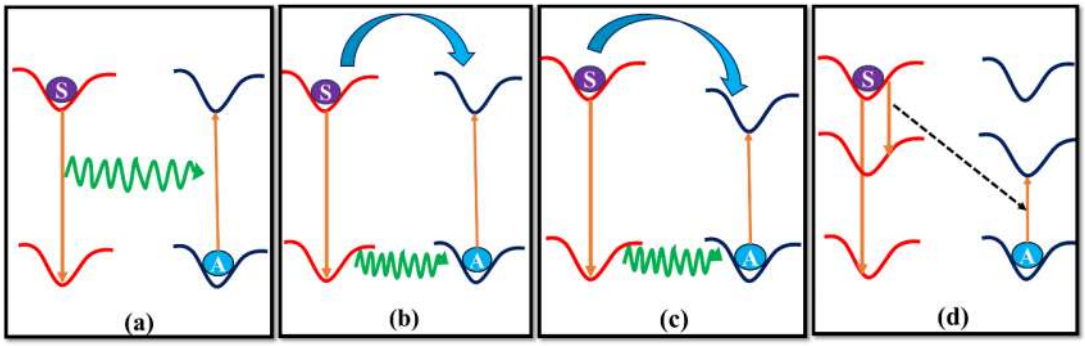

Fig.1.05: *ET processes (a) resonant radiative energy transfer between sensitizer and activator ion; (b) non-radiative energy transfer with resonance between sensitizer and activator; (c) multi phonon assisted ET; and (d) CR between two RE ions.*

The overlap between the excitation spectrum of the activator and the emission spectrum of the sensitizer is a crucial prerequisite for efficient energy transfer. The stimulation of activator ions by sensitizer emission is the primary factor that determines the efficiency of radiative energy transfer, as illustrated in Fig. 1.05(a). When the first scenario occurs, the decay time of the sensitizer remains unchanged, regardless of the activator ion concentration, due to occurrence of radiative energy transfer between the activator and the sensitizer. In the second case, for the energy transfer mechanism, there should be an identical energy difference between the excited states of the sensitizer and the activator, as shown in Fig. 1.05(b). In this instance, the non-radiative energy transfer is indicated by the decay time of sensitizer, which drastically decreases with increasing activator concentration. When there is a significant energy variation between the excited state energy level of the sensitizer and the activator ions, the probability of energy transfer becomes negligible. This phenomenon is referred to as phonon assisted non-radiative transitions, as illustrated in Fig. 1.05(c). If the two ions possess dissimilar excited

states, the cross relaxation process increases, leading to an enhanced ET probability between two identical adjacent doping ions. Fig. 1.05(d) illustrates the excited state energy levels associated with the cross relaxation process. In this scenario, the first ion is predominantly in an excited state and exchanges energy with the second ion, which is initially at the ground state. This interaction results in both ions occupying intermediate states within the energy range between two initial states [54–56].

1.3. Fundamentals of RE Ions

The lanthanide elements are classified in the periodic table from $^{139}_{57}$La to $^{175}_{71}$Lu. These elements are referred to as rare earth elements due to their sporadic occurrence in nature, being dispersed and not readily available in concentrated mineral forms. The RE elements are typically trivalent, although some exhibit different valences [51]. Rare earth elements are utilized across various domains, including material science, physics, and chemistry, as well as in nearly every branch of science and technology. The RE ions comprise 14 lanthanide elements known for their remarkable optical properties, which are linked to the occurrence of their incompletely filled deep lying $4f$ shells shielded by *5s* and *5p* shells [53]. These elements demonstrate comparable chemical behaviour; however, their physical attributes are notably different, encompassing aspects such as color, luminescence behaviour, and nuclear magnetic properties. The inadequate mutual shielding effect of $4f$ electrons result in the phenomenon known as lanthanide contraction, which subtly affects luminescence properties. Rare earth ions can serve as sensitizers, activators, or co-activators in various applications. The incorporation of RE ions into host crystals has garnered significant attention due to their wide range of applications. Due to the influence of the crystal field in the host material, the energy levels of the rare earth ions have fragmented into a multitude of Stark levels. The subsequent expansion of the spectral profiles of transitions among those levels governs the luminescence phenomena,

which is suitable for SSL and anti-counterfeiting applications. The electronic transitions of RE ions are unique, as elaborated in the following sections [51].

1.3.1. Electronic Transitions of RE Ions

The RE elements have a wide range of oxidation states and valency. RE ions often exist as divalent (RE^{2+}) or trivalent (RE^{3+}) cations, with electronic configuration $4f^{n-1}5d\ 5s^2\ 5p^6$ or $4f^n\ 5s^2\ 5p^6$. The specific electronic configuration provides a range of intriguing optical features that are effectively utilized in commercial applications, and considerable effort continues to be dedicated for the development of innovative materials and the investigation of physical processes. Table 1.01 presents the atomic number of RE elements, their ground state, electronic configuration, and ionic radii of the trivalent RE ions. The optical absorption profile of these rare earth ions in either liquid or solid form reveals distinct lines corresponding to intra $4f$ transitions. The transition moment must depend on the spin orbit coupling of the electrons in both the ground and excited states. The RE ions activated luminescent materials demonstrate the distinct narrow lines associated with the electronic transitions from $^{2S+1}L_J$ to free ion levels or J manifolds within the $4f$ subshell, as depicted in Fig. 1.06 [51,57]. The RE ions exhibit a significant Stokes shift, which serves as a crucial criterion for the development of luminescent materials.

In RE doped solids, photoluminescence is noted as a result of the partially filled 4f subshell. This phenomenon can be attributed to intra configurational $4f^n$ transitions, inter configurational $4f^n\ to\ 4f^n5d^1$transitions, or charge transfer transitions.

Table 1.01: Atomic number of RE elements, electronic configuration, ground state, and ionic radius of RE^{3+} ions.

Atomic Number	Trivalent RE^{3+} ions	Ionic radius (RE^{3+}) (Å)	Electronic configuration (RE^{3+})	Ground state
57	La^{3+}	1.032	$[Xe]4f^{0}$	$^{1}S_{0}$
58	Ce^{3+}	1.010	$[Xe]4f^{1}$	$^{2}F_{9/2}$
59	Pr^{3+}	0.990	$[Xe]4f^{2}$	$^{3}H_{4}$
60	Nd^{3+}	0.995	$[Xe]4f^{3}$	$^{4}I_{9/2}$
61	Pm^{3+}	0.983	$[Xe]4f^{4}$	$^{5}I_{4}$
62	Sm^{3+}	0.958	$[Xe]4f^{5}$	$^{6}H_{5/2}$
63	Eu^{3+}	0.947	$[Xe]4f^{6}$	$^{7}F_{0}$
64	Gd^{3+}	0.938	$[Xe]4f^{7}$	$^{8}S_{7/2}$
65	Tb^{3+}	0.923	$[Xe]4f^{8}$	$^{7}F_{6}$
66	Dy^{3+}	0.912	$[Xe]4f^{9}$	$^{6}H_{15/2}$
67	Ho^{3+}	0.901	$[Xe]4f^{10}$	$^{5}I_{8}$
68	Er^{3+}	0.890	$[Xe]4f^{11}$	$^{4}I_{15/2}$
69	Tm^{3+}	0.880	$[Xe]4f^{12}$	$^{3}H_{6}$
70	Yb^{3+}	0.868	$[Xe]4f^{13}$	$^{2}F_{7/2}$
71	Lu^{3+}	0.861	$[Xe]4f^{14}$	$^{1}S_{0}$

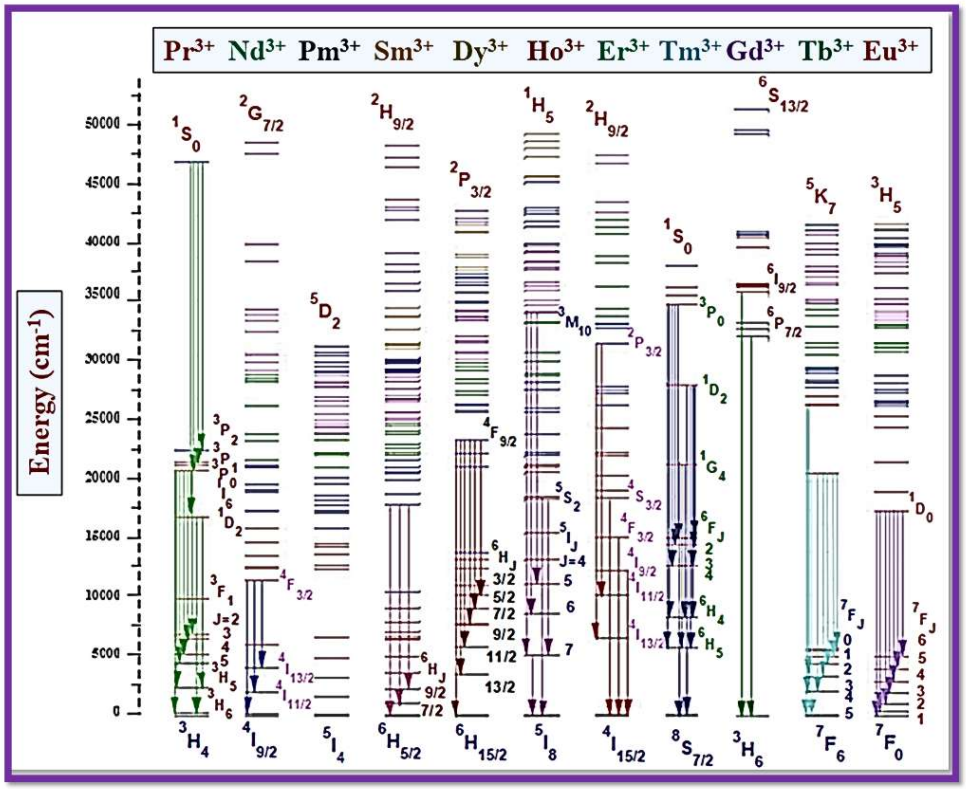

Fig. 1.06: *Energy levels and specific transitions of trivalent RE ions*.

The photoluminescent characteristics of rare earth ion activated phosphors are comprehensively understood through the analysis of their degenerated energy levels. The interaction among different levels is typically classified according to $f-f$ transitions as follows [58]:

(i) Intra configurational $4f^n - 4f^n$ interaction

(ii) $4f^n - 5d$ transitions

(i) *Intra-configurational* $4f^n - 4f^n$ interaction

In $4f^n - 4f^n$ transitions, the excitation and emission energies remain invariant by the host material in which doping ions are embedded, considering that they eventually get shielded from *5s* and *5p* electrons. The spectra induced by the RE ions display a fine line width as a result. The transitions within $4f$ shells are strictly prohibited due to the fact that the parity remains unchanged in accordance with Laporte's rule. The constrained transitions were

apparent due to the interaction of RE ions with the crystal field or lattice vibrations, which can blend states of varying parities into $4f$ states, or such transitions become permissible when spin orbit interaction occurs. The luminescence lifetime associated with $4f - 4f$ transitions fall within the millisecond range due to the forbidden nature of the photoluminescence transition. The $4f - 4f$ transitions in the RE ions can be classified into three distinct categories as follows [51,56]:

(a) Electric dipole/Induced electric dipole transitions

(b) Magnetic dipole transitions

(c) Electric quadrupole transitions

(a) Electric dipole/Induced electric dipole transitions

The incoming light source of excitation possesses both electric and magnetic field vector components. The interaction between the electric field component of the source light and RE activator ions results in induced electric dipole transitions. The electric dipole transition often comes from the linear motion of charges. Laporte's selection rule dictates that such transitions are forbidden, but non-centrosymmetric interactions generate electronic states of opposite parity, referred to as induced electric dipole transitions. The selection rules regulating induced electric dipole transitions are as follows: $\Delta l = \pm 1$; $\Delta \tau = 0$; $\Delta S = 0$; $|\Delta L| \leq 6$; $|\Delta J| \leq 6$, with $|\Delta J|$ being 2, 4, or 6 when J = 0 or J' = 0. The occurrence of forbidden f-f electric dipole transitions arises from the admixing of $4f^n$ configuration with the excited configuration of the opposite parity, for instance $4f^{n-1}\,5d$. The mixing of the electron states of opposite parity is allowed due to the non-centrosymmetric interactions [51,59].

(b) Magnetic dipole transitions

A transition involving the interaction of the magnetic field vector of the light source with activator ions, is referred to as a magnetic dipole transition. In a magnetic dipole transition,

the magnitude of the total spin angular momentum remains unchanged. The magnetic dipole transition is conceptualized as a rotating displacement of charge, while the direction of rotation endures constant under inversion via a point. Consequently, magnetic dipole transitions have symmetrical transformation properties under inversion and are accompanied by transitions of the same parity. The Laporte's selection rule permits magnetic dipole transitions, and the selection criteria follow as: $\Delta\tau = \Delta S = \Delta L = 0$; $\Delta J = 0, \pm 1$; (with $J = 0 \leftrightarrow 0$ transition is forbidden) [20,60].

(c) Electric quadrupole transitions

Electric quadrupole transitions occur when a charge possesses a null dipole moment and exhibits quadrupole characteristics. Electric quadrupole transitions exhibited even parity and were much weaker than both magnetic dipole and electric dipole transitions. Under the current circumstances, the majority of the investigational indications for the electric quadrupole transitions of RE activator ions are not present. However, certain specific transitions, termed hypersensitive transitions, might adhere to the selection principles of quadrupole transitions. An electric quadrupole transition is classified as hypersensitive transition, sometimes also called as pseudo-quadrupole transitions [51].

(ii) $4f^n - 5d$ *transitions*

The transfer of electrons between the *4f* and *5d* subshells is permitted by parity considerations. The *d* orbitals experience considerable influence from the ligand field effect, making the strength of $4f^n - 5d$ transitions highly sensitive to the presence of rare earth ions, which leads to increased energy levels. The variation in crystal field splitting among different host lattices results in corresponding differences in the spectral location of the absorption bands associated with a specific 4*f* -5*d* transition. In contrast, the emission bands do not consistently rely on the splitting of 5d orbitals and 4*f* -5*d* de-excitation. The emission wavelength ranges from near ultraviolet to the red area, mostly influenced by the host crystal field [50].

1.3.2. Concentration Quenching Mechanism

Typically, each phosphor material demonstrates its highest luminescence output at a specific concentration of dopant ions. This specific concentration of dopant ions is influenced by several factors, including the phase of the host matrices and the characteristics of the activator. The PL intensity escalates to a particular concentration of RE ions before subsequently decreasing beyond the threshold. This phenomenon is known as concentration quenching. The increase in PL intensity results from an enhancement in absorption efficiency, which remains at its peak up to a certain concentration of doping ions known as the critical concentration. The primary source of concentration quenching in any rare earth ion-doped phosphor host lattice is the energy transfer between activator ions. At a certain concentration, the proximity between acceptor and donor atoms diminishes, resulting in energy transfer that induces luminous concentration quenching. The phenomenon of concentration quenching may be elucidated from two distinct perspectives: (i) The excitation energy is primarily conveyed among various luminescent centres before emission occurs. This mechanism of energy transfer enables the reallocation of excitation energy among different centres. The luminescent centres, upon excitation may subsequently transition back to their ground state through mechanism such as multi phonon relaxation. Furthermore, certain centres may operate as energy sinks within the transfer chain, ultimately resulting in a decrease in emission intensity, known as luminescence quenching [61]. (ii) The excitation energy will be dissipated from the emitted state through a cross relaxation process, occurring via resonant energy transfer between the two neighbouring activator ions. Fig. 1.07 illustrates the energy level diagram that includes cross-relaxation. When the energy difference E_3-E_2 of one luminescent centre (donor) matches the energy difference E_0-E_1 of a nearby centre (acceptor), resonance energy occurs, which strongly depends on the nature of the energy levels.

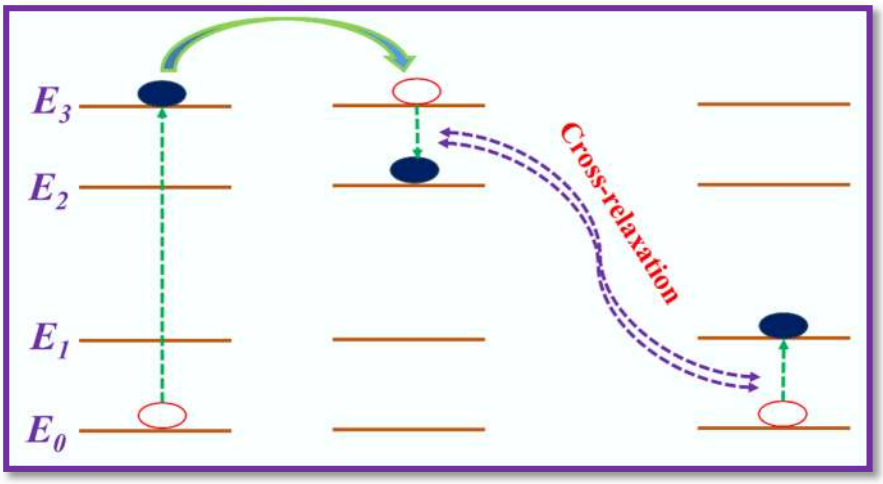

Fig. 1.07: *Cross relaxation between pairs of centres*.

In a cross relaxation process, the excited ion falls from E_3 to E_2, functioning as a donor centre, and subsequently releases energy that was absorbed by another ion at E_0, which then moves from E_0 to E_1 levels, acting as an acceptor. The non-radiative energy transfer among the nearest activator ions results in the quenching of emission intensity.

The reduction in emission intensity due to concentration quenching may arise from an increase in the possibility of non-radiative energy transfer among the doped rare-earth ions. The dopant ions within the lattice possess identical excited states, and boost the probability of ET non-radiatively, which is basically influenced by the critical distance separating the two nearest dopant ions. The energy transfer takes place via following three main processes, including exchange interaction, reabsorption, and multipolar interactions. Whereas to analyze the type of interaction (multipole or exchange), the critical distance is estimated by employing the expression given by Blasse [56].

$$R_c = 2\left(\frac{3V}{4\pi X_C N}\right)^{1/3} \tag{1.01}$$

where R_c is the critical distance, V is the unit cell volume, X_C is the optimized doping ion concentration (mol), and N is the number of cation sites in the host unit cell. R_c value defined the types of interaction among the doped ions. The exchange interaction occurs when R_c is less

than 5 Å. If this condition do not satisfy, then multipolar interaction will become prominent since the R_c value more than 5 Å [62].

Furthermore, Dexter defined the luminescence intensity *I* and doping ion concentration *x* relation as below [63,64]:

$$\frac{I}{x} = K[1 + \beta(x)^{Q/3}]^{-1} \quad (1.02)$$

Here, K and β are constants for the same excitation of a given host lattice. The value of Q explains the type of multipolar interactions presented in luminescent materials, having the values of Q = 6, 8, and 10 describe the interaction to be dipole-dipole, dipole-quadrupole, and quadrupole-quadrupole, respectively [24]. Assuming that $\beta(x)^{Q/3} >> 1$, equation (1.02) can be approximately reduced as follows:

$$log\frac{I}{x} = K' - \frac{Qlog(x)}{3};\ (K' = logk - log\beta) \quad (1.03)$$

The value of Q has been assessed using the slope of the plotted graph among $log(I/x)$ and $log\ (x)$ The estimated value of Q confirms the type of energy transfer occurs among the two closest doping ions.

1.4. Colorimetric properties

The emission spectrum of RE ions doped phosphor exhibits emission peaks in the visible region, characterized by varying intensities, and their correlation with human eye sensitivity forms a crucial aspect of luminescence. The true color of the light emission spectrum is validated by its wavelength and the associated chromaticity coordinates. The Commission Internationale de L'Eclairage (CIE) color coordinates are utilized to analyze the true color of the emission spectrum of luminescent materials. The various colors within the visible spectrum can be examined by contrasting CIE color coordinates derived from PL spectra with standard equal energy points. To determine the CIE color coordinates, the initial step involves assessing the tristimulus values (X, Y, and Z) based on the power spectral density as outlined [2]:

$$X = \int \bar{x}(\lambda)P(\lambda)d\lambda \tag{1.04}$$

$$Y = \int \bar{y}(\lambda)P(\lambda)d\lambda \tag{1.05}$$

$$Z = \int \bar{z}(\lambda)P(\lambda)d\lambda \tag{1.06}$$

in the above equations, $\bar{x}$, $\bar{y}$ and $\bar{z}$ signifies the matching functions well defined in the CIE diagram as revealed in Fig. 1.08. CIE color coordinates were assessed with help of calculated X, Y and Z values via employing the following expressions:

$$x = \frac{X}{X+Y+Z} \tag{1.07}$$

$$y = \frac{Y}{X+Y+Z} \tag{1.08}$$

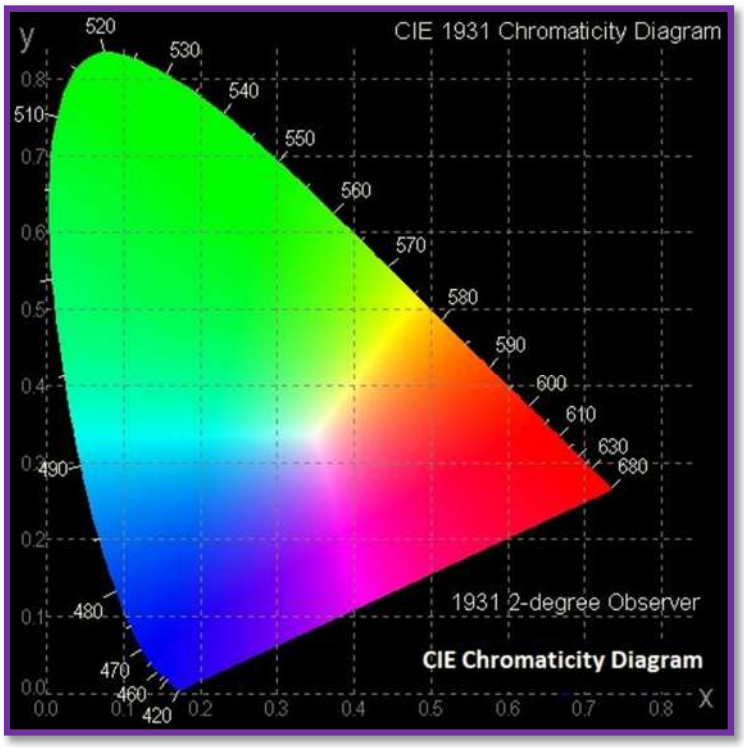

Fig. 1.08: *CIE chromaticity diagram*.

The temperature of the ideal blackbody radiator is referred as the correlated color temperature (CCT) of the light emitting source. A black body is an ideal physical entity that completely absorbs all incoming radiation, irrespective of the angle of incidence or wavelength,

and does not emit any radiation at absolute zero (0 K). The CCT is characterized as the absolute temperature of a blackbody that exhibits chromaticity comparable to the color of the light source. The CCT serves as a crucial metric for distinguishing between cool and warm white lighting devices. A lamp exhibiting a low CCT value (below 5000 K) presents a warm appearance in the emitted light. The lighting devices with a color temperature greater than 5000 K indicates the cool quality of the emitted light. CCT refers to the hue of light emitted by the lamp as well as the visual color of the lamp itself. The expression for estimating the CCT was established by McCamy [65]:

$$CCT = -449n^3 + 3525n^2 - 6823.2n + 5520.3 \quad (1.09)$$

here, $n = \frac{x-x_e}{y-y_e}$, $x_e = 0.332, y_e = 0.186$, which denotes the coordinates for epicentres.

1.5. Selection and Importance of Host

Phosphors are the critical components, which are basically used in various applications including lighting, imaging, display, and anti-counterfeiting. Phosphors have the numerous advantages which can fulfil the demand and consumption of power requirement and can approach the theoretical limits of energy efficient photonic devices. In the current decades, a number of luminescent materials have been prepared and reported in support of energy efficient photonic devices. There are challenges to prepare a versatile efficient phosphor that meets the prerequisite of photonic devices [66–69]. Hence, the major challenges that can be explicate from the necessities in energy efficient luminescent devices as: i) High bandgap host with high RE ions doping capability. ii) Efficiently absorbs UV/n-UV/blue light and emits in the desirable visible region. iii) Excellent thermal and chemical stability. iv) High quantum efficiency with less effect of temperature on luminescence characteristics. Hence, the selection of single phase host lattice is one of the crucial steps for the development of energy efficient versatile phosphor.

Various luminescent host materials, including oxides, nitrides, and fluorides, have been explored for numerous applications in science and technology. Recent studies have shown that inorganic oxides serve as promising host materials, offering advantages such as cost-effectiveness, ease of preparation, environmental friendliness, and exceptional chemical and thermal stability. Due to these commendable advantages of inorganic host materials, various inorganic oxides, such as tungstates, niobates, vanadates, silicates, phosphates, zirconates, molybdates, and aluminates, have captivated the attention of numerous experimentalists for further investigation.

Among the various oxide phosphor hosts, the tungstate based materials have attracted as effective phosphor due to tungstates having good chemical, thermally stability and have broad optical transparencies from visible to the NIR regions [70,71]. Also, tungstate based phosphors are the most preferred choice for optoelectronic devices applications due to their low crystallization temperature, low cost, exceptional chemical and thermal stability, strong UV absorption, low phonon energy materials, and high luminous efficiency [72,73]. The synthesized tungstate based phosphors can be found in many domestic and industrial applications such as in SSL, advanced optical displays, optical waveguides, lasers, etc. This will further find usage in forensic science and security ink in anti-counterfeiting technology.

The metal tungstates can be categorized into two distinct groups based on the environment of tungsten: (i) scheelite-type structures featuring WO_4^{2-} tetrahedral groups and (ii) wolframite-type structures containing WO_6^{6-} octahedral groups. Tungstates exhibit intriguing photoluminescence properties as a result of charge transfer associated with tetrahedral or octahedral groups. Tungstates compounds with rare earth elements represented as $BiREWO_6$ (where RE = rare earth, including Y, La, Lu, Gd) fall into the wolframite-type structure of the Aurivillius layered perovskite, featuring distorted WO_6 units, and have garnered significant interest in luminescence studies [74,75]. The host material $BiYWO_6$

covers the wolframite structure of irregular Aurivillius-type $[BiYO_2]^{2+}$ layers introduced amongst $[WO_4]^{2-}$ perovskite layers. There is a WO_6 octahedron with corner-linked and mixed edge chains. According to the defined crystal assembly, Y^{3+}/Bi^{3+} ions are dispersed within the unit cell of the BYW host lattice. Evidently, the crystal encounters a non-centrosymmetric local symmetry group as the RE^{3+} ions penetrate the crystal lattice.

For easy adaptation of the preparation method of phosphors by any industry, the focus will be on scaling up the processing parameters to a certain extent. Based on the literature survey mentioned above, a comprehensive investigation into the new Aurivillius layered perovskite tungstate ($BiYWO_6$) phosphor doped with RE ions has been done for SSL and anti-counterfeiting applications, which has not been explored to the best of our knowledge. Therefore, the final aim of the present proposal is to develop most efficient phosphor with improved luminescent properties by incorporating suitable RE ions. Also, the present research work is deeply focused on the strategic synthesis of $BiYWO_6$ luminescent material, and tune the emission color in the visible region.

1.6. Outline of the Problem and Objectives

Phosphor materials based on solid inorganic materials play an important role in the development of various advanced optoelectronic devices as well as advanced anti-counterfeiting techniques [76–78]. Nowadays, a large number of inorganic phosphors have been synthesized via various solid state or chemical routes. The foremost role of phosphor is to convert the radiation energy into visible or infrared light. The wavelength of the emitted light depends on the doped rare earth or transition metal ion. Therefore, rare earth or transition metal ions plays crucial role in phosphor.

Over the past few decades, rare earth or transition metal ions doped phosphors have drawn significant attention of researchers for practical applications in scintillators, light converters, field emission displays, sensors, optoelectronic applications, and

thermoluminescent dosimeters, anti-counterfeiting security ink [49,76,79]. As a high efficiency luminescence center, RE dopant ions with abundant absorption and emission levels can exhibit excellent optical performances and efficient spectral conversion capability, achieving the desired emission via multimode excitation. To improve color tunability and to obtain multicolor emission and multimode excitation in the advanced anti-counterfeiting technology, development of excitation dependent color tunable single phase phosphor has become an essential task. Therefore, multimode excitation based multicolor emission from a single phase phosphor has gained significant attention compared to single mode excited phosphor. Phosphors have the capability to transform both high and low energy photons into a spectral range that is beneficial for addressing problems in anti-counterfeit technology.

In recent years, rare earth or transition metal ions doped phosphor used in solid state lighting (SSL) devices. Phosphor based LEDs have made a substantial contribution to the success and functionality of regulated, small, and advanced artificial lighting systems [80]. This study aims to synthesize rare earth activated $BiYWO_6$ phosphor with enhanced luminescence characteristics and to investigate the process of producing white light and also to develop excitation dependent multicolor emitting $BiYWO_6$ phosphor for advanced anti-counterfeiting applications. Moreover, this ongoing study is deeply focused on the enhancement of luminescence in rare earth doped $BiYWO_6$ phosphor via various synthesis methods, followed by the optimization of activator and sensitizer doping concentrations. The comprehensive thermal, structural, morphological, compositional, and photoluminescence characterizations are examined to elucidate key research findings that fulfil the research objectives of the thesis. Therefore, the below mentioned objectives of the present proposal for producing most efficient phosphor with improved luminescent properties by scaling up the process for comfortable industrial adaptation.

Objectives:

- To select and synthesize a single phase host matrix.
- Comprehensive study of structural, morphological, optical and luminescent properties of the phosphor prepared by various routes.
- To optimize the synthesis procedure for the single phase rare earth doped phosphor using various synthesis techniques.
- To enhance the luminescent properties, by identifying the appropriate activator as well as sensitizer ions and optimize the concentration of doping ions.
- To analyze energy transfer properties of rare earth doped and co-doped bismuth yttrium tungstate phosphor.
- To develop excitation dependent multicolor emitting single phase phosphor for advanced anti-counterfeiting applications.
- Finally, to design and develop color tunable, single/multimode phosphor for their utilization in advanced anti-counterfeiting and solid state lighting applications.

CHAPTER 2

Experimental Work and Characterization Techniques

The evaluation of materials' performance for specific application involves the characterization of samples using various characterization techniques. This chapter includes the experimental works and characterization techniques required for the synthesis of an efficient phosphor with excellent PL characteristics. The advancement of effective multifunctional materials requires an in-depth comprehension of diverse synthesis methods, along with the proper characterization techniques to evaluate the applicability of RE ion activated $BiYWO_6$ phosphors for cutting-edge photonic device applications. In this study, the properties of RE ion doped phosphors thoroughly examined through various characterization techniques to reveal their structural, elemental, morphological, optical, and luminescent properties pertinent to the integration of photonic devices. This chapter offers a comprehensive description of the operational principles, instrumentation associated with the characterization tools utilized in the current study.

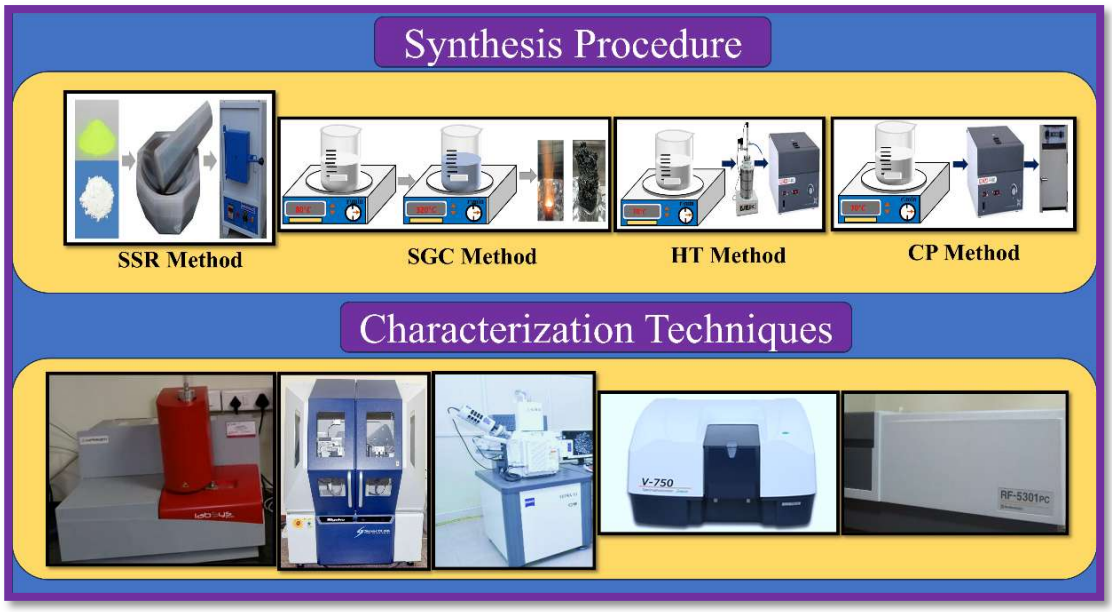

2.1. Experimental Work

The development of efficient multifunctional materials necessitates a rigorous comprehension of diverse synthesis methodologies and appropriate characterization techniques. This chapter delineates the detailed experimental methods as well as corresponding analytical techniques applied throughout the thesis. Specifically, it describes the synthesis of rare earth ion doped phosphors and the methodologies employed to evaluate their structural, vibrational, morphological, and optical properties, for their integration into advanced photonic applications, as depicted in Fig. 2.01. The structural, morphological, and elemental characteristics of the synthesized phosphor have been thoroughly analyzed using X-ray diffraction, Field emission scanning electron microscopy (FE-SEM), and X-ray photoelectron spectroscopy (XPS), respectively. The optical and luminescent characteristics of the phosphors were studied using equipment such as a UV-Vis spectrophotometer and spectrofluorophotometer, respectively.

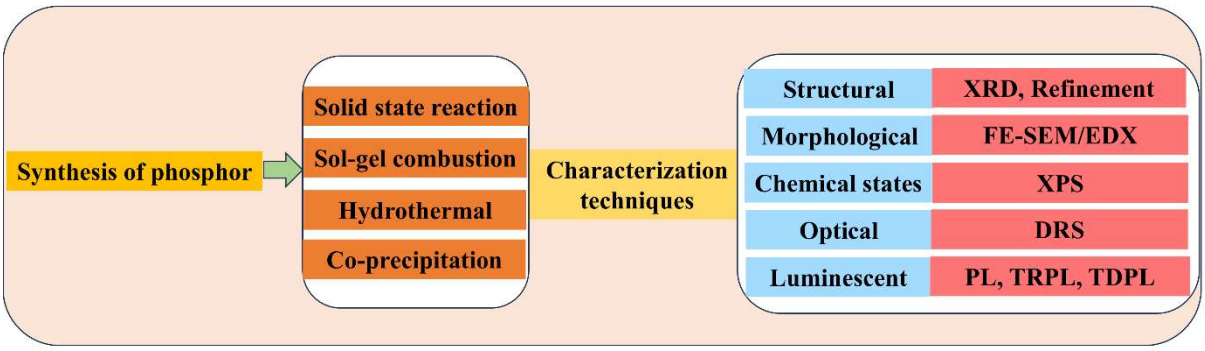

Fig. 2.01: *Schematic representation of phosphor synthesis and characterization techniques*.

2.2. Synthesis Techniques

The synthesis of phosphor samples is an essential step in the material analysis process. In this section, several synthesis techniques have been employed to synthesize phosphors, including solid-state reaction (SSR), sol-gel combustion (SGC), co-precipitation (CP), and hydrothermal (HT) methods [81–83].

2.2.1. Solid State Reaction (SSR) Method

The SSR method is a recognized process for synthesizing crystalline form of phosphor powder material. The SSR technique, acknowledged as a dry media reaction process utilized to synthesize phosphors for industrial applications. The industrial applications demand high volume manufacturing and cost efficiency within a limited timescale [84]. This method involves weighing high purity chemicals in stoichiometric ratios and dispersing them in acetone or ethanol. The mixture of starting precursors is subsequently ground for the desired time frame to guarantee uniform grinding of the precursors [85]. Consequently, it is necessary to heat the mixed precursor to elevated temperatures. The grounded powder materials were subjected to a high temperature calcination process in a programmable muffle furnace, followed by natural cooling to room temperature. The resulting powder material is ground to achieve uniform calcination of the samples.

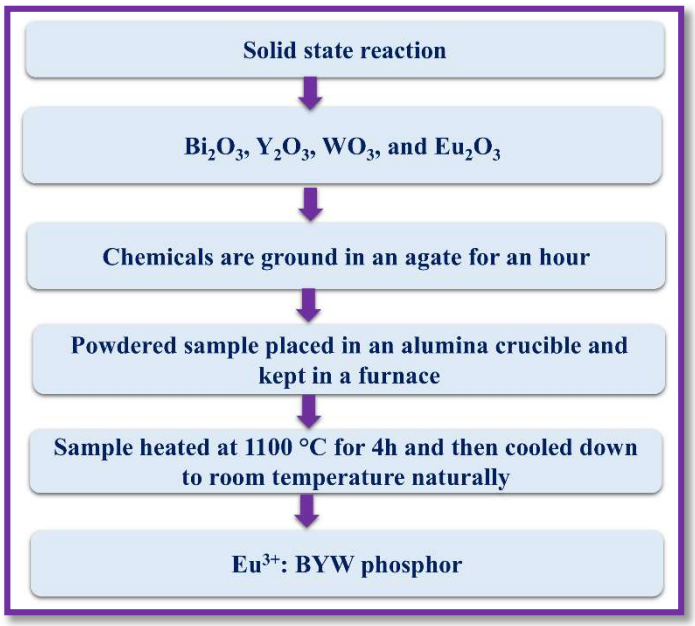

Fig. 2.02: *Flowchart of Eu^{3+} activated $BiYWO_6$ phosphors preparation via SSR method.*

Aurivillius type Eu^{3+} activated $BiYWO_6$ phosphors have been synthesized using the SSR method as outlined in the flowchart in Fig. 2.02. The precursor materials utilized for the synthesis of the phosphor included highly pure Bi_2O_3, Y_2O_3, WO_3, and Eu_2O_3. The

stoichiometric ratio of the precursor materials was accurately measured using an electronic balance, and using the following process, as mentioned in the flowchart to obtain the desired phosphor material for further studies.

The luminescent properties of the phosphor are influenced by the synthesis technique, as it impacts particle morphology, size, homogeneity, and calcination temperature, among other factors. The SSR process is known to consume a significant amount of energy and is also associated with the presence of impurities. Furthermore, this leads to an uneven composition and morphology of the final products. Therefore, the SSR process is particularly ill-suited for phosphors that require controllable morphologies and non-agglomerated regular particles. Therefore, the chemical methods, favored for the synthesis of effective homogeneous phosphor particles, have been employed for the synthesis of RE doped $BiYWO_6$ phosphor.

2.2.2. Sol-gel Combustion (SGC) Method

The process of combustion synthesis involves the heating of a metal nitrate solution, which serves as an oxidizer, in conjunction with a fuel or complexing agent such as urea, glycine, carbohydrazide, or citric acid. Additionally, the SGC method is characterized by a rapid, self sustaining, and highly exothermic reaction, resulting in the formation of the product after the reaction. This method is prominent due to its straightforward experimental setup and rapid reaction rate, and low energy consumption. Also, it employs low cost chemicals to achieve the final product, thereby enhancing cost-effectiveness and reproducibility. The substantial energy released during an exothermic reaction elevates the temperature of the reacting species, potentially leading to ignition and the onset of fire. A combustion reaction is a self-propagating process characterized by the evolution of gases, leading to the formation of the desired product.

The Eu^{3+} activated $BiYWO_6$ phosphors have been synthesized using SGC method as illustrated in the flowchart of Fig. 2.03. In SGC synthesis, the precise quantities of the

chemicals $Y(NO_3)_3.6H_2O$, $Bi(NO_3)_3.5H_2O$, Eu_2O_3, citric acid, and polyethylene glycol (PEG) were utilized as precursors. The precursors, $Bi(NO_3)_3.5H_2O$ and Eu_2O_3, were dissolved in a minimal volume of HNO_3, whereas $Y(NO_3)_3.6H_2O$, $H_{42}N_{10}O_{42}W_{12}$, and citric acid were dissolved in deionized water. The solutions of $H_{42}N_{10}O_{42}W_{12}$, and $Y(NO_3)_3.6H_2O$, $Bi(NO_3)_3.5H_2O$ represented as A and B, respectively. Subsequently, precursor solutions A & B were combined with the Eu_2O_3 solution and stirred for 1 hour at 80 °C, resulting in solution C. Then, it was mixed with citric acid, followed by addition of ethylene glycol. In this method, citric acid serves as both a fuel for combustion and a chelating agent, while ethylene glycol acts as a surfactant. After mixing all the precursors, an ammonia solution is used to maintain a pH value of 7 and heated at 80 °C for the formation of a gel. Furthermore, the temperature of the magnetic stirrer was increased to 350 °C, resulting in the self-ignition and combustion process. After combustion, the sample was ground and calcined at different temperatures in the range from 700 to 1000 °C to synthesize Eu^{3+}: BYW sample for further characterization.

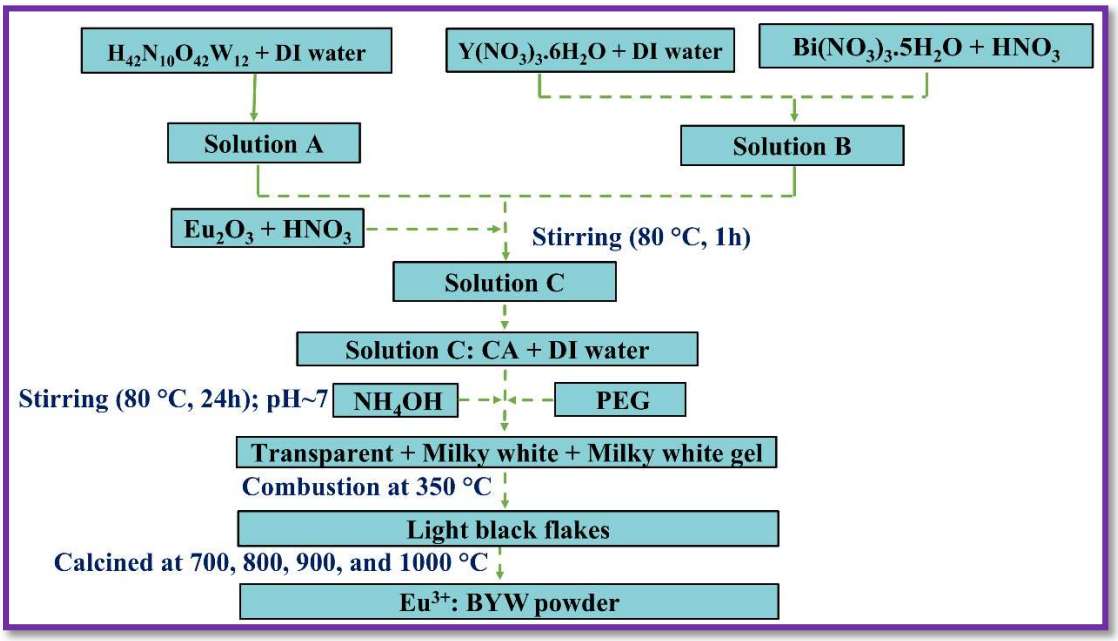

Fig. 2.03: *Flowchart of Eu^{3+} activated $BiYWO_6$ phosphors preparation via SGC method.*

2.2.3. Hydrothermal (HT) Method

Hydrothermal synthesis represents a widely utilized approach for the preparation of nanomaterials. In hydrothermal synthesis, the generation of nanomaterials can occur across a broad temperature spectrum, spanning from ambient conditions to elevated temperatures. To enhance the morphology of the synthesized materials, one may employ either low pressure or high pressure conditions, contingent upon the vapor pressure of the primary composition involved in the reaction. The hydrothermal synthesis method offers notable advantages over alternative approaches. Also, this method enables the production of nanomaterials with elevated vapor pressures while minimizing material loss. The synthesis of nanomaterials can be precisely regulated in hydrothermal conditions through liquid phase or multiphase chemical reactions. Due to these special features of the hydrothermal synthesis, researchers have focused on synthesizing nanoparticles, nanorods, nanotubes, hollow nanosheets, and graphene nanosheets for application in energy harvesting and biosensing.

The precise quantities of the chemicals $Y(NO_3)_3.6H_2O$, $Na_2WO_4.2H_2O$, $Bi(NO_3)_3.5H_2O$, and Eu_2O_3 were utilized as precursors. The initial precursors $Y(NO_3)_3.6H_2O$ and $Na_2WO_4.2H_2O$ were dissolved in the appropriate amount of deionized water from solution B, and precursor $Bi(NO_3)_3.5H_2O$ was dissolved in an appropriate amount of HNO_3, represented as solution A, as mentioned in the flow chart of Fig. 2.04. The precursor Eu_2O_3 dissolved in HNO_3. Subsequently, all the dissolved precursor solutions were mixed together, followed by stirring for one hour at 60 °C, illustrated as solution C. Once the transparent solution has been obtained, it was neutralized using the ammonia solution (NH_4OH) at 60 °C, resulting in the transformation of the clear solution into a milky white. The milky white solution was subsequently aged for 2 hours on a magnetic stirrer. The obtained sample was placed in an autoclave at 180 °C for 24 hours with auto-generated pressure in a compact reactor. After

cooling to room temperature, the obtained milky white sample was centrifuged several times with deionized water for 30 minutes, followed by multiple washes with deionized water and

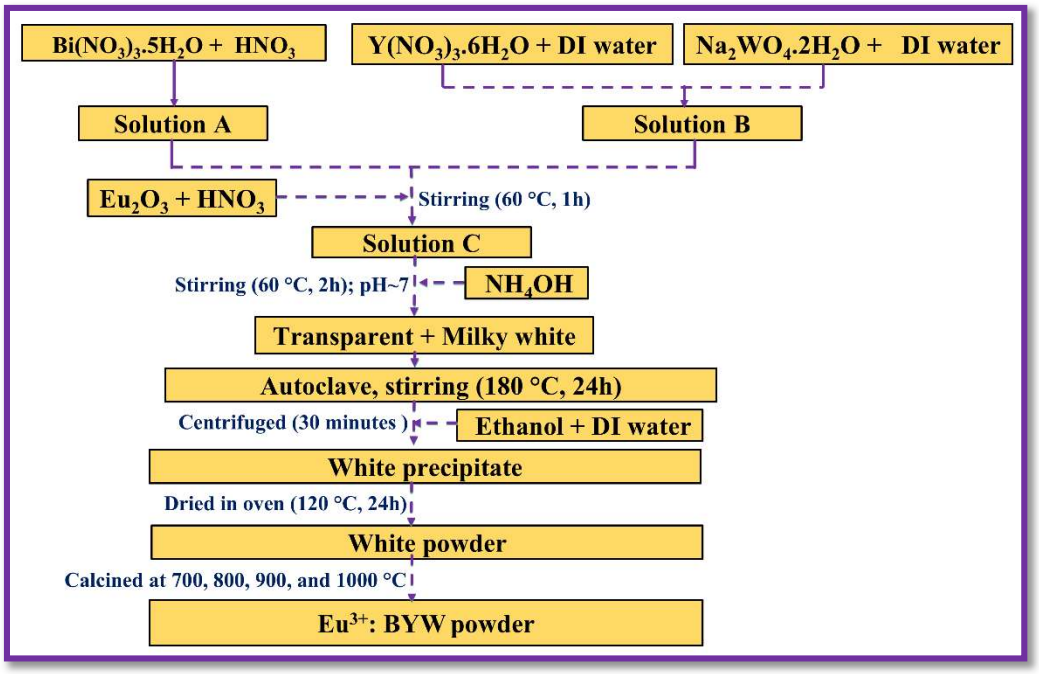

Fig. 2.04: *Flowchart of Eu^{3+} activated $BiYWO_6$ phosphors preparation via the Hydrothermal method.*

ethanol to eliminate any residual chemicals. A white precipitated clay was obtained, which was dried in an oven at 120 °C for 24 hours. Finally, the dried sample was calcined at different temperatures (700 °C - 1000 °C) for 4 hours to produce the crystalline sample. The calcined samples were allowed to cool to room temperature (RT) and was then ground using an agate mortar and pestle for further characterization.

2.2.4. Co-precipitation (CP) Method

Co-precipitation is an efficient and economically feasible method for the rapid synthesis of oxide-based phosphor/nanophosphor. Co-precipitation is a chemical process whereby solid particles are separated from a solution that contains precursor molecules or ions [86,87]. The incorporation of these ions into the solid occurs through adsorption on the surface of the growing particles and physical assembly within the pore spaces. Adsorption serves as a

fundamental mechanism in the co-precipitation method. This process involves introducing a solid species, known as the adsorbent, into a solution containing various ions referred to as adsorbates. The adsorbates are attached to the surface of the solid through physical or chemical interactions between the adsorbate and the adsorbent. The primary benefits of the co-precipitation method include high product purity, elevated yield, cost-effectiveness, and ease of reproducibility.

A systematic procedure is illustrated in Fig. 2.05 for the preparation of BYW doped with rare earth (Dy^{3+}, Eu^{3+}, Sm^{3+}, Dy^{3+}/Eu^{3+}) phosphor through the use of co-precipitation method. The precise quantities of the chemicals $Y(NO_3)_3.6H_2O$, $Na_2WO_4.2H_2O$, $Bi(NO_3)_3.5H_2O$, and rare earth oxides were utilized as precursors.

Initially, the necessary quantity of $Y(NO_3)_3.6H_2O$, $Na_2WO_4.2H_2O$ was dissolved in deionized water. The necessary quantities of $Bi(NO_3)_3.5H_2O$ and rare earth oxides were dissolved in a minimal volume of HNO_3. Subsequently, the precursor solutions were combined,

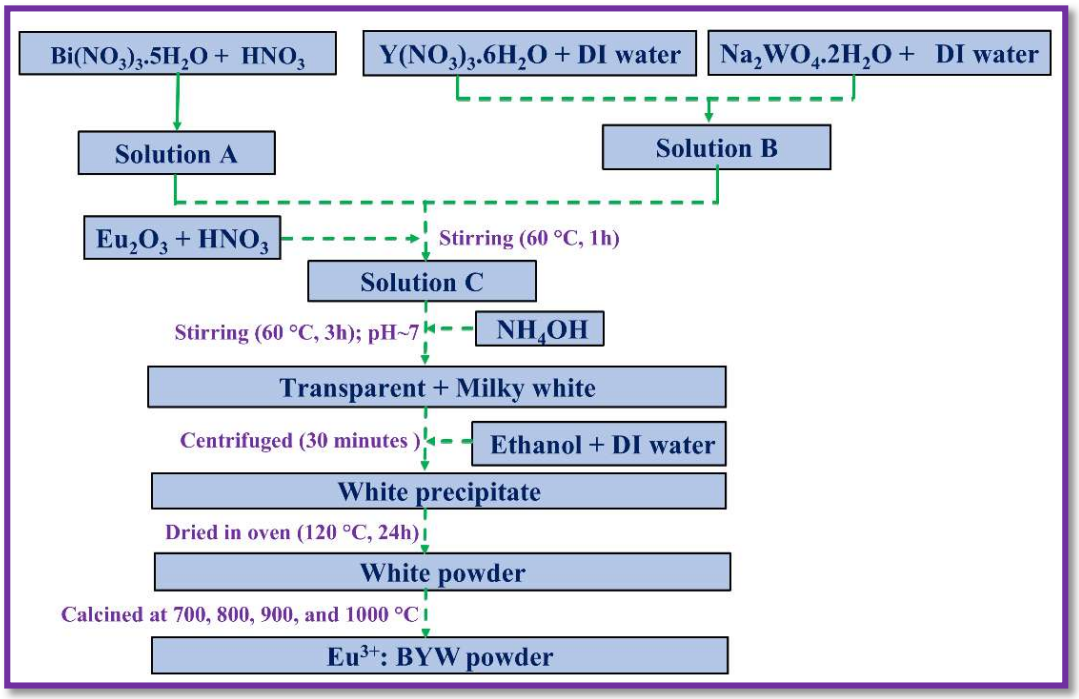

Fig. 2.05: *Flowchart of Eu^{3+} activated $BiYWO_6$ phosphors preparation via co-precipitation route.*

followed by stirring at 60 °C for one hour. The resulting solution exhibited transparency and highly acidic. Subsequently, the pH value was adjusted from 1 to 7 using an ammonia solution, resulting in the transformation of the clear solution into a milky white. The milky white solution was subsequently aged for a duration of 3 hours at 60 °C. The milky white solution was isolated using a centrifuge, followed by multiple washings with deionized water and ethanol to eliminate any residual chemicals. The resulting white precipitate was subjected to drying at 120 °C for 24 hours and subsequently calcined at different temperatures (700 °C- 1000 °C) for 4 hours to produce the crystalline samples. Following this, the calcined sample was allowed to cool to room temperature (RT) and was then ground using an agate mortar and pestle. Employing standardized instrumentation, we systematically examined the crystal structure, micro- and nano-scale morphology, and photoluminescent behavior of the prepared phosphor materials.

2.3. Characterization Techniques

In order to clarify the structural characteristics of the synthesized phosphors and to establish connections between their inherent mechanical, optical, and electrical properties and their functional roles in diverse technological applications, advanced material characterization techniques were essential to this study. The invention and improvement of high performance phosphors suited to certain scientific, technical, and daily applications required thorough investigation. Advanced analytical tools were employed to investigate the phosphors' structural, vibrational, morphological, and luminescent properties. The following sections present detailed explanations of each characterization method, elucidating their theoretical bases and practical implementations. This chapter offers an in-depth review of the experimental tools and methodologies essential for the comprehensive characterization of the synthesized phosphors.

2.3.1. Thermal characterization using TGA & DSC

Upon heating, a substance experiences unique physical and chemical transformations. Physical transformations include phase transitions such as vaporization, melting, crystallization, and processes involving the adsorption, absorption, or desorption of gases. Chemical transformations comprise processes leading to the formation of new compounds by mechanisms such as oxidation, dehydration, corrosion, decomposition, and compound linkage. These alterations take place throughout a broad spectrum of temperatures. Comprehensive characterisation of materials over multiple thermal domains is necessary to establish the exact temperatures at which the compounds remain stable. The analytical techniques applied to examine changes in physical aspects as a function of temperature are collectively referred to as thermal analysis methods.

2.3.1.1. Thermogravimetric analysis (TGA)

This technique entails the continuous monitoring of a substance's mass within a regulated atmosphere, documented as a function of temperature over time. The sample's temperature exhibits a linear increase over time. A thermogram or thermal curve depicts mass or mass percentage as a function of temperature, while its first derivative is termed the derivative thermogram. The fluctuation in a sample's weight due to temperature changes reveals the precise temperature at which the substance undergoes weight loss or growth. The weight loss in the sample indicates the disintegration or evaporation of some initial chemical interaction with the atmosphere present at the time heating process. The temperature at which no weight variations occur signifies the material's stability in relation to thermal conditions. The thermogravimetric setup is illustrated in Fig. 2.06.

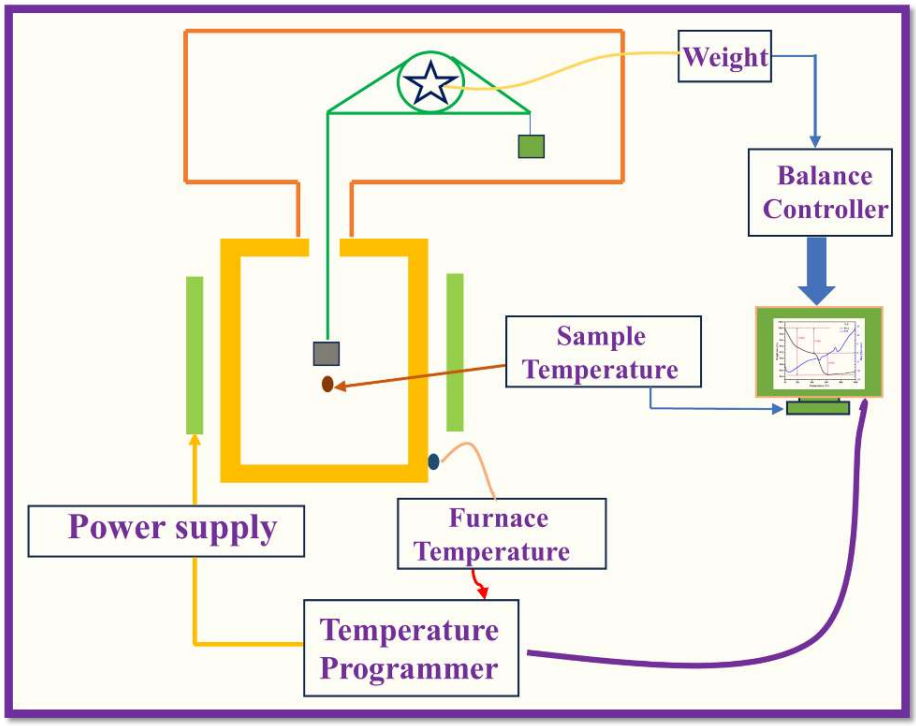

Fig. 2.06: *Thermogravimetric setup.*

2.3.1.2. Differential scanning calorimetric (DSC)

An approach to thermal analysis that is similar to differential thermal analysis (DTA) is differential scanning calorimetry (DSC). The fundamental distinction between DSC and DTA lies in the fact that DSC is a calorimetric technique that measures the difference in energy. On the other hand, temperature fluctuations are recorded in DTA. DSC is an instrument in identifying the endothermic events in which heat flow (ΔH) is positive, and exothermic (ΔH) is negative events that take place in the sample as the temperature varies. DSC is employed in the assessment of melting, phase change, purity evaporation, and material crystallization. The TGA-DSC apparatus is composed of a sample holder that includes sample containers, thermocouples, and either a ceramic or metallic block, along with a temperature programmer, furnace, and recording system.

Fig. 2.07: *TGA-DSC Setaram (Model: LABSYS evo).*

The primary characteristic is the presence of two thermocouples linked to a voltmeter, in which one thermocouple is situated within an inert material, specifically Al_2O_3. Whereas the other is positioned within the sample of the material being investigated. Upon increasing the temperature, a transient deflection of the voltmeter is observed if the sample is experiencing a phase transition. The operating temperatures typically fall within the range of room temperature up to approximately 1600 °C. In this study, thermogravimetric analysis (TGA) - differential scanning calorimetry (DSC) was carried out by Setaram (Model: LABSYS evo), as displayed in Fig. 2.07.

2.3.2. X-ray Diffraction (XRD)

In the domain of materials synthesis, a key focus is the phase identification of the synthesized compounds, ensuring that they possess either the appropriate crystalline structure or amorphous. The phase identification of the materials is analyzed using XRD techniques, which serve as a crucial instrument in materials science for quantifying, identifying, and illustrating single or polycrystalline compounds. XRD patterns reveal the measurement of various crystalline structural properties, including single/multiphase characteristics, defects, purity, stress, strain, and crystallite size. Before discussing the theory of X-ray diffraction, there

is a need to know the two concepts. First is unit cell and second is how the diffraction through the lattice plane happens conveniently. The smallest definite three-dimensional arrangement of atoms containing necessary chemical and structural information of material is known as a unit cell. Crystal is defined as ordered arrangement of the large number of the such unit cells. Individual atoms have three coordinates in the unit cell along the x, y and z axis.

For the diffraction to be happen, the wavelength of X-rays must be matching with the order of unit cell dimensions of the crystal. When X-rays are incident on the sample, scattering is produced in all directions. Intensity is redistributed from the whole scattering sphere to the distinct directions. The XRD technique operates based on Bragg's law, as the monochromatic X-rays interact with crystalline material, which facilitates constructive interference adhering to the principles of diffraction. The diffraction peak is observed when the wavelength of the incident X-ray radiation is comparable to the atomic spacing of the sample, resulting in constructive interference as described by Bragg's law. X-ray radiation was incident on the surface of the sample at various angles θ and was scattered from different lattice planes of the samples. The scattered X-ray radiations were produced by constructive interference when the path travelled by each wave is comparable to an integer multiple of the wavelength, in accordance with Bragg's law [88]:

$$n\lambda = 2d\ sin\theta \tag{2.01}$$

In Bragg's equation, n represents an integer, λ signifies the X-ray wavelength, approximately 1.54 Å for a $CuK\alpha$ source, θ indicates the glancing angle, and d refers to the spacing between planes. The schematic representation of the X-ray diffractometer is illustrated in Fig. 2.08. An X-ray diffractometer featuring a movable X-ray tube, various types of slits, a sample holder, a goniometer, and a rotating X-ray line detector. The X-ray is directed at the positioned sample, which is oriented at an angle θ relative to the trajectory of the incident X-ray beam. The

goniometer is capable of controlling the rotation angle of both the sample and the detector. When the incident X-ray subsequently strikes the surface of the sample and satisfies Bragg's

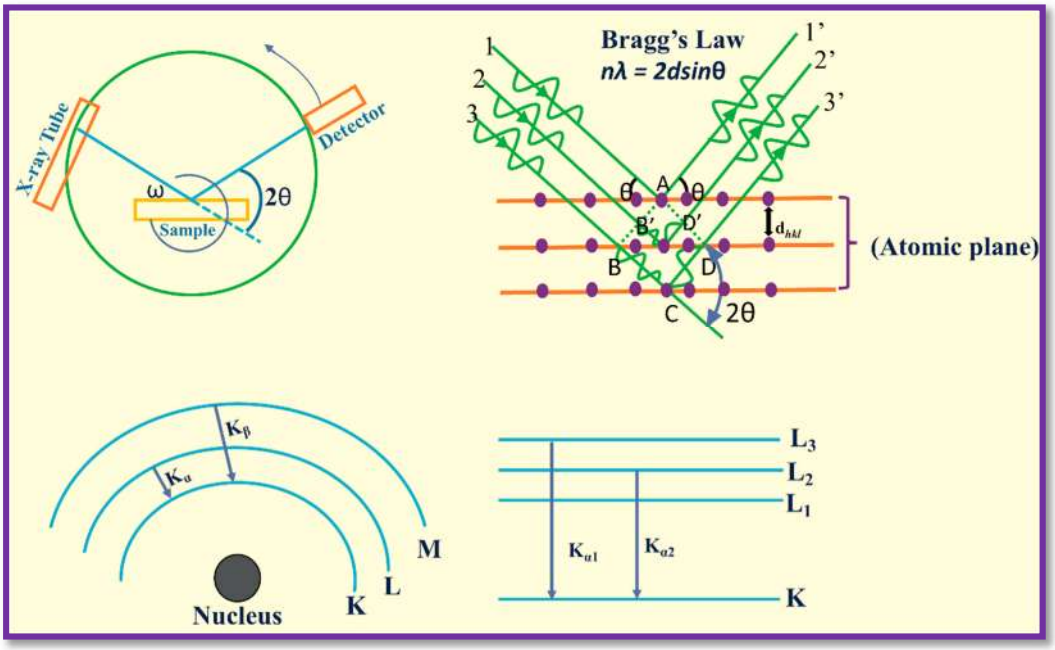

Fig. 2.08: *XRD instrumentation and diffraction of X-rays.*

equation, constructive interference occurs. The detector operates at an angle of 2θ relative to the trajectory of the incoming X-ray beam, enabling it to identify the diffracted X-ray signals and convert them into a count rate. The detected X-ray counts were directly input into the computer, which generated a graph plotting the X-ray counts against the angle 2θ for further processing. The Rigaku Smart Lab advanced X-ray diffractometers were employed to obtain the XRD profiles for the prepared crystalline powder samples, as illustrated in Fig. 2.09. The recorded XRD crystalline patterns were compared with the available standard data from the JCPDS (Joint Committee on Powder Diffraction Standards) to identify the most appropriate matched patterns. The matched standard data provides information regarding crystal structures, including unit cell parameters, Wyckoff positions, space groups, and more. Various structural studies, including Rietveld refinement, have been conducted using this information.

Fig. 2.09: *Rigaku Smart lab advance X-ray diffraction machine.*

Additionally, from the XRD patterns utilizing the positions of crystalline peaks and corresponding peak broadening , one can estimate the crystallite size of the material sample through the application of Debye Scherrer's formula and the Williamson Hall (W-H) equation as outlined in references [89,90]:

$$D = \frac{K\lambda}{\beta Cos\theta} \tag{2.02}$$

$$\beta Cos\theta = \frac{K\lambda}{D} + 4\varepsilon Sin\theta \tag{2.03}$$

where D represents the average crystallite size, K denotes the shape factor (typically ~0.94), λ indicates the X-ray wavelength (1.54 Å, for CuK_α radiation), θ is the Bragg's diffraction angle, ε signifies the microstrain, and β refers to the full width at half maxima (FWHM). The FWHM is primarily affected by the small size of the crystallites and the microstrain present in the sample. The estimation of the average crystallite size and lattice strain was conducted through the analysis of the plot of $\beta Cos\theta/\lambda$ versus $Sin\theta/\lambda$. The plot illustrates that the slope

signifies the microstrain in the prepared powder sample, while the reciprocal of the y-axis intercept provides an estimate of the average crystallite size (D) of the material sample.

2.3.3. Rietveld Refinement Analysis

Since its invention in the late 1970s, the Rietveld method has been widely used to refine crystal and magnetic structures based on obtained X-ray or neutron diffraction patterns [91]. A variety of phase analysis and quantitative methods have been developed based on XRD data. The Rietveld refinement is a method introduced by Hugo M. Rietveld. It is widely recognized for its comprehensive pattern fitting approach rather than focusing on single peak analysis. Rietveld refinement analysis techniques demonstrate several advantages, as they can effectively reduce or eliminate inaccuracies stemming from preferred particle statistics, orientation, peak overlapping, and the detection of trace phases. The Rietveld method employs a least squares fitting analysis to refine a theoretical line profile through multiple iterations, aligning it with the measured profile. The least square refinement method refines the structure, lattice parameters, atomic positions, and occupancies, until the best fit is obtained between the observed powder diffraction pattern and the calculated pattern, and gives quantitative information on phase percent, crystallite size, and micro-strain [92].

Refinement parameters, including background, peak shape, and lattice parameters, can be optimized utilizing Rietveld refinement software such as Full Prof Suite. The peak shape and background were characterized using a pseudo Voigt function and linear interpolation among a defined set of background points, respectively. The Rietveld refinement offers significant benefits for quantifiable phase analysis, space group symmetry, residual stress assessment, crystal structure determination, and microstructural analysis.

2.3.4. Diffuse Reflectance Spectroscopy (DRS)

The DRS represents a distinctive characterization technique for investigating the optical phenomena associated with powder samples. DRS provides molecular spectroscopic information of the powder sample with minimal sample preparation across the UV to infrared regions. A DRS spectrum is obtained through the collection and analysis of surface reflected electromagnetic radiation across the wavelength range from ultraviolet to infrared. There are primarily two types of reflection that can occur: the first is specular or regular reflection, which takes place on smooth, polished surfaces, and the second is diffuse reflection, which occurs on dull or matte surfaces, such as powders. These types of internal or exterior reflection provide the materials' spectroscopic information, as illustrated in Fig. 2.10.

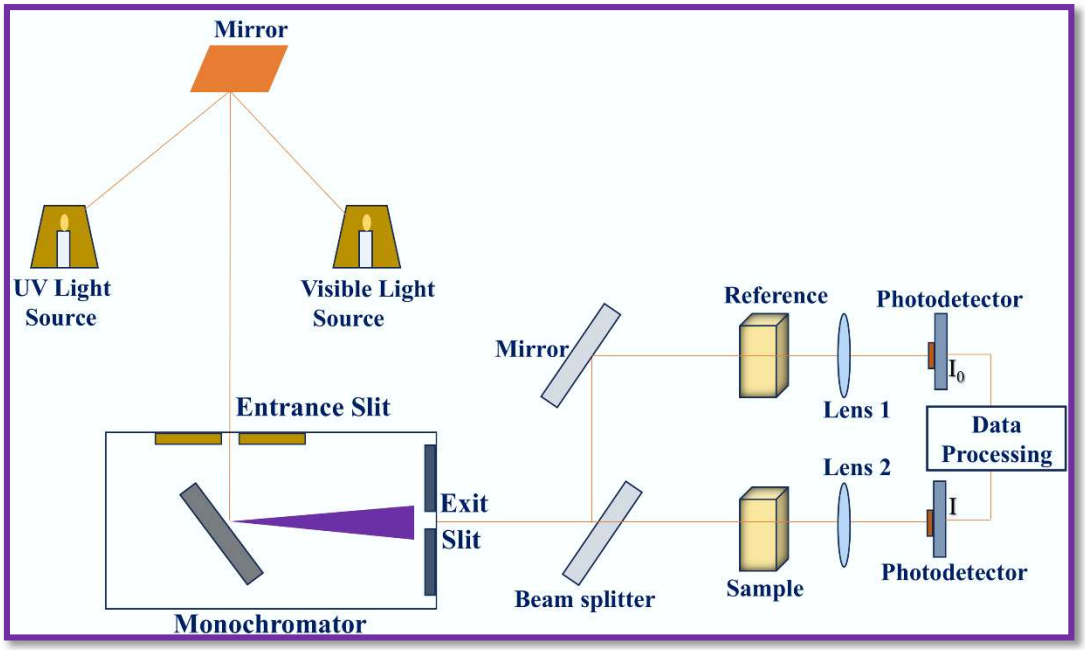

Fig. 2.10: *Schematic representation of a UV-VIS spectrophotometer.*

An opaque sample with a nonuniform surface that scatters incident light in various directions can be characterized using DRS techniques. The DRS profile was obtained using a Jasco spectrophotometer, model V770, as illustrated in Fig. 2.11. The spectrophotometer comprises a light source, monochromators, a standard reference sample ($BaSO_4$), a UV-Vis NIR detector,

an amplifier, and a computer equipped with appropriate software for data recording. Computers that are equipped with the necessary software can function as recording devices, effectively capturing all data and visualizing the recorded spectrum [93].

Fig. 2.11: *UV-VIS spectrophotometer made by Jasco, model V770.*

The DRS profile illustrates the various absorption peaks across different wavelength ranges, which depend on the sample host and activator ions. The optical bandgap can be estimated using the Kubelka Munk function based on the recorded spectrum. The optical (E_g) bandgap was determined using the following equation [94,95].

$$F(R)h\nu = C\left(h\nu - E_g\right)^n \tag{2.04}$$

In this context, $h\nu$ represents the incident photon, while C denotes a constant. The variable n specifies the type of transition, with values of 1/2 and 2 corresponding to direct and indirect allowed transitions, respectively. The Kubelka-Munk function $F(R)$ has been evaluated [34,96]:

$$F(R) = \frac{(1-R)^2}{2R} = \frac{\alpha}{S} \tag{2.05}$$

In the equation presented, α represents the absorption coefficient, R is defined as reflectance, and S denotes the scattering coefficient. $F(R)$ exhibits a direct proportionality to

the absorption coefficient, given that S remains independent of wavelength. A graph depicting the relationship between $[F(R)hv]^2$ and incident energy hv allows for the determination of the x-axis intercept by extrapolating the slope to $\alpha = 0$. The x-axis intercept represents the optical bandgap of the sample.

2.3.5. Field Emission Scanning Electron Microscope (FE-SEM)

Field emission scanning electron microscopy (FE-SEM) is an advanced instrument to capture the nano/micro-structure image of high resolution of the testing sample.

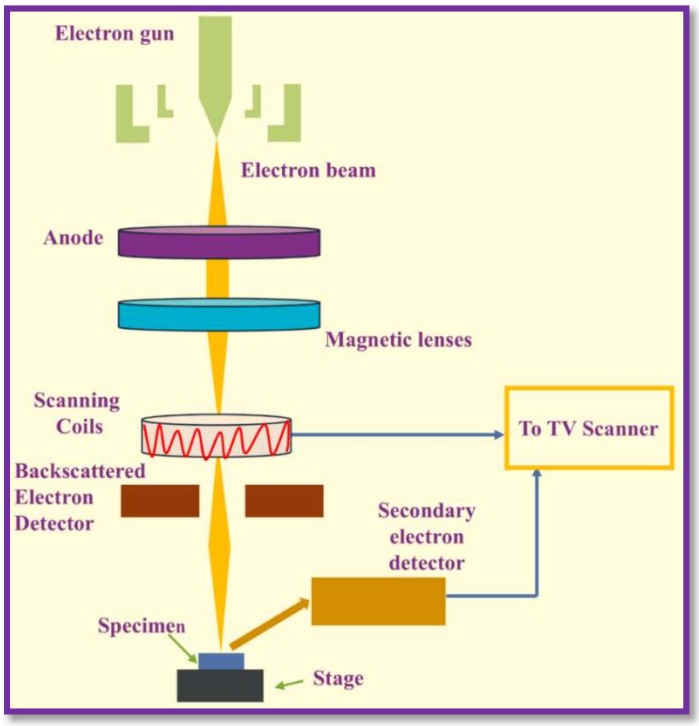

Fig. 2.12: *Schematic illustration and working of FE-SEM.*

FE-SEM is a crucial tool utilized for examining the morphology, including particle shape, size, and arrangement, as well as the topography, and degree of disorder of solid specimens. It provides direct visualization of the cross-section and surface of the material, either in powder form or coated on the glass substrate. FE-SEM generates high resolution images of a sample by meticulously scanning its surface with a focused electron beam. The signals emitted by

electrons during interactions with the sample provide insights into the specimen, encompassing the external morphology of the solid materials [97].

Fig. 2.13: *FE-SEM, Zeiss Supra-55.*

It is performed in high vacuum to avoid the disturbances in the path of the electron beam caused by gas molecules present in the surroundings of the sample. Image of the sample surface is produced by the bombardment of highly energetic electron beam, several electron lenses, a sample stage, multiple detectors (including secondary electrons, backscattered electrons, and an X-ray detector), and a scanning coil, as illustrated in Fig. 2.12.

A field emission gun made of tungsten filament is used as an electron emitter in a high vacuum environment. Electron beams are produced through field emission or thermionic emission processes utilizing an electron gun positioned at the top of the microscope. The generated electron beam accelerates downward in a vacuum, influenced by a strong electrical field potential gradient, while traversing through an anode to produce a focused beam. The primary electron beam is deflected and focused through a series of electronic lenses, resulting in a finely directed electron beam. The scan coils regulate the positioning of the electron beam in relation to the objective lens. The coils facilitate the scanning of the beam across the sample's surface, thereby enabling the collection of information pertaining to a specific area. The interaction between the sample and the electron results in the production of various signals, including secondary electrons, backscattered electrons, and characteristic X-rays. These signals are subsequently detected by detectors, which generate an electronic signal. The electronic signal facilitates imaging through two distinct modes: the first involves utilizing the detected secondary electron signal, while the second employs backscattered electrons. The electronic signal information was collected on the cathode ray tube, which is displayed on a computer screen. Computers equipped with appropriate software can operate as recording devices, capturing all data and visualizing the microscopic images of specimens [97]. In this work, Field emission scanning electron microscope (model: ZEISS, SUPRA-55) is used as shown in Fig. 2.13.

2.3.6. Energy Dispersive X-Ray Spectroscopy (EDX)

Energy dispersive X-ray spectroscopy (EDX) is a characterization technique used to detect the elements and also examine the weight percent of the elements in the particular area of the sample. It is also employed to map out the presence of the elements in the mapping area [33]. The EDX setup is attached to the FE-SEM. The EDX instrument has very high sensitivity (< 0.1%) for each element present in the periodic table. It is a non-destructive technique.

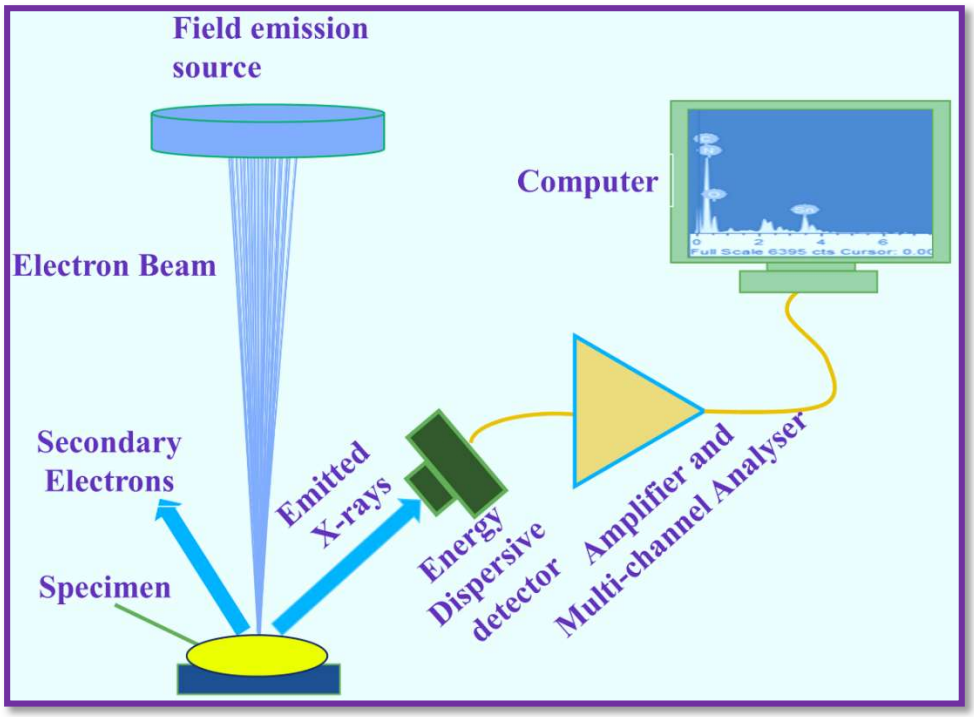

Fig. 2.14: *Schematic illustration of the EDX working and instrumentation.*

The principle of EDX is based on the bombardment of electrons on the sample surface which caused to detect X-rays on the detector. In this case, X-rays are produced when atoms are excited to the upper level and releases enough amount of energy. X-ray energy produces distinct peaks in the EDX spectrum for the different elements. Schematic representation of the working of EDX instrument is shown in Fig. 2.14. In this work, EDX analysis was done by instrument (model: Oxford Liquid Nitrogen free SDD X MAX 50 EDS).

2.3.7. X-Ray Photoelectron Spectroscopy (XPS)

X-ray photoelectron spectroscopy (XPS) is a characterization technique used to confirm the presence of the elements as well as their chemical oxidation states on the surface of the sample. The working principle of XPS is based on the well-known photoelectric effect. In this phenomenon, when X-rays of high energy (200 eV - 1400 eV) are bombarded on the sample, core electrons are ejected, having kinetic energy (E_k), which is shown in Fig. 2.14. As per

Einstein's photoelectric principle kinetic energy (E_k) of electrons is calculated by following relation:

$$E_k = h\vartheta - E_b - \emptyset_s \qquad (2.06)$$

where $h\vartheta$ stands for energy of the incident X-rays, E_b is denoted as binding energy of the chemical oxidation states and $\emptyset_s$ is defined as the work function. XPS is performed in the ultrahigh vacuum to minimize the reaction of the sample to the water molecules and gases present in the atmosphere. When electrons are ejected in the ultra-high vacuum chamber, they are collected by the electron energy analyser, which determines their kinetic energy. The ejected electrons are then counted by the electron detector, providing information to the computer system. Thus, the information collected from electron detector and electron analyser will produce the spectrum (intensity vs binding energy) which exhibit distinct peaks for each and every element present in the sample. In the thesis work, XPS spectra were recorded using the PHI 5000 Versa Probe III. Working principle and instrumentation is demonstrated schematically in the following Fig. 2. 15.

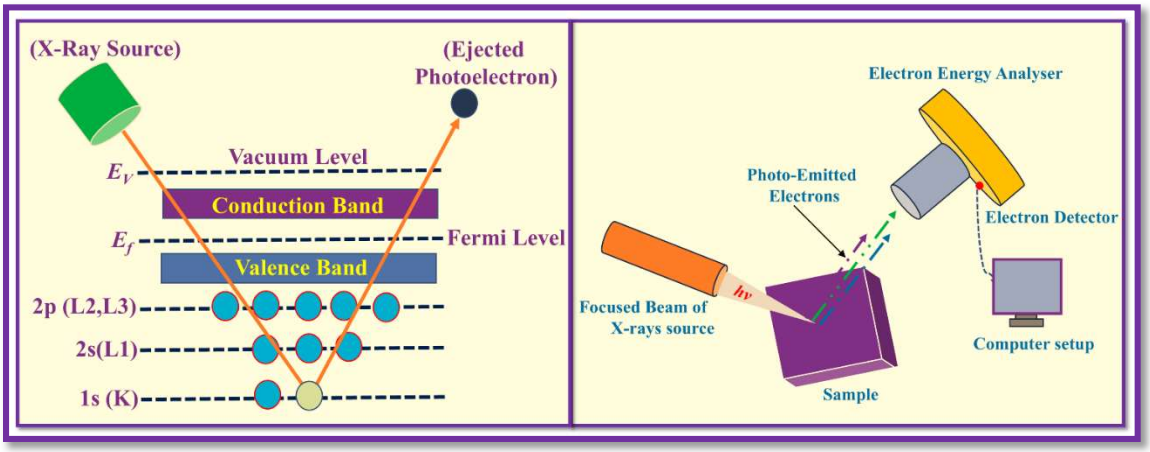

Fig. 2.15: *Energy level diagram and schematic illustration of XPS setup.*

2.3.8. Photoluminescence Spectroscopy

PL spectroscopy is a non-destructive, versatile technique that allows for contact free measurement of photo excitation and emission in various light sensitive materials, including

powders, liquids, glasses, and thin film samples. PL studies have been recognized as one of the most sensitive and commonly employed tactics for exploring the luminescent properties. Typically, a beam of radiations is directed onto a sample, where a portion of the light is absorbed, leading to excitation. This is followed by de-excitation, which occurs through the release of radiative emissions, primarily in the visible region, alongside some non-radiative relaxations [42,98]. PL spectroscopy is powerful technique to examine excitation/emission characteristics, concentration quenching and radiative/non-radiative relaxations in the light influenced materials. PL spectroscopy can offer applicability in the fields of molecular electronics, environmental sciences, medical diagnostics, industries, cell biology, and day to day life devices.

The PL spectrofluorophotometer comprises an excitation light source, monochromator, sample cell, a number of lenses, photodetector, amplifier etc. and connected with computer, and records the experiential spectrum as demonstrated in Fig. 2.16. The excitation source utilized must provide a continuum spectrum within the specified wavelength range. The xenon lamp offers a moderately continuous light output and serves as a light source, emitting light within the 220-800 nm range. The emitted light beam is passing the monochromator in which collimated light illuminates a grating and leavings with a different angle depending on the wavelength. Excitation monochromator is select the particular wavelength of light from incident beam. A portion of incident light is absorbed by the sample, and emits light in all directions. The light is emitted at angle of 90 ° and some of the light passes through the emission monochromator and reaches detector. The emitted light detected by the photomultiplier tube as detector. Detector can be a single-channel (senses only one wavelength at a time) or multichannel (detects all emitted wavelength). Finally, the detected spectrum by the photomultiplier tube is amplified, converted in signal form and recorded by computer for

further investigation. The observed spectrum displays on the computer screen in terms of intensity as a function of the wavelength of emitted light.

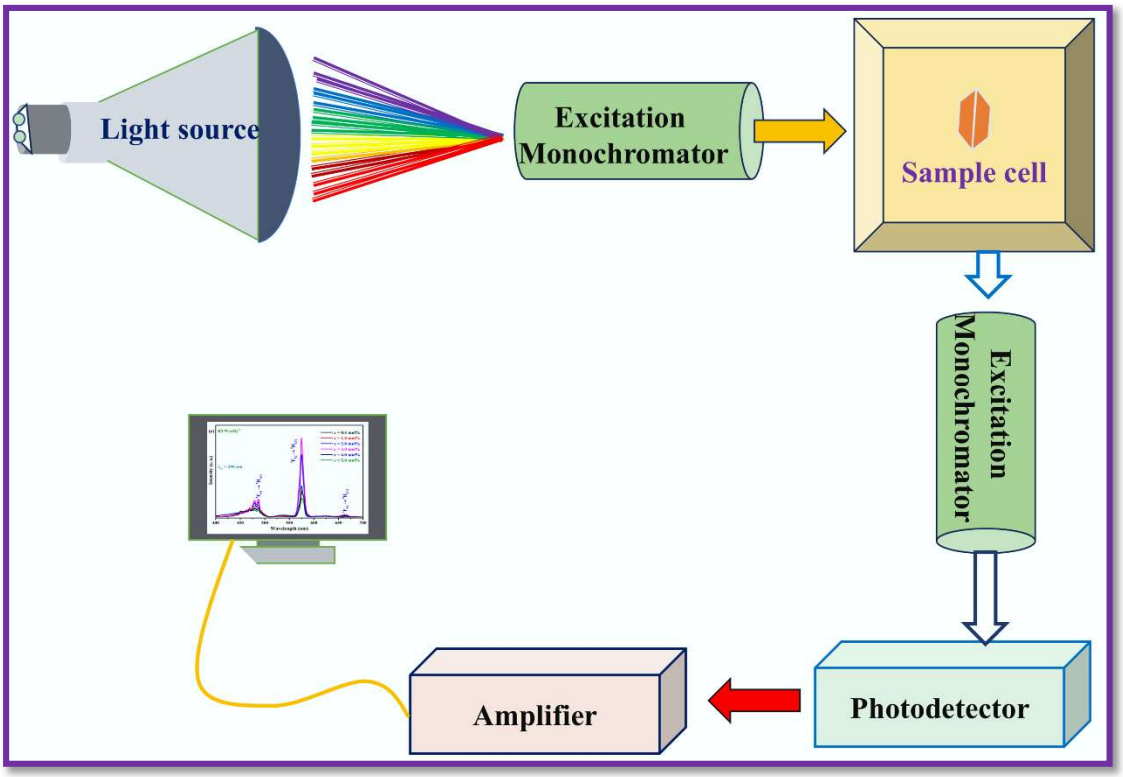

Fig. 2.16: *Schematic representation of PL spectrofluorophotometer.*

PL is the physical phenomena in which emission of light obtained from material under various excitation wavelengths of light source. The PL characteristics were recorded by Shimadzu, RF-5301PC spectrofluorophotometer equipped with 150-watt Xenon lamp as a source of excitation as seen in Fig. 2.17. To record the PL characteristics, initially sample holder is completely filled with prepared phosphor, placed at appropriate position in the path of incident source of excitation beam. The excitation and emission spectra were obtained by selecting the suitable emission/excitation wavelength using scan mode at a moderate scan rate, with a slit width of 0.1 nm and a high voltage PMT configuration. The excitation profile is derived by observing a specific and constant emission band within a defined range of wavelengths.

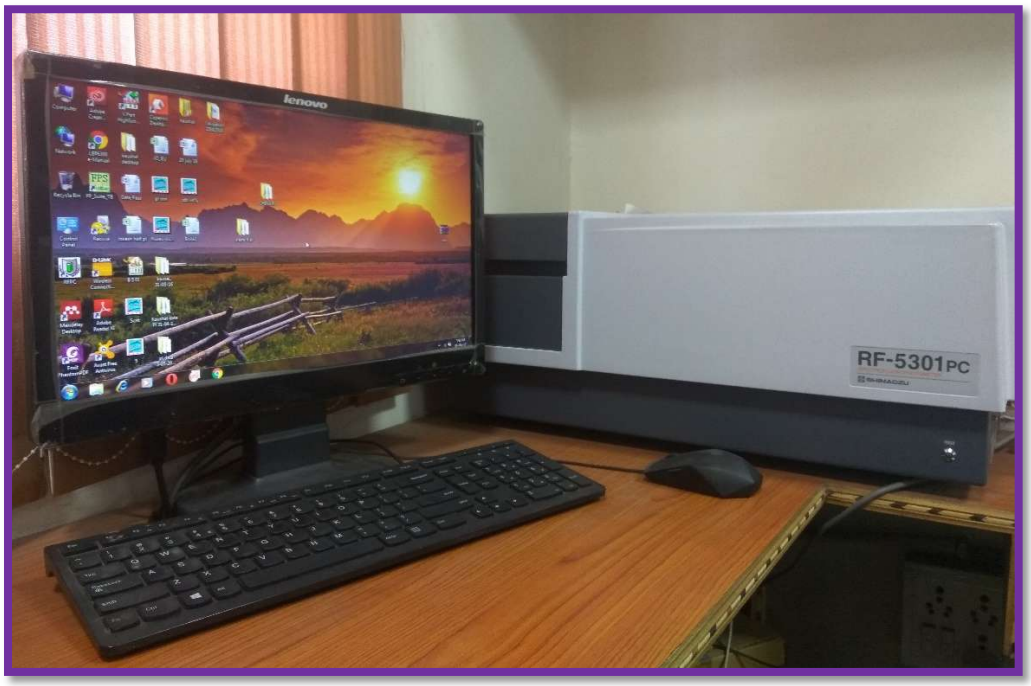

Fig. 2.17: *Shimadzu, RF-5301PC spectrofluorophotometer connected with a computer.*

The identified bands in the excitation spectrum will subsequently be utilized to record the emission spectrum. Ultimately, the software presents the spectrum through a plot that illustrates the relationship between the intensity of emitted light and wavelength.

2.3.9. Time Resolved Photoluminescence (TRPL) Spectroscopy

TRPL represents a prominent option for investigating the rapid and gradual electronic deactivation processes that lead to photon emission from specific excited energy levels in luminescent materials when subjected to particular excitation source, a phenomenon referred to as PL decay time or lifetime. The PL lifetime is an intrinsic property of a luminescent materials, which provides the understanding into the material excited state dynamics. The PL lifetime of any luminescent materials can be influenced by the molecular environment such as presence of ions, solvent, temperature, quenchers as well as interactions with other molecules. PL Lifetime variations can therefore provide evidence about the local chemical environment of the materials.

The essential elements of TRPL include a pulsed light source, such as a Xenon flash lamp or pulsed laser, an excitation and emission monochromators, and a single-photon sensitive detector, all managed by computers equipped with specialized software. A pulsed light source serves as the excitation source, while a rapid photodetector is employed to capture the emission of a sample over time in response to the designated excitation source. This system is applicable for describing material quality, identifying spectral emissions with specific emissive states, or investigating energy transfer properties in mixed composites or samples. The recorded lifetime serves as an inherent attribute of photoluminescence properties, offering valuable insights into the excited state dynamics of the species [99,100].

Fig. 2.18: Horiba PTI Quanta Master 8450-11 *fluorometer.*

The PL lifetime curves were recorded at room temperature by Horiba PTI Quanta Master 8450-11 fluorometer as seen in Fig. 2.18. Microsecond Xenon flash lamp source and single photon count photomultiplier tube detector attached with the instrument.

The PL lifetime curves were fitted with different exponential equations. It can be observed that all the decay curves were fit biexponentially with the following equation [101,102]:

$$I(t) = I_o + A_1 exp\left(-\frac{t}{\tau_1}\right) + A_2\, exp\left(-\frac{t}{\tau_2}\right) \quad (2.07)$$

where $I(t)$ and I_o signify the luminescence intensities at time *t* and *0*, respectively. A_1 and A_2 are fitting constants. τ_1 and τ_2 represent the rapid and slow decay lifetimes for exponential mechanisms. The average value of the decay time for samples was evaluated from given formula [103]:

$$\tau_{avg} = \frac{A_1\tau_1^2 + A_2\tau_2^2}{A_1\tau_1 + A_2\tau_2} \quad (2.08)$$

The PL lifetime for the RE ions doped luminescent materials usually ranges from a few microseconds to milliseconds.

2.3.10. Temperature Dependent Photoluminescence (TDPL) Spectroscopy

TDPL spectroscopy represents one of the most powerful, fundamental, and widely utilized techniques for probing thermal stability of luminescent materials. In this approach, PL spectra of the synthesized luminescent materials are systematically recorded over a range of temperatures to monitor the evolution of PL characteristics as a function of temperature. The temperature dependent PL data serves as a basis for elucidating thermal stability, defect-induced nonradiative recombination processes, and carrier transport mechanisms within the material system.

The key components of a TDPL spectrofluorophotometer include a light source (typically a Xenon lamp or laser), monochromator, temperature controlled sample holder, photodetector, and computer system equipped with the dedicated data acquisition and analysis software, as illustrated in Fig. 2.19. In the present study, a Xenon lamp, emitting broadband radiation in the 200-800 nm range. The emitted light is directed through a monochromator, which isolates the desired excitation. The selected wavelength is then guided via an optical fiber to the temperature controlled sample holder, where it excites the luminescent sample. Upon excitation, the sample emits the PL spectrum, which is collected through another optical fiber and subsequently detected by a photodetector. The resulting emission spectra are recorded

and processed using a computer interface. For the present investigation, the TDPL characteristics of the synthesized phosphor materials were measured using an Ocean Optics (FLAME-S-XR1-ES) spectrofluorophotometer as demonstrated in Fig. 2.20.

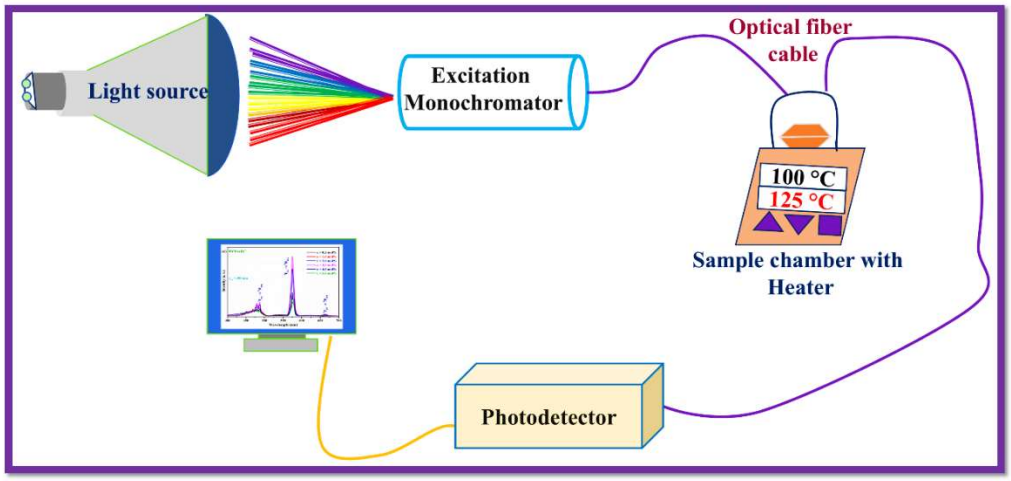

Fig. 2.19: *Schematic representation of TDPL spectrofluorophotometer.*

In TDPL data, the emission intensity of luminescent materials under certain source of excitation wavelength can be increased/decreased with elevated temperatures. The effect of temperature on the photoluminescence properties of phosphor materials is one of the significant features of the applicability of phosphor in various photonic applications. Typically, phosphors used in lighting devices require high thermal stability as the UV/blue LED chips generate temperature around 120 to 150 °C while operating time. Based on TDPL spectra recorded at elevated temperatures, a methodological theory has been established to examine the thermal stability of luminescent materials. The (ΔE) activation energy is one of the crucial parameters for the phosphor to identify the thermal stability of luminescent materials, which was reckoned using the Arrhenius equation as [104]:

$$I_T = \frac{I_o}{1+C\ exp\left(-\frac{\Delta E}{K_B T}\right)} \tag{2.09}$$

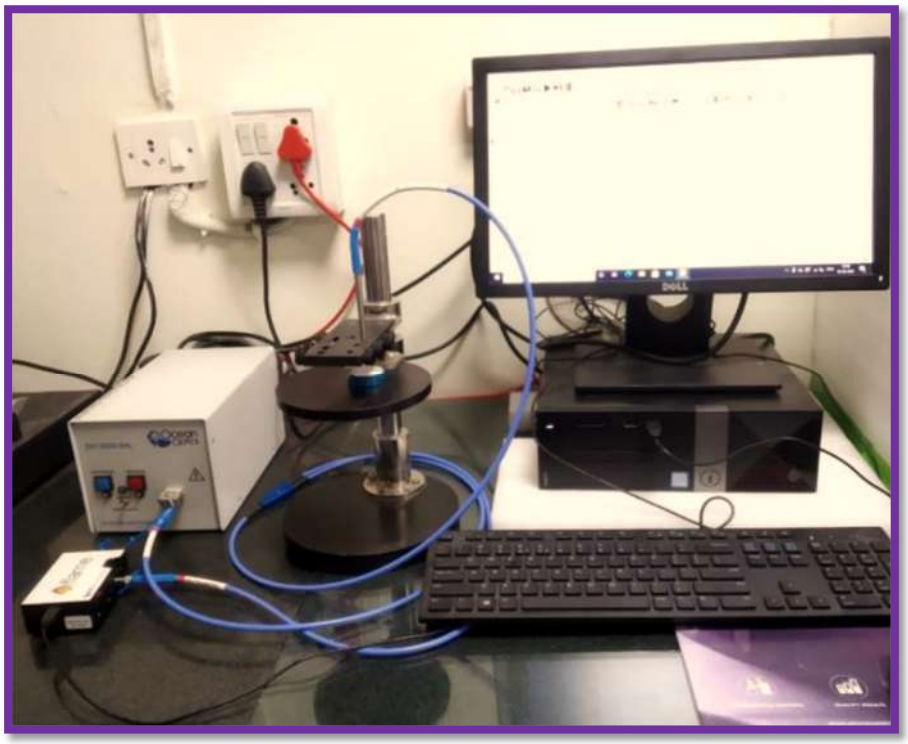

Fig. 2.20: *TDPL characterization setup with ocean Optics spectrofluorophotometer.*

where, I_0 and I_T represents the PL intensity at initial or room temperature and at a specific temperature *T (K),* respectively. C and k_B signify an arbitrary constant and the Boltzmann constant, respectively. As per the Arrhenius equation, the activation energy ΔE was assessed on the basis of linear fitted slope among $ln[(I_o/I_T)-1]$ and $1/K_BT$ [105,106].

CHAPTER 3

Red Light Emitting Eu^{3+} Doped Bismuth Yttrium Tungstate Phosphor for Solid State Lighting Applications

The current chapter includes the synthesis of the crystalline monoclinic phase of Eu^{3+} doped bismuth yttrium tungstate (BYW: Eu^{3+}) phosphors via the sol-gel combustion (SGC) method. X-ray diffraction (XRD) confirms the pure monoclinic crystalline phase formation of the BYW: Eu^{3+} phosphors. The irregular shape and agglomerated dense packaging of the particles of BYW: Eu^{3+} phosphors have been revealed with the help of field emission scanning electron microscopy (FE-SEM) analysis. Defuse reflectance spectra (DRS) revealed the numerous absorption peaks in the UV and visible regions. When excited with blue light, the BYW: Eu^{3+} phosphors radiate several emission peaks and an intense emission peak has been observed at 613 nm (red region). CIE coordinates of the BYW: Eu^{3+} phosphors are positioned in the red region of the chromaticity diagram. The aforementioned results of the BYW: Eu^{3+} phosphors indicate their promising properties for usage in the field of white light emitting diodes (w-LEDs) and other photonic device applications.

3.1. Introduction

Luminescent materials based on rare earth/transition metal ions have attracted significant attention from researchers/scientists owing to their direct applicability in photonic/optoelectronic devices [107–109]. In the field of modern lighting, phosphor-converted white light emitting diodes (pc-w-LEDs) have emerged as a leading technology for the next generation of solid state lighting (SSL) sources. With rapid advancements, pc-w-LEDs are expected to replace traditional incandescent and fluorescent lamps owing to their numerous advantages, including superior brightness, high luminous efficiency, reduced energy consumption, compact size, enhanced durability, and environmental friendly operation [110,111].

Commercially available pc-w-LEDs often emit a bluish white light with high correlated color temperature (CCT), mostly owing to a deficit of red spectral component. To address this constraint and produce warm white light suitable for advanced lighting applications, the incorporation of an efficient red emitting phosphor is indispensable [3,112]. Furthermore, red emitting phosphor plays a vital character in achieving the desired correlated color temperature and enhancing the color rendering index (CRI), both of which are vital for generating high quality white light [107,113,114]. However, many commercially available blue pumped red emitting phosphors, including nitrides and sulfides, suffer from reduced luminescent efficiency and poor chemical stability [115,116]. Additionally, the heat generated by LED chips during operation can adversely affect the luminescent properties of phosphors, leading to diminished emission intensity and, consequently, reduced functioning of pc-w-LEDs [104,117]. Therefore, thermal stability is a key factor in evaluating the reliability and performance of w-LEDs. This emphasizes the urgent need to develop novel, efficient red emitting phosphors with good thermal and chemical stability.

The thermal stability and emission efficiency features of the phosphors are highly dependent on the appropriate selection of both host materials and dopant RE ions. Nevertheless, the host material not only serves as a structural matrix to accommodate dopant ions in close proximity but also plays a crucial role in sensitizing their luminescence [118,119]. Due to the critical demand for efficient red emitting phosphors in the development of SSL devices, particularly w-LEDs, a wide range of host materials have been explored and synthesized so far. Amongst various inorganic host lattices, oxide-based materials known as exceptional candidates for a wide range of photonic applications. Tungstates, in particular, are known for their structural versatility and have emerged as promising hosts, with certain crystal phases exhibiting notable photoluminescent properties upon doping with suitable activator ions [120,121]. Bismuth based perovskite monoclinic tungstate ($BiYWO_6$) has been identified as a promising host material to develop as red emitting phosphors suitable for solid state lighting applications. $BiYWO_6$ has been synthesized using sol-gel combustion synthesis technique and is regarded as an excellent host material, especially for the development of high performance luminescent devices.

RE ions typically exist in either trivalent or divalent oxidation states and exhibit a sequence of well defined emission and excitation peaks, attributed to their exceptional radiative recombination rates and distinct (*f-f*) energy levels. Amongst all RE ions, europium (Eu^{3+}/Eu^{2+}) ions are particularly notable and widely utilized as activators in numerous applications, including photoluminescence, biological fields, optical data storage and electroluminescence. Their popularity stems from the availability of multiple energy levels, which allow for versatile emission characteristics across a broad spectral range [122,123].

In this study, $BiYWO_6$ phosphors doped with Eu^{3+} ions were synthesized with the help of the sol-gel combustion (SGC) method. An investigation was carried out to evaluate their structural, morphological, photoluminescence, time resolved photoluminescence (TRPL),

and temperature dependent photoluminescence (TDPL) properties of the Eu^{3+} activated $BiYWO_6$ phosphor, highlighting their potential for use in the field of w-LEDs and other advanced photonic devices.

3.2. Materials and synthesis of BYW: Eu^{3+} samples

In sol-gel combustion (SGC) synthesis, the precursors employed for the manufacture of BYW: $x Eu^{3+}$ (x = 0.0 to 9.0 mol%) phosphor, such as $Y(NO_3)_3{\cdot}6H_2O$, $H_{42}N_{10}O_{42}W_{12}$, $Bi(NO_3)_3{\cdot}5H_2O$, Eu_2O_3, citric acid, and ethylene glycol, were taken in stoichiometric ratio. The detailed synthesis process was explained in section 2.2.2. in chapter 2. The BYW: Eu^{3+} phosphor sample obtained at 900 °C from SGC for further characterization.

3.3. Results and discussion

3.3.1. Structural analysis

Fig. 3.01 exemplifies the diffraction patterns of the synthesized BYW: $x Eu^{3+}$ (x = 0.0, 1.0, 5.0, and 9.0 mol%) phosphors calcined at 900 °C along with standard data (JCPDS-33-0224). The diffraction profiles of the BYW: $x Eu^{3+}$ phosphors exhibit good agreement with the diffraction peaks of the standard data (JCPDS-33-0224) for 2θ values, with no impurities detected in the synthesized phosphor. This confirms that the BYW host lattice has a pure crystalline monoclinic structure along with lattice parameters, a = 8.1235 Å, b = 3.7535 Å, and c = 16.0351 Å in the space group P2/a. The absence of peaks other than those corresponding to standard data indicates the successful incorporation of the dopant ions into the BYW host lattice. The ionic radii with a coordination number of six are as follows: Bi^{3+} = 1.03 Å, Y^{3+} = 0.90 Å, and Eu^{3+} = 0.947 Å. This indicates that the ionic radius of the Eu^{3+} ion was less than that of the Bi^{3+} ion, while both possessed the same ionic state. As a result, Eu^{3+} ions can efficiently substitute with Bi^{3+} ions. Consequently, Eu^{3+} ions were expected to predominantly occupy the Bi^{3+} site, with the possibility of occupying the Y^{3+} site at higher concentrations of Eu^{3+} ions. As the doping level of the Eu^{3+} ion increases, the diffraction

patterns exhibit a minor shift towards lower angles, which can be attributed to the increased strain within the crystal lattice [124,125].

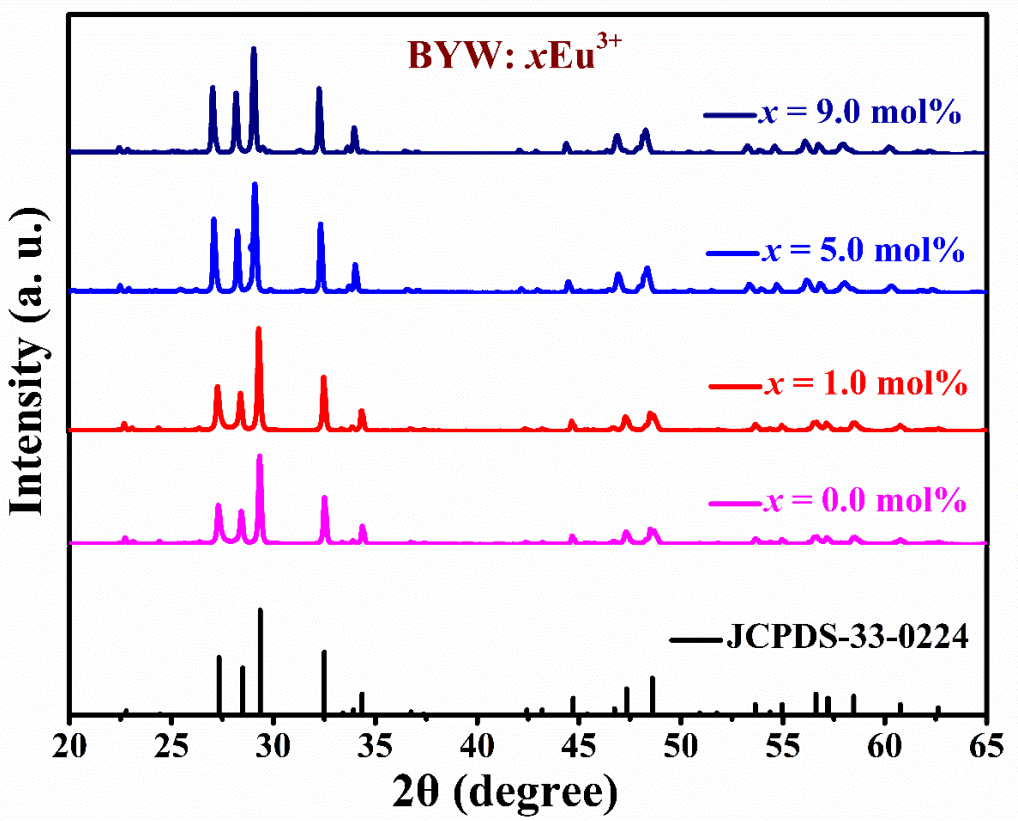

Fig. 3.01: *X-ray diffraction patterns of $BiYWO_6$: Eu^{3+} phosphor.*

It has also been noted that Bi^{3+}/Y^{3+} ions occupied identical crystallite sites within the BYW crystal structure, which was derived from Bi_2WO_6 [126]. The BYW host material consists of alternating Aurivillius type $[BiYO_2]^{2+}$ layers interconnected with the $[WO_4]^{2-}$ type of layers. The Y^{3+}/Bi^{3+} ions are randomly distributed throughout the BYW unit cell, as per the specified crystal structure [127]. The average crystallite size (D) of the synthesized BYW: xEu^{3+} phosphors were computed using Debye Scherer's equation, as depicted in equation no. (2.02) in the section 2.3.2 [33]. The D values for the synthesized BYW: xEu^{3+} phosphors were observed in the range of 14 to 60 nm.

3.3.2. Morphological studies

Fig. 3.02(a) illustrates the surface morphology of the synthesized BYW: xEu^{3+}, x = 1.0 mol% phosphor, at a nano scale resolution.

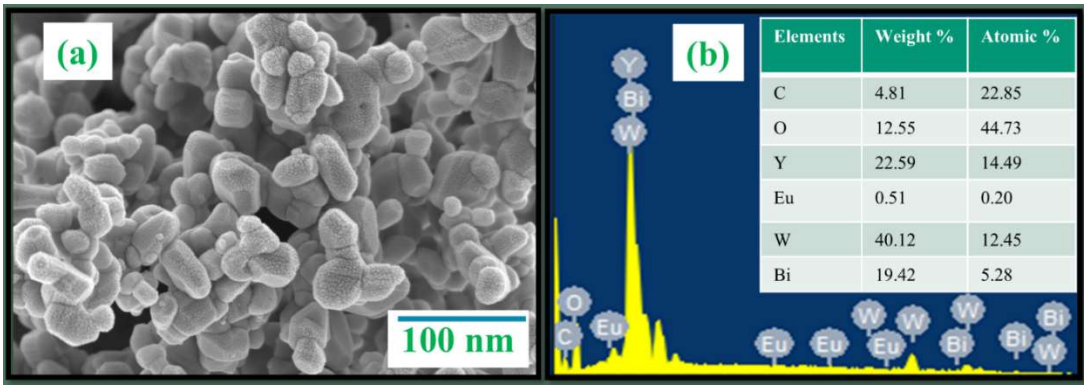

Elements	Weight %	Atomic %
C	4.81	22.85
O	12.55	44.73
Y	22.59	14.49
Eu	0.51	0.20
W	40.12	12.45
Bi	19.42	5.28

Fig. 3.02: *(a & b) FE-SEM micrograph and EDX pattern of the 1.0 mol% Eu^{3+} doped $BiYWO_6$ phosphor (Inset shows the table of elemental composition).*

The synthesized BYW: xEu^{3+}, x = 1.0 mol% phosphor exhibits an uneven morphology, significant grain growth with less agglomeration, which may be due to the proper calcination temperature of the synthesized phosphor. The BYW: xEu^{3+} phosphor synthesized using the SGC technique is influenced by the proportions of water as well as various reactants, including surfactants and chelating agents in the initial precursors, which results in improved grain development of the morphology [128]. Micro to nanometer sized crystalline particles are potentially effective for luminescence and are highly beneficial in solid state lighting applications.

Fig. 3.02(b) demonstrates the EDS results, which show the consistent presence of various elements in the synthesized BYW: xEu^{3+}, x = 1.0 mol% phosphor. The compositional analysis confirms that the synthesized phosphor contains bismuth, oxygen, tungsten, europium, and yttrium, validating the successful synthesis of the BYW: Eu^{3+} sample. Moreover, the weight and atomic percentage of each element in the BYW: xEu^{3+}, x = 1.0 mol% phosphor are shown in the inset table of Fig. 3.02(b).

3.3.3. Optical band gap studies

The DRS profile of the BYW host material was recorded at RT in the range of 200-1200 nm, as depicted in Fig. 3.03.

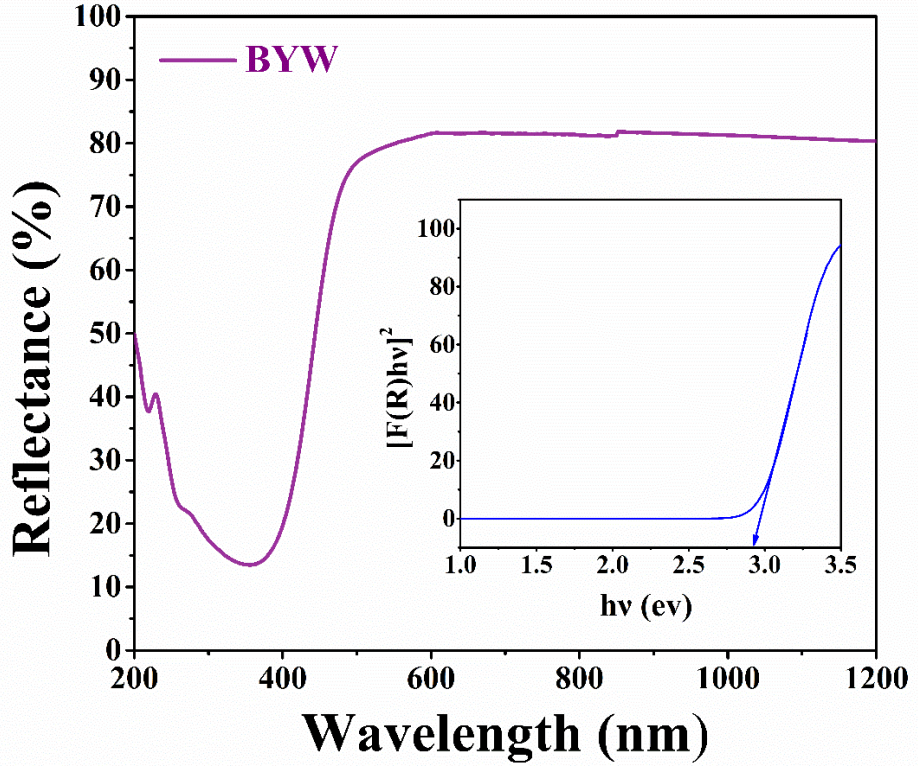

Fig. 3.03: *DRS profile of BYW host lattice. Inset represents the assessment of the band gap employing the Kubelka Munk function.*

The synthesized BYW host sample exhibits a broad band around 300 nm attributed to the characteristics of the W-O group present in the host material. The reflectance data were utilized to compute the optical band gap of BYW host using the equation as described in equations 2.04 & 2.05 in the section 2.3.4. [113]. The inset in Fig. 3.03 displays a plot of photon energy ($h\upsilon$) versus $[F(R)h\upsilon]^2$. By extrapolating the linear region to the energy axis (where $\alpha = 0$), the direct E_g of BYW host sample was estimated to be approximately 2.91 eV.

3.3.4. Photoluminescence characteristics

The room temperature excitation spectrum for the synthesized BYW: xEu^{3+}, where x = 1.0 mol%, phosphor has been observed in the wavelength range of 350-500 nm, while

maintaining a fixed intense red emission wavelength of 613 nm, as shown in Fig. 3.04(a). The excitation spectrum exhibits multiple peaks, with the most prominent peak observed at 465 nm ($^7F_0 \rightarrow {}^5D_2$ transition) of Eu^{3+} ions. The inset magnified diagram highlighted several additional excitation peaks at 363, 382, 393, and 417, which are attributed to the transitions from the ($^7F_0$) ground state to different excited states, as designated in Fig. 3.04(a). Furthermore, the dominant excitation peak at 465 nm (blue) was chosen to capture the emission spectral profiles of the BYW: xEu^{3+} phosphors.

The emission profiles of the synthesized BYW: xEu^{3+} phosphors with varying dopant concentrations (x = 1.0 to 9.0 mol%, at fixed intervals of 2.0 mol%) were captured in the range of 550 to 750 nm under blue excitation, as illustrated in Fig. 3.04(b). As observed in Fig. 3.04(b), the synthesized phosphor exhibits multiple emission peaks corresponding to the

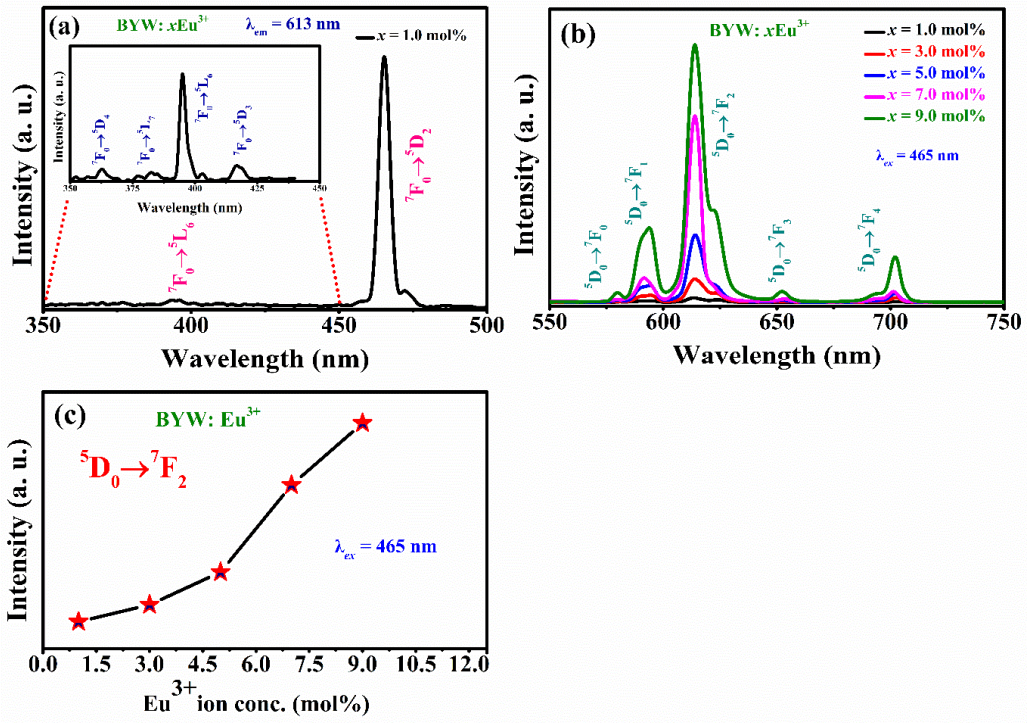

Fig. 3.04: *(a) Excitation spectrum of the 1.0 mol% Eu^{3+} doped $BiYWO_6$ phosphor under 613 nm emission wavelength, (b) Emission spectral profiles of the BYW: Eu^{3+} phosphor under blue excitation wavelength, and (c) The variation of emission intensity with different Eu^{3+} ion concentrations.*

characteristic transitions of Eu^{3+} ions. These emission peaks are situated at 579, 593, 613, 653, and 704 nm, associated with transitions from the lowest energy level $^5D_0$ to various excited ^7F_J (J = 0, 1, 2, 3, and 4) manifolds of the Eu^{3+} ion [116,129]. Among these, the most predominant emission peak is the $^5D_0 \rightarrow {}^7F_2$ transition centered at 613 nm in the red region, which is attributed to the forced electric dipole transition. The forced ED ($^5D_0 \rightarrow {}^7F_2$) transition is related to the hypersensitive transition and is significantly influenced by the ligand ions that are present in the crystal structure [130]. In contrast, the emission peak centred at 594 nm corresponds to the $^5D_0 \rightarrow {}^7F_1$ magnetic dipole transition, which is independent of the site symmetry and surrounding crystal field [121,129].

When Eu^{3+} occupies a site lacking inversion symmetry, the forced ED transition will be stronger than the MD transition. Conversely, if Eu^{3+} ions are situated at sites with inversion symmetry, the MD transition will dominate the emission profiles [31]. The broadening of the peaks may be due to improved morphological features by the incorporation of citric acid in the SGC synthesis process, and *4f-4f* characteristic transitions. With an upsurge in the dopant concentrations, the emission intensity also increases, and no concentration quenching has been observed in these BYW: xEu^{3+} phosphors up to 9.0 mol%, as presented in Fig. 3.04(c). This observation highlights another significant aspect of this lattice, which exhibits a high solubility for rare earth elements.

3.3.5. CIE coordinates

In order to evaluate the final emission color of the synthesized Eu^{3+} doped BYW phosphor, CIE coordinates were computed.The CIE coordinates of the BYW: xEu^{3+}, x = 9.0 mol% phosphor were estimated with the help of the emission profile measured under blue excitation. The computed CIE coordinate values (0.653, 0.346), placed in the red zone of the chromaticity plot, as illustrated in Fig. 3.05. Notably, these coordinates are in close proximity to those of the

commercially available red emitting phosphors, such as Y_2O_2S: Eu^{3+} (0.647, 0.343) and the standard NTSC (0.670, 0.330) [104]. Moreover, the color purity of the synthesized BYW: xEu^{3+}, x = 9.0 mol% phosphor was assessed following the method outlined in the literature [104], yielding a high color purity of 99.0% under blue excitation. These findings suggest that the BYW: xEu^{3+} phosphors may be a promising candidate for use as an efficient red emitting component in w-LEDs and other advanced photonic applications.

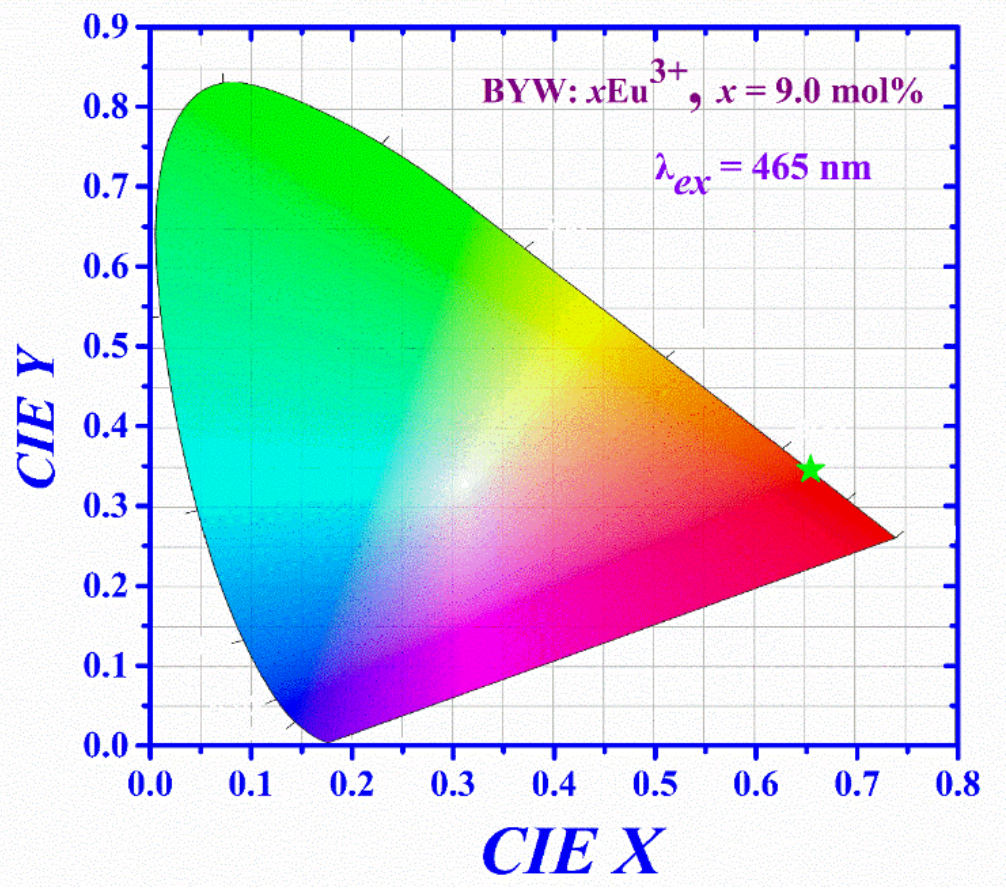

Fig. 3.05: *CIE color coordinates of 9.0 mol% Eu^{3+} doped $BiYWO_6$ phosphor under the excitation wavelength of 465 nm.*

3.3.6. Lifetime analysis

The room temperature PL lifetime profile for the synthesized BYW: xEu^{3+}, x = 9.0 mol% phosphor was measured for the $^5D_0$ energy level via monitoring the intense red emission (613 nm) at blue excitation wavelength, as shown in Fig. 3.06.

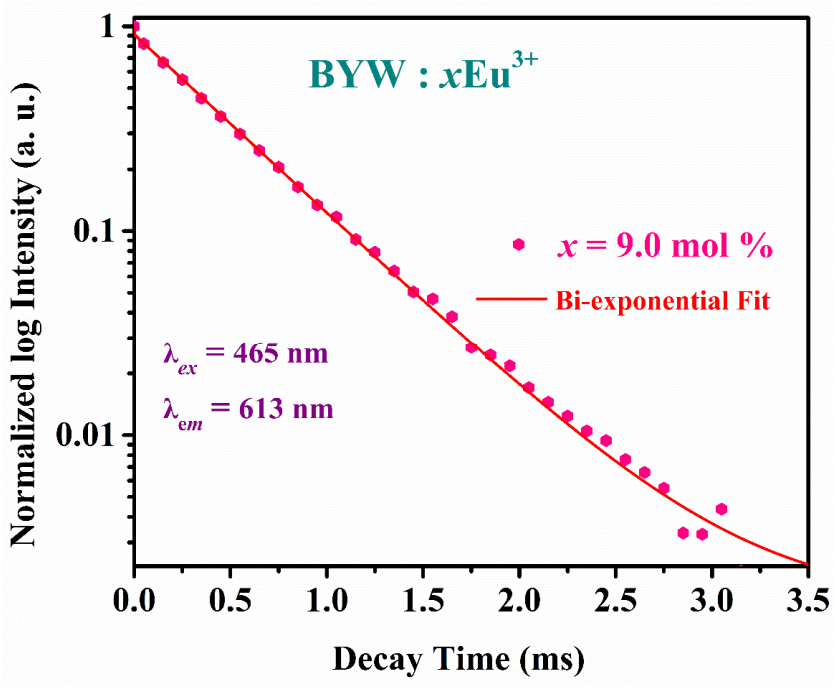

Fig. 3.06: *Decay curves of the BYW: xEu^{3+} (x = 9.0 mol%) phosphor under blue excitation.*

The measured lifetime profile of the BYW: xEu^{3+}, x = 9.0 mol% phosphor divulges exponential behaviour and was best fitted with double exponential equation, as depicted in equation 2.07 in the section 2.3.9 [101,102]. Furthermore, the average lifespan (τ_{avg}) value was calculated using equation 2.08, as mentioned in the section 2.3.9 [113]. The τ_{avg} value of the synthesized BYW: xEu^{3+}, x = 9.0 mol% phosphor was found to be 250.78 µs.

3.3.7. Temperature dependent PL studies

To investigate the practicability of the synthesized phosphor for multifunctional solid state lighting and other advanced photonic applications, the TDPL analysis was conducted on the synthesized BYW: xEu^{3+}, x = 9.0 mol% phosphor. The measurements were carried out over a temperature range of 298 to 448 K under blue excitation, as represented in Fig. 3.07(a). It has been noted that as the temperature increased from 298 to 448 K, the emission intensity of the synthesized phosphor gradually decreased, while the peak positions remained unchanged. The correlation between the relative emission intensity ($^5D_0 \rightarrow {}^7F_2$) and temperature is illustrated in the inset of Fig. 3.07(b). Notably, the synthesized phosphor retained approximately 73% of

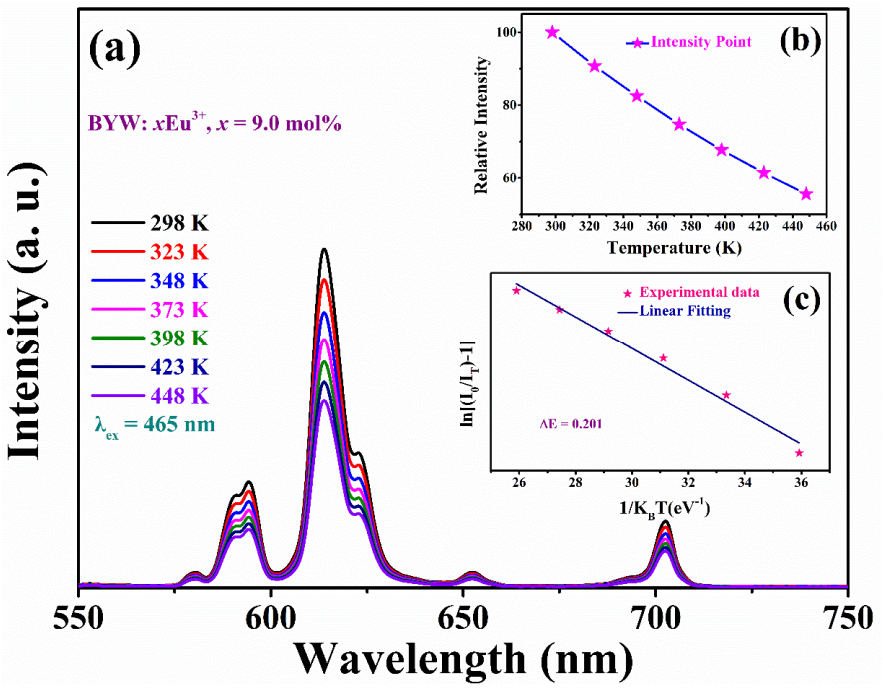

Fig. 3.07: *(a) Temperature dependent PL spectra of Eu^{3+} doped $BiYWO_6$ phosphor, [Inset (b) shows the relative emission intensity of $^5D_0 \rightarrow {}^7F_2$ peak with varying temperature from room temperature 298 K to 448 K, and (c) Plot of $ln[(I_0/I_T)-1]$ Vs $1/K_BT$ of the Eu^{3+} doped $BiYWO_6$ phosphor.*

its initial emission intensity at 373 K and 60% at 423 K, suggesting good thermal stability. Moreover, the activation energy (ΔE_a) is another vital parameter for the thermal stability of the synthesized BYW: xEu^{3+}, x = 9.0 mol% phosphor and evaluated via employing the Arrhenius relation as mentioned in equation 2.09 in the section 2.3.10 [131]. The ΔE_a was determined from the slope of the linear fit to the plot of $ln[(I_o/I_T)-1]$ versus $1/K_BT$, as demonstrated in Fig. 3.07(c). The evaluated value of ΔE_a is found to be 0.201 eV for the synthesized BYW: 9.0 mol% Eu^{3+} phosphor, indicating that the synthesized BYW: xEu^{3+} phosphor exhibits superior thermal stability.

3.4. Conclusions

In summary, the SGC method has been successfully employed to synthesize thermally stable red emitting BYW: xEu^{3+} phosphors. The diffraction patterns revealed the formation of

a monoclinic BYW crystal structure, with the Eu^{3+} ions effectively occupying the Bi^{3+} ions without altering the host lattice structure. The optical band gap (E_g) for the BYW host was determined to be 2.91 eV. BYW: $x$$Eu^{3+}$phosphor shows multiple emission peaks, with a prominent emission peak observed at 613 nm, when excited via blue radiation. The CIE chromaticity color coordinates of the synthesized phosphor lie in the red zone with a high value of color purity. The lifetime profile of the BYW: $x$$Eu^{3+}$, x = 9.0 mol% phosphor reveals a bi-exponential characteristic with an average lifetime in the microsecond range. Furthermore, the TDPL studies indicate that the emission intensity retained 73% of its initial temperature at 100 °C, demonstrating good thermal stability. These results indicate that Eu^{3+}-activated BYW phosphor can be an appropriate candidate for the red emitting component in pc-w-LEDs and other advanced photonic applications.

CHAPTER 4

Optimization of Synthesis Method for $BiYWO_6$: Eu^{3+} Phosphors

Europium activated bismuth yttrium tungstate (BYW: Eu^{3+}) phosphors were synthesized by four various synthesis techniques, such as solid state reaction (SSR), sol-gel combustion (SGC), co-precipitation (CP), and hydrothermal (HT) methods. Relative investigations such as thermal, structural, morphological, and luminescence characterizations have been carried out to optimize the synthesis process of BYW: Eu^{3+}phosphor. The TGA-DSC curves signify the endothermic/exothermic peaks and corresponding weight loss during heating. X-ray diffraction analysis and Rietveld refinement have been used to identify the phase and crystal structure of the undoped and doped $BiYWO_6$ sample. The field emission scanning electron microscope (FE-SEM) with energy dispersive x-ray (EDX) was carried out to examine the morphological and compositional behaviour of the synthesized BYW: Eu^{3+}phosphor. The compared photoluminescence (PL) results signify that the phosphor synthesized by the CP method at calcination temperature 900 °C exhibits the strongest emission than the phosphor synthesized via other methods (SGC, SSR, and HT) and is especially two times higher than the phosphor synthesized by the SSR method. Further, the PL intensity enhanced with increasing activator concentration of Eu^{3+} ions up to 20 mol%. The obtained results suggest that the $BiYWO_6$ activated with Eu^{3+} ions phosphor synthesized by the CP method has distinctive PL characteristics with good morphology, which can be employed as an intense red emitting component in photonics devices.

4.1. Introduction

In the recent decade, phosphor based white light emitting diodes (w-LEDs) have revolutionized the lighting industry by providing a more energy efficient, small size, short response time, durable, and versatile lighting solution for various applications [108,132,133]. Also, w-LEDs have set the standard for energy efficient lighting devices to minimize climate change and environmental costs due to carbon emissions during the generation of electric power based on the burning of fossil fuel [134]. Commercially available phosphor converted w-LED is the combination of YAG: Ce^{3+} phosphor and blue light emitting InGaN chip [113]. This lighting device produces light in the blue to yellow portion of the visible spectrum and exhibits poor red emitting content. As a result, it has a low color rendering index (CRI), and high correlated color temperature (CCT >6500 K) [135–137]. However, the readily accessible red phosphor (Y_2O_2S: Eu^{3+}) has poor color rendering characteristics, is very sensitive to moisture, thermally unstable, and also releases sulfide gas into the environment [113–115,138]. Therefore, it is indispensable to explore a thermally stable and efficiently blue pumped inorganic red illuminating phosphor.

An efficient phosphor requires a good host lattice, which is one of the essential prerequisites of the potential phosphor. Tungstates have direct utility and applicability in the fields of photonics, optoelectronics, quantum electronics, scintillators, lasers, and humidity sensing [72,73]. The Aurivillius family of layered perovskites includes the compound $BiYWO_6$, which recently received much attention for its microwave dielectric and photocatalytic capabilities [126].

After selecting the host lattice, the synthesis of phosphor using various synthesis routes may affect the structural, morphological and luminescence characteristics of phosphors. Hence, different synthesis routes have been used to optimize the synthesis process and morphology of

the $BiYWO_6$ phosphor material for the enhancement of luminescence properties. Among various synthesis routes, the commercially feasible solid state reaction (SSR) method is one of the most generally accepted techniques to synthesize bulk phosphor materials due to its reproducibility, economically viable, and a large quantity of powder that can be easily produced [20]. Further, the sol-gel combustion (SGC) approach is one of the attractive chemical methods for synthesizing powder materials in deep microns or nano-size [139]. This approach has a number of benefits, including low cost, short reaction time, simple preparation, and attaining products with high yield. Moreover, the hydrothermal (HT) synthesis takes place at a desired temperature and pressure during chemical reaction to produce the nanomaterials with the desired morphology [140]. The foremost feature of this method is that it generates nanomaterials with minimum loss of materials. In addition to the above mentioned methods, the co-precipitation (CP) method has gained popularity due to its benefits, including its simplicity, homogenous mixing of the reactants, high yield, affordability, and short reaction time in the synthesis process [141]. Several researchers/scientists have analyzed and reported that numerous rare earth activated tungstates such as $NaY(WO_4)_2:Eu^{3+}$, Y_2WO_6, and $ZnWO_4$ have been synthesized by solid state reaction, hydrothermal, and sol-gel process [142–146]. In recent years, R. Kamal et al. investigated the luminescent properties of $BaWO_4$: Tb^{3+} nano phosphor for latent print and anti-counterfeiting applications [147]. J. Huagng et al. synthesized $NaBi(WO_4)_2$: Dy^{3+}, Tm^{3+} phosphors and investigated its electronic and photoluminescence studies in detail. Also, Dy^{3+}/Tm^{3+} co-doped $NaBi(WO_4)_2$ phosphor may be a promising candidate in UV excited single host w-LEDs [148]. Further, it is confirmed that no study has been reported on the optimization of synthesis and luminescent features of Eu^{3+} doped $BiYWO_6$ (BYW: Eu^{3+}) phosphor.

In the present work, Eu^{3+} doped $BiYWO_6$ (BYW: Eu^{3+}) phosphors have been synthesized using four different methods: SSR, SGC, HT, and CP. The purpose of the current

study is to reveal the most appropriate and efficient method to synthesize BYW: Eu^{3+}phosphor to act as a red component for w-LEDs. A comparative study of the structural, morphological, and luminescent characteristics was conducted for the phosphors synthesized via numerous methods to disclose the most suitable synthesis method. Optimized $BiYWO_6$ phosphor has been synthesized by varying dopant (Eu^{3+}) concentrations. Further, the suitability of the prospective BYW: Eu^{3+} phosphor for solid state lighting applications was thoroughly investigated.

4.2. Materials and synthesis

Eu^{3+} doped $BiYWO_6$ phosphors have been synthesized via four different synthesis techniques as follows:

Synthesis of BYW: Eu^{3+} by SSR method

Eu^{3+} activated $BiYWO_6$ phosphors have been prepared employing SSR method as described in section 2.2.1. in chapter 2 and detailed flowchart is presented in Fig. 2.02. The highly pure Bi_2O_3, Y_2O_3, WO_3, and Eu_2O_3 were used as precursor materials for the synthesis of phosphor. Finally, the prepared Eu^{3+} activated $BiYWO_6$ phosphors have been characterized and analyzed using various tools.

Synthesis of BYW: Eu^{3+} by SGC method

In sol-gel combustion synthesis, the precursors were used in the preparation of BYW: $x Eu^{3+}$ (x = 0.0 and 1.0 mol%) phosphor, such as $Y(NO_3)_3{\cdot}6H_2O$, $H_{42}N_{10}O_{42}W_{12}$, $Bi(NO_3)_3{\cdot}5H_2O$, citric acid, and ethylene glycol taken in stoichiometric ratio. The detailed synthesis process has been displayed in section 2.2.2. in chapter 2 and Fig. 2.03. Further, the synthesized BYW: Eu^{3+} samples used by various characterization tools.

Synthesis of BYW: Eu^{3+} by HT method

In hydrothermal synthesis, the initial precursors $Y(NO_3)_3{\cdot}6H_2O$, $Na_2WO_4{\cdot}2H_2O$, $Bi(NO_3)_3{\cdot}5H_2O$, and Eu_2O_3 were taken in stoichiometric ratio to obtain the expected phosphor

powder of BYW: xEu^{3+} (x = 0.0 and 1.0 mol%). The detailed synthesis process was illustrated in section 2.2.3. in chapter 2 and Fig. 2.04. Finally, the dried samples were used for further characterization.

Synthesis of BYW: Eu^{3+}by CP method

In co-precipitation synthesis, to prepare BYW: xEu^{3+} (where x = 0.0, 1.0, 5.0, 10.0, 15.0, and 20.0 mol%) phosphor, the precursors $Y(NO_3)_3{\cdot}6H_2O$, $Na_2WO_4{\cdot}2H_2O$, $Bi(NO_3)_3{\cdot}5H_2O$, and Eu_2O_3 were taken in stoichiometric ratio. The detailed synthesis process was illustrated in section 2.2.4. in chapter 2 and Fig. 2.05. Finally, the prepared Eu^{3+} activated $BiYWO_6$ phosphors have been characterized and analyzed using various tools.

4.3. Results and discussion

4.3.1. TGA & DSC analysis

The thermal behavior of $BiYWO_6$ with different synthesis routes was investigated by utilizing TGA and DSC profiles within the temperature range from 30 to 1000 °C, as shown in Fig. 4.01(a-d). Fig. 4.01(a) represents the thermal behaviour of the precursor sample to be prepared via SSR method. The total weight loss from temperature 30 °C to 1000 °C is about 1.40%. First stage weight loss 0.70% was observed from 30 to 500 °C due to the annealing process of the oxide compounds and adsorbed water molecules, which was also supported by the DSC curve. The observation of a plateau region reaching 700 °C signifies the end of volatile material evaporation. The peak observed at 725 °C in the SSR method in Fig. 4.01(a) is the indication of the crystallization process for the $BiYWO_6$ sample. Fig. 4.01(b) shows the TGA-DSC curve corresponding to the $BiYWO_6$ sample prepared via SGC method. The total weight loss was about 6.45% in the temperature range 30 – 1000 °C. In which, the first stage weight loss is about 2.54% around 30 – 150 °C, originated may be due to the evaporation of residual water and the corresponding DSC curve exhibit the endothermic peak. The second part of TGA curve exhibits weight loss of 2.51% in the temperature range 150 – 650 °C due to

removal of some -NO_3 groups that could be related to one or more of the alkoxy nitrate species in the precursor present after the combustion [149]. Moreover, the mass loss was observed to be relatively low in the 650 – 1000 °C temperature range and is about 1.40% due to the

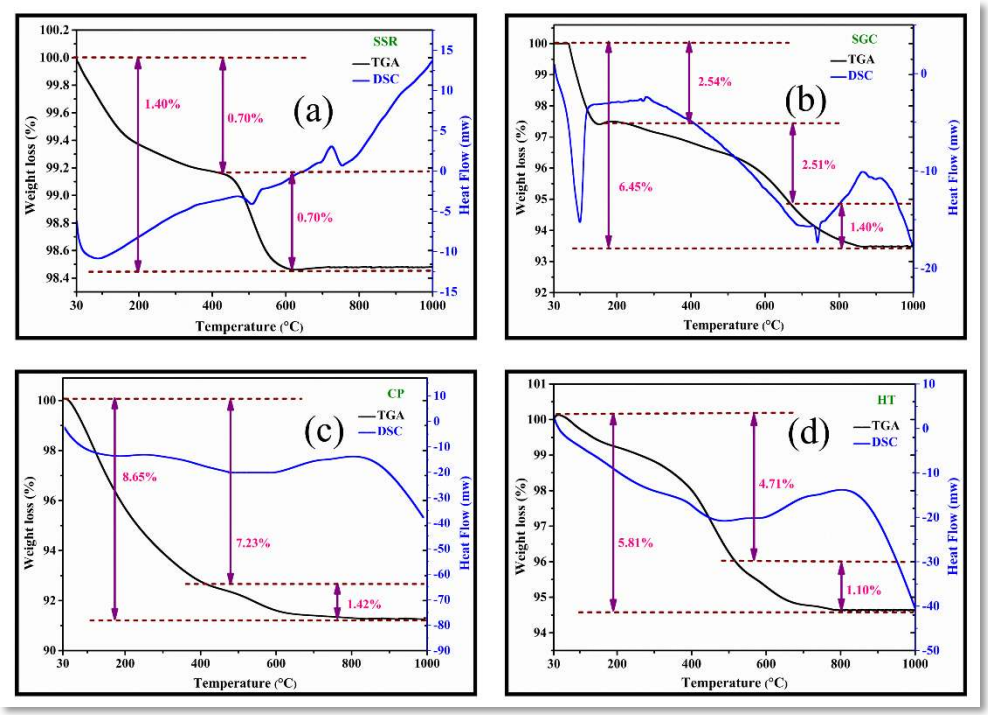

Fig. 4.01: *TGA-DSC curves for $BiYWO_6$ powder materials synthesized via different routes (a) SSR (b) SGC (c) CP (d) HT.*

pyrolysis of an organic compound and degradation of intermediate species formed during the combustion process [150]. This type of observation is reflected in the small endothermic peak at 740 °C of the DSC curve. After this temperature, the broad exothermic peak around 860 °C attributed to the crystallization process of the $BiYWO_6$ material. Fig. 4.01(c) represents the thermal behaviour of sample $BiYWO_6$ synthesized via CP method. The TGA plot exhibits a total weight loss of 8.65% in the temperature 30 to 1000 °C range. The total weight loss consists of two stages. The first stage represents 7.23% in the temperature range of 30 – 400 °C. The weight loss due to evaporation of absorbed moisture, ethanol, and ammonia content, which is correlated with the endothermic peak appeared within the 30 °C – 200 °C range. The weight

loss in the range of 200 – 600 °C, owing to the ejection of some nitrate group and ammonia decomposition, present in the precipitated material as broad small endothermic peaks reflected in the DSC curve. The second stage weight loss shows 1.42% in the temperature range of 400 °C – 1000 °C, which is quite small in comparison to the first stage weight loss. Fig. 4.01(d) presents the TGA–DSC curve of the $BiYWO_6$ sample prepared by employing HT method. The total weight loss consists of two stages in the temperature range 30 – 1000 °C was found to be 5.81%. The first stage of weight loss was found to be 4.71% in the temperature range of 30 – 600 °C, due to the removal of absorbed moisture, ethanol, ammonia, and nitrate groups present in the precursor. The second stage weight loss was found to be about 1.10% in the temperature range of 400 – 1000 °C as reflected in the DSC curve related to a broad exothermic peak, which signifies the crystallization process of the hydrothermally prepared $BiYWO_6$ phosphor. As per the observed TGA/DSC curves, the $BiYWO_6$ sample was calcined at different temperatures (>700°C) to optimize the crystalline phase. The X-ray diffraction profiles recorded for all the synthesized phosphors to confirm the presence of pure phase in the material.

4.3.2. XRD structural analysis

Structural and phase purity of the prepared $BiYWO_6$ samples were analyzed with the help of diffraction patterns as shown in Fig. 4.02(a-d). Fig. 4.02(a) demonstrates the diffraction patterns of $BiYWO_6$ samples prepared via the SSR method, calcinated at 1000 and 1100 °C. The diffraction pattern for $BiYWO_6$ prepared at 1100 °C completely matches the standard data without any impurity peaks. While other diffraction patterns calcined at 1000 °C have little bit shifting of peaks, as well as not analogous with the standard data. Hence, the pure crystalline phase of the $BiYWO_6$ sample synthesized after calcination at 1100 °C via the SSR method has a monoclinic structure with the space group of P2/a (13) [151]. Fig. 4.02(b, c & d) demonstrated XRD patterns for $BiYWO_6$ samples synthesized via SGC, CP, and HT methods, calcinated at numerous temperatures (i.e., 700, 800, 900 & 1000 °C), respectively. The samples initially

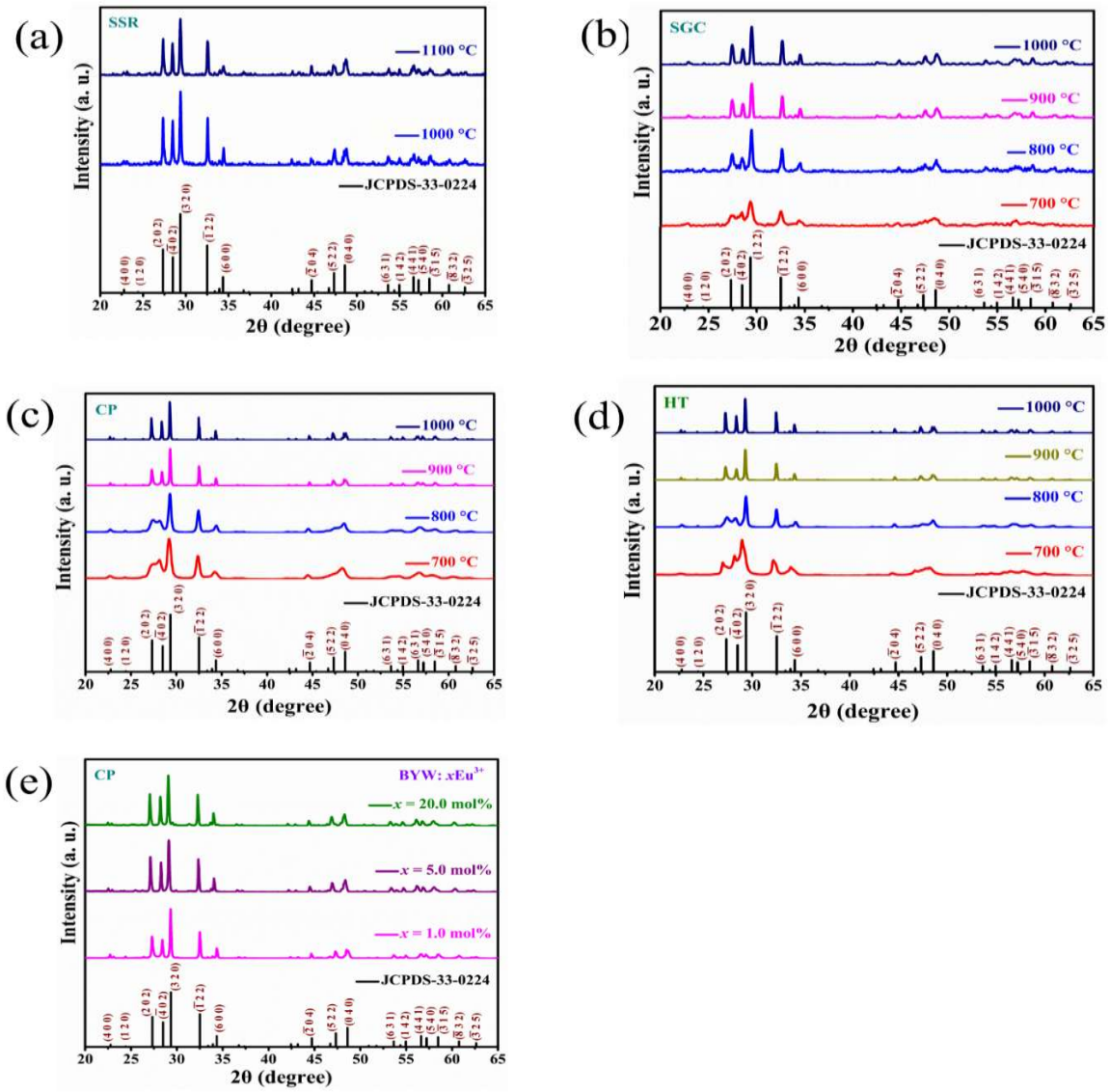

Fig. 4.02: *X-ray diffraction patterns of $BiYWO_6$ via (a) SSR calcined at 1000 °C and 1100 °C (b) SGC route (c) CP route and (d) HT route calcined at various temperatures (e) Eu^{3+} (1.0, 5.0 and 20.0 mol%) doped $BiYWO_6$ phosphor synthesized via CP route at 900 °C.*

exhibit broad crystalline peaks at 700 °C due to the formation of small crystallites and reduced full width at half maxima (FWHM) value with increasing the calcination temperature beyond 700 °C due to enhancement in crystallite size as indicated in Table 4.01. Among all the patterns observed in Fig. 4.02(b, c, and d), the diffraction peaks are completely analogous to the standard data (JCPDS-33-0224) when the samples were calcined at 900 °C.

Table 4.01: *Crystallite size of BYW powder materials synthesized via different routes (SSR, CP, SGC and HT methods).*

Synthesis rotes	Crystallite size (nm)				
	700 °C	800 °C	900 °C	1000 °C	1100 °C
SSR	-	-	-	-	69.31
CP	12.44	14.21	46.15	60.10	-
HT	16.90	19.14	41.20	56.48	-
SGC	18.60	21.82	31.25	48.20	-

Fig. 4.02(e) represents the diffraction patterns of BYW: xEu^{3+} (x = 1.0, 5.0, 20.0 mol%) samples synthesized via CP method at 900 °C calcination temperature. The ionic radii (Bi^{3+} = 1.03 Å, Y^{3+} = 0.90 Å, and Eu^{3+} = 0.947 Å) for coordination number (N= 6), which shows that the ionic radii of Eu^{3+} ion is smaller than the ionic radii of Bi^{3+} ion and having similar ionic state. Hence, Eu^{3+} ions can effectively replace the Bi^{3+} ions. Further, it has been observed that Bi^{3+}/Y^{3+} have the same crystallite site in the the crystal structure of $BiYWO_6$ derived from Bi_2WO_6 [126]. Thus, Eu^{3+} ions are expected to occupy preferably Bi^{3+} site and there is a possibility of occupying Y^{3+} site in the case of higher concentrations of Eu^{3+} ions. All the patterns were compared with JCPDS data and are well matched with the observed peaks, which suggest the effective incorporation of Eu^{3+} ions in $BiYWO_6$ host sample. With increase in the concentration of the Eu^{3+} ion, the diffraction patterns slightly shifted towards lower angle due to increase in strain present in the crystal lattice [124,125]. According to the described crystal structure, the Y^{3+}/Bi^{3+} ions are dispersed at random within the $BiYWO_6$ unit cell [127].

The average crystallite size (D) of the $BiYWO_6$ powder samples synthesized via various routes were calculated using Debye Scherer's equation as depicted in equation no. (2.02) in

section 2.3.2 [152]. The average crystallite size increased with the calcination temperature in various synthesis methods, falls in the range from 12 to 70 nm.

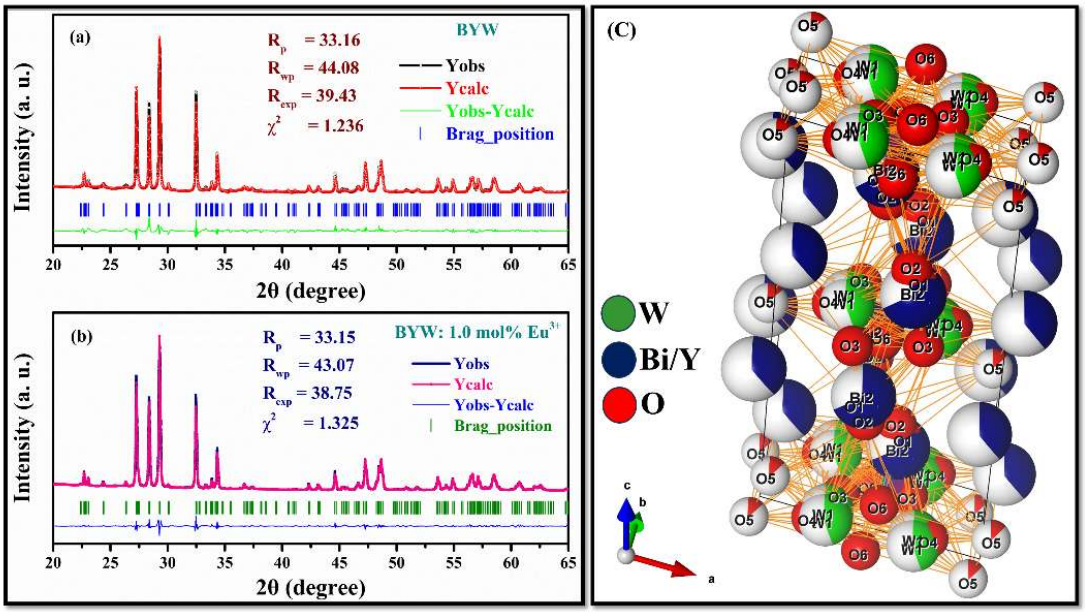

Fig. 4.03: *The Rietveld refinement profiles of (a) $BiYWO_6$, (b) 1.0 mol% Eu^{3+} doped $BiYWO_6$ phosphor synthesized via SSR route and (c) crystal structure of $BiYWO_6$.*

Rietveld refinement has been performed via FullProf suite software for the prepared undoped and doped (1.0 mol% Eu^{3+}) $BiYWO_6$ samples. The resultant refinement patterns were shown in Fig. 4.03(a and b), which depict the experimental and evaluated patterns along with difference between them. The assessed result discloses that the undoped and doped (1.0 mol% Eu^{3+}) $BiYWO_6$ samples having single monoclinic phase with the lattice parameters a = 8.1244 Å, b = 3.7534 Å, c = 16.0345 Å, and a = 8.1253 Å, b = 3.7539 Å, c = 16.0334 Å, respectively. The goodness of fit was found to be close to the unity denotes good refinement results. On the basis of refinement data, $BiYWO_6$ structure was prepared using VESTA software as demonstrated in Fig. 4.03(c).

4.3.3. *Morphological studies*

The surface morphology of $BiYWO_6$ synthesized via different routes and calcinated at different temperatures with micro to nano resolution are shown in Fig. 4.04. The sample

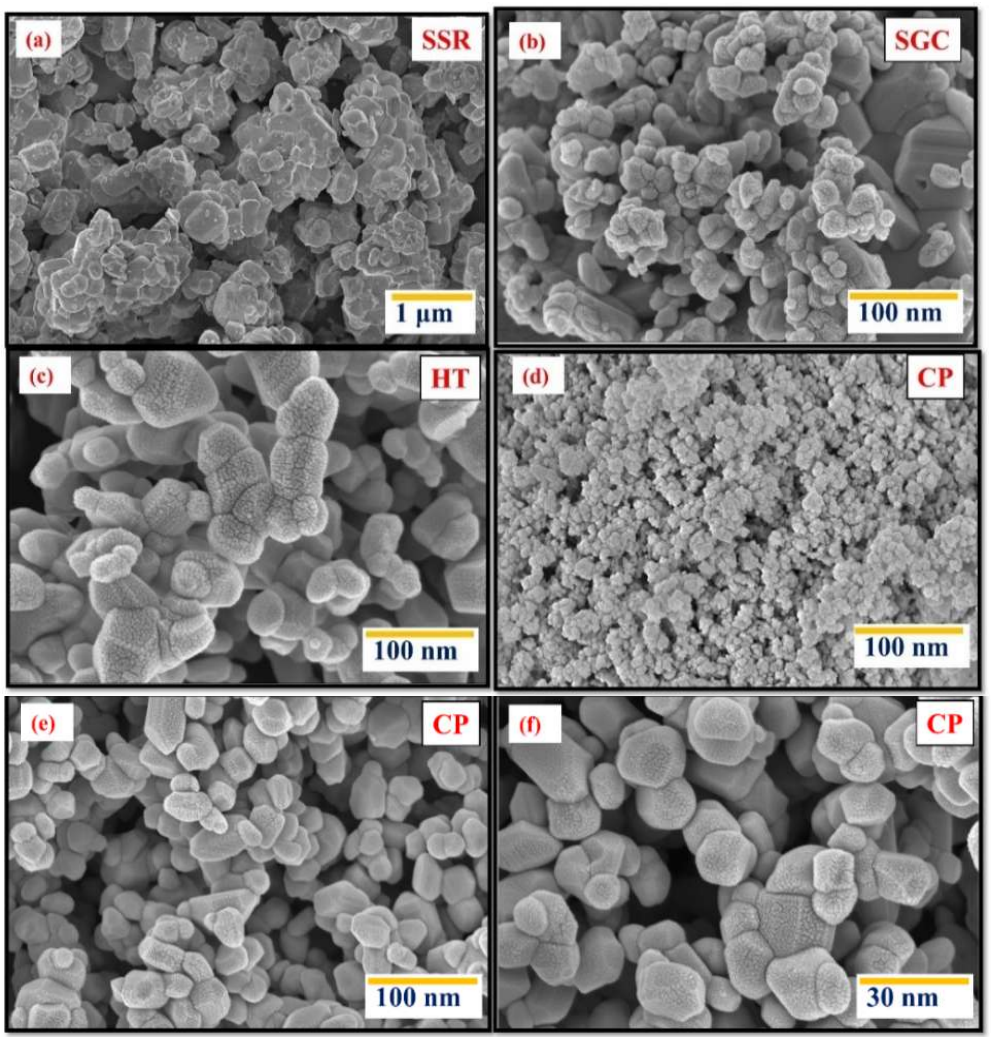

Fig. 4.04: *FE-SEM images of 1.0 mol% Eu^{3+} doped $BiYWO_6$ synthesized via (a) SSR at 1100 °C, (b) SGC at 900 °C, (c) HT at 900 °C, (d) CP at 700 °C, and (e & f) CP at 900 °C with different magnifications.*

prepared via SSR gives the agglomerated, irregular shape and the average particle size (in micro range) of BYW at calcination temperature 1100 °C, as shown in Fig. 4.04(a). The BYW sample synthesized via chemical routes clearly demonstrates the average particle size distribution in the nano range (200 – 300 nm) as indicated in Figs. 4.04(b, c, and d). The sample prepared via the SGC method displays inhomogeneous morphology as well as huge agglomeration when compared to the sample prepared using SSR, CP, and HT methods, which may be due to a calcination temperature of 900 °C [20]. Generally, the SGC method is the

function of the concentration of water and other reactants, including chelating agent and surfactant in the starting precursors, showing an improvement in grain growth of the morphology [128]. In comparison to the SSR, the reduced particle size and accumulation of particles have been observed while preparing the samples from SGC, HT, and CP methods. The micrographs also illustrate the non-uniform distribution of closely packed particles and the size of BYW particles enhanced with increasing calcination temperature as depicted in Fig. 4.04(d, e, and f), which was already reflected in the earlier section (XRD). The micro to nano meter crystalline particles may be appropriate to gain efficient luminescence and very much appropriate for solid state lighting applications.

The EDS results fully disclose the uniform existence of numerous elements in the synthesized BYW phosphor via SSR and CP routes, calcined at 1100 °C and 900 °C, respectively, as indicated in Fig. 4.05(a & b). The EDX profile confirms the existence of the compositional elements such as bismuth (Bi), yttrium (Y), tungsten (W), oxygen (O) and europium (Eu) in the prepared samples along with carbon (C) element.

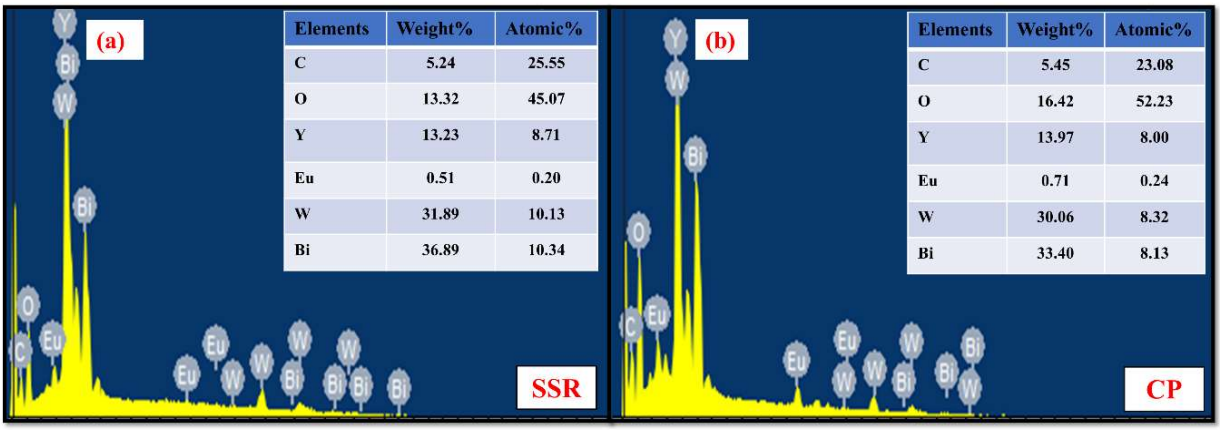

Fig. 4.05: *EDX image of 1.0 mol% Eu^{3+} doped $BiYWO_6$ (Inset shows the table of elemental composition) synthesized via (a) SSR at 1100 °C, (b) CP at 900 °C.*

The C element was observed due to the sample was coated with carbon material for FE-SEM characterization. Additionally, the inset table of Fig. 4.05 represents the weight% and atomic%

of each compositional element for the Eu^{3+} doped $BiYWO_6$ sample, which confirms the presence all elements along with Eu doping ions.

4.3.4. *Photoluminescence characteristics*

The PL characteristics of all Eu^{3+} doped $BiYWO_6$ phosphors prepared via different synthesis routes were analyzed at room temperature. Fig. 4.06(a) illustrates the PL excitation spectral profile of the BYW: xEu^{3+} (x = 1.0 mol%) phosphor synthesized via the SSR method at 1100 °C by monitoring the λ_{em} = 613 nm. The excitation spectrum exhibits various peaks in the range of 350-500 nm, with the most intense peak centered at 465 nm corresponding to the transition $^7F_0 \rightarrow {}^5D_2$ of Eu^{3+} ions. The inset plot clearly shows the other excitation peaks at 363, 382, 393, and 417, owing to the transitions from the $^7F_0$ level to numerous levels, as mentioned in Fig. 4.06(a). An intense excitation wavelength at 465 nm is selected to record the emission spectra for all BYW: xEu^{3+} phosphors, which was well matched with the blue emitting GaN-based LED chips. PL spectrum of BYW: xEu^{3+} (x = 1.0 mol%) phosphor consists of several peaks at λ_{ex} = 465 nm excitation, as shown in Fig. 4.06(b). PL spectrum has five peaks situated at 579, 593, 613, 653, and 704 nm caused by the transition of ($^5D_0 \rightarrow {}^7F_0$), ($^5D_0 \rightarrow {}^7F_1$), ($^5D_0 \rightarrow {}^7F_2$), ($^5D_0 \rightarrow {}^7F_3$), and ($^5D_0 \rightarrow {}^7F_4$), respectively. The most intense emission peak situated at 613 nm is a forced electric dipole in nature, corresponding to the transition $^5D_0 \rightarrow {}^7F_2$, which is hypersensitive and strongly influenced by the ligand ions in the crystal. On the other hand, the peak at 595 nm corresponds to the transition of $^5D_0 \rightarrow {}^7F_1$, indicating the magnetic dipole in nature and being independent of the crystal environment of the host material [137,153]. When Eu^{3+} occupies a site without inversion symmetry, the electric dipole transition ($^5D_0 \rightarrow {}^7F_2$) will become stronger than the magnetic dipole transition. Whereas, if Eu^{3+} ions are placed at the inversion symmetry sites, the magnetic dipole transition ($^5D_0 \rightarrow {}^7F_1$) will predominate in the PL profile [154,155]. In the BYW: xEu^{3+} phosphor, the electric dipole transition was stronger

than the magnetic dipole, which discloses that the Eu^{3+} ions occupy without inversion symmetry site in the $BiYWO_6$ phosphor host.

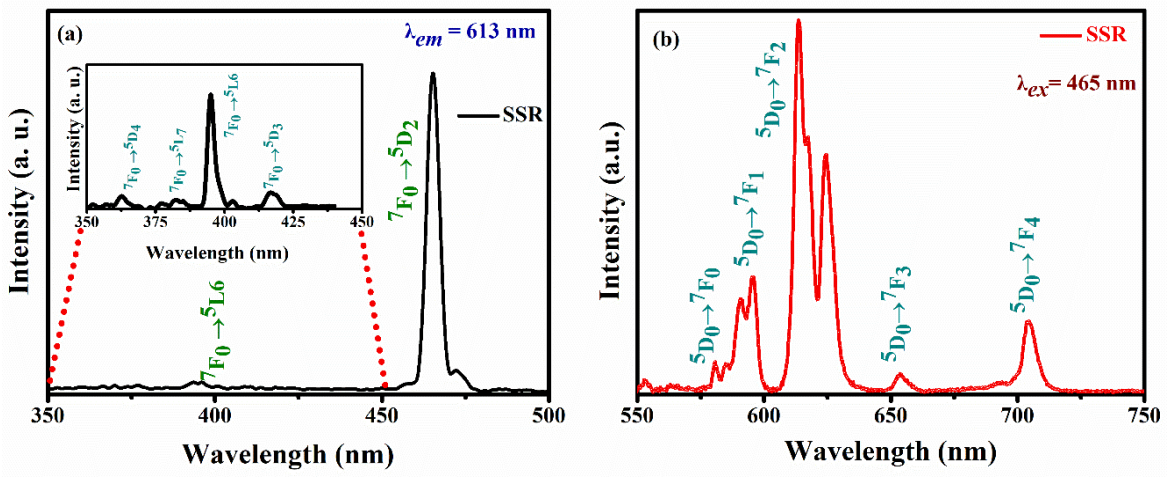

Fig. 4.06: *(a) PLE spectrum of 1.0 mol% Eu^{3+} doped $BiYWO_6$ phosphor. (The inset plot shows the magnifying of the PL excitation in the 350-450 nm wavelength range.) (b) Emission spectra of 1.0 mol% Eu^{3+} doped $BiYWO_6$ under an excitation wavelength of 465 nm.*

For the comparison of the PL characteristics and to identify the best synthesis route along with the calcination temperature, BYW: xEu^{3+} phosphors (x = 1.0 mol%) were synthesized via HT, SGC and CP method and calcined at different temperatures as depicted in Fig. 4.07. PL spectra reveals that the phosphor synthesized via CP method is efficient over the samples synthesized via SGC, HT method, and it exhibit highest emission intensity at all calcination temperatures (i.e. 700, 800, 900 and 1000 °C). Further, compared the PL characteristics of BYW: xEu^{3+} phosphor (x = 1.0 mol%) synthesized via CP method at various temperatures (700, 800, 900, and 1000 °C), as shown in Fig. 4.08(a). The recorded PL spectra exhibit an increase in the emission intensity with the rise in calcination temperature from 700 to 900 °C, and the intensity decreases for the phosphors calcined beyond 900 °C. Also, the inset plot of Fig. 4.08(a) discloses that the BYW: xEu^{3+} (x = 1.0 mol%) phosphor calcined at 900 °C has the highest emission intensity as compared with the phosphors calcined at 700, 800, and 1000 °C.

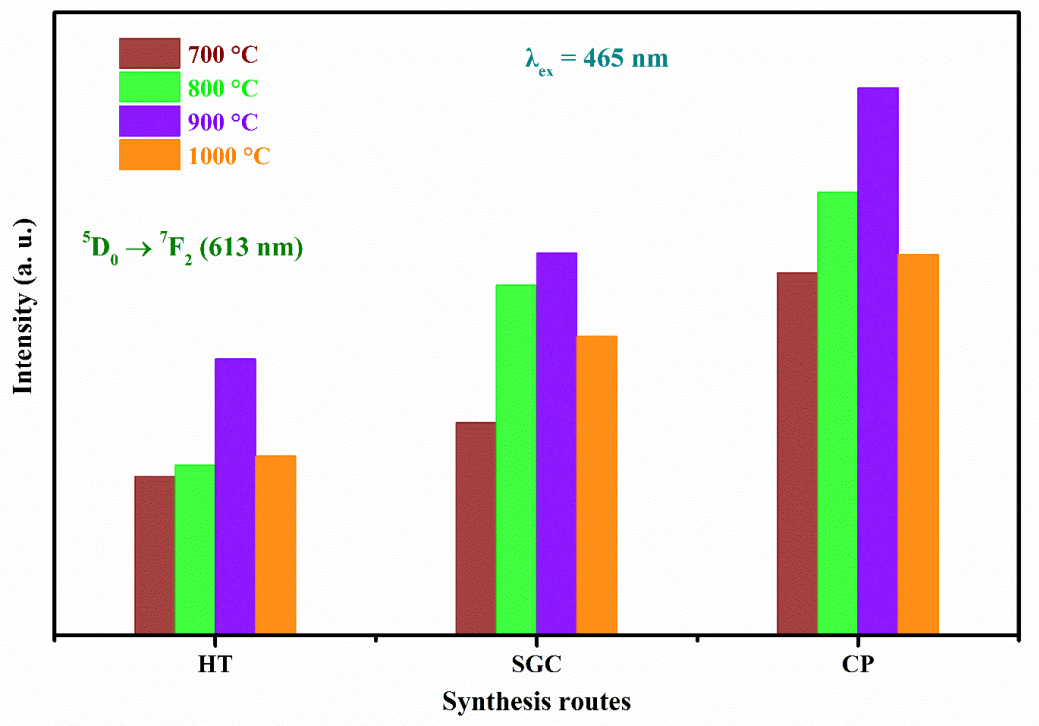

Fig. 4.07: *Comparison of emission intensity of $^5D_0 \rightarrow {}^7F_2$ for 1.0 mol% Eu^{3+} doped $BiYWO_6$, synthesized via CP, SGC, and HT at various calcination temperatures.*

On the basis of PL characteristics, it was concluded that the best way to synthesize BYW: xEu^{3+} phosphor is by employing the CP method at 900 °C calcination temperature.

Moreover, the PL spectra of the BYW: xEu^{3+} phosphor synthesized via CP method at 900 °C was compared with the same phosphor synthesized via SSR method at 1100 °C in Fig. 4.08(b). The compared PL result indicates that the phosphor synthesized by CP method exhibit strongest emission intensity and two times higher than the phosphor prepared by SSR method as shown in the inset of Fig. 4.08(b). This is due to the CP chemical route producing the more homogeneous phosphor crystalline particle with uniform morphology, as seen in the FE-SEM micrograph. Accordingly, the CP approach has been chosen for further exploration, and it has been confirmed that this method is more efficient for producing BYW: xEu^{3+} phosphor with optimized emission intensity. To explore the effect of Eu^{3+} ion doping

concentration on PL spectra of BYW: xEu^{3+} phosphor, PL spectra measured by varying dopant (Eu^{3+}) concentration from x = 1.0 to 20.0 mol% under an excitation wavelength of 465 nm

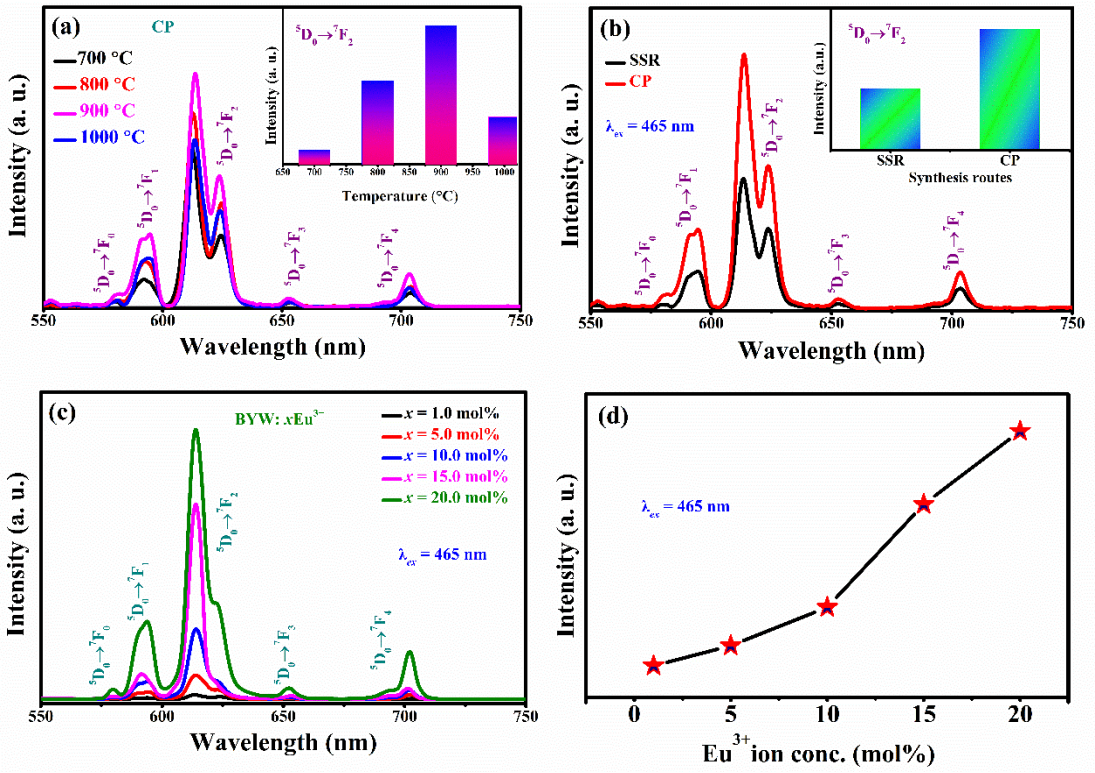

Fig. 4.08: *(a) Comparison of emission spectra for 1.0 mol% Eu^{3+} doped BiYWO$_6$ phosphor synthesized via co-precipitation route and calcined in the temperature range 700 - 1000 °C. (b) comparison of emission spectra of BYW: Eu^{3+} phosphor synthesized via CP route at 900 °C and SSR route at 1100 °C. (c) Emission spectra of BYW: xEu^{3+} (x = 1.0, 5.0, 10.0, 15.0, 20.0 mol %) synthesized via CP route and calcined at 900 °C. (d) The variation of emission intensity with varying the concentration of Eu^{3+} ions under 465 nm.*

as depicted in Fig. 4.08(c). The emission intensity of the characteristic transitions of Eu^{3+} enhanced with an increase in activator ion concentration of Eu^{3+} from 1.0 to 20.0 mol% without any concentration quenching, as shown in Fig. 4.08(d), which is another key feature of this host lattice having high rare earth solubility.

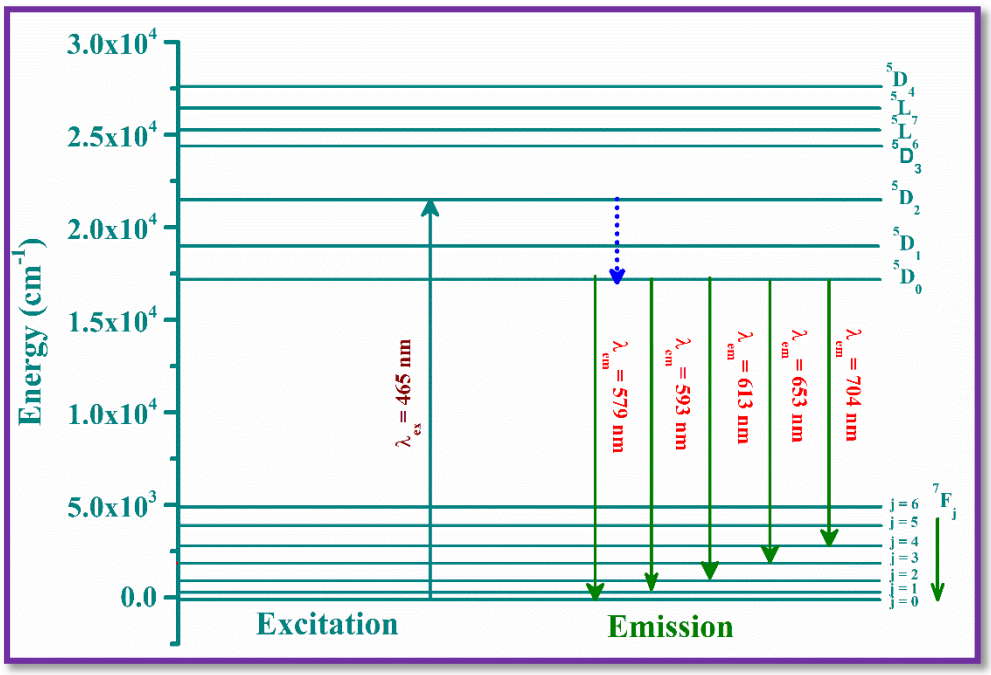

Fig. 4.09. *Energy level diagram of Eu^{3+} in $BiYWO_6$ phosphor.*

To illustrate the luminescence phenomena involved in Eu^{3+} doped $BiYWO_6$ phosphor, the simplified energy level diagram is displayed in Fig. 4.09. The population of Eu^{3+} ions finally relax to the $^5D_0$ level via non-radiatively after being excited by blue light at 465 nm (to the $^5D_2$ level) and subsequently exhibits radiative emission in the visible region starting from the $^5D_0$ level.

In order to further analyze the luminescence performance of BYW: xEu^{3+}, x = 20.0 mol% phosphor, its luminescence quantum yield has been assessed using a $BaSO_4$ integrated sphere [156,157]. The PL quantum yield for the BYW: xEu^{3+}, x = 20.0 mol% phosphor is 51.39%, which is higher than the previously reported phosphors [158,159].

4.3.5. CIE coordinates

CIE color coordinates have been estimated using the recorded PL spectra of BYW: xEu^{3+} phosphor, (x = 20.0 mol%). Fig. 4.10, represents the CIE chromaticity diagram of the

synthesized phosphor via CP method at 900 °C. The estimated coordinates (0.654, 0.345) were situated in the red region of the CIE diagram, which is very close to the standard data (National Television System Committee) for red light (0.670, 0.330) and comparable with the commercial red emitting phosphors Y_2O_3: Eu^{3+} (0.645, 0.347) and Y_2O_2S: Eu^{3+} (0.647, 0.343) [160]. Further, the color purity was estimated on the basis of chromaticity coordinates for the same phosphor via the following equation:

$$Color\ Purity = \sqrt{\frac{(x-x_{ee})^2+(y-y_{ee})^2}{(x_d-x_{ee})^2+(y_d-y_{ee})^2}} \times 100\% \qquad (4.01)$$

where, (x, y), (x_d, y_d) and (x_{ee}, y_{ee}) specify the CIE coordinates of the phosphor, dominant wavelength point, and standard white point, respectively. The color purity for BYW: xEu^{3+} phosphor (x = 20.0 mol%) was found to be greater than 99.0%, which is comparatively higher than the reported values in Table 4.02.

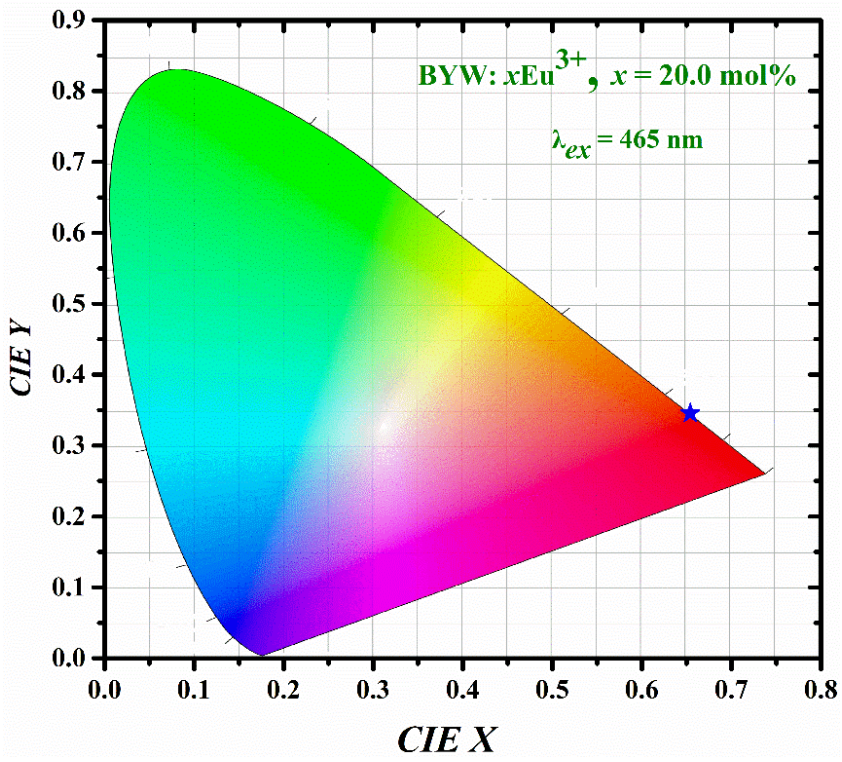

Fig. 4.10: *CIE color coordinates of 20.0 mol% Eu^{3+} doped $BiYWO_6$ phosphor synthesized via CP route.*

Table 4.02: *CIE coordinates and color purity of Eu^{3+} doped red phosphors.*

Sample	Color coordinates (x, y)	Color purity	Reference
Ca_2GdTaO_6:0.4Eu^{3+}	(0.667, 0.332)	96.0%	[161]
$Na_5W_3O_9F_5$:0.25Eu^3	(0.646, 0.353)	97.4%	[118]
$Y_2Si_8WO_8$:0.12Eu^{3+}	(0.665, 0.335)	96.6%	[162]
$BaY_4Si_3O_{13}$:Eu^{3+}	(0.636, 0.362)	91.5%	[163]
Y_2O_3:Eu^{3+}	(0.610, 0.390)	83.0%	[140]
Y_2O_2S:Eu^{3+}	(0.636, 0.321)	71.0%	[164]
$BiYWO_6$:0.2Eu^{3+}	(0.654, 0.345)	99.0%	This work

The aforesaid results suggested that BYW: $x$$Eu^{3+}$ phosphors could be used as an effective red emitting constituent for the development of w-LEDs and other photonic device applications.

4.3.6. *Lifetime analysis*

By altering the Eu^{3+} ion concentration in $BiYWO_6$ phosphor at room temperature, the decay curves were measured in order to calculate the average lifetime for the excited level $^5D_0$, under 465 nm excitation as shown in Fig. 4.11.

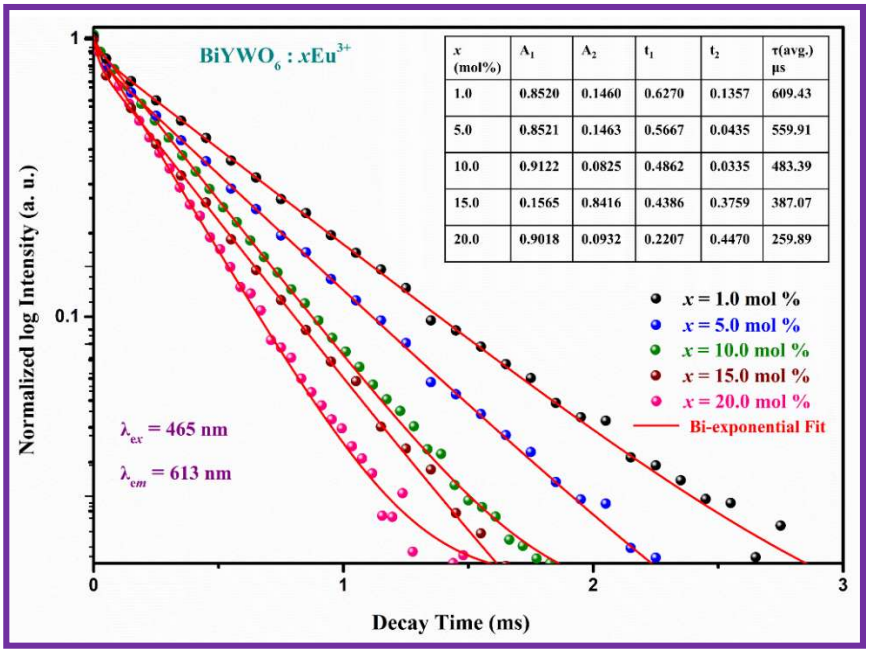

Fig. 4.11: *Decay curves for Eu^{3+} doped $BiYWO_6$ phosphors.*

The decay curves were fitted using different exponential equations and it was observed that the best fit was achieved with a bi-exponential function, as depicted in Fig. 4.11. The bi-exponential equation illustrated in equation (2.07) in the section 2.3.9 [101,102].

The average lifetime (τ_{avg}) values have been computed with the help of equation (2.08), section 2.3.9 [165]. The observed values of the slow lifetime component (τ_1), fast lifetime component (τ_2) and average lifetime (τ_{avg}) for the synthesized BYW: xEu^{3+} phosphor were tabulated in inset of Fig. 4.11. The τ_{avg} values of the synthesized BYW: xEu^{3+} phosphor (x = 1.0 to 20.0 mol%) were observed in the range of 609.43 to 259. 89 μs. The average lifetime values of the synthesized phosphor decline with an increase in the concentration of the dopant ions (Eu^{3+}). This decline in the average lifetime values is generally owing to a decrement in the distance between dopant ions (Eu^{3+}).

4.4. Conclusions

In summary, various methods have been used to synthesize europium activated $BiYWO_6$ phosphors, including SSR, SGC, CP, and HT. The investigation is focused on examining the thermal, structural, morphological, and luminescent characteristics of the as-synthesized phosphors. The crystalline monoclinic phase purity of Eu^{3+} doped $BiYWO_6$ has been confirmed using x-ray diffraction. Rietveld refinement analysis also authorizes the formation of a single monoclinic phase of the BYW host and BYW: xEu^{3+}, x = 1.0 mol% phosphor. Under blue excitation (465 nm), all the synthesized Eu^{3+} doped BYW phosphor samples exhibit intense emission peak in the red region. The BYW: Eu^{3+} phosphor sample exhibit strong emission intensity when synthesized by CP technique at 900 °C and considered as an optimized synthesized procedure for this phosphor. The CIE chromaticity color coordinates were estimated for the phosphor synthesized via the optimized CP method, and it was concluded that the coordinates of all the samples were positioned in the red region along

with high value of colour purity. Furthermore, the PL quantum yield for the BYW: xEu^{3+}, x = 20.0 mol% phosphor has been observed as 51.39%. The photoluminescence decay curve exhibits bi-exponential in nature for the optimized BYW phosphor with an average decay time in the microsecond range. The obtained results strongly recommend that Eu^{3+} activated BYW phosphor synthesized by CP method can act as a blue excited potential red illuminating participant for the applications in pc-w-LEDs and other photonic devices.

CHAPTER 5

Structural and Spectroscopic Features of Single Phase Dy^{3+} Activated $BiYWO_6$ Phosphor for Luminescent Device Applications

Dysprosium activated bismuth yttrium tungstate ($BiYWO_6$: Dy^{3+}) phosphors have been synthesized in an ambient atmosphere using a co-precipitation (CP) method. The synthesized phosphor has been investigated by the diffraction patterns and Rietveld refinement analysis. The morphological and elemental analysis of the host and BYW: $x$$Dy^{3+}$($x$ = 3.0 mol%) phosphor using FE-SEM micrograph and EDX measurement. The composition of elements and their corresponding chemical/oxidation states present in the as synthesized phosphor were confirmed using X-ray photoelectron spectroscopy (XPS). The photoluminescent (PLE and PL), PL decay, chromaticity characteristics as well as temperature dependent emission profiles, were thoroughly investigated in detail by employing photoluminescence technique. Photoluminescence studies of the Dy^{3+} activated BYW phosphor reveal that the CIE chromaticity coordinates of the phosphor fall in near white region under 290 nm wavelength. The average decay time (τ_{avg}) for the $^4F_{9/2}$ energy state of Dy^{3+} ions has been found to be in microseconds. The PL spectra has been measured from room temperature to 448 K to ensure good thermal stability of the phosphor. Thus, the synthesized phosphor might be a promising candidate for UV excited phosphor converted white LEDs (pc-w-LEDs).

5.1. Introduction

In the modern era, power saving is essential for reducing the amount of climate change caused by carbon-based gas emissions, produced during the generation of electric power from burning fossil fuels, which can be quantified in terms of both financial worth and environmental cost [2,3,166]. The majority of power has been utilized for both interior and outdoor artificial illumination. The advancements in artificial lighting have been remarkable, commencing with the utilization of oil lanterns and progressing to the development of incandescent and fluorescent lamps, ultimately culminating in the current era of solid state lighting devices. The increasing adoption of SSL can be attributed to its capacity to provide vibrant illumination, facilitate the emergence of novel lighting paradigms, and contribute to investigating various regions of the electromagnetic spectrum [167]. These days, w-LEDs are the most popular option for interior and exterior illumination. Researchers and scientists have been concentrating on the latest generation of phosphor based w-LEDs to enhance the quality of white light emission, decrease power consumption, and increase financial and environmental benefits. Due to their various advantageous, phosphors are particularly suitable to use in pc-w-LEDs, solid state lasers, display devices, medical equipment, lighting devices, as well as other applications. In this regard, rare earth ion activated inorganic pc-w-LEDs have been widely studied. These LEDs offer several advantages such as compact, small size, energy saving, good material stability, environmental protection, high luminous efficiency, fast switching, and long service life (>100 000 h) [3,153,168]. Though pc-w-LEDs have many advantages, they have some drawbacks to restrict their usage in a wide range of applications. The commercial available pc-w-LEDs, which have been made from combining a blue light emitting InGaN chip with yellow emitting trivalent cerium activated phosphor (YAG: Ce^{3+}) [169–171]. However, this commercial w-LEDs have severe drawbacks such as highly correlated colour temperature as well as low colour rendering index, owing to the lack of their red characteristics [2,172]. In

order to address these challenges, there has been a notable focus on the advancement of a single phase UV pumped white illuminating phosphor that offers adjustable emission colour, enhanced luminous output along with low CCT, improved thermal and chemical stability. As a result, single RE ion based monophase white light emitting phosphors are currently the subject of extensive research.

Selecting an appropriate environmental friendly host material for dispersing Dy^{3+}ions is a critical factor in the process. The crystal structure, morphology influenced by synthesis, and other related factors significantly affect the luminescent material's performance [173–175]. However, high luminous efficiency in commercial w-LEDs is accompanied by certain adverse effects, such as the generation of hazardous gases and other toxic by-products during the synthesis process of the phosphors [176]. In this regard, the luminescent, photocatalytic, and optical properties of oxide based tungstate host materials have gathered substantial interest among researchers due to their non-toxic characteristics, moderate synthesis requirements, cost-effectiveness, environmental friendly nature, exemplary charge stabilization, and elevated thermal, chemical, and hydrolytic stability [142,177,178]. Additionally, tungstate host material with alkali or alkaline earth elements are well known compounds as it can offer rare earth ions a sufficient ligand field environment [74]. Furthermore, the tetrahedron WO_4 exhibits flexibility to provide different coordination environments through modulation of the W–O bond lengths [145].

The prime objective of the present study is to synthesize a series of novel Dy^{3+} activated BYW phosphors using the CP route, and their comprehensive investigation was undertaken to examine the crystallinity, structural attributes, particle size, as well as morphology analysis. Further, the suitability of the probable BYW: Dy^{3+} phosphor for w-LEDs applications was thoroughly investigated.

5.2. Materials and synthesis of BYW: Dy^{3+} samples

Dy^{3+} activated BYW phosphors and BYW host material were synthesised via the co-precipitation technique. The starting precursors $Y(NO_3)_3.6H_2O$, $Na_2WO_4.2H_2O$, $Bi(NO_3)_3.5H_2O$, and Dy_2O_3 were taken in the stoichiometric ratio. The detailed synthesis process were illustrated in the section 2.2.4. in chapter 2 and Fig. 2.05**.** The synthesized Dy^{3+} doped $BiYWO_6$ phosphor samples has been used for further characterization.

5.3. Results and discussion

5.3.1. XRD structural analysis

Structural and phase purity of the prepared series of Dy^{3+} (x = 0.0, 0.5, 1.0, 2.0, 3.0, 4.0 and 5.0 mol%) induced BYW samples were analyzed, and compared with the standard diffraction pattern (JCPDS card no.: 33-0224) as depicted in Fig. 5.01(a). The diffraction pattern corresponding to the host material BYW was completely matched with standard data without any shifting.

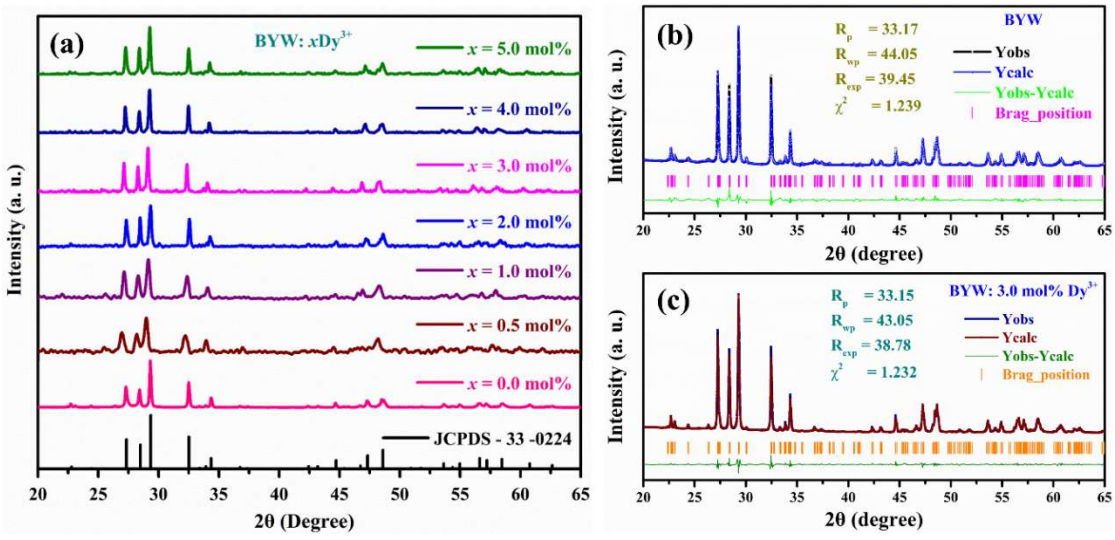

Fig. 5.01: (*a) X-ray diffraction patterns of Dy^{3+} doped $BiYWO_6$ samples. The Rietveld refinement profiles of (b) $BiYWO_6$, (c) 3.0 mol% Dy^{3+} doped $BiYWO_6$ phosphor synthesized via CP route.*

Moreover, the diffraction patterns for Dy^{3+} doped BYW samples were absolutely analogous to the standard data. Hence, the pure crystalline monoclinic structure of BYW has been attained without any impurities, which implies Dy^{3+} dopant ions were effectively dispersed in the BYW host sample. According to the described crystal structure, the Y^{3+} ions are dispersed evidently at random positions of Bi^{3+} within the BYW unit cell [126,151].

The crystallite size (D) of the as-synthesized BYW: $x$$Dy^{3+}$ (x- 0.0, 0.5, 1.0, 2.0, 3.0, 4.0 and 5.0 mol%) powder samples were calculated using Debye Scherer's equation, as depicted in equation no. (2.02) in section 2.3.2. With an upsurge in the content of Dy^{3+} ions, the average crystallite size slightly increases and is realized in the range of 30-50 nm.

Rietveld refinement has been performed via Fullprof suite software for the prepared undoped and doped (3.0 mol% Dy^{3+}) BYW samples. The resultant refinement patterns were depicted in Fig. 5.01(b & c), which illustrates the experimental and evaluated patterns along with difference between them. The assessed result discloses that the undoped and doped (3.0 mol% Dy^{3+}) BYW samples having single monoclinic phase with the lattice parameters, a = 8.1235 Å, b = 3.7535 Å, c = 16.0351 Å and a = 8.1246 Å, b = 3.7538 Å, c = 16.0352 Å, respectively. The goodness of fit was found to be close to the unity denotes good refinement results.

5.3.2. Morphological studies

The morphology is an important factor influencing both the performance and the luminescence efficiency of the phosphor material. The FE-SEM micrograph of the as-synthesized BYW host material and BYW: $x$$Dy^{3+}$ (x = 3.0 mol%) phosphor with nano order resolution micrograph were depicted in Fig. 5.02(a & b). FE-SEM images clearly show that the grain sizes are distributed in the range of 100-200 nm diameter for undoped and Dy^{3+} doped samples, and no significant changes have been observed in the morphology by doping ions.

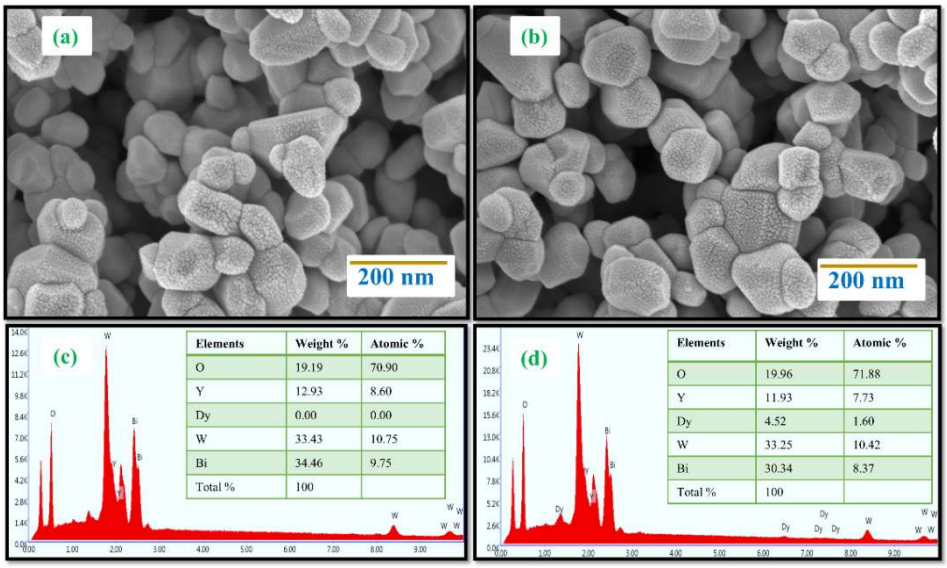

Elements	Weight %	Atomic %
O	19.19	70.90
Y	12.93	8.60
Dy	0.00	0.00
W	33.43	10.75
Bi	34.46	9.75
Total %	100	

Elements	Weight %	Atomic %
O	19.96	71.88
Y	11.93	7.73
Dy	4.52	1.60
W	33.25	10.42
Bi	30.34	8.37
Total %	100	

Fig. 5.02: *FE-SEM images of (a) host $BiYWO_6$ (b)3.0 mol% Dy^{3+} doped $BiYWO_6$ phosphor, EDX patterns of (**c**) host $BiYWO_6$ and (d) 3.0 mol% Dy^{3+} doped $BiYWO_6$ phosphor (Inset shows the table of elemental composition).*

The micrographs illustrate the irregular size and non-uniform distribution of closely packed particles of the powder samples, and grains tend to agglomerate (individual grains were not clearly observed). The nano order crystalline particle may be appropriate to gain efficient luminescence and very much convenient for solid state lighting applications.

The elemental composition of doped and undoped BYW was analysed with the help of EDX patterns, as illustrated in Fig. 5.02(c & d). The EDX results fully disclose the presence of all compositional elements of the synthesized samples, such as bismuth (Bi), yttrium (Y), tungsten (W), oxygen (O), and dysprosium (Dy). Additionally, the inset table of Fig. 5.02(c & d) represents the weight% and atomic% of each compositional element for Dy^{3+} doped BYW sample, which confirms the presence of all elements along with Dy doping ions.

5.3.3. XPS

To study the additional clarification related to the composition of elements and their corresponding chemical/oxidation states present in the as-synthesized phosphor material, XPS

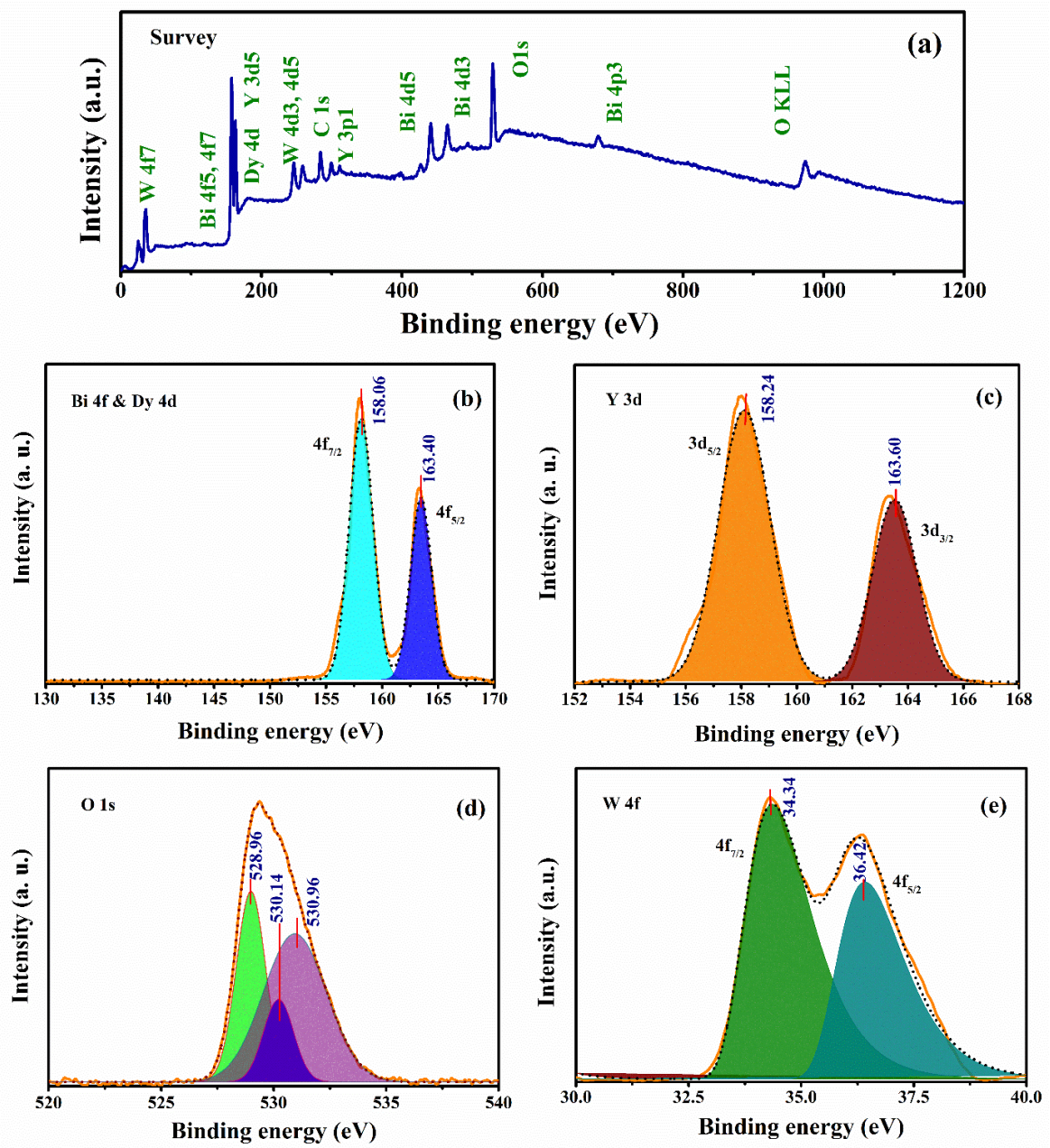

Fig. 5.03: *X-ray photoelectron spectroscopy (XPS) of (a) survey, (b) Bi, (c) Y, (d) O, (e) W of the Dy^{3+} doped $BiYWO_6$ phosphor.*

spectra were demonstrated in Fig. 5.03. The whole XPS survey of the BYW: Dy^{3+} phosphor has been displayed in Fig. 5.03(a). It reveals the existence of the primary elements Bi, Y, W, O, and Dy in BYW: Dy^{3+} phosphor and does not show any additional impurity peaks. Furthermore, the chemical states of the individual components in the BYW: Dy^{3+} phosphor are represented by the high-resolution XPS spectra as depicted in Fig. 5.03(b-e). The XPS

spectrum of Bi 4f & Dy 4d attributed to Bi^{3+} and Dy^{3+}, which is responsible for two peaks at 158.06 and 163.40 eV associated with the $4f_{7/2}$ and $4f_{5/2}$, respectively, as revealed in Fig. 5.03(b). The dual peaks at the location of 158.24 and 163.60 of the XPS spectrum of Y 3d, which correspond to $3d_{5/2}$ and $3d_{3/2}$, respectively, are indicative of yttrium in the Y^{3+} state as illustrated in Fig. 5.03(c). Fig. 5.03(d) shows that O 1s peaks at 528.96, 530.14, and 530.96 eV. These peaks are caused by surface adsorbed water molecules (O–H) and metal-oxygen bonds seen in the XPS survey profile of BYW: Dy^{3+} [179,180]. Further, the W 4f exhibits two peaks at 34.34 and 36.42 eV for $4f_{7/2}$ and $4f_{5/2}$, which represent W^{6+} state of $BiYWO_6$ as shown in Fig. 5.03(e) [181,182]. In view of the above, the data confirms that BYW: Dy^{3+} is present in the as synthesized phosphor.

5.3.4. Diffuse reflectance spectral analysis

The diffuse reflectance spectra displayed from 200 to 1000 nm range to provide insight about the optical properties of the samples. Fig. 5.04 illustrates the diffuse reflectance spectra

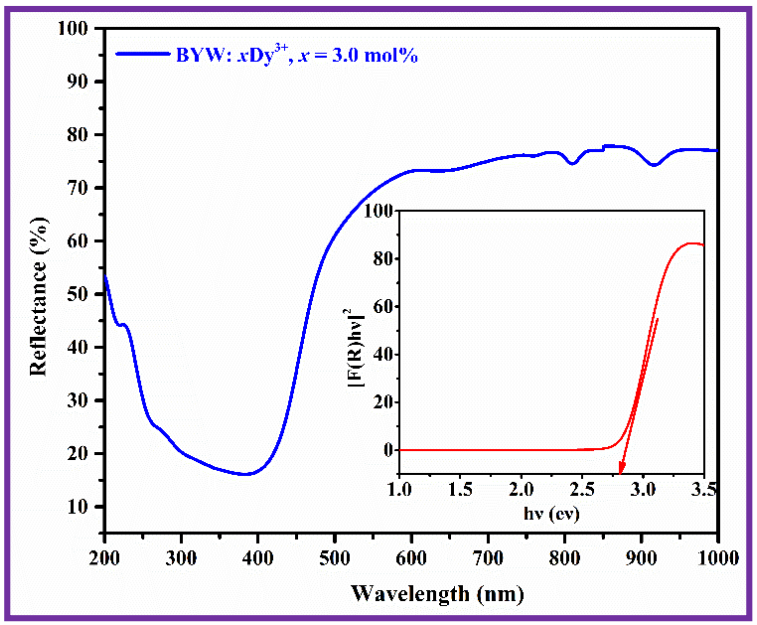

Fig. 5.04: *Diffuse reflectance spectra of 3.0 mol% Dy^{3+} doped $BiYWO_6$ phosphor. The Inset plot reveals the assessment of the band gap by employing the Kubelka-Munk function.*

of BYW: xDy^{3+} (x = 3.0 mol%) phosphor. Fig. 5.04 signifies that the appearance of new absorption bands beyond 700 nm can be signified by the characteristic peaks of Dy^{3+} ions in the BYW. Phosphor demonstrate pronounced absorption bands within the 200-400 nm wavelength range, which include the Y/Dy–O charge transfer band (CTB) and the ligand to metal charge transfer transition (LMCT) associated with W–O bonds [183,184]. The estimation of the optical band gap of the as synthesized materials can be derived from the DRS profile, using the equations as described in equations (2.04) & (2.05) in section 2.3.4 [113]. As a result, the determination of the optical band gap involves the linear relationship between $[F(R)h\vartheta]^{1/n}$ and $h\vartheta$ by extrapolating the linear graphical region to zero. For the electronic transition n = ½, the representation of fit for the graph depicted in the inset as Fig. 5.04, and the estimated band gap values are assessed to be 2.79 eV for the Dy^{3+} doped BYW samples.

5.3.5. Photoluminescence studies

Fig. 5.05(a) demonstrates the PLE spectrum of BYW: xDy^{3+} (x = 3.0 mol%) phosphor by fixing 575 nm emission wavelength. The excitation spectrum contains absorption peaks in a range of 270-500 nm, which contain characteristics of charge transfer band (CTB) as well as characteristic electronic transitions of Dy^{3+} ions. The peaks obtained due to 4f electronic transitions are magnified in a 320-500 nm wavelength range, and revealed in the inset of Fig. 5(a). The excitation peaks are centred at 352, 366, 387, 427, 455, and 475 nm positions and are associated with the transitions from the ground state i.e. $^6H_{15/2}$, to various higher states viz. $^6P_{7/2}$, $^4I_{11/2}$, $^4F_{7/2}$, $^4G_{11/2}$, $^4I_{15/2}$ and $^4F_{9/2,}$ respectively in BYW lattice [185,186]. The prominent peaks were observed at 290 and 455 nm as depicted in excitation spectra. The intense broadband situated at 290 nm may be owing to an overlapping between $O^{2-} \rightarrow Dy^{3+}$ charge transfer band, and the ligand to metal charge transfer transition (LMCT) associated with the WO_6^{-6} group, indicating the strong covalency between O^{2-} and W^{6+} in the $BiYWO_6$ lattice [183,184]. The next intense excitation band centred at 455 nm resembles the $^6H_{15/2} \rightarrow {}^4I_{15/2}$

electronic transition of the Dy^{3+} ions. Based on the PLE result, the excitation wavelengths, 290 and 455 nm are selected to record further emission characteristics.

Fig. 5.05(b & c) shows the emission spectra of BYW: xDy^{3+} (x = 0.5, 1.0, 2.0, 3.0, 4.0, and 5.0 mol%) phosphors recorded using 290 and 455 nm excitation wavelengths, respectively.

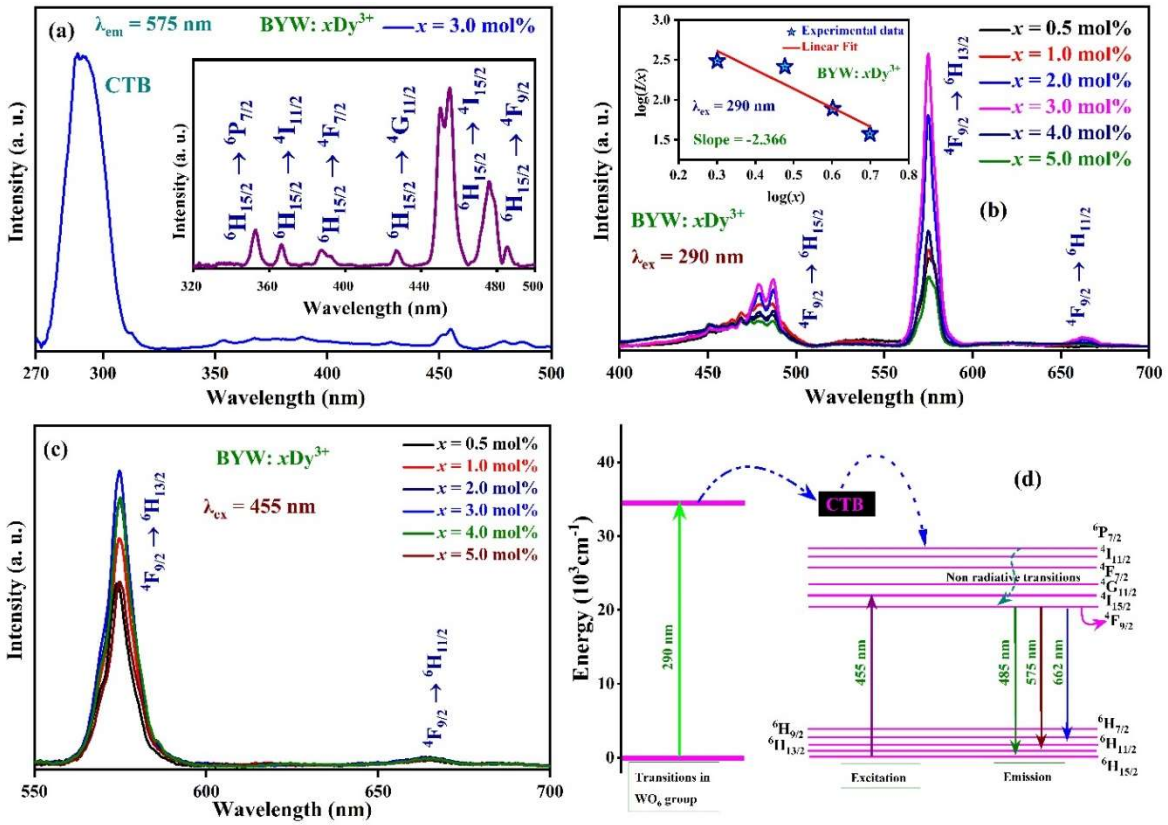

Fig. 5.05: *(a) PLE spectrum of 3.0 mol% Dy^{3+} doped $BiYWO_6$ phosphor. (Inset plot shows the magnified PL excitation in 320-500 nm wavelength range.), Emission spectra of Dy^{3+} doped $BiYWO_6$ under excitation wavelength of (b) 290 nm (Inset: Plot between log(I/x) vs. log(x) with varying concentrations of Dy^{3+} ions), (c) 455 nm, respectively, and (d) Partial energy level diagram of Dy^{3+} doped $BiYWO_6$ phosphor.*

Fig. 5.05(b) depicts the emission spectra consisting of a broad emission band, and three emission bands were positioned at 485, 575, and 662 nm wavelengths, which are ascribed to

the $^4F_{9/2} \rightarrow {}^6H_{15/2,}$ $^4F_{9/2} \rightarrow {}^6H_{13/2,}$ and $^4F_{9/2} \rightarrow {}^6H_{11/2}$ transitions, under 290 nm excitation wavelength. In this emission spectra, a broad intense emission band was overlapped with the band positioned at 485 in the 450-500 nm region and a second intense band positioned at 575 in the 560-590 nm region (yellow), with dissimilar emission intensity. The blue emission observed in this study is attributed to the magnetic allowed dipole ($^4F_{9/2} \rightarrow {}^6H_{15/2}$) electronic transition of Dy^{3+} ions. This emission is found to be minimally affected by the strength of the crystal field around the dysprosium ions. On the other hand, the yellow emission is associated with the forced electric dipole ($^4F_{9/2} \rightarrow {}^6H_{13/2}$) transition, which follows the selection rule $\Delta J = 2$ [187,188]. In the event that Dy^{3+} ions are positioned at a site of high symmetry featuring an inversion centre, it is expected that the intense transition shall be observed from the $^4F_{9/2}$ to the $^6H_{15/2}$ energy level. Conversely, if ions are located at a site of low symmetry and lacking an inversion centre, the predominant transition observed in the emission spectra will be the hypersensitive transition from $^4F_{9/2}$ to the $^6H_{13/2}$ energy level. According to this principle, Dy^{3+} ions potentially occupy the lower symmetry sites of Bi^{3+} ions in the BYW structure without any inversion centre due to their equal oxidation state and smaller ionic radii compared to Bi^{3+} (coordination no. (N = 6), ionic radii of Bi^{3+} = 1.03 Å and Dy^{3+} = 0.912 Å). Hence, forced electric transition (yellow) emission intensity remained to be stronger than magnetic dipole transition (blue emission intensity) in this BYW: $x$$Dy^{3+}$ phosphor. Whereas the emission spectra recorded using a 455 nm excitation wavelength consist of two emission bands, which are positioned at wavelengths of 575 and 662 nm corresponding to the $^4F_{9/2} \rightarrow {}^6H_{13/2}$ and $^4F_{9/2} \rightarrow {}^6H_{11/2}$ transitions of Dy^{3+} ions, respectively. In both cases, the emission intensity alters with Dy^{3+} ion content, as displayed in Fig. 5.05(b & c), and was realized to be highest at 3.0 mol% of Dy^{3+} ions, which is considered as optimized concentration for the $BiYWO_6$ host.

5.3.6. Dexter's theory

In order to examine the impact of dopant ions on the host lattice, the Dy^{3+} ions were systematically varied from x = 0.5 to 5.0 mol% under the excitation wavelength 290 nm, as depicted in Fig. 5.05(b). The graph illustrates that the emission peak intensity of $^4F_{9/2} \rightarrow {}^6H_{13/2}$ transition initially increases until reaching Dy^{3+} ion content of 3.0 mol%, which subsequently declines owing to concentration quenching. The observed spectacle can be ascribed to the increased proximity of Dy^{3+} - Dy^{3+} ions at higher doping concentrations, resulting in a prevalence of non-radiative energy transfer over radiative emission. Therefore, the non-radiative energy transfer is mostly influenced by the critical distance (R_c) corresponding to the adjacent Dy^{3+} ions within the host lattice. The equation was proposed by Blasse for determining the critical distance (R_c) as described in equation 1.01, section 1.3.2 [19]. The critical distance has been found to be 19.63 Å, with the given parameters V = 950.87 Å^3, X_c = 0.03, and N = 8. Based on the Van Uitert concept, when the assessed value of R_c is significantly beyond the critical distance threshold (5Å), the process of energy transfer takes place via multipolar interaction [110]. In the current scenario, the value of R_c exceeds 5Å, thereby facilitating non-radiative energy transfer through multipolar interaction in agreement with Dexter's theory. This relationship can be expressed as the correlation between luminescence intensity (I), specific type of multipolar interaction (Q), and concentration of dopant ions (x) as depicted equation 1.02 in the section 1.3.2. [171]. The value of Q can be determined by evaluating the slope of linear regression line between the $\log\left(\frac{I}{x}\right)$ and $log(x)$. The inset of Fig. 5.05(b), illustrates the relation between ($\log\left(\frac{I}{x}\right)$ and $log(x)$. This graph is derived from the emission spectra of BYW: xDy^{3+}, when excited by 290 nm wavelength. The slope of the curve is determined to be -2.366, and the obtained Q value is 7.098 (~8), which provides evidence supporting the hypothesis that the exchange of energy between neighbouring Dy^{3+}

ions is primarily attributed to dipole quadrupole interaction in the concentration quenching mechanism.

5.3.7. Energy level diagram

The process of observed excitation and emission corresponding to Dy^{3+} ions incorporated BYW host material, represented by the partial energy level diagram is as disclosed in Fig. 5.05(d). The Dy^{3+} ions are stimulated to fascinating energy levels of CTB or excited state of Dy^{3+} ($^4I_{15/2}$) as shown with upward arrows in Fig. 5.05(d). When subjected to excitation wavelength 290 nm, the higher excited state of WO_6^{-6} groups undergoes a non-radiative relaxation process to the intermediate state. Subsequently, energy is transferred from the intermediate state ($^4F_{9/2}$) to the numerous lower energy levels of Dy^{3+} ions. The energy gap between the $^4F_{9/2}$ energy level of Dy^{3+} ions and the next lower energy state is significantly higher. As a result, only radiative transitions (downward arrows) to lower energy levels of Dy^{3+} ions are possible, leading to emission in the blue, yellow and red regions. A similar mechanism is expected during 455 nm excitation, the energy is non-radiatively discharged to the $^4F_{9/2}$ energy state, followed by a subsequent radiative emissions, as described in section 5.3.5.

5.3.8. Chromaticity coordinates

To determine the colorimetric performance of the synthesized Dy^{3+} activated BYW phosphor, the chromaticity coordinates have been measured using the emission spectral data under UV (290 nm) excitations. The colour coordinates (x, y) for the synthesized BYW: $x$$Dy^{3+}$, x = 3.0 mol% phosphor is found to be (0.460, 0.370) under the excitations 290 nm wavelength, as demonstrated in Fig. 5.06. The estimated (x, y) coordinates for the synthesized BYW: 3.0 mol% Dy^{3+} phosphor falls near the standard white light region under 290 nm wavelength [104]. Moreover, the correlated colour temperature (CCT) for the synthesized BYW: $x$$Dy^{3+}$, x = 3.0 mol% phosphor has been computed using equation (1.09) in the section

1.4 [189]. The estimated CCT value for the synthesized BYW: xDy^{3+}, x = 3.0 mol% phosphor was observed to be 2305 K for the excitation wavelength of 290 nm. The observed values of

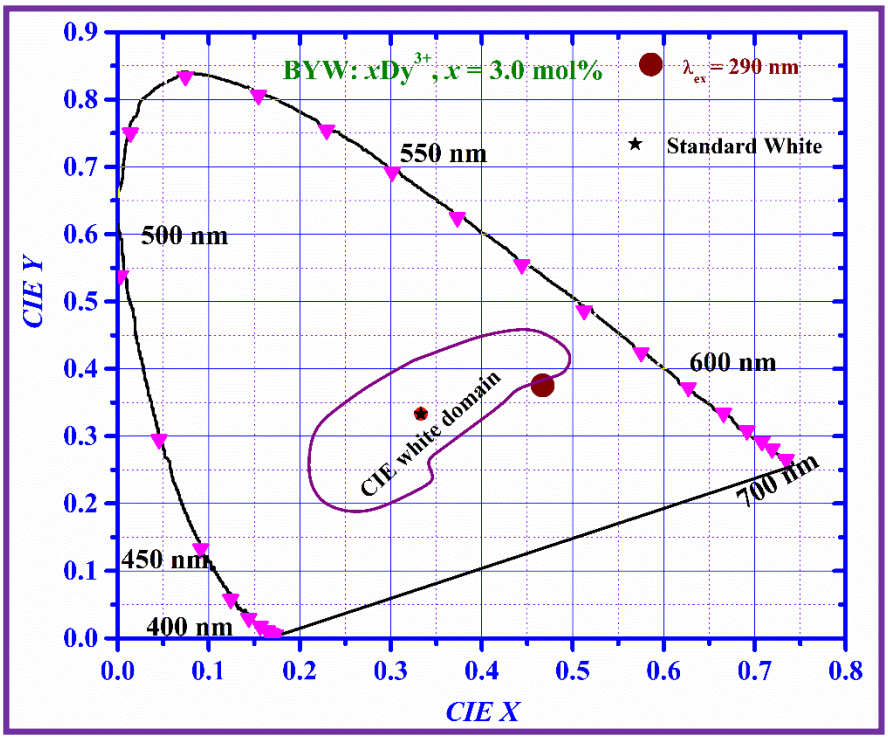

Fig. 5.06: *CIE color coordinates of Dy^{3+} doped $BiYWO_6$ phosphor under the excitation wavelength of 290 nm.*

CCT are lower than that of 5000 K, which suggests that the synthesized phosphors emit warm white light under UV excitation. In view of the above, this phosphor material is effectively excited under a UV source with the wavelength of 290 nm.

5.3.9. PL decay analysis

The decay curves of BYW: xDy^{3+} (x = 0.5 to 5.0 mol%) phosphors corresponding to the $^4F_{9/2}$ level were measured using 290 nm excitation wavelength by fixing the emission peak at 575 nm, as depicted in Fig. 5.07(a). All the BYW samples have exhibited the most accurate alignment decay curves with a bi-exponential function. The equation used to represent the bi-exponential fit for all the decay curves mentioned in the equation (2.07) in the section 2.3.9 [101,102]. The average value (τ_{avg}) of the decay time for the series of Dy^{3+} activated $BiYWO_6$

phosphor powder samples was estimated from the equation described in equation (2.08) in the section 2.3.9 [101,102]. The observed average lifetime (τ_{avg}) values for the synthesized BYW: xDy^{3+} (x = 0.5 to 5.0 mol%) phosphors were found to be 218, 193, 183, 146, 134 and 132 μs, respectively.

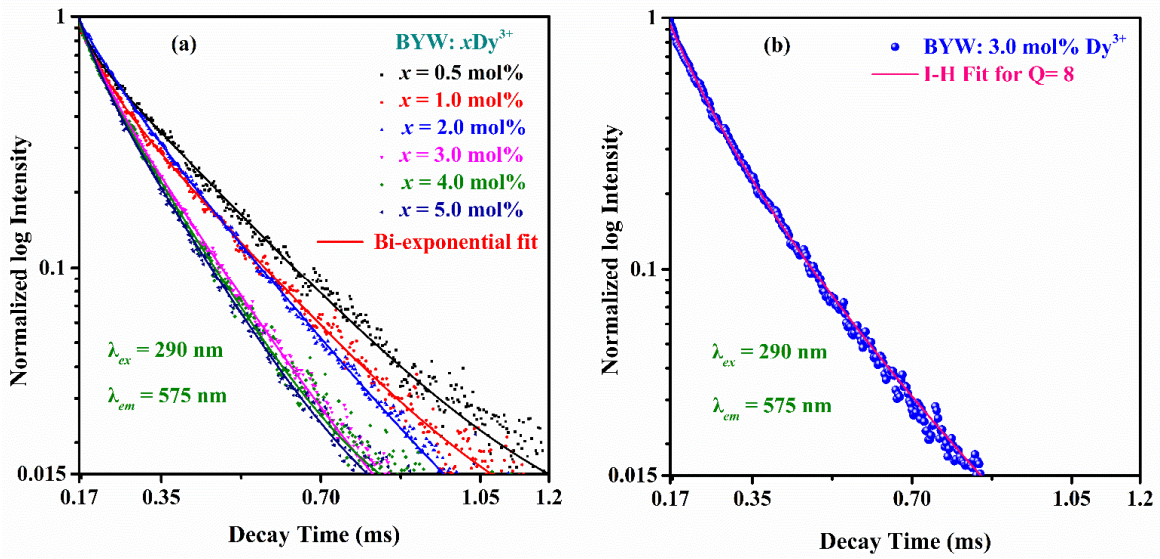

Fig. 5.07: *(a) Decay curves for $^4F_{9/2}$ level in the Dy^{3+} doped $BiYWO_6$ phosphors, (b) I-H fit for the synthesized 3.0 mol% Dy^{3+} doped $BiYWO_6$ phosphor.*

The average lifetime values of the BYW: xDy^{3+} phosphor decline as the content of Dy^{3+} increases. This decline in the average lifetime values is normally due to a deterioration in the distance between Dy^{3+} ions, which results in energy transfer from donor to acceptor ion of Dy^{3+}. The Inokutti Hirayama (I-H) model provides a clear understanding of the energy transfer mechanism between Dy^{3+} ions. According to the I-H model, energy transfers through multipolar interactions between the dopant Dy^{3+} ions result in non-exponential decay curves. The time and decay intensity can be associated with these energy transfers are as follows [190]:

$$I_t = I_0 \exp\left[-\frac{t}{t_0} - \eta\left(\frac{t}{t_0}\right)\right]^{\frac{3}{Q}} \qquad (5.01)$$

where, I_t attributed to the luminesce intensity at time t and I_0 corresponding to the t_0, after the excitation. The lifetime of the donor ions without any acceptor ions represented as t_0. The

energy transfer parameter represented by η. The value of $Q = 6$ due to d-d, $Q = 8$ represents the d-q, and $Q = 10$ attributed to the q-q type of interaction. The decay curve for 3.0 mol% Dy^{3+} doped BYW phosphor is well fitted with the equation (5.01) corresponding to the value of $Q = 8$, as depicted in Fig. 5.07(b). Therefore, energy transfer justified by d-q interaction between Dy^{3+} ions, as well as support the data obtained with Dexter's theory.

5.3.10. Temperature dependent PL analysis

In order to achieve comprehensive temperature dependent luminescent characteristics of the BYW: xDy^{3+} (x = 3.0 mol%) phosphor, the photoluminescence spectra were recorded under 455 nm excitation wavelength while exposing the sample within the range from 298 to 448 K temperatures as illustrated in Fig. 5.08. These spectra provide the information related to the variation in the intensity of the optimised phosphor as a function of temperature.

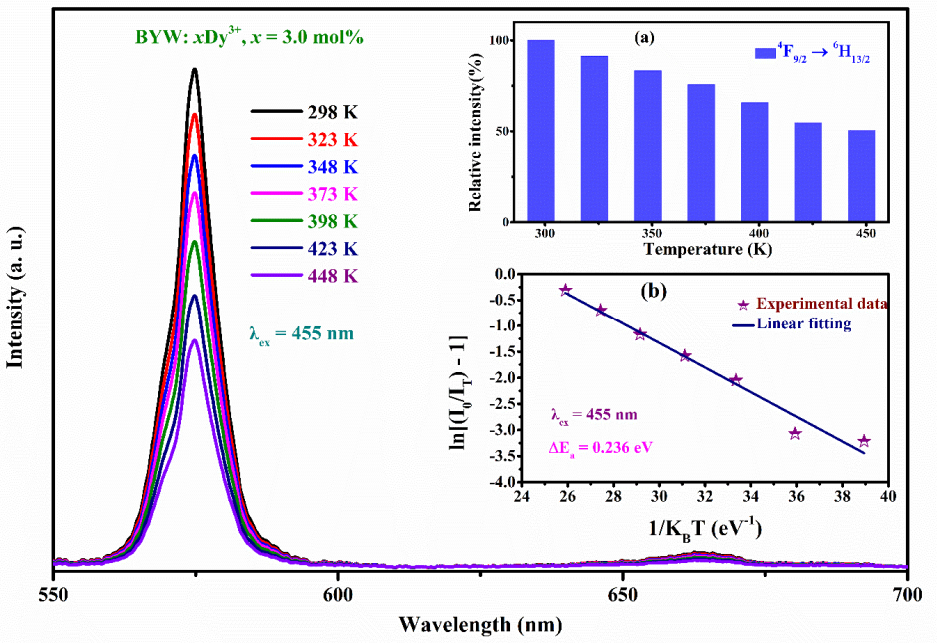

Fig. 5.08: *Temperature dependent PL spectra of Dy^{3+} doped $BiYWO_6$ phosphor, [Inset (a) shows the relative emission intensity of $^4F_{9/2} \rightarrow {}^6H_{13/2}$ peak with varying temperature from room temperature (298 K) to 448 K, and (b) Plot of $ln[(I_0/I_T)-1]$ Vs $1/K_BT$ of the Dy^{3+} doped $BiYWO_6$ phosphor.*

The phosphor material exhibits a decrease in the emission intensity as the temperature rises. The study revealed that the emission intensity corresponding to the $^4F_{9/2} \rightarrow {}^6H_{13/2}$ transition retains 76% of its initial intensity at 373 K, as described in the inset Fig. 5.08(a). In addition, the thermal stability of the BYW: xDy^{3+}(x = 3.0 mol%) phosphor can be assessed through the determination of activation energy (ΔE_a), and it was determined using the Arrhenius equation, as described in equation (2.09) in the section 2.3.10. The estimation of the activation energy (ΔE_a) can be derived from the linear regression analysis of the graph between $ln[(I_0/I_T)-1]$ and $1/K_BT$ as represented in the Fig. 5.08(b), and the activation energy (ΔE_a) for BYW: xDy^{3+} (x = 3.0 mol%) phosphor is found to be 0.236 eV. The photoluminescence result, which is dependent on the temperature, indicates that the BYW: xDy^{3+} (x = 3.0 mol%) phosphor consists of good thermal stability.

5.4. Conclusions

Thermally stable multicolour emitting BYW phosphor activated by dysprosium has been successfully synthesized using the CP method. The study of the structural, morphological, oxidation states of the elements and luminescent characteristics of the as-synthesized phosphor have been investigated. The crystalline monoclinic phase purity of Dy^{3+} doped $BiYWO_6$ has been established by the X-ray diffraction and Rietveld refinement. The optical bandgap (E_g) values are found to be 2.79 eV for the BYW: xDy^{3+} (x = 3.0 mol%) phosphor material. The BYW: xDy^{3+} displays the numerous excitation peaks in UV/n-UV and visible regions due to typical transitions of WO_6^{6-} group and Dy^{3+} ions. Dy^{3+} activated $BiYWO_6$ phosphor manifests excellent emission under excitation wavelengths of 290 and 455 nm, which shows the maximum emission intensity around 575 nm related to the $^4F_{9/2} \rightarrow {}^6H_{13/2}$ transition and gives an intense emission in the yellow region. The emission intensity differs through the content of Dy^{3+} ions. The intense emission was observed at 3.0 mol% among all Dy^{3+} doped $BiYWO_6$ phosphor samples and this concentration has been regarded as optimised. The CIE chromaticity

coordinates were determined for each concentration, revealing that all samples are located within the near white region, when excited at wavelength of 290 nm. The photoluminescence decay curves of the Dy^{3+} doped BYW phosphors exhibit a bi-exponential nature, characterized by an average decay time in the microsecond range. The luminescent characteristics of the phosphor material display temperature dependence, which serves as evidence for its thermal stability. The aforementioned results make Dy^{3+} doped BYW phosphors as a promising candidate for use in various luminescent devices, including pc-w-LEDs under UV excitation.

CHAPTER 6

Color Tunable Emitting Dy^{3+}/Eu^{3+} co-doped $BiYWO_6$ Phosphor for w-LEDs and Anti-counterfeiting Applications

Dysprosium (Dy^{3+}) and Europium (Eu^{3+}) co-activated bismuth yttrium tungstate ($BiYWO_6$: BYW) phosphors were synthesized by co-precipitation route. X-ray diffraction (XRD), field emission scanning electron microscope (FE-SEM), and energy dispersive x-ray (EDX), characterization techniques have been used to examine the structural, morphological, and compositional analysis of the prepared phosphors. The diffraction patterns of the as-synthesized phosphors confirmed the formation of pure monoclinic structure with single phase BYW nanoparticles. The optimized Dy^{3+} ion concentration was recognized as 3.0 mol%, and for co-doped phosphor, intensity increases without concentration quenching. Moreover, Dy^{3+}/Eu^{3+} co-doped BYW phosphors exhibit flexible color tunability with increasing Eu^{3+} concentration under different excitations. As appeared color tunable emission with Dy^{3+}/Eu^{3+} concentration in BYW suggests that the energy transferred to the sensitizer to activator, when the host matrix was doped with Dy^{3+}/Eu^{3+} ions. The significant accomplishments, like warm white light emission and controllable spectral composition in Dy^{3+}/Eu^{3+} co-doped BYW phosphor by altering the excitation energy and co-dopant (Eu^{3+}) concentration, designate it as a potential candidate in the field of lighting, anti-counterfeiting, and display devices.

6.1. Introduction

The substantial growth of industrial manufacturing production and economic sectors has exacerbated the global energy crisis and environmental pollution, garnering significant attention from researchers worldwide [191–193]. White light emitting diodes (w-LEDs) have emerged as a promising solution and are recognized as cutting-edge lighting technology due to their exceptional attributes, operational lifespan, high energy efficiency, rapid response time, and superior stability [180,194,195]. There are different strategies to fabricate the w-LEDs, which frequently utilize the down converting phosphors, to serve as luminescent materials that transform shorter wavelength light into desired spectral regions. The most commonly adopted configuration involves a blue emitting InGaN LED chip combined with yellow phosphor layer, typically YAG: Ce^{3+} [192,196]. While this system offers notable advantages such as high luminous efficacy, cost-effective production, and robust thermal stability, it suffers from inherent limitations, including a low color rendering index (CRI<80) and elevated correlated color temperature (CCT>4500 K). These deficiencies are primarily attributed to the inadequate red component in the emission characteristics, which restricts its applicability for both indoor and outdoor lighting applications [21,197,198]. To overcome these limitations, researchers have explored alternative approaches, such as employing multi phosphors comprising a suitable blend of phosphors using red, green, and blue (RGB) coated on UV or n-UV LED chips. However, this method is hindered by reduced efficiency, often caused through the reabsorption of blue emission by the red and green phosphors [109,117]. An advanced strategy to address these challenges involves the utilization of single phase co-activated phosphors on UV/n-UV LED chips. This sophisticated approach enables the generation of warm white light with enhanced spectral properties, including precise color reproducibility, tunable CCT, and optimized spectral output. Lanthanide based inorganic phosphors, particularly, red emitting activators with Eu^{3+} ions have been extensively investigated as potential candidates to mitigate

the aforementioned drawbacks. These materials exhibit superior photoluminescent properties and offer a viable pathway for achieving high-performance w-LEDs with balanced emission spectra.

The advancement of efficient single phase phosphors has underscored the pivotal role of host materials in shaping their luminescent properties [199,200]. As such, the selection of an ideal host material is paramount. In this regard, inorganic oxides have gained prominence as exceptional candidates due to their excellent luminescence characteristics, environmental friendliness, consistent quality, and ease of preparation [173–175]. These compelling qualities have positioned a wide range of inorganic oxides, including silicates, vanadates, niobates, tungstates, aluminates, and phosphates, as the subject of intense scientific exploration [2,21,141]. Among these, tungstate based compounds stand out, captivating the attention of researchers with their unparalleled fluorescent properties. Their versatility makes them indispensable across a spectrum of cutting edge applications, from advanced display technologies and optical thermometry to solar energy systems, anti-counterfeiting solutions, scintillators, and solid state laser devices [72,73]. By incorporating rare earth ions within tungstate matrices, multi color light producing phosphors can be realized. These ions exhibit exceptional stability under ambient conditions and generate sharp, narrow band emissions arising from f-f electronic transitions. Among the available RE^{3+} ions, Dy^{3+} activated tungstate based single phase phosphors are efficient candidates for white light generation, driven by the intensity ratio of two dominant emission bands as discussed in the previous chapter. However, the inherent deficiency in the red spectral component results in fabricated w-LEDs with low CRI and elevated CCT, limiting their utility. To address this challenge, Eu^{3+} co-doping with Dy^{3+} activated phosphors has emerged as a strategic solution, enabling tunability from cool to warm white light as well as significantly enhancing the CRI value [21,201]. Consequently, developing Dy^{3+}/Eu^{3+} co-doped inorganic phosphors has garnered substantial research interest.

The primary purpose of contemporary investigation is to synthesize a series of novel Dy^{3+}-activated and Dy^{3+}/Eu^{3+} bi-activated BYW phosphors, using the Co-precipitation (CP) method. The developed phosphor's phase purity and particle distribution have been determined through structural and morphological investigations. Furthermore, the photoluminescent (PLE and PL), decay dynamics, and colorimetric properties are thoroughly investigated in detail. This work also focuses on energy transfer mechanism between the Dy^{3+} and Eu^{3+} ions, facilitating color tunning through modulation of excitation energy and precise control of dopant ion concentrations for w-LEDs and anti-counterfeiting applications.

6.2. Materials and Synthesis of BYW: Dy^{3+}/Eu^{3+} samples

Dy^{3+}/Eu^{3+} co-activated $BiYWO_6$ phosphors were synthesized using the coprecipitation method. The initial precursors $Y(NO_3)_3.6H_2O$, $Na_2WO_4.2H_2O$, $Bi(NO_3)_3.5H_2O$, Dy_2O_3, and Eu_2O_3 were utilized in a stoichiometric ratio. The detailed synthesis process were illustrated in section 2.2.4 in chapter 2 and Fig. 2.05.

6.3. Results and discussion

6.3.1. XRD

Fig. 6.01 displays the XRD patterns of the synthesized BYW host material and BYW: Dy^{3+}/Eu^{3+} co-doped phosphors, along with the reference pattern from JCPDS card no. 33-0224. The diffraction profile of the BYW host material matches well with the standard data, confirming the phase purity and the absence of impurities. The XRD patterns indicate a monoclinic crystal structure (space group P2/a (13)) with lattice parameters a = 8.1244 Å, b = 3.7534 Å, and c = 16.0345 Å. The host material BYW consists of Aurivillius-type $[BiYO_2]^{2+}$ layers interspersed with $[WO_4]^{2-}$ perovskite layers, featuring corner sharing WO_6 octahedron and edge linked chains [126,202]. The XRD patterns of the Dy^{3+}/Eu^{3+} co-doped BYW samples closely resemble that of the undoped BYW host and the JCPDS reference pattern, indicating that Dy^{3+}/Eu^{3+} incorporation does not alter the crystal structure. This is attributed to the

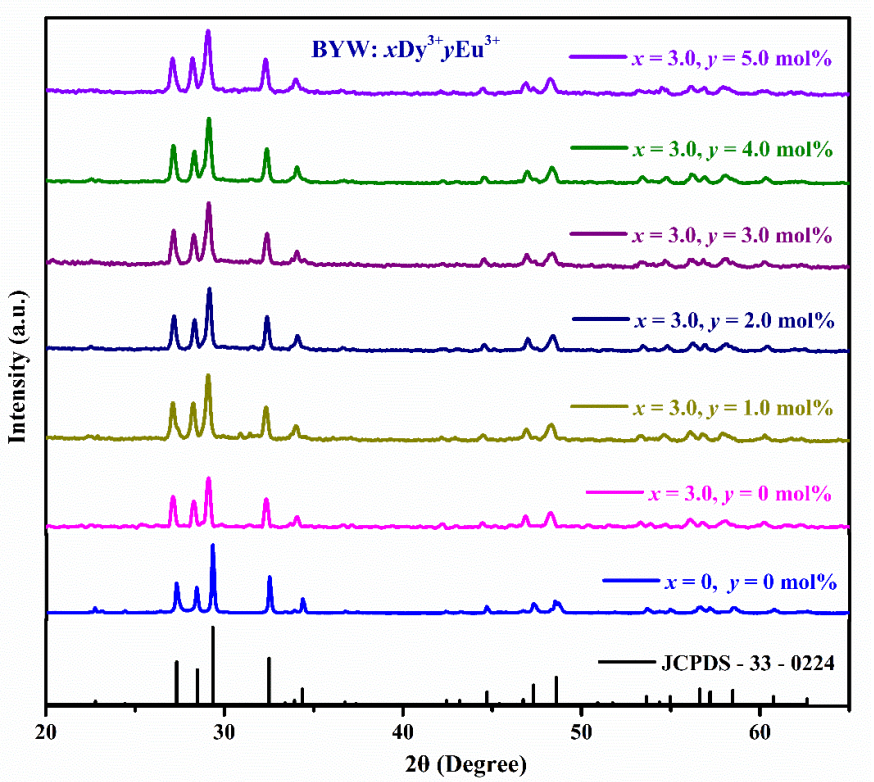

Fig. 6.01: *XRD patterns of pure BYW host material, Dy^{3+} singly doped, and Dy^{3+}/Eu^{3+} co-doped BYW phosphors.*

Isovalent substitution of the site of Bi^{3+} ions by Dy^{3+}/Eu^{3+} ions, enabled by their similar oxidation states and slightly smaller ionic radii. Moreover, the value of the average crystallite size (D) of the synthesized BYW: Dy^{3+}/Eu^{3+} phosphors was determined employing the Debye-Scherrer equation as depicted in equation (2.02) in section 2.3.2 of chapter 2 [110,153]. The average crystallite size of the BYW and BYW: Dy^{3+}/Eu^{3+} samples found between in the range of 40 and 55 nm.

6.3.2. Morphological studies

The surface morphology significantly influences the luminescence efficiency of the synthesized phosphor. Fig. 6.02(a) displays FE-SEM micrographs of the host material BYW and Dy^{3+}/Eu^{3+} (x = 3.0 mol%) co-doped BYW phosphor with nano-scale resolution, revealing uniformly distributed grains with a diameter between 50-200 nm. Doping with Dy^{3+}/Eu^{3+} ions causes no noticeable morphological changes, likely due to the high melting point of Dy_2O_3 and

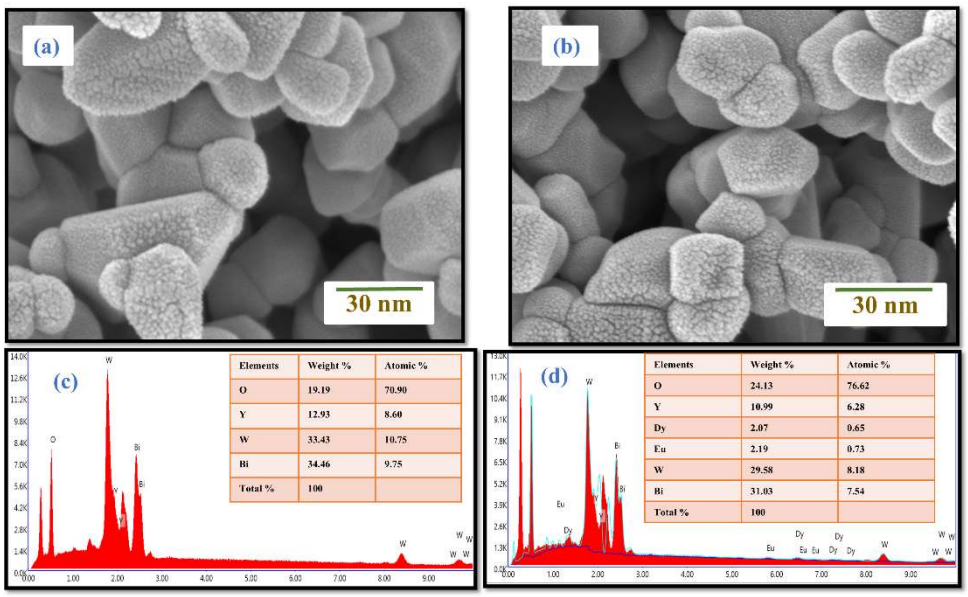

Fig. 6.02: *FE-SEM images of (a) host $BiYWO_6$, (b) 3.0 mol% Dy^{3+}/Eu^{3+} co-doped $BiYWO_6$ phosphor, EDX patterns of (c) host $BiYWO_6$ and (d) 3.0 mol% Dy^{3+}/Eu^{3+} doped $BiYWO_6$ phosphor (Inset shows the table of elemental composition).*

Eu_2O_3 compared to other precursors used during synthesis. The observed microstructure shows uniformly distributed, irregularly shaped grains that are closely packed, highlighting the consistency in particle size and formation. Such submicron crystalline particles are advantageous for enhancing luminescent efficiency, making them highly suitable for w-LEDs and anticounterfeiting applications.

The elemental analysis via EDX confirms the uniform distribution of dysprosium (Dy), Europium (Eu), tungsten (W), bismuth (Bi), yttrium (Y), and oxygen (O), as shown in Fig. 6.02(b). The corresponding table validates the presence and successful incorporation of Dy^{3+} and Eu^{3+} ions through their atomic and weight percentage as shown in Fig. 6.02(c).

6.3.3. Photoluminescence (PL) analysis and kinetic properties

6.3.3.1. PL analysis of Dy^{3+}doped BYW phosphors

The PLE spectrum of the BYW: 3.0 mol% Dy^{3+} phosphor material were identified by monitoring the 575 nm emission wavelength in the range of 272-500 nm. The excitation

spectrum includes charge transfer band (CTB), as displayed in Fig. 6.03(a), and the 4f electronic transitions associated with the Dy^{3+} ions are shown in the 320–500 nm region, as illustrated in the magnified plot in the inset of Fig. 6.03(a). The 4f electronic transitions in the $BiYWO_6$ lattice is responsible for the transition from the ground state ($^6H_{15/2}$) to a number of higher energy states. The strong peak detected at 290 nm represents the CTB band allied through the transition of Y/Dy–O charge transfer band (CTB), and the ligand to metal charge transfer transition (LMCT) associated with W–O bonds, indicates the substantial covalency between O^{2-} and W^{6+} [183,184]. The other strong excitation wavelength, centred at 455 nm,

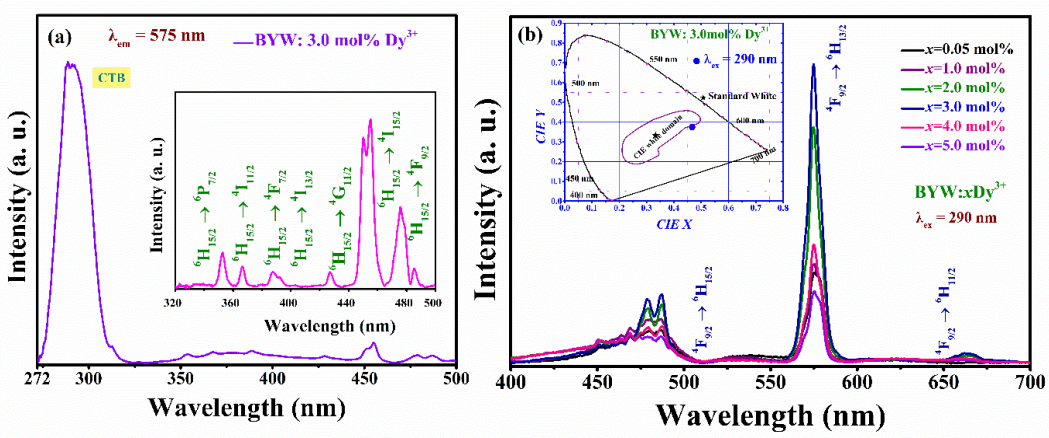

Fig. 6.03: *(a) Excitation spectra of $BiYWO_6$: 3.0 mol% Dy^{3+} phosphor by monitoring at 575 nm wavelength (Inset plot shows the magnifying of the PL excitation in 320-500 nm wavelength range), (b) Emission spectra of $BiYWO_6$: Dy^{3+} (Inset plot shows the CIE for optimized concentration).*

represents the electronic transition of the Dy^{3+} ions from $^6H_{15/2}$ to $^4I_{15/2}$. Among all the excitation peaks, the most intense excitation wavelength at 290 nm highlights the most significant absorption potential at this specific wavelength. Emission spectral analysis has thus been performed for an excitation wavelength of 290 nm for all BYW: Dy^{3+} phosphors. Thus, the emission spectra of BYW: xDy^{3+} (x = 0.5, 1.0, 2.0, 3.0, 4.0, and 5.0 mol%) phosphors obtained at the excitation wavelength 290 nm are displayed in Fig. 6.03(b). Emission spectra

with three emission bands at wavelengths of 485, 575, and 665 nm are linked to the $^4F_{9/2}\rightarrow{}^6H_{15/2}$, $^4F_{9/2}\rightarrow{}^6H_{13/2}$, and $^4F_{9/2}\rightarrow{}^6H_{11/2}$ transitions. These emission spectra showed that the emission strength of the two lights differed, with broad, intense emission bands located at 482 nm in the 450–500 nm area (blue) and second intense bands located at 575 nm in the 560–590 nm region (yellow). Furthermore, because of the well known concentration quenching mechanism, it was shown that the intensity of the luminescence spectrum increased with an increase in Dy^{3+} content to 3.0 mol% and decreased beyond that, and this concentration is known as optimized. Additionally, the chromaticity coordinates for the BYW: 3.0 mol% Dy^{3+} phosphor were attained to be (0.460, 0.370) under the 290 nm excitation wavelength, as illustrated inset of Fig. 6.03 (b). Which conclude that optimal Dy^{3+} ion concentration for the BYW host matrix is thus 3.0 mol%, with emission color falling in the near-white zone, as illustrated in Fig. 6.03. Such BYW phosphors doped with Dy^{3+} ions alone show a much weaker red emission. Therefore, an optimized (3.0 mol%) Dy^{3+} doped BYW phosphor sample has been co-activated with varying content of Eu^{3+} ions to improve emission color in the red region, as well as to provide color tunability and pure white light.

6.3.3.2. PL analysis of Eu^{3+} doped BYW phosphors

PL properties of BYW: 1.0 mol% Eu^{3+} were examined and depicted in Fig. 6.04. The PL excitation spectra monitoring at λ_{em} = 613 nm is shown in Fig. 6.04(a). The dominant peak, which corresponds to the transition $^7F_0\rightarrow{}^5D_2$ of Eu^{3+} ions, was seen at 465 nm, while the excitation spectrum shows several peaks in the 350–500 range. This specifies that the BYW: 1.0 mol% Eu^{3+} phosphor sample may be efficiently stimulated by the blue (465 nm) light. Also, the emission spectrum of the BYW: 1.0 mol% Eu^{3+} phosphor was monitored with the blue excitation wavelength in the 500-750 nm range as represented in Fig. 6.04(a). Numerous peaks in the emission spectrum ascribed to the transition of $^5D_0\rightarrow{}^7F_0$, $^5D_0\rightarrow{}^7F_1$, $^5D_0\rightarrow{}^7F_2$, $^5D_0\rightarrow{}^7F_3$, and $^5D_0\rightarrow{}^7F_4$ are responsible for the Eu^{3+} transitions, which are located

at 579, 593, 613, 653, and 704 nm, respectively. Moreover, under the blue excitation wavelength, the CIE coordinate was observed to be (0.657. 0.347), which is positioned in the red domain of the CIE 1931 graph and illustrated in Fig. 6.04(c).

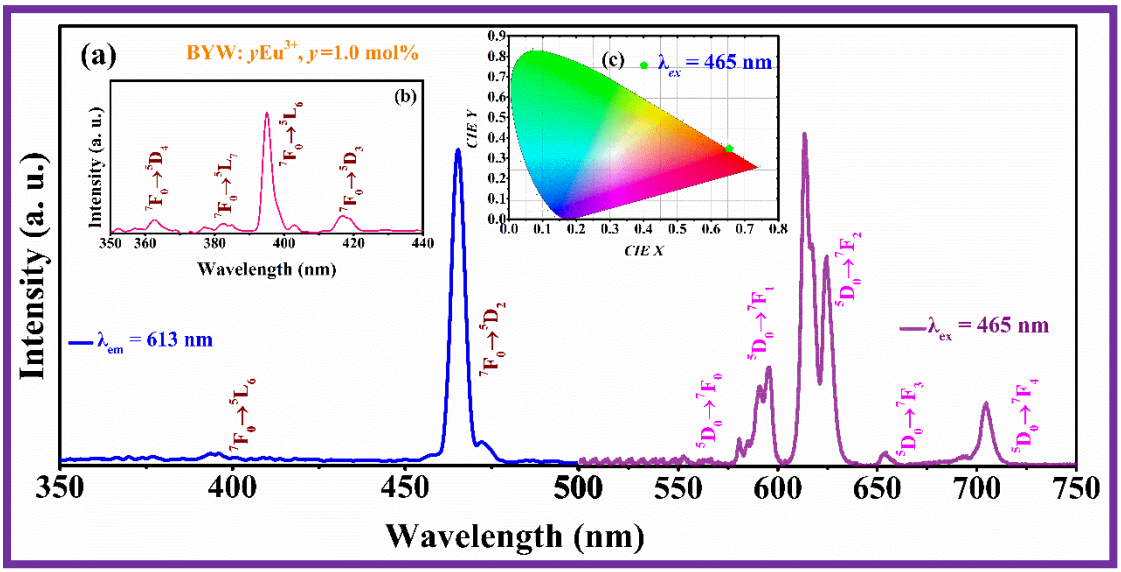

***Fig.6.04**: (a) Excitation and emission spectra of $BiYWO_6$: 1.0 mol% Eu^{3+} phosphor sample, (b) Magnification of the excitation spectra, and (c) Chromaticity coordinate for the $BiYWO_6$: 1.0 mol% Eu^{3+} phosphor sample under blue excitation.*

6.3.3.3. PL analysis Dy^{3+}/Eu^{3+} co-doped phosphors

The photoluminescence characteristics of the BYW phosphor material through the co-doping of Dy^{3+}/Eu^{3+} were performed. Fig. 6.05(a) depicts the photoluminescence excitation spectrum profile for the BYW: $xDy^{3+}yEu^{3+}$(x =3.0 mol%, y = 3.0 mol%) phosphor sample, recorded within the 230 to 500 nm range, by monitoring the most significant emission intensity of Dy^{3+} (575 nm), and Eu^{3+} (613 nm). This phosphor displays characteristic excitation spectra of dopant ions (Dy^{3+} and Eu^{3+}), displaying a blend of broad (centered at 290 nm, associated with CTB) and sharp bands in the UV/n-UV and blue areas, as previously noted. Within these excitation bands, certain 4f transitions of Dy^{3+}/Eu^{3+} ions occur in the region of 320-460 nm, as seen by the magnified PLE spectra of BYW: $xDy^{3+}yEu^{3+}$(x =3.0 mol%, y = 3.0 mol%), depicted

in Fig. 6.05(c). The transitions from the ground state, specifically $^7F_0$, to $^5L_6$ (393 nm) and $^5D_2$ (465) of Eu^{3+} ions, are characterized by prominent peaks [109,198].

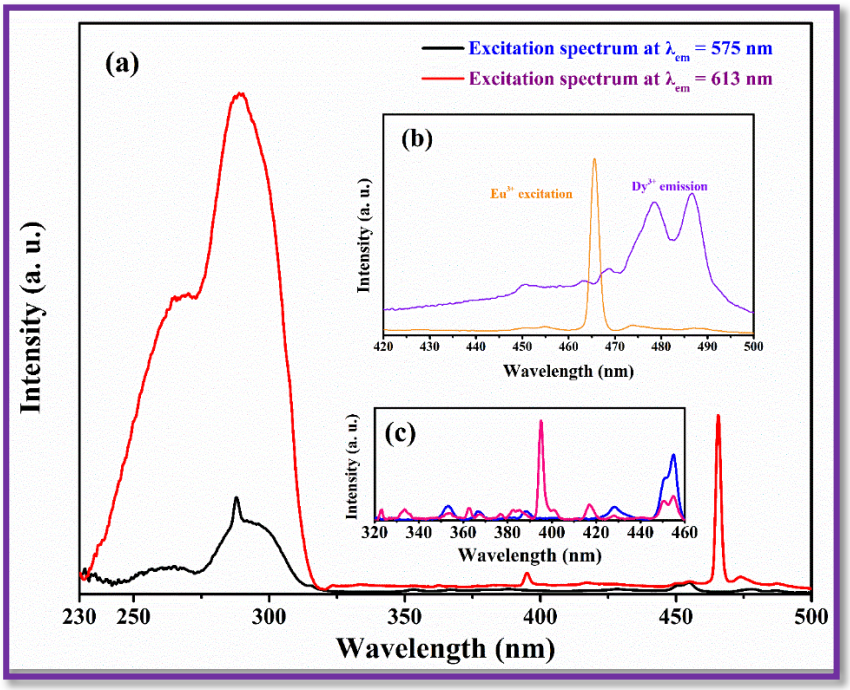

Fig. 6.05: *(a) Excitation spectra for 3.0 mol% Dy^{3+}/Eu^{3+} co-doped $BiYWO_6$ phosphor by monitoring emission at 575 nm and 615 nm wavelengths, (b) Spectral overlap of sensitizer (Dy^{3+}) emission and acceptor (Eu^{3+}) excitation, (c) Magnifying of the PL excitation in 320-460 nm wavelength range.*

Furthermore, Fig. 6.05(b) illustrates the overlapping spectrum of the photoluminescence properties of the sensitizer (Dy^{3+}) emission ($^4F_{9/2} \rightarrow {}^6H_{15/2}$) and activator ($Eu^{3+}$) excitation ($^7F_0 \rightarrow {}^5D_2$), which is essential for the energy transfer from Dy^{3+} to Eu^{3+}. In order to comprehend the process of energy transfer and color tuning in Dy^{3+}/Eu^{3+} bi-activated BYW phosphors, the co-doped BYW phosphor was stimulated at wavelengths 290, and 465 nm, which fall within the UV and the blue regions, respectively. The BYW: xDy^{3+}yEu^{3+} (x =3.0 mol%, y = 3.0 mol%) phosphor shows an elevated probability of energy absorption in the blue and UV/n-UV spectra when examined at 575 and 613 nm emission wavelengths, suggesting that blue or UV/n-UV LEDs are potential to use as pumping sources.

The emission spectra of Dy^{3+}/Eu^{3+}co-activated BYW phosphors at excitations of 290, and 465 nm are illustrated in Fig. 6.06. The concentration of Eu^{3+} ions is altered between 1.0 and 5.0 mol%, while the concentration of Dy^{3+} ions is maintained at its ideal level of 3.0 mol%. The PL spectra display distinct bands in the blue, orange, yellow, and red portions of the visible spectrum, which are recognized as various transitions of Dy^{3+} and Eu^{3+} ions. As stated earlier, the luminescence peaks detected in the co-doped BYW: Dy^{3+}/Eu^{3+} phosphor samples at wavelengths of 537, 579, 593, 613, 653, and 704 nm are attributed to distinct electronic spectral energy levels of Eu^{3+} ions from $^5D_1$ and $^5D_0$ levels to various lower energy states. On the other hand, the emission band observed at wavelengths 485, 575, and 662 nm can be ascribed to Dy^{3+} transitions ($^4F_{9/2} \rightarrow {}^6H_J$, where J = 15/2, 13/2, 11/2), [21,201].

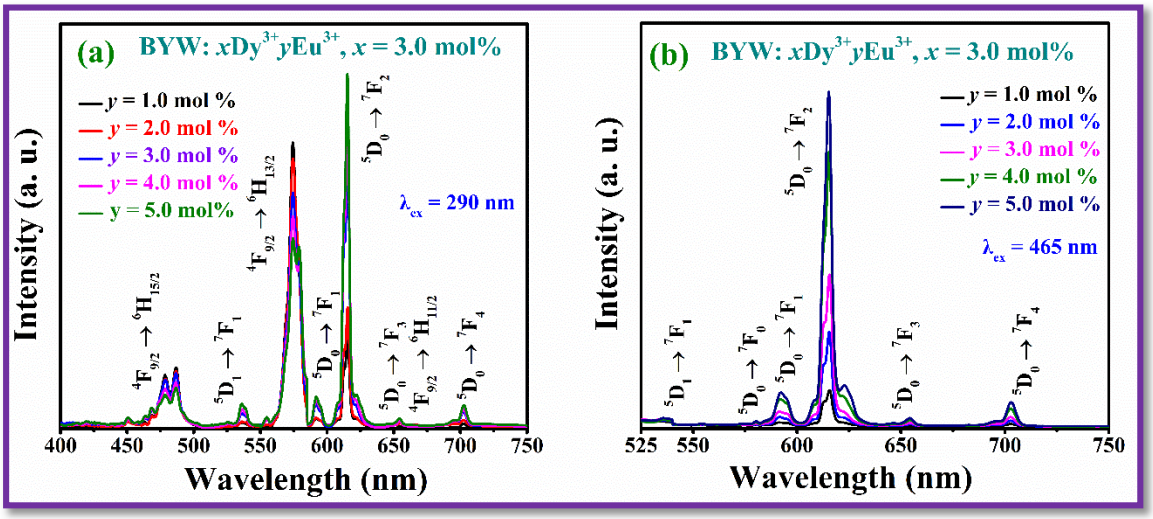

Fig. 6.06: *(a & b) Emission spectra of BYW: $xDy^{3+}yEu^{3+}$(x =3.0 mol%, y = 1.0, 2.0, 3.0, 4.0, and 5.0 mol%) samples under the excitation wavelengths (λ_{ex} = 290 and 465 nm.)*

The emission spectra prominently feature Eu^{3+} emission alongside the observation of several characteristic peaks of Dy^{3+} ions under excitation at 290 nm, as displayed in Fig. 6.06(a) [117,196,203]. Moreover, it has become evident that variations in excitation wavelength and activator ion content can expressively influence the emission peaks and intensities of Dy^{3+} and Eu^{3+} ions. The transfer of energy resulting from the interaction between Dy^{3+} ions to Eu^{3+} ions

at excitation wavelength 290 nm demonstrates that the emission from Eu^{3+} intensifies with an increase in Eu^{3+} concentration, as demonstrated in Fig. 6.06(a). The emission spectra initially exhibit a predominance of Dy^{3+} emission at excitation of 290 nm; however, with an increase in the concentration of Eu^{3+} ions, the emission from Dy^{3+} begins to wane. In contrast, the emission spectra display peaks exclusively corresponding to Eu^{3+} ions upon excitation at 465 nm, indicating a lack of reverse energy transfer from Eu^{3+} to Dy^{3+} ions, as demonstrated in Fig. 6.06(b). The emission of Eu^{3+} demonstrates an increase with concentration, attaining a maximum at 5.0 mol% across all excitation wavelengths. Thus, by alteration of the excitation wavelength and concentration of the activator ion, the color tunable property of the as-synthesized phosphor could be established through energy transfer between the sensitizer and activator ions.

6.3.4. Energy level diagram and energy transfer efficiency

The energy level diagram used to illustrate the several PL and energy transfer processes as shown in Fig. 6.07. When the incident light falls on the BYW: Dy^{3+}/Eu^{3+} phosphor sample,

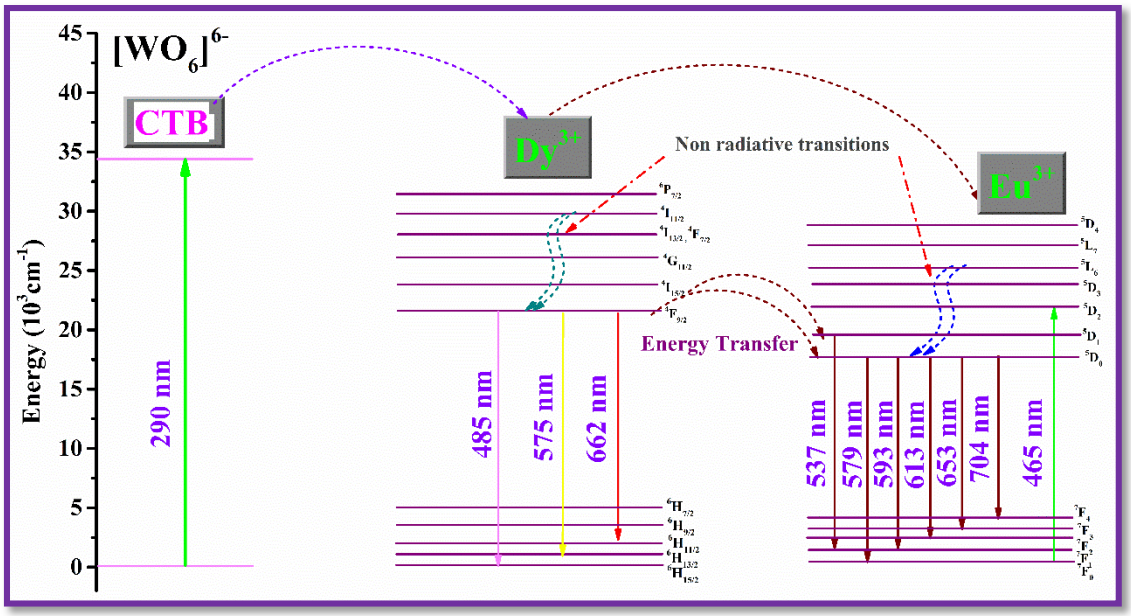

Fig. 6.07: *Energy level diagram indicating energy transfer in BYW: Dy^{3+}/Eu^{3+} phosphors.*

the incident energy may be absorbed by the energy state of WO_6^{6-} groups and then gets excited to the LMCT/WO_6^{6-} group (CTB). After that, the higher state of LMCT/WO_6^{6-} group can either relax non-radiatively or it can transfer its energy to the nearest Dy^{3+} ions in the excited state, and further resulting radiatively in blue and yellow regions. The energy levels ($^4I_{15/2}$ and $^4F_{9/2}$) of Dy^{3+} ions are comparable to Eu^{3+} ions' $^5D_1$ and $^5D_0$ energy levels, respectively [21,201]. Therefore, phonon induced non-radiative relaxation may facilitate energy transfer from excited states of Dy^{3+} ions to Eu^{3+} ions in BYW phosphor, followed by radiative transitions in Eu^{3+} ions to produce red color emission [21,201].

Energy transfer may occur non-radiatively from a donor (Dy^{3+}) to an acceptor (Eu^{3+}) ion through several processes, such as exchange or multipole-multipole interactions. The application of Dexter's theory and Reisfeld's approximation, elucidates the general dependence of quantum efficiencies, specifically η_{s0} and η_s of Dy^{3+} emission, both in the absence and presence of Eu^{3+} ions, on the cumulative concentrations of Dy^{3+} and Eu^{3+} ions ($C_{Dy^{3+}+Eu^{3+}}$) [60,201]:

$$\frac{\eta_{s0}}{\eta_s} \alpha\ C_{Dy^{3+}+Eu^{3+}}^{n/3} \tag{6.01}$$

where, the multipolar interaction type is indicated by the letter "*n*," which appears as dipole-dipole (d-d, n = 6), diploe-quadrupole (d-q, n = 8), and quadrupole-quadrupole (q-q, n = 10). It is possible to measure the quantum efficiencies ($\frac{\eta_{s0}}{\eta_s}$) of Dy^{3+} emission with and without Eu^{3+} ions by comparing the corresponding emission intensity ratios ($\frac{I_{s0}}{I_s}$). In this case, I_{s0} and I_s are thought to be the intensities of emission bands observed under 290 nm excitation caused by Dy^{3+} emission while Eu^{3+} is present and absent, respectively. Therefore, the above equation can be expressed as:

$$\frac{I_{s0}}{I_s} \alpha\ C_{Dy^{3+}+Eu^{3+}}^{n/3} \tag{6.02}$$

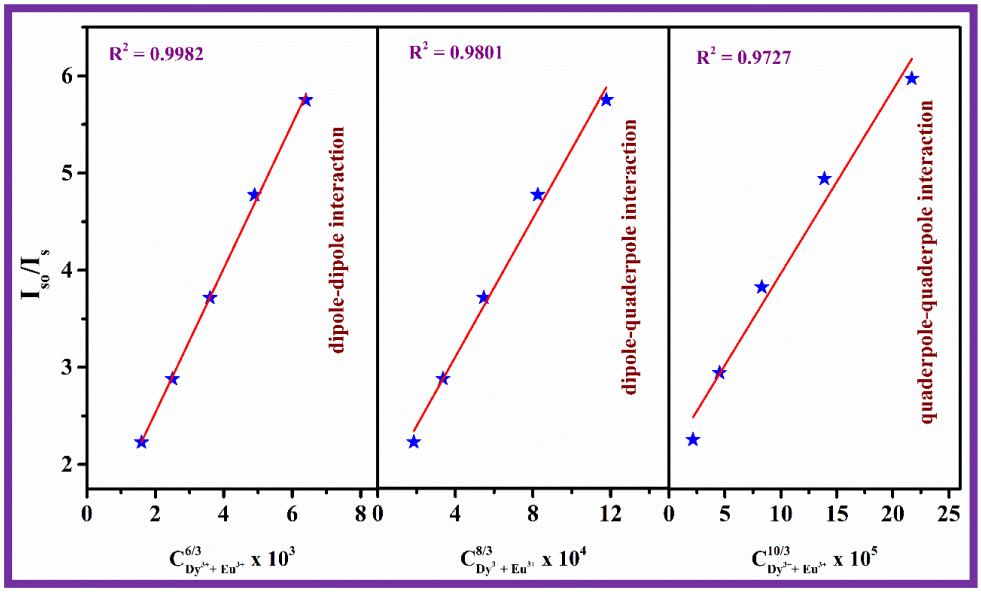

Fig. 6.08: *The dependence of* $\frac{I_{S0}}{I_S}$ *versus* $C^{n/3}_{Dy^{3+}+Eu^{3+}}$, *for the BYW:* Dy^{3+}/Eu^{3+} *phosphor sample under 290 nm excitation.*

Fig. 6.08 displays the plot between the $(\frac{I_{S0}}{I_S})$ *Vs* $C^{n/3}_{Dy^{3+}+Eu^{3+}}$ for values of *n* in the range of 6, 8, and 10 under 290 nm excitation wavelength. The best linear fit was obtained with n = 6, indicating that the ET from Dy^{3+} to Eu^{3+} is due to a non-radiative d-d interaction. The below mentioned relation can be used to assess the participation of d-d interactions for the Dy^{3+} to Eu^{3+} energy transfer efficiency (η_{ET}) from donor (Dy^{3+}) to acceptor (Eu^{3+}) [60,201]:

$$\eta_{ET} = 1 - \frac{I_S}{I_{S0}} \tag{6.03}$$

The energy transfer efficiencies for BYW: $x$$Dy^{3+}$$y$$Eu^{3+}$($x$ =3.0 mol%, y = 1.0, 2.0, 3.0, 4.0, and 5.0 mol%) are listed in Table 6.02.

6.3.5. Chromaticity coordinates

For the purpose of determining the potentiality for white light emission and the adaptability of color tunability in Dy^{3+}/Eu^{3+} bi-activated BYW phosphors, the color coordinates that were produced from the emission data have been thoroughly analyzed and recorded in the CIE 1931 diagram, as illustrated in Fig. 6.09 [21]. The optimized Dy^{3+} doped BYW phosphor (x = 3.0 mol%) exhibits color coordinates of (0.460, 0.370) when excited at 290 nm. The

synthesized BYW: 3.0 mol% Dy^{3+} phosphor has the estimated (x, y) coordinates that lie near white light region at 290 nm wavelength. Fig. 6.09 displays the multicolor emission from BYW: $xDy^{3+}yEu^{3+}$(x =3.0 mol%, y = 1.0 to 5.0 mol%) phosphors under 290 and 465 nm excitations, as mentioned in Table 6.01, respectively. Further, it has also been discovered that the coordinates change towards the red region due to variation in the concentration of the co-dopant (Eu^{3+}) ion under 290 excitation. One possible explanation for the achieved color tunability is the energy transfer capability from $Dy^{3+}\rightarrow Eu^{3+}$, which is beneficial for a variety of applications.

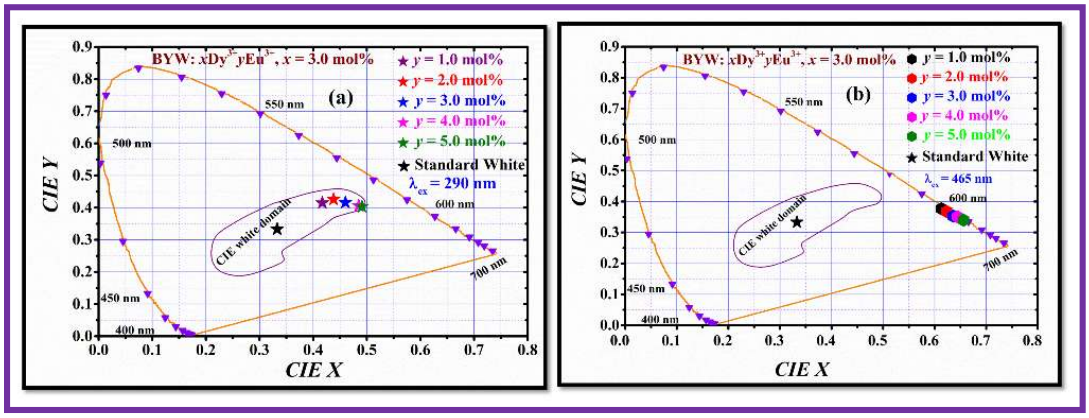

Fig. 6.09: *CIE coordinates of the as-synthesized BYW: Dy^{3+}/Eu^{3+} phosphors under (a) 290 nm, (b) 465 nm excitation.*

Table 6.01: *CIE color coordinates and CCT values for BYW: Dy^{3+}/Eu^{3+} phosphors under different excitations.*

Parameter	λ_{ex} (nm)	Sample (BYW: $xDy^{3+}yEy^{3+}$, x = 3.0 mol%)				
		y = 1.0 mol%	y = 2.0 mol%	y = 3.0 mol%	y = 4.0 mol%	y = 5.0 mol%
CIE coordinates (x, y)	290	(0.417, 0.415)	(0.438, 0.426)	(0.460, 0.416)	(0.485, 0.406)	(0.491, 0.403)
	465	(0.613, 0.377)	(0.623, 0.368)	(0.636, 0.353)	(0.644, 0.351)	(0.656, 0.340)
CCT(K)	290	3642	3570	2942	2552	2459
	465	3089	2970	2646	2397	2058

Under excitation wavelength of 290 nm, the color coordinates fall inside the CIE white domain, suggesting that Dy^{3+}/Eu^{3+} co-doped BYW phosphors are a suitable choice for UV/n-UV light-pumped w-LEDs. Under 465 nm, the color coordinates of all BYW: Dy^{3+}/Eu^{3+} phosphors lie

in the pure red area, indicating minor color fluctuation. This further supports the previously stated lack of back transfer of energy from Eu^{3+} to Dy^{3+}. Additionally, the associated correlated color temperature (CCT) has been assessed. The CCT values of BYW: Dy^{3+}/Eu^{3+} phosphors with various excitations (shown in Table 6.01), are adjustable and show warm white light emission by the co-doping of Eu^{3+} ions. The aforementioned colorimetric characteristics of the as-synthesized BYW: Dy^{3+}/Eu^{3+} phosphors enable their use in color tunable devices, anti-counterfeiting, and solid state lighting applications.

6.3.6. Decay time analysis

Fig. 6.10 shows the decay plots with suitable exponential fitting of BYW: $xDy^{3+}yEu^{3+}$(x =3.0 mol%, y = 1.0, 2.0, 3.0, 4.0, and 5.0 mol%) phosphor for $^4F_{9/2}$ level (Dy^{3+}) under 290 nm excitation. Different exponential equations were used to fit the decay curves, the decay curves are most precisely fitted via a bi-exponential equation mentioned in equation (2.07) in the section 2.3.9 [3,110]. Using the fitting results, the average value of the decay time for all Dy^{3+}/Eu^{3+} co-activated $BiYWO_6$ phosphor powder samples was estimated from equation (2.08) in the section 2.3.9 [3,204].

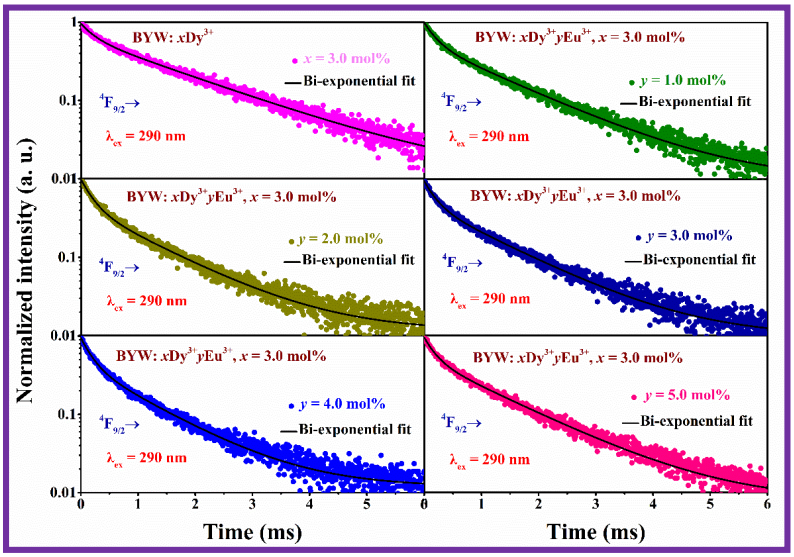

Fig. 6.10: *Decay profiles for the BYW: $xDy^{3+}yEu^{3+}$(x =3.0 mol%, y = 1.0, 2.0, 3.0, 4.0, and 5.0 mol%) phosphors for $^4F_{9/2}$ level under λ_{ex} = 290 nm excitation.*

The values of the estimated average decay time for the $^4F_{9/2}$ level of Dy^{3+} with 290 nm excitation for BYW: Dy^{3+}/Eu^{3+} BYW phosphors, indicating a downtrend with increasing Eu^{3+} ion content, and confirming the Dy^{3+} to Eu^{3+} energy transfer, are listed in Table 6.02.

Table 6.02: Average lifetime, energy transfer efficiency, and energy transfer probability rates, for Dy^{3+} doped and Dy^{3+}/Eu^{3+} co-doped BYW phosphors.

Sample BYW: $xDy^{3+}yEu^{3+}$ (x, y in mol%)	Average decay time (μs)	Energy transfer probability rate (P)	Energy transfer efficiency (η_{ET})
(x=3.0 , y=0.0)	150.959	-	-
(x=3.0 , y=1.0)	141.356	0.4500	5.90
(x=3.0 , y=2.0)	135.72	0.7437	8.30
(x=3.0 , y=3.0)	127.486	1.2196	17.63
(x=3.0 , y=4.0)	121.022	1.6386	25.40
(x=3.0 , y=5.0)	114.545	2.1058	33.20

Using decay time measurements with (τ) and without (τ_0) Eu^{3+} ions in BYW phosphors, the associated energy transfer probability rate (P) of dipolar-dipolar interaction may be calculated using the equation [21,201]:

$$P = \frac{1}{\tau} - \frac{1}{\tau_0} \tag{6.04}$$

The estimated lifetime values, energy transmission efficiency, and energy transmission probability rate for the BYW: $xDy^{3+}yEu^{3+}$(x =3.0 mol%, y = 1.0, 2.0, 3.0, 4.0, and 5.0 mol%) phosphors were mentioned in Table 6.02, it is demonstrated that the energy transfer probability rate improves with an increase in the content of Eu^{3+} ions in BYW phosphor.

6.4. Conclusions

A series of Dy^{3+} activated, as well as Dy^{3+}/Eu^{3+} bi-activated BYW phosphors, were effectively synthesized using the CP approach. The XRD investigation confirms the production of a pure monoclinic structure in BYW: Dy^{3+}/Eu^{3+} phosphors, as all diffraction patterns align

with JCPDS standard data, card no. 33-0224. The FE-SEM micrographs reveal an uneven, uniform distribution of closely spaced particles with smooth edges. The emission spectral profile recorded for BYW: Dy^{3+} phosphors under 290 nm excitation displays pronounced white emission, while the BYW: 1.0 mol% Eu^{3+} phosphor sample reveals emission in the red area under blue (465 nm) excitation. Moreover, by alteration of the activator (Eu^{3+}) ion and under 290, 465 nm excitation in the Dy^{3+}/Eu^{3+} co-doped BYW phosphor, emission color tunability was noted towards red region of the Chromaticity diagram. Furthermore, the approximation of Dexter and Reisfeld's ET relation was used to validate that the process of energy transfer from Dy^{3+} to Eu^{3+} occurs due to the involvement of non-radiative dipolar-dipolar interaction. The decay plots are best represented by bi-exponential equations, indicating a decrease in lifetime values as the concentration of Eu^{3+} ions increases in the synthesized BYW: Dy^{3+}/Eu^{3+} phosphor. The aforementioned research findings demonstrate that titled BYW: Dy^{3+}/Eu^{3+} phosphors will be promising candidate for w-LEDs, color tunable display devices, and anti-counterfeiting applications.

CHAPTER 7

Excitation dependent Multicolor Emitting $BiYWO_6$: Sm^{3+} Phosphor for Anti-counterfeiting Applications

Samarium doped bismuth yttrium tungstate ($BiYWO_6$: Sm^{3+}) phosphors have been synthesized using the co-precipitation (CP) technique. X-ray diffraction (XRD) patterns of the synthesized phosphor confirmed the formation of a single phase $BiYWO_6$ (BYW) with a monoclinic structure. The FE-SEM micrograph of the BYW: $x$$Sm^{3+}$, x = 3.0 mol% phosphor, illustrates the irregular and uniform distribution of closely spaced particles. The EDX result fully discloses the compositional behaviour of the synthesized BYW: $x$$Sm^{3+}$, x = 3.0 mol% phosphor. The Sm^{3+} activated BYW phosphor exhibits a strong deep red emission centered at 646 nm ($^4G_{5/2} \rightarrow {}^6H_{9/2}$), when excited with 290 nm, whereas an orange-red emission around 600 nm ($^4G_{5/2} \rightarrow {}^6H_{7/2}$) is observed under excitations (λ_{ex} = 406 and 465 nm). The chromaticity characteristics for the synthesized BYW: Sm^{3+} phosphor have been computed under selected excitations. The estimated average decay time was found in the microseconds range for BYW: Sm^{3+} phosphor under UV/blue excitations. All the findings mentioned above validate the potentiality of the synthesized BYW: Sm^{3+} phosphor for solid state lighting (SSL) and anti-counterfeiting applications.

7.1. Introduction

In recent years, the globalization of the economy, as well as rapid advancements in research and technology, have increasingly exposed sensitive information to substantial security risks [205–207]. Consequently, the development of robust anti-counterfeiting strategies aimed at enhancing encryption security has become both crucial and necessary. Various anti-counterfeiting technologies, including QR codes, digital watermarking, radio frequency identification (RFID) tags, barcodes, and magnetic resonance based techniques, have been explored [13,208–210]. However, many of these methods are relatively easy to replicate and are hindered by high production costs, limiting their widespread adoption. An effective anti-counterfeiting system should provide unique identifiers within a specific condition, be cost-efficient, and resist unauthorized duplication of protected information [13,211–213]. Lanthanide doped materials are attractive for security applications due to their excellent tunable luminescent properties, optical, electrical characteristics, chemical durability, and low toxicity [11,178,213,214]. However, conventional fluorescent materials that rely on single excitation luminescence encryption have become less effective, especially given recent advances in decryption technologies [13,208–210]. Therefore, modifications such as tuning the excitation wavelength by suitable mechanisms are necessary to achieve a dynamic and distinguishable luminescence response suitable for high security applications.

In the modern era, environmental sustainability and energy conservation are critical priorities. Rare earth (RE) doped phosphors have emerged as highly promising materials in advanced lighting technologies, offering significant potential across a range of applications, including LED based indoor cultivation systems, display panels, automotive lighting, and general illumination systems [110,204]. Among these, RE doped phosphor converted white light emitting diodes (pc-w-LEDs) have gained prominence as an efficient alternative to

traditional fluorescent and incandescent lighting owing to their high luminous efficacy, long operational life, low operating temperature, and reduced power consumption [204,215]. Currently, most of the commercially available w-LEDs rely on the yellow emitting phosphor $Y_3Al_5O_{12}$: Ce^{3+} (YAG: Ce^{3+}), typically combined with an InGaN blue emitting chip. However, this configuration has several inherent drawbacks, including a low CRI, high CCT, and a deficiency in red spectral components [19,216]. One promising approach to overcome these limitations involves designing w-LEDs based on UV/n-UV excitation sources combined with trichromatic (red, green, and blue) phosphors or dichromatic systems utilizing cyan and orange emitting phosphors with a blue excitation source. The development of w-LEDs with red or orange emitting phosphors that exhibit strong absorption in the UV/n-UV and blue spectral regions becomes essential. To achieve this, the selection of a thermally stable host matrix and appropriate activator ions is crucial for fabricating efficient red/orange-emitting phosphors that meet the performance requirements of next generation SSL applications.

RE doped luminescent materials play a vital role in the advancement of optoelectronic devices owing to their environmental friendliness, strong light absorption capabilities, and exceptional physical and chemical properties [199,200]. RE ions are characterized by unique electronic transitions such as *4f-4f* and *4f-5d*, which enable the host to exhibit efficient luminescence within the visible spectral range when excited by UV/n-UV or blue light. Among various RE activators, samarium (Sm^{3+}) ions are particularly attractive due to their characteristic orange to red emissions when incorporated into a suitable host lattice excited by UV/n-UV or blue light. This makes them promising candidates for use in lighting and display technologies.

Among various oxide based hosts, tungstate based materials have attracted considerable attention for optoelectronic applications owing to their excellent characteristics, including high

thermal and chemical stability, low calcination temperature, strong UV absorption, low phonon energy, and high luminescent efficiency [73,217]. Within the tungstate based materials, $BiYWO_6$ compound has recently gained interest due to its promising microwave dielectric and photocatalytic properties [126].

To the best of our knowledge, this study describes the synthesis as well as comprehensive characterization of BYW: Sm^{3+} phosphors. Extensive structural and morphological studies were conducted to evaluate the fundamental properties of synthesized materials. Phase purity was rigorously confirmed using standard JCPDS reference diffraction patterns. In addition, the optical and photoluminescence (PL) characteristics, and temperature dependent PL features, were systematically examined to assess the potential of Sm^{3+} activated BYW phosphors as advanced functional materials for applications in SSL and anti-counterfeiting applications.

7.2. Materials and synthesis of BYW: Sm^{3+} sample

$BiYWO_6$ (BYW) host material and Sm^{3+} activated BYW phosphors were synthesized by the co-precipitation route. In the first step, the stoichiometric amounts of the precursors, including $Y(NO_3)_3{\cdot}6H_2O$, Sm_2O_3, $Na_2WO_4{\cdot}2H_2O$, and $Bi(NO_3)_3{\cdot}5H_2O$ were used as initial raw materials. The detailed synthesis process was depicted in the section 2.2.4. in chapter 2 and Fig.2.05.

Furthermore, the security ink was prepared using polyvinyl alcohol (PVA) and DI water. The initial precursors were taken as 0.9 g of PVA and 0.1 g of the optimized (3.0 mol% Sm^{3+} doped BYW) phosphor. To prepare the uniform solution, the PVA was dissolved in 15 ml of DI water, ensuring that no bubbles were formed during the process. The mixture was then heated to 80 °C until a clear solution was obtained. Subsequently, 0.1 g of the optimized phosphor was added slowly and stirred continuously at ambient temperature for 3 hrs to achieve homogeneous dispersion, resulting in a stable slurry.

7.3. Results and discussion

7.3.1. XRD analysis

Fig. 7.01 displays the XRD patterns of the synthesized BYW host material and BYW: xSm^{3+} (x = 1.0 to 5.0 mol% at the interval of 1.0 mol%) phosphors along with the reference pattern from JCPDS card no. 33-0224. The diffraction profile of the undoped BYW host matches perfectly with the standard JCPDS data, confirming the formation of pure single phase material and the absence of any impurity phases. Comparative analysis with the reference pattern confirms that $BiYWO_6$ crystallizes in a monoclinic structure having space group P2/a (13) and the corresponding lattice parameters are a = 8.1244 Å, b = 3.7534 Å, and c = 16.0345 Å. The XRD patterns of the BYW: xSm^{3+} phosphors are identical to those of the undoped BYW host and the reference JCPDS pattern, indicating that the Sm^{3+} doping does not induce any structural distortion in the host lattice. This can be attributed to the substitution in the Bi^{3+} site by Sm^{3+} ions, which is facilitated by their similar oxidation states.

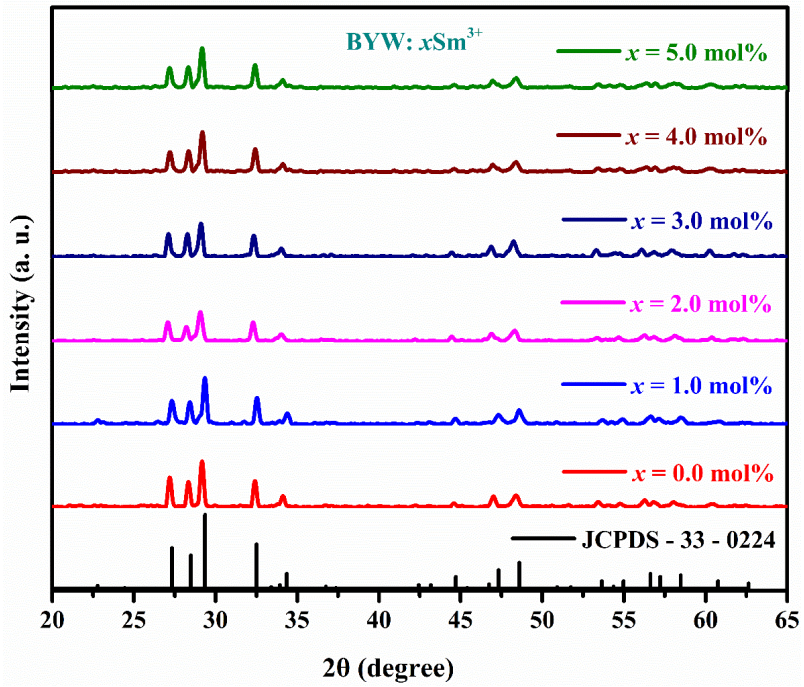

Fig. 7.01: *XRD patterns of the undoped BYW host lattice and Sm^{3+} doped BYW phosphors.*

Moreover, the comparable ionic radius of Sm^{3+} relative to Bi^{3+} allows this substitution to occur without disrupting the crystallographic integrity of the host.

The average crystallite size (D) of the synthesized BYW: xSm^{3+} phosphors was determined employing the Debye-Scherrer equation, as depicted in equation no. (2.02) in section 2.3.2 [110,204]. The average crystallite sizes of the synthesized BYW: xSm^{3+} samples were found to be in the range from 40 to 55 nm.

7.3.2. Morphological studies

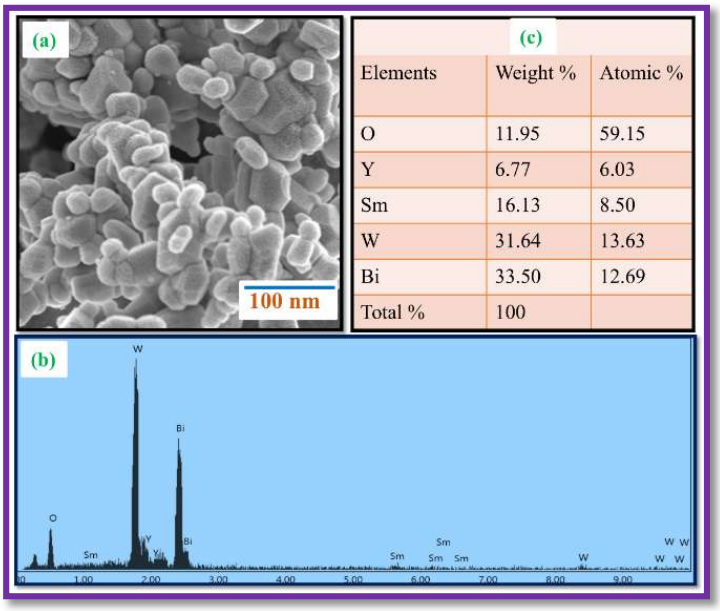

Fig. 7.02: ***(a)*** *FE-SEM micrograph of the* ***(b)*** *EDX pattern* ***(c)*** *Table of elemental composition of the synthesized BYW: xSm^{3+}, x = 3.0 mol% phosphor.*

Fig. 7.02(a) illustrates the FE-SEM micrograph of the BYW: xSm^{3+}, x = 3.0 mol% phosphor at nano scale resolution. The micrograph reveals a relatively uniform distribution of irregularly shaped grains, indicating a consistent morphology across the sample. The presence of submicron crystalline particles suggests their suitability for enhanced luminescence performance, making them promising candidates for applications in w-LEDs and anti-counterfeiting technologies.

The elemental composition of the BYW: xSm^{3+}, x = 3.0 mol% phosphor was further analyzed with the help of the EDX spectrum. The EDX pattern confirms the uniform distribution of all compositional elements, including samarium (Sm), tungsten (W), bismuth (Bi), yttrium (Y), and oxygen (O), within the synthesized BYW: xSm^{3+}, x = 3.0 mol% phosphor, as shown in Fig. 7.02(b). Additionally, the corresponding table in Fig. 7.02(c) presents the weight as well as atomic percentages of each element, further verifying the availability of all elements in the BYW host matrix.

7.3.3. Diffuse reflectance spectral analysis

The optical characteristics of the synthesized BYW: xSm^{3+}, x = 3.0 mol% phosphor was analyzed using DRS profile and recorded at ambient temperature over the wavelength range of 200 -1600 nm, as depicted in Fig. 7.03. The spectrum exhibits a strong and broad absorption

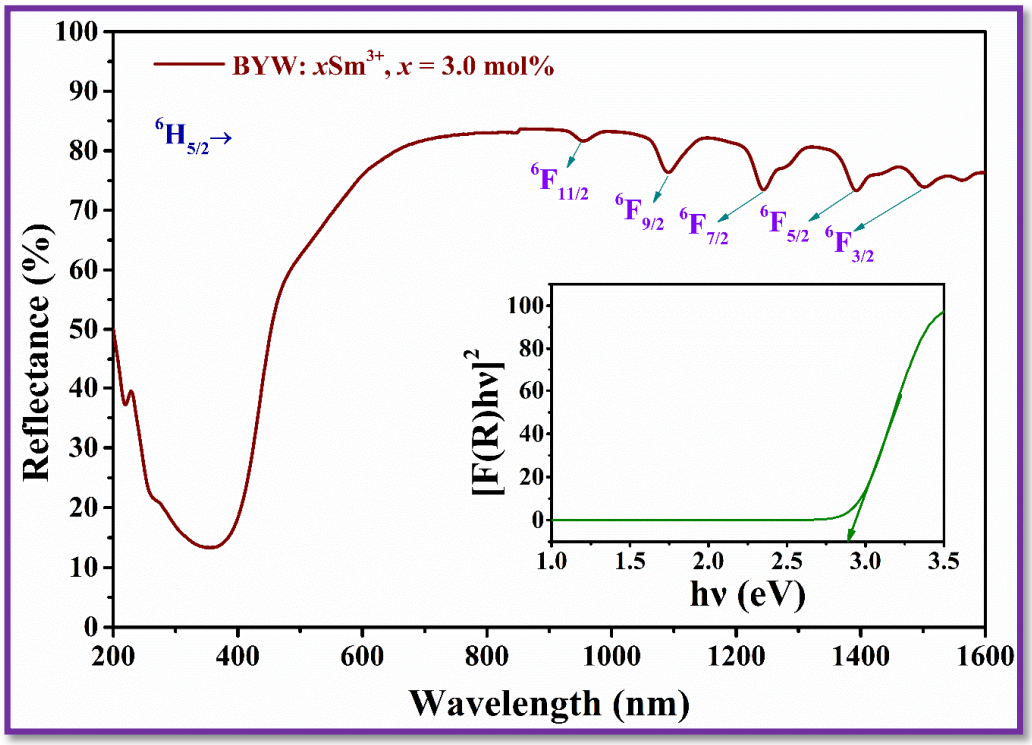

Fig. 7.03: *DRS profile of the synthesized BYW: xSm^{3+}, x = 3.0 mol% phosphor. Inset represents the assessment of the band gap by employing the Kubelka Munk function.*

band associated to the combined absorption processes in the UV/n-UV region (200 to 400 nm). These include the Y/Sm–O charge transfer band (CTB) and the ligand to metal charge transfer transition (LMCT) associated with W–O bonds [183,184]. In addition, sharp absorption bands appearing above 900 nm were ascribed to intra-*4f* transitions of Sm^{3+} ions, corresponding to $^6H_{5/2} \rightarrow {}^6F_j$ (where J = 11/2, 9/2, 7/2, 5/2, and 3/2) [218]. With the help of the DRS spectrum, the optical band gap energy of the synthesized BYW: xSm^{3+}, x = 3.0 mol% phosphor was calculated using the equations as described in equations 2.04 & 2.05 in the section 2.3.4. [219]. In the present case, the optical band gap was determined by plotting $[F(R)h\vartheta]^{1/n}$ versus $h\vartheta$ and extrapolating the linear portion of the curve to the energy axis, where it intersects the photon energy ($h\vartheta$) axis at zero, as shown in the inset of Fig. 7.03. The estimated band gap value was found to be 2.87 eV for the BYW: xSm^{3+}, x = 3.0 mol% phosphor.

7.3.4. PL analysis of Sm^{3+} doped BYW phosphors

The PL and PLE spectral profiles of the synthesized BYW: xSm^{3+} phosphors are depicted in Fig. 7.04(a-d). The PLE spectrum of the synthesized BYW: xSm^{3+}, x = 3.0 mol% phosphor was recorded by monitoring the emission wavelength of 646 nm. It exhibits prominent excitation peaks in the UV, n-UV, and blue regions, as presented in Fig. 7.04(a). A prominent broad excitation band centered at 290 nm was observed within the 275-325 nm range, along with several sharp excitation peaks between 350 and 500 nm. These sharp peaks correspond to intra-configurational *4f-4f* transitions of Sm^{3+} ions located at 363, 377, 406, 418, 443, and 465 nm involving transitions from the ground energy state ($^6H_{5/2}$) to various excited states, as designated in Fig. 7.04(a). The broad excitation band at 290 nm is attributed to the charge transfer band (CTB) of Y/Sm – O and the ligand to metal charge transfer transition (LMCT) associated with W–O bonds [220,221]. The charge transfer excitation band is more intense than the typical *4f-4f* transition, suggesting strong host-to-activator energy transfer and

effective sensitization of Sm^{3+} ions by the BYW host lattice [222,223]. The most intense peaks in the PLE spectrum appear at 290 (UV region), 406, and 465 nm (blue region), indicating that the BYW: Sm^{3+} phosphors can be efficiently excited via UV/n-UV/blue radiation. This excitation flexibility highlights its potential for applications, such as SSL and anti-counterfeiting technologies.

The emission spectral profiles of the synthesized BYW: *x*Sm^{3+} phosphors with varying the Sm^{3+} ion concentration from 0.5 to 5.0 mol% were captured in the wavelength range of 550 to 750 nm under the above mentioned excitation wavelengths, as illustrated in Fig. 7.04 (b, c, and d). It has been observed that the synthesized phosphor reveals multiple emission peaks attributed to the characteristic transitions of Sm^{3+} ions. Under 290 nm excitation, the emission spectral profiles of the synthesized phosphor exhibit four distinct peaks centered at 565, 600, 646, and 707 nm, which correspond to the $^4G_{5/2} \rightarrow {}^6H_J$ (where J = 5/2, 7/2, 9/2, and 11/2) transitions of Sm^{3+} ions, respectively [224,225]. These emission transitions are also observed under 406 and 465 nm excitations, as illustrated in Fig. 7.04(c and d). All emission peaks/bands arise from the *4f-4f* transition of Sm^{3+} ions, indicating successful incorporation and activation of the Sm^{3+} ions within the BYW host lattice. The most predominant emission peak under 290 nm excitation is the $^4G_{5/2} \rightarrow {}^6H_{9/2}$ transition centered at 646 nm in the deep red region. In contrast, the $^4G_{5/2} \rightarrow {}^6H_{7/2}$ transition at 600 nm demonstrates the highest emission intensity under 406 and 465 nm excitations. Furthermore, the emission peak at 565 nm corresponds to a purely magnetic dipole (MD) transition, which is generally insensitive to the surrounding crystal field. The emission at 600 nm arises from both MD and electric dipole (ED) transitions, while the intense 646 nm peak is attributed to a purely ED transition, which may be significantly affected by the local crystal field environment [222,226,227]. The relative intensity of ED and MD transitions serves as a reliable indicator of the site symmetry around the dopant (Sm^{3+}) ions. Under 290, 406, and 465 nm excitations, the

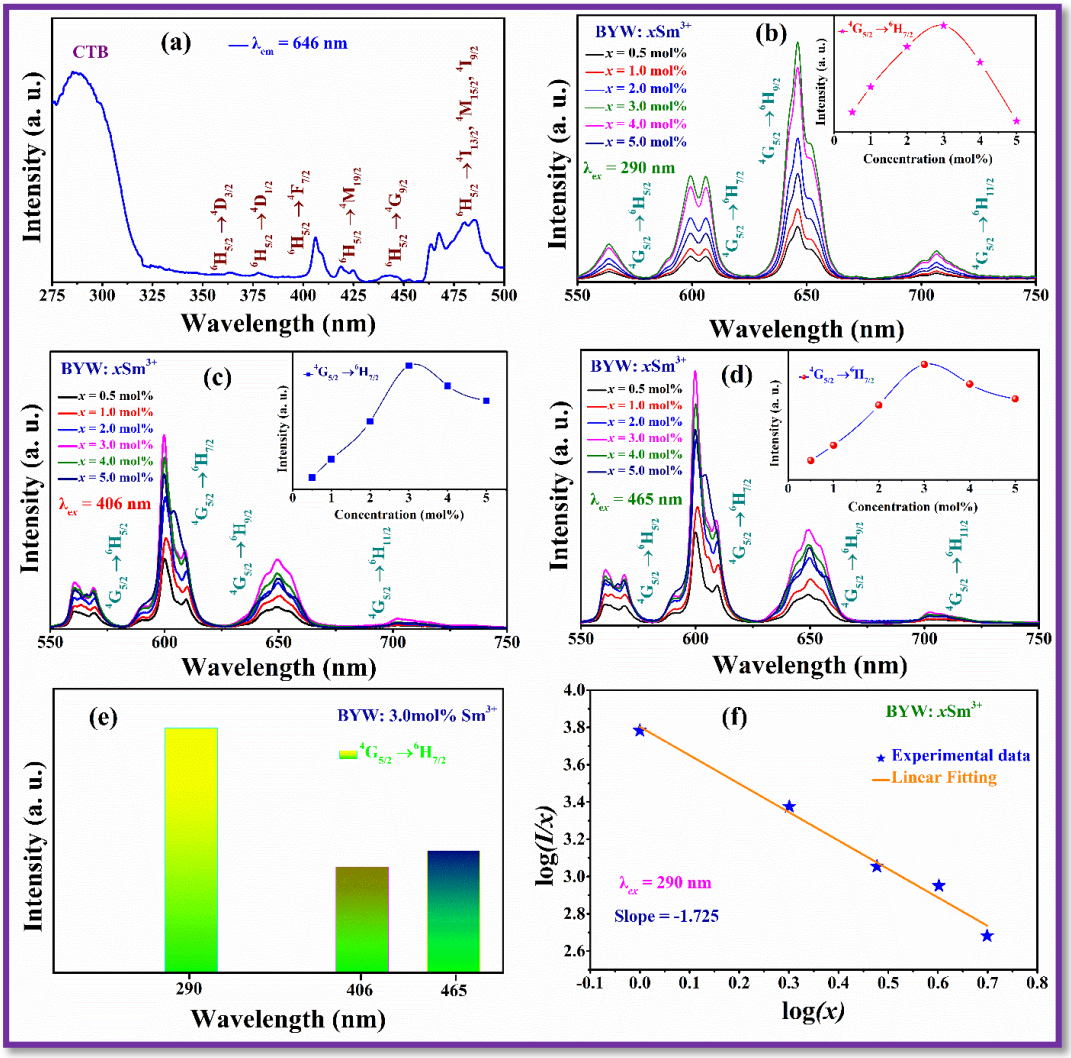

Fig. 7.04*: (a) Excitation spectrum of the synthesized BYW: xSm^{3+}, x = 3.0 mol% phosphor by monitoring 646 nm emission wavelength, (b) Emission spectral profiles of Sm^{3+} doped $BiYWO_6$ under 290 nm, (c) 406 nm, (d) 465 nm (Inset represents the variation of emission intensity along with dopant ion concentrations), (e) Variation of emission intensity under different excitation wavelengths of the synthesized BYW: xSm^{3+}, x = 3.0 mol% phosphor, and (f) Plot of log (I/x) Vs log (x) at varying concentration of Sm^{3+} ions.*

dominance of the ED transition suggests that Sm^{3+} ions occupy low symmetry sites lacking an inversion center [220,226]. The sample exhibits the highest emission intensity in the deep red (646 nm) region under the excitation of 290 nm, whereas under 406 and 465 nm excitation, it

exhibits in orange-red (600 nm) region, demonstrating the suitability of this phosphor for anti-counterfeiting and SSL applications. Furthermore, the variation in the emission intensity at different excitation wavelengths for the BYW: xSm^{3+}, x = 3.0 mol% phosphor is illustrated in Fig. 7.04(e). From Fig. 7.04, it is evident that the present phosphor exhibits excitation wavelength dependent multicolor emission, highlighting its potential for use in anti-counterfeiting applications.

7.3.5. Effect of Sm^{3+} concentration on emission intensity (Dexter's theory)

To scrutinize the effect of Sm^{3+} dopant ion concentration on the emission profiles of the synthesized BYW: xSm^{3+} phosphor, the Sm^{3+} concentration was varied from x = 0.5 to 5.0 mol%. The variation in emission intensity ($^4G_{5/2} \rightarrow {}^6H_{7/2}$) with different Sm^{3+} concentrations under excitation wavelengths of 290, 406, and 465 nm is shown in the insets of Fig. 7.04(b, c, and d), respectively. For all the excitation wavelengths, the emission intensity increases with increasing Sm^{3+} concentration up to 3.0 mol%, beyond which it decreases due to the concentration quenching effect. This decline can be attributed to the proximity of neighbouring Sm^{3+} ions at higher doping levels, which promotes non-radiative energy transfer over radiative emission. The critical distance (R_c) between adjacent Sm^{3+} ions is a key factor governing this non-radiative transfer. According to Blasse's equation, the critical distance can be computed using the unit volume (V = 950.87 Å^3) as described in equation 1.01 in the section 1.3.2 [110]. Where, $N = 8$ is the number of available activator sites in the BYW unit cell and $X_c = 0.03$ is the critical concentration of the Sm^{3+} ions. Based on this formula, the computed R_C value is 19.63 Å. According to Van Uitert's theory, when the critical distance exceeds ~5 Å, energy transfer occurs predominantly via multipolar interaction, supporting the occurrence of concentration quenching in the present system [141,219].

According to Dexter's theory, in the present case, the non-radiative energy transfer occurs via multipolar interaction as illustrated in equation 1.02 in the section 1.3.2 [119,169]. The slope of the linear fit to the plot of $\log\left(\frac{I}{x}\right)$ versus $\log x$, as depicted in Fig. 7.04(f), enables the estimation of the Q value. The slope obtained from the graph was -1.725, corresponding to a calculated Q value of 5.175. This value is close to 6, indicating that the dominant multipolar interaction responsible for non-radiative energy transfer is of the dipole-dipole type.

7.3.6. Energy level diagram

Fig. 7.05 illustrates the emission, excitation, and energy transfer mechanism involved in the Sm^{3+} doped BYW phosphor. Under 290 nm excitation, the electrons in the high energy levels of the $(WO_6)^{-6}$ groups transfer energy non-radiatively to the intermediate Sm^{3+} states.

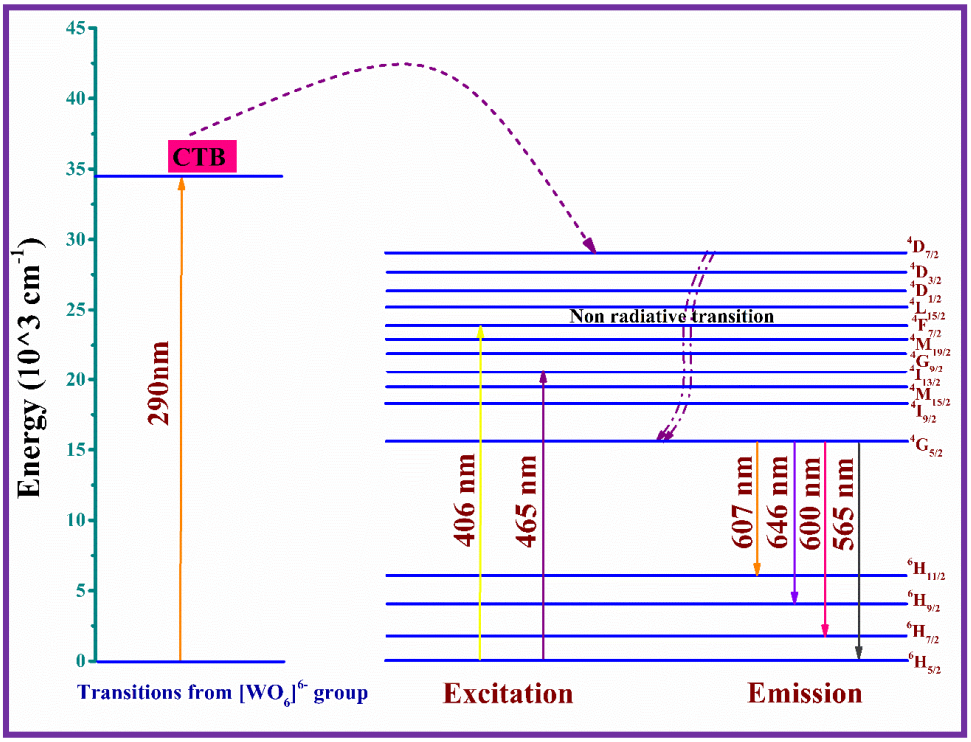

Fig. 7.05: *Partial energy level diagram of Sm^{3+} in $BiYWO_6$ phosphor.*

These electrons then cascade to the $^4G_{5/2}$ energy level, from which radiative transitions occur to the lower energy states, such as ^6H_J (where J = 5/2, 7/2, 9/2, and 11/2), producing emission in the visible spectral region. A similar mechanism can be observed under 406 and 465 nm

excitations when non-radiative relaxation to the $^4G_{5/2}$ level is followed by the characteristic radiative emissions.

7.3.7. Chromaticity coordinates

In order to assess the final emission colour of the synthesized BYW: Sm^{3+} phosphor, the Commission Internationale de l'Eclairage (CIE) chromaticity coordinates have been computed. The chromaticity coordinates were derived from the emission spectral profiles recorded under the above mentioned UVn-UV/blue excitations.

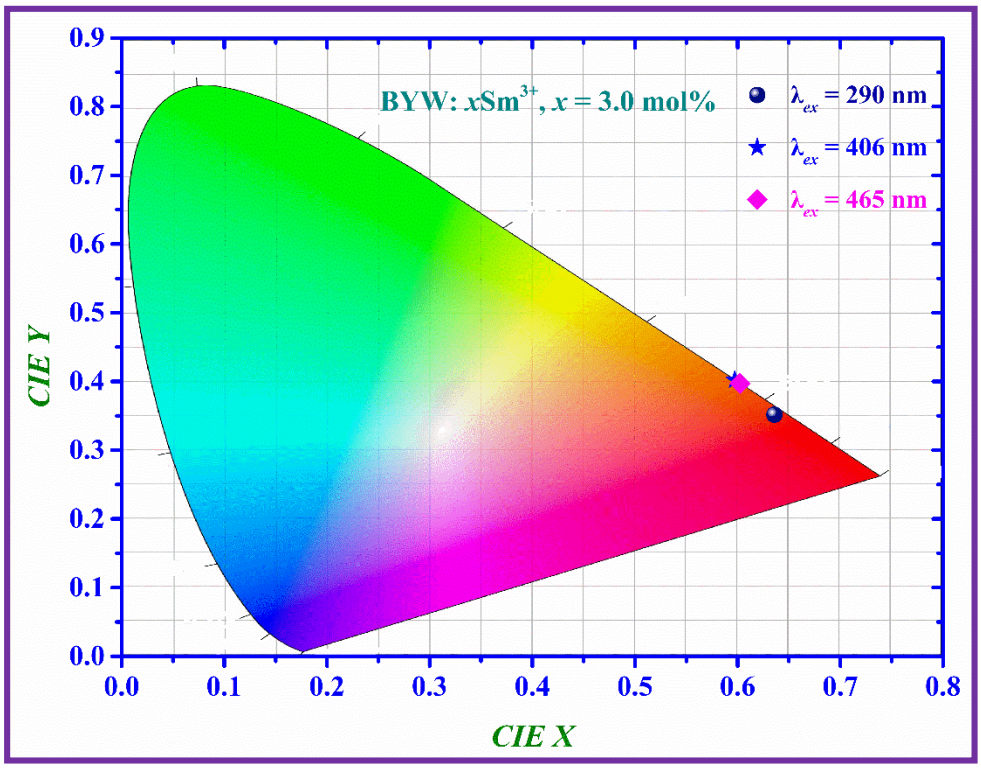

Fig. 7.06: *CIE coordinates of the synthesized BYW: xSm^{3+}, x = 3.0 mol% phosphor under different excitation wavelengths at 290 nm, 406 nm, and 465 nm.*

The (x, y) coordinates of the optimized BYW: xSm^{3+}, x = 3.0 mol% phosphor were accomplished to be (0.635, 0.351), (0.597, 0.402), and (0.602, 0.397) under 290, 406, and 465 nm, respectively, and are presented in Fig. 7.06. The estimated chromaticity coordinates reveal that under 290 nm excitation, the sample's emission falls towards the deep red region of

the CIE 1931 chromaticity diagram. However, under 406 and 465 nm excitations, the emission shifts towards the orange-red region. This excitation wavelength dependent multicolour emission behaviour makes the synthesized BYW: Sm^{3+} phosphor a promising candidate for advanced anti-counterfeiting and SSL applications.

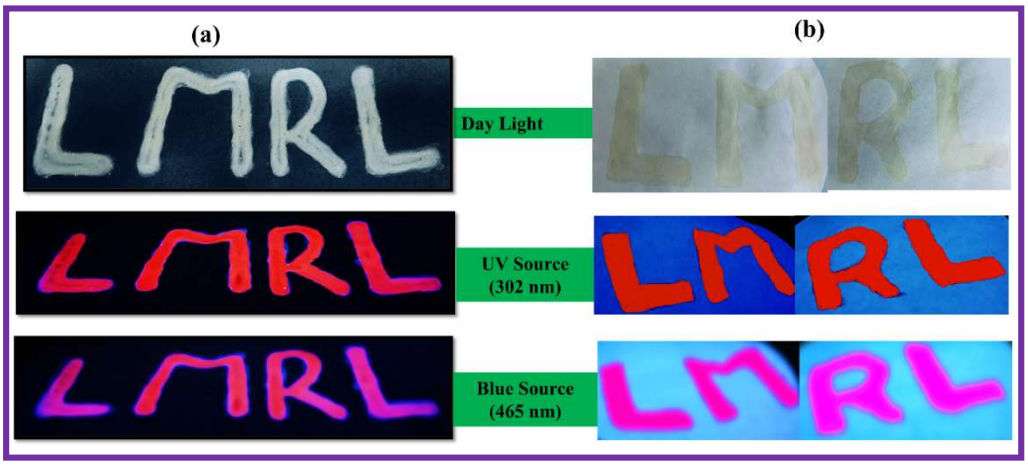

Fig. 7.07: *Anticounterfeiting tags on (a) black paper and (b) filter paper.*

To demonstrate its practical applicability in data security, a luminescent security ink was prepared using the optimized (3.0 mol% doped) phosphor dispersed in a polyvinyl alcohol (PVA) matrix. As shown in Fig. 7.07, the security ink produces a deep-red emission under UV (302 nm) excitation and an orange-red emission under blue (465 nm) excitation, which could be useful for luminescence based anti-counterfeiting applications [228,229] The ink was successfully applied to various substrates, including black paper and filter paper, highlighting its versatility and effectiveness for security labelling.

7.3.8. PL decay analysis

Fig. 7.08(a and b) illustrates the decay curves at room temperature for the BYW: Sm^{3+} phosphor were recorded for the $^4G_{5/2}$ energy level under excitation wavelengths of 290 and 406 nm with corresponding emission wavelengths set at 646 and 600 nm, respectively.

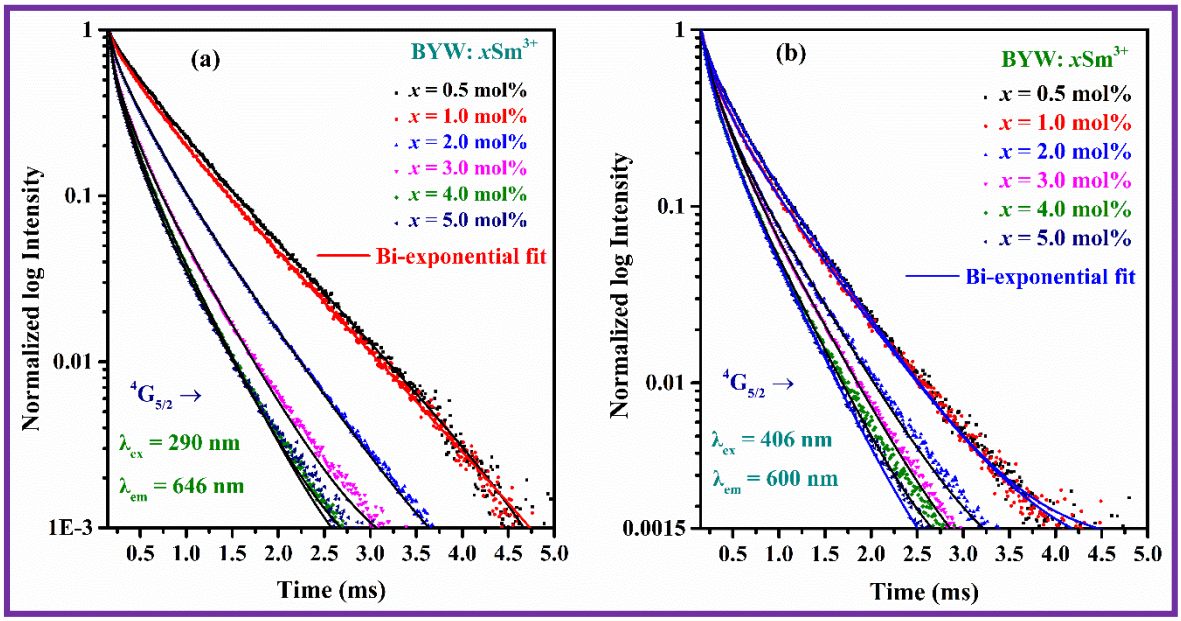

Fig. 7.08: *Decay curves for the synthesized Sm^{3+} doped $BiYWO_6$ phosphor under (a) 290 nm (λ_{em} = 646 nm) and (b) at 406 nm (λ_{em} = 600 nm).*

The decay profiles were fitted using various exponential functions, and the bi-exponential function, described in equation (2.07) in the section 2.3.9, was found to be the best fit for all the decay curves [104]. The average lifespan (τ_{avg}) values for the synthesized BYW: Sm^{3+} phosphor under selected excitations were estimated from the equation (2.08) in the section 2.3.9. The estimated τ_{avg} values for the synthesized BYW: xSm^{3+} phosphors were found to be in the range from 564.00 to 169.98 µs under 290 excitation and from 423.35 to 112.32 µs under 406 nm excitation wavelength. It has been further noted that the τ_{avg} values of the synthesized phosphor decrease with an increase in the concentration of dopant ions due to the non-radiative energy transfer among the dopant (Sm^{3+}) ions.

7.3.9. Temperature dependent PL analysis

To assess the potentiality of the synthesized phosphor materials for advanced SSL applications, the TDPL analysis has been studied on the optimized BYW: xSm^{3+}, x = 3.0 mol% phosphor. This measurement has been conducted within a certain temperature range of 298 to

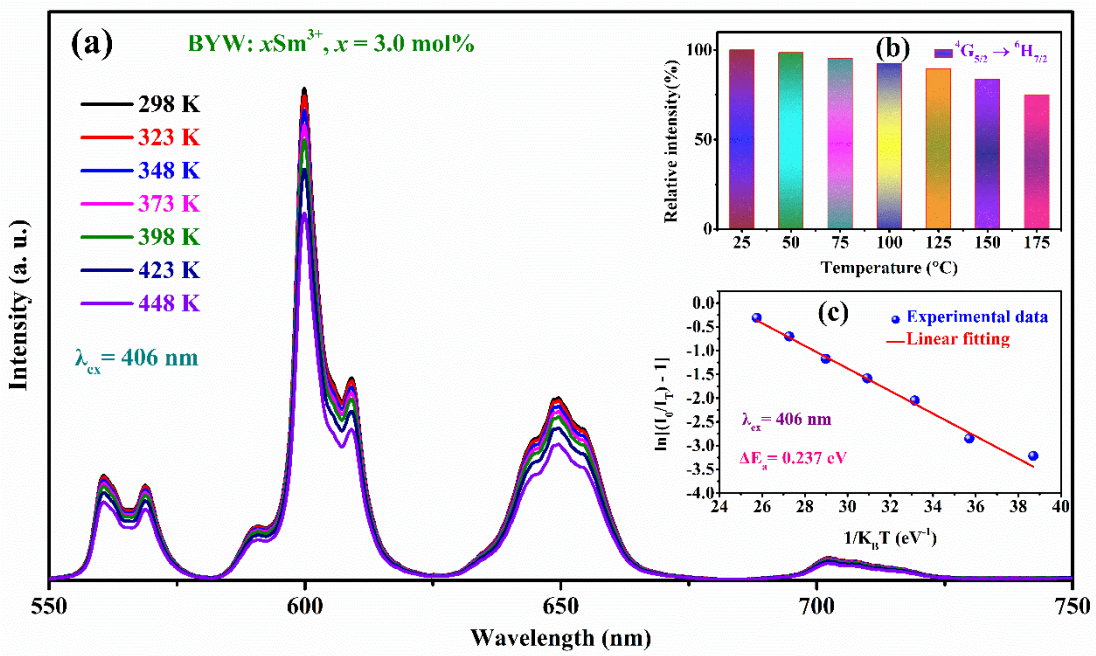

Fig. 7.09: ***(a)*** *Temperature dependent PL spectra of Sm^{3+} doped $BiYWO_6$ phosphor, [Inset* ***(b)*** *shows the relative emission intensity of $^4G_{5/2} \rightarrow {}^6H_{7/2}$ peak with varying temperature from room temperature 298 K to 448 K, and* ***(c)*** *Plot of $ln[(I_0/I_T)-1]$ Vs $1/K_BT$ of the Sm^{3+} doped $BiYWO_6$ phosphor.*

448 K under excitation wavelength of 406 nm, as displayed in Fig. 7.09(a). As the temperature profile increased from 298 to 448 K, a gradual decline in the emission intensity was perceived, while the emission peak positions remained stable. The relationship between the relative emission intensity of the highest emission peak (600 nm) corresponding to the $^4G_{5/2} \rightarrow {}^6H_{7/2}$ transition and temperature profiles is presented in the inset of Fig. 7.09(b). Notably, the emission intensity of the optimized phosphor maintained 76% of its original intensity at 423 K in comparison to the intensity at the initial temperature of 298 K, indicating excellent thermal stability of the optimized phosphor.

Moreover, the activation energy (ΔE_a) is another critical parameter for evaluating the thermal stability of the optimized BYW: xSm^{3+}, x = 3.0 mol% phosphor, and it was determined using the Arrhenius equation, as described in section 2.3.10, equation number (2.18) [104]. A

linear fit for the plot of $\ln[(I_0/I_T) - 1]$ versus $1/K_BT$, is as shown in Fig. 7.09(c) was used to estimate the activation energy (ΔE_a). Based on the slope, the ΔE_a value for the optimized BYW: xSm^{3+}, x = 3.0 mol% phosphor is found to be 0.237 eV. The above mentioned TDPL results confirm that the synthesized BYW: xSm^{3+} phosphor exhibits good thermal stability.

7.4. Conclusions

In summary, multicolor emitting samarium activated BYW phosphors have been synthesized by co-precipitation route. The synthesised phosphor has been studied for its structural, morphological, optical and luminescent properties. The XRD patterns have confirmed the purity of the crystalline monoclinic phase and the BYW: xSm^{3+} (x = 3.0 mol%) phosphor has an optical bandgap (E_g) of 2.87 eV. The BYW: 3.0 mol% of Sm^{3+} exhibits the strong excitation peaks in the UV/n-UV, and blue region, and this phosphor exhibits excellent emission under the excitation wavelengths viz. 290, 406, and 465 nm wavelengths. The maximum emission intensity at 646 nm under 290 nm excitation and an intense emission peak at 600 nm obtained under 406 and 465 nm excitation wavelengths, respectively. The intensified emission was detected at 3.0 mol % in Sm^{3+} doped $BiYWO_6$ phosphor samples under all the strong excitation wavelengths, and this concentration has been regarded as optimised. The CIE chromaticity coordinates were estimated for the optimized concentration of Sm^{3+} ion, and it was concluded that all the samples are positioned in deep red when excited with 290 nm, and orange-red, under 406 and 465 nm wavelengths. The photoluminescence decay curves represents a bi-exponential in nature for all the concentrations of Sm^{3+} doped BYW phosphors under the excitation wavelengths 290 and 406 nm, with an average decay time in the range of microseconds. The summary of the above mentioned results indicates that this excitation wavelength dependent multicolour emitting Sm^{3+} doped $BiYWO_6$ phosphor could be a promising applicant for the anti-counterfeiting and w-LEDs applications

CHAPTER 8

Conclusions, Future Scope, and Social Impact of the Research Work

This chapter presents the detailed outcomes of the current research work and outlines the future scope of the research. The overall objective of this thesis was to develop thermally stable rare earth activated bismuth yttrium tungstate phosphor with improved color tunability and white light emission by effective excitation via UV/n-UV/ blue light for solid state lighting and anti-counterfeiting applications. The developed RE activated bismuth yttrium tungstate phosphors exhibit PL characteristics in the pre-requisite spectral range for w-LEDs, and anti-counterfeiting applications. The future scope related to the current research work is also discussed and highlights the social impact of the research work in the current chapter.

8.1. Conclusions of the present work

The present thesis work is centered on the synthesis and characterization of RE ions doped $BiYWO_6$ phosphor for use in solid state lighting and anti-counterfeiting applications. Substantial focus has been devoted towards improve emission characteristics by varying synthesis methods, increasing dopant ion concentrations, and also via co-doping. The preceding chapters have highlighted the current surge in interest in pc-w-LEDs, due to their distinctive attributes, including improved luminescent efficiency, durability, energy saving, cost effective, and environmental friendly features. These advanced pc-w-LEDs have found diverse applications in display technologies, biosensors, and artificial lighting for general illumination. Also, to improve the traditional anti-counterfeiting technology, development of multimode excitation and color tunable emitting phosphor, is required. In this context, it is essential to develop new phosphors with enhanced luminescent characteristics. In this regard, primarily, extensive investigation has been carried out to explore structural, morphological, optical, PL, TDPL, and TRPL properties of single phase Eu^{3+} doped BYW phosphor synthesized by sol-gel combustion (SGC) method. This phosphor exhibit intense and pure red emission under blue excitation to act as a red emitting constituent to combine with commercial YAG: Ce^{3+} phosphor and coated over blue (InGaN) chip to improve CRI of w-LEDs. Various other synthesis methods, such as solid state reaction (SSR), hydrothermal (HT), and co-precipitation (CP) methods were employed to optimize the calcination temperature and synthesis method for Eu^{3+} doped BYW phosphor. The optimized calcination temperature has been found to be 900 °C, and the optimized synthesis process has been revealed as CP method by analysing the relative thermal, structural, morphological, and luminescent properties. The Eu^{3+} doped BYW phosphors have shown red emission with excellent color purity as well as thermal stability, confirming the potential usage in w-LEDs applications. Furthermore, single phase Dy^{3+} doped BYW phosphor has been successfully synthesized by CP method. The Dy^{3+}

doped BYW phosphors exhibit blue, yellow, and red peaks under the UV/blue excitation. The combination of blue, yellow, and red emission peaks in the as-prepared phosphor yields near white light with good thermal stability. Moreover, Dy^{3+}/Eu^{3+} co-doped BYW phosphors (accomplishing the pre-requisite property of efficient spectral overlap between Dy^{3+} emission and Eu^{3+} excitation for energy transfer) were synthesized via CP method to generate white light and also to develop color tunable phosphor. Luminescent properties of Dy^{3+}/Eu^{3+} co-doped BYW phosphors confirmed the color tunable (white to red) behaviour of the phosphor via varying excitation wavelength and the concentration of activators, which is reliable for w-LEDs and anti-counterfeiting applications. Additionally, it is pertinent to mention that as synthesized thermally stable Sm^{3+} doped BYW phosphors via CP method have exhibited the wavelength dependent multicolor emission, and high color purity to use them in multifunctional w-LEDs and anti-counterfeiting applications. In the view of the above results, RE ions doped tungstate phosphors are promising candidates for their utility in w-LEDs and anti-counterfeiting applications.

8.2. Important Findings

The research meticulously examines significance of the host lattice ($BiYWO_6$), the selection of the synthesis procedure, and the appropriate choice of activator ions, along with systematic optimization of emission characteristics and thermal stability to ensure the applicability of the synthesized phosphors for various photonic applications such as solid state lighting, photovoltaic cells, optical sensing systems, and anti-counterfeiting applications.

The single phase formation of $BiYWO_6$ material has been achieved via various synthesis routes such as SSR, SGC, HT, and the CP method. The thermal analysis of un-sintered $BiYWO_6$ powder was accomplished to analyze its crystallization temperature. The crystallization temperature for SSR route was found to be 1100 °C. While for other synthesis routes, the crystallization of BYW sample began beyond 700 °C, and the crystallite size

increases with the calcination temperature. The calcination temperature has been optimized as 900 °C for the samples synthesized via chemical route. The XRD patterns of all synthesized samples were completely in accordance with the standard JCPDS card no. 33-0224, indicating the development of pure phase with monoclinic structure. The structural characteristics of BYW: RE^{3+} phosphors, synthesized using various methods, have been examined using the XRD technique. Additionally, Rietveld refinement calculations have been performed to verify phase purity using XRD data. The morphological analysis of RE doped BYW phosphor was accomplished by recording FE-SEM micrographs. Among these four synthesis methods discussed in the previous chapters, the SSR method shows irregular agglomerated particles, and chemical routes (SGC, HT, and CP) show uniform irregular morphology of the particles.

Advancing into the investigation of the photoluminescence properties of RE doped BYW phosphors, the key highlights of the present thesis are outlined as follows:

BYW: xEu^{3+}phosphor exhibit multiple emission peaks, with a prominent emission peak observed at 613 nm when excited via blue radiation. The computed CIE coordinate values (0.653, 0.346), are located in the red zone of the CIE diagram, which are in close proximity to those of the commercially available red emitting phosphors, such as Y_2O_2S: Eu^{3+} (0.647, 0.343) and the standard NTSC (0.670, 0.330). The lifetime profile of the BYW: xEu^{3+}, x = 9.0 mol% phosphor reveals a bi-exponential characteristic with an average lifetime in the microsecond range. Furthermore, the TDPL studies indicate that the emission intensity retained 73% of its initial temperature at 100 °C, demonstrating good thermal stability.

To identify the best synthesis route along with the calcination temperatures, PL characteristics of BYW: xEu^{3+} phosphor (x = 1.0 mol%) have been investigated. Under blue excitation (465 nm), all the synthesized Eu^{3+} doped BYW phosphor samples exhibit intense emission peak in the red region. PL spectra reveal that the phosphor synthesized via the CP

method is efficient over the samples synthesized via SSR, SGC, and HT methods, and it exhibits highest emission intensity at all calcination temperatures (i.e. 700, 800, 900, and 1000 °C). The phosphor synthesized by CP method exhibit strongest emission, and two times higher than the phosphor prepared by the SSR method. The BYW: Eu^{3+} phosphor sample attributed to the strong emission intensity, when synthesized by CP technique at 900 °C and considered this technique as an optimized synthesized procedure for this phosphor. The CIE chromaticity color coordinates were estimated for the phosphor synthesized via the optimized CP method, and it was concluded that the coordinates of all the samples were positioned in the red region along with high values of colour purity. Furthermore, the PL quantum yield for the BYW: xEu^{3+}, x = 20.0 mol% phosphor has been observed to be 51.39%. The photoluminescence decay curve exhibits bi-exponential in nature for the optimized BYW phosphor with an average decay time in the microsecond range. These results indicate that Eu^{3+} activated BYW phosphor synthesized by CP method could be an appropriate candidate for the red emitting component in pc-w-LEDs and other advanced photonic applications.

Further, PL studies have been studied to characterize the luminescent properties of BYW: Dy^{3+} phosphors. The BYW: xDy^{3+} displays the numerous excitation peaks in UV/n-UV and visible regions due to characteristics transitions of Dy^{3+} ions. Dy^{3+} doped BYW phosphor could be effectively excited by UV LED chips, which gives intense emission bands in blue and yellow regions at 485 ($^4F_{9/2}\rightarrow{}^6H_{15/2}$) and 575 nm ($^4F_{9/2}\rightarrow{}^6H_{13/2}$), respectively. The CIE chromaticity coordinates were determined for the BYW: 3.0 mol% Dy^{3+}, revealing that they fall within the near white, when excited at wavelength of 290 nm. The photoluminescence decay curves of the Dy^{3+} doped BYW phosphors exhibit a bi-exponential nature, characterized by an average decay time in the microsecond range. The temperature dependent PL indicates good thermal stability of the as synthesized phosphor. The CIE coordinates of the Dy^{3+} doped

BYW phosphor demonstrate near white emission, which makes it a promising candidate for use in various luminescent devices, including pc-w-LEDs under UV excitation.

For Dy^{3+}/Eu^{3+} co-doped BYW phosphors, emission color tunability has been observed from white region to red region of the chromaticity diagram under 290 and 465 nm excitations along with the varying concentration of activator ions. Furthermore, the approximation of Dexter and Reisfeld's ET relation was used to validate that the process of energy transfer from Dy^{3+} to Eu^{3+} occurs due to the involvement of non-radiative dipolar-dipolar interactions. The decay plots are best represented by bi-exponential equations, indicating a decrease in lifetime values for the $^4F_{9/2}$ level as the concentration of Eu^{3+} ions increases in the synthesized BYW: Dy^{3+}/Eu^{3+} phosphor. The aforementioned research findings demonstrate that titled BYW: Dy^{3+}/Eu^{3+} phosphors will be promising candidate for w-LEDs, color-tunable display devices, and anticounterfeiting applications.

The BYW: Sm^{3+} exhibits the strong excitation peaks in the UV/n-UV and blue region, and the emission spectral profiles of the synthesized phosphors demonstrate four distinct peaks centered at 565, 600, 646, and 707 nm, which correspond to the $^4G_{5/2} \rightarrow {}^6H_J$ (where J = 5/2, 7/2, 9/2, and 11/2) transitions of Sm^{3+} ions, respectively. The higher emission intensity has been observed in the deep red ($^4G_{5/2} \rightarrow {}^6H_{9/2}$) region under the excitation of 290 nm, and in the orange-red ($^4G_{5/2} \rightarrow {}^6H_{7/2}$) region under 406 and 465 nm excitations. The estimated chromaticity coordinates reveal that under 290 nm excitation, the sample emission falls towards the deep red region of the CIE 1931 chromaticity diagram. However, under 406 and 465 nm excitations, the emission shifts towards the orange-red region. The photoluminescence decay curves represent a bi-exponential in nature for all the concentrations of Sm^{3+} doped BYW phosphors under the excitation wavelengths 290 and 406 nm, with an average decay time in the range of microseconds. The summary of the above-mentioned results indicates that this

excitation wavelength dependent multicolour emitting Sm^{3+} doped $BiYWO_6$ phosphor could be a promising candidate for advanced anti-counterfeiting and SSL applications.

The aforementioned results substantiate that the thermally stable, and efficient RE doped/co-doped $BiYWO_6$ phosphors developed through this research work possess significant potential for use in solid state lighting and anti-counterfeiting applications.

8.3. Future Scope

- To enhance the luminescence properties for RE doped $BiYWO_6$ phosphor by using suitable flux and surfactant.
- To enhance and optimize emission intensity using up and down conversion phosphors for efficient white LED and advanced anti-counterfeiting applications.
    - By exciting at different wavelengths
    - Host ions substitution
    - By co-doping suitable rare earth/transition metal ions.
- To design and fabricate color-tunable, single /multi-mode phosphors for their utilization in w-LED and advanced anti-counterfeiting applications.
- To extend the utility of this phosphor for applications in bio-imaging, display devices, and dynamic multicolor emission based security ink.

8.4. Social Impact

The research on tungstate based perovskite material, as presented in thesis, holds the potential for social impact on exhibiting as phosphor based efficient luminescent material. Below are the key areas where the social benefits of this work could be emphasized.

(i) ***Application in Photonic Devices*****:** Beyond solid state lighting and anti-counterfeiting applications, tungstate based perovskites could potentially be used in electronics and

display technology, offering safer alternative to current materials and spurring innovation in more sustainable consumer products.

(ii) ***Energy Efficiency and Sustainability*:** Tungstate based Aurivillius layered perovskites offer high luminous characteristics, thermal stability enabling high efficiency w-LEDs, which results in lower power consumption compared to traditional lighting systems.

(iii) ***Cost effectiveness and Global Accessibility:*** By making the affordable longer lifespan of SSL devices, tungstate based perovskite material offers pathways to address energy poverty in undeserved regions.

(iv) ***Consumer safety and Trust:*** Tungstate-based Aurivillius perovskite material can be engineered for multicolor or invisible luminescent signature, enhancing security tags, QR codes, or labels. This could be helpful in preventing fake pharmaceuticals, electronics, and food products, protecting consumer from harmful or substandard goods.

(v) ***Aligned with National Interest:*** Tungstate based Aurivillius layered perovskites used for solid state lighting applications are well aligned with the Government Missions such as Atmanirbhar Bharat (Self-reliant India), Make in India, Smart Cities Mission etc. helping to achieve the national growth targets and gain prosperity for the citizens.

In summary tungstate based Aurivillius layered perovskite materils have the potential to transform society by promoting energy efficient lighting and strengthening anti-counterfeiting mechanism. Their dual use in environmental sustainability and consumer protection reflects a strong contribution to technological progress with social responsibility.

References:

[1] T. Krishnapriya, R. Mohan P, A. Jose, J.R. Jose, C. Joseph, P.R. Biju, Mater. Chem. Phys. 280 (2022) 125827.

[2] A.K. Vishwakarma, K. Jha, M. Jayasimhadri, B. Sivaiah, B. Gahtori, D. Haranath, Dalton Trans. 44 (2015) 17166–17174.

[3] M.K. Sahu, H. Kaur, B. V. Ratnam, J.S. Kumar, M. Jayasimhadri, Ceram. Int. 46 (2020) 26410–26415.

[4] W. Abrahamse, L. Steg, C. Vlek, T. Rothengatter, J. Environ. Psychol. 25 (2005) 273–291.

[5] H. Allcott, S. Mullainathan, Science 327 (2010) 1204–1205.

[6] M. Sharif Hossain, Energy Policy 39 (2011) 6991–6999.

[7] R.K. V.K, D.V. M, Asia Pac. J. Res. 01 (2016) 140–151.

[8] J. McKittrick, L.E. Shea-Rohwer, J. Ame. Ceram. Soc. 97 (2014) 1327–1352.

[9] S. Ye, F. Xiao, Y.X. Pan, Y.Y. Ma, Q.Y. Zhang, Mater. Sci. Eng. R Rep. 71 (2010) 1–34.

[10] J. Wang, J. Ma, J. Zhang, Y. Fan, W. Wang, J. Sang, Z. Ma, H. Li, ACS Appl. Mater. Interface 11 (2019) 35871–35878.

[11] P. Pei, Y. Bai, J. Su, Y. Yang, W. Liu, Sci. China Mater. 65 (2022) 2809–2817.

[12] J. Helen Ratna Monica, Jyoti, Pranav Y., J. Adv. Chem. Sci. 7 (2021) 706–710.

[13] P. Pei, R. Wei, B. Wang, J. Su, Z. Zhang, W. Liu, Adv. Funct. Mater. 31 (2021) 1–9.

[14] R. Ziniuk, A. Yakovliev, H. Li, G. Chen, J. Qu, T.Y. Ohulchanskyy, Front. Chem.

9 (2021) 1–10.

[15] R.B. Basavaraj, H. Nagabhushana, B. Daruka Prasad, S.C. Sharma, S.C. Prashantha, B.M. Nagabhushana, Optik 126 (2015) 1745–1756.

[16] G. Chen, W. Zhuang, R. Liu, Y. Liu, Y. Hu, H. He, J. Rare Earths 31 (2013) 944–949.

[17] P. Kumar, S. Singha, B.K. Gupta, Nanoscale 8 (2018) 14297–14340.

[18] T. Wang, X. Ji, Z. Tao, X. Zhou, Z. Hao, X. Wang, X. Gao, S. Wang, Y. Liu, RSC Adv. 10 (2020) 15573–15578.

[19] A.K. Vishwakarma, M. Jayasimhadri, J. Lumin. 176 (2016) 112–117.

[20] B. V. Ratnam, M.K. Sahu, A.K. Vishwakarma, K. Jha, H.J. Woo, K. Jang, M. Jayasimhadri, J. Lumin. 185 (2017) 99–105.

[21] H. Kaur, M. Jayasimhadri, Solid State Sci. 122 (2021) 106776.

[22] M. Li, X. Zhang, H. Zhang, W. Chen, L. Ma, X. Wang, Y. Liu, B. Lei, J. Mater. Chem. C 7 (2019) 3617–3622.

[23] E.F. Schubert, J.K. Kim, Science 308 (2005) 1274–1278.

[24] S. Kaur, M. Jayasimhadri, A.S. Rao, J. Alloys Compd. 697 (2017) 367–373.

[25] K. Jha, M. Jayasimhadri, J. Alloys Compd. 688 (2016) 833–840.

[26] H. Yang, G. Zhu, L. Yuan, C. Zhang, F. Li, H. Xu, A. Yu, J. Ame. Ceram. Soci. 95 (2012) 49–51.

[27] H.K. Yang, J.H. Jeong, J. Phys. Chem. C 114 (2010) 226–230.

[28] G. Blasse, A. Bril, Appl. Phys. Lett. 11 (1967) 53–55.

[29] X. Li, J.D. Budai, F. Liu, J.Y. Howe, J. Zhang, X.J. Wang, Z. Gu, C. Sun, R.S. Meltzer,

Z. Pan, Light Sci. Appl. 2 (2013) 1–8.

[30] L. Wang, R.J. Xie, Y. Li, X. Wang, C.G. Ma, D. Luo, T. Takeda, Y.T. Tsai, R.S. Liu, N. Hirosaki, Light Sci. Appl. 5 (2016) 1–9.

[31] L. Mishra, A. Sharma, A.K. Vishwakarma, K. Jha, M. Jayasimhadri, B. V. Ratnam, K. Jang, A.S. Rao, R.K. Sinha, J. Lumin. 169 (2016) 121–127.

[32] P. Suthanthirakumar, K. Marimuthu, J. Mol. Struct. 1125 (2016) 443–452.

[33] K. Vivekanandan, S. Selvasekarapandian, P. Kolandaivel, M.T. Sebastian, S. Suma, Mater. Chem. Phys. 49 (1997) 204–210.

[34] Z. Xia, Y. Zhang, M.S. Molokeev, V. V. Atuchin, J. Phys. Chem. C 117 (2013) 20847–20854.

[35] Y. Gao, S. Murai, K. Shinozaki, J. Qiu, K. Tanaka, ACS Appl. Electron. Mater. 1 (2019) 961–971.

[36] F. Kang, Y. Zhang, M. Peng, Inorg. Chem. 54 (2015) 1462–1473.

[37] S. Choi, Y.J. Yun, S.J. Kim, H. Jung, Opt. Lett. 38 (2013) 1346–1348.

[38] Y. Deng, S. Yi, J. Huang, J. Xian, W. Zhao, Mater. Res. Bull. 57 (2014) 85–90.

[39] M. Shang, C. Li, J. Lin, Chem. Soc. Rev. 43 (2014) 1372–1386.

[40] S. Gai, C. Li, P. Yang, J. Lin, Chem. Rev.114 (2014) 2343–2389.

[41] B. Valeur, N. Berberan-santos, J. Chem. Educ. (2011) 731–738.

[42] C. R. Ronda, Luminescence-From Theory to Application, Wiley-VCH, India (2007).

[43] K.N. Shinde, S.J. Dhoble, Critical Rev. Solid State Mater. Sci. 39 (2014) 459–479.

[44] S.W.S. McKeever, Thermolumin. Solids 84 (2011) 1–19.

[45] T. Jüstel, H. Nikol, C. Ronda, Angew. Chem. Int. Ed. 37 (1998) 3084–3103.

[46] H.C. Swart, O.M. Ntwaeaborwa, Module Chem. Mol. Sci. Chem. Eng. 4 (2013) 73-86.

[47] F. Wang, X. Liu, Chem. Soc. Rev.38 (2009) 976–989.

[48] N. Deopa, A.S. Rao, J. Lumin. 192 (2017) 832–841.

[49] K. Jha, A.K. Vishwakarma, M. Jayasimhadri, D. Haranath, J. Alloys Compd. 719 (2017) 116–124.

[50] G. Blasse, B.C. Grabmaier, Springer Series Fluoresc. 7 (1994) 121.

[51] S.K. Sharma, D.S. Verma, L.U. Khan, S. Kumar, S.B. Khan, Handbook of Materials Characterization, springer cham (2018) ISBN 978-3-030-06555-3.

[52] K.A. Gschneidner, B. Jacquire, Handbook on the Physics and Chemistry of rare earth 40 (2010) 550.

[53] W.T. Carnall, P.R. Fields, K. Rajnak, J. Chem. Phys. 49 (1968) 4424–4442.

[54] X. Chen, P. Dai, X. Zhang, C. Li, S. Lu, X. Wang, Y. Jia, Y. Liu, Inorg. Chem. 53 (2014) 3441–3448.

[55] Z. Zhang, W. Tang, J. Lumin. 169 (2016) 367–373.

[56] G. Blasse, Philips Res. Rep. 24 (1969) 131-144.

[57] A. Bednarkiewicz, K. Trejgis, J. Drabik, A. Kowalczyk, L. Marciniak, ACS Appl. Mater. Interfaces 9 (2017) 43081–43089.

[58] W.T. Carnall, P.R. Fields, K. Rajnak, J. Chem. Phys. 49 (1968) 4447–4449.

[59] S. Kaur, A.S. Rao, M. Jayasimhadri, Ceram. Int. 43 (2017) 7401–7407.

[60] M.K. Sahu, M. Jayasimhadri, K. Jha, B. Sivaiah, A.S. Rao, D. Haranath, J. Lumin. 202 (2018) 475–483.

[61] D.L. Dexter, J.H. Schulman, J. Chem. Phys. 22 (1954) 1063–1070.

[62] L.G. Van Uitert, J. Electrochem. Soc. 114 (1967) 1048.

[63] Y. Tian, B. Chen, B. Tian, R. Hua, J. Sun, L. Cheng, H. Zhong, X. Li, J. Zhang, Y. Zheng, T. Yu, L. Huang, Q. Meng, J. Alloys Compd. 509 (2011) 6096–6101.

[64] B. Tian, B. Chen, Y. Tian, X. Li, J. Zhang, J. Sun, H. Zhong, L. Cheng, S. Fu, H. Zhong, Y. Wang, X. Zhang, H. Xia, R. Hua, J. Mater. Chem. C 1 (2013) 2338–2344.

[65] C.S. McCamy, Color Res. Appl. 17 (1992) 142–144.

[66] S.S. Shinde, P.S. Shinde, Y.W. Oh, D. Haranath, C.H. Bhosale, K.Y. Rajpure, Appl. Surf. Sci. 258 (2012) 9969–9976.

[67] G.C. Righini, F. Enrichi, L. Zur, M. Ferrari, J. Phys. Conf. Ser. 1221 (2019) 6–11.

[68] N. Yao, J. Huang, K. Fu, X. Deng, M. Ding, X. Xu, RSC Adv. 6 (2016) 17546–17559.

[69] X. Huang, S. Han, W. Huang, X. Liu, Chem. Soc. Rev. 42 (2013) 173–201.

[70] Z. Xia, W. Zhou, H. Du, J. Sun, Mater. Res. Bull. 45 (2010) 1199–1202.

[71] J. Zhang, B. Ji, G. Chen, Z. Hua, Inorg. Chem. 57 (2018) 5038–5047.

[72] G.N. Rocha, L.F.L. Melo, P.B.A. Fechine, P.V.S. Silva, M.A.S. Da Silva, A.S.B. Int. Microwave Optoelectron. Conf. Proc. (2011) 642–646.

[73] H. Ait Ahsaine, M. Ezahri, A. Benlhachemi, B. Bakiz, S. Villain, J.C. Valmalette, F. Guinneton, M. Arab, J.R. Gavarri, RSC Adv. 5 (2015) 96242–96252.

[74] P.S. Berdonosov, D.O. Charkin, K.S. Knight, K.E. Johnston, R.J. Goff, V.A. Dolgikh,

P. Lightfoot, J. Solid State Chem. 179 (2006) 3437–3444.

[75] L. Zhang, B. Deng, S. Shu, Y. Wang, H. Geng, R. Yu, Spectrochim. Acta Part A Mol. Biomol. Spectrosc. 224 (2020) 117454.

[76] D. Haranath, N. Gandhi, S. Sahai, M. Husain, V. Shanker, Chem. Phys. Lett. 496 (2010) 100–103.

[77] Z. Mu, Y. Hu, L. Chen, X. Wang, G. Ju, Z. Yang, Y. Jin, J. Lumin. 146 (2014) 33–36.

[78] X. Huang, C. He, X. Zhu, C. Yang, Y. Liu, M. Wu, X. Min, R. Mi, Z. Huang, Ceram. Int. 47 (2021) 32130–32137.

[79] J. Wang, W. Chen, L. Peng, T. Han, C. Liu, Z. Zhou, Q. Qiang, F. Shen, J. Wang, B. Liu, J. Lumin. 250 (2022) 119066.

[80] G. Li, Y. Tian, Y. Zhao, J. Lin, Chem. Soc. Rev. 44 (2015) 8688–8713.

[81] Y. Chen, J. Wang, M. Gong, Q. Su, J. Solid State Chem. 180 (2007) 1165–1170.

[82] R.K. Tamrakar, D.P. Bisen, N. Brahme, J. Radiat. Res. Appl. Sci. 7 (2014) 550–559.

[83] P. Godlewska, A. Matraszek, L. Macalik, K. Hermanowicz, M. Ptak, P.E. Tomaszewski, J. Hanuza, I. Szczygieł, J. Alloys Compd. 628 (2015) 199–207.

[84] R.K. Tamrakar, D.P. Bisen, K. Upadhyay, I.P. Sahu, J. Phys. Chem. C 119 (2015) 21072–21086.

[85] D. Jugović, D. Uskoković, J. Power Sources 190 (2009) 538–544.

[86] N. Jain, N. Marwaha, R. Verma, B.K. Gupta, A.K. Srivastava, RSC Adv. 6 (2016) 4960–4968.

[87] X. Li, T. Odoom-Wubah, Z. Chen, B. Zheng, J. Huang, Ceram. Int. 40 (2014)

16317–16321.

[88] B. D. Cullity, Elements of X-Ray Diffraction, Addison-Wesley Publishing Company, Inc, Philippines (1978).

[89] L. Alexander, H.P. Klug, J. Appl. Phys. 21 (1950) 137–142.

[90] A. Khorsand Zak, W.H. Abd. Majid, M.E. Abrishami, R. Yousefi, Solid State Sci. 13 (2011) 251–256.

[91] H.M. Rietveld, J. Appl. Crystallogr. 2 (1969) 65–71.

[92] R. A. Young, The Rietveld Method: International Union of Crystallography, Oxford University Press (1996) 298p. ISBN 0-19-855577-6.

[93] R.E. Hummel, T. Dubroca, Optical properties of Metals and Alloys, Characterization of the, in Encyclopedia of the Analytical Chemistry, John Wiley & Sons (2000) 1–25.

[94] R. López, R. Gómez, J. Sol-Gel Sci. Technol. 61 (2012) 1–7.

[95] D. Xu, Z. Yang, J. Sun, X. Gao, J. Du, J. Mater. Sci. Mater. Electron. 27 (2016) 8370–8377.

[96] J. Zhou, Z. Xia, M. Yang, K. Shen, J. Mater. Chem. 22 (2012) 21935–21941.

[97] S.K. Sharma, D.S. Verma, L.U. Khan, S. Kumar, S.B. Khan, Handbook of materials and characterization, Springer Cham. (2018) ISBN 978-3-319-92955-2.

[98] J.R. Lakowicz, Principles of Fluorescence Spectroscopy, Springer (2006) ISBN-13: 978-0387-31278-1.

[99] K. Wakabayashi, Y. Yamaguchi, T. Sekiya, S. Kurita, J. Lumin. 112 (2005) 50–53.

[100] D. Phillips, R.L. Christensen, Instrument. Sci. Technol. 14 (1985) 267–292.

[101] K. Jha, M. Jayasimhadri, J. Ame. Ceram. Soc. 100 (2017) 1402–1411.

[102] K. Li, X. Liu, Y. Zhang, X. Li, H. Lian, J. Lin, Inorg. Chem. 54 (2014) 323–333.

[103] J. Sun, X. Zhang, Z. Xia, H. Du, Mater. Res. Bull. 46 (2011) 2179–2182.

[104] Vikas, M. Jayasimhadri, D. Haranath, Curr. Appl. Phys. 58 (2024) 11–20.

[105] K. Li, M. Shang, H. Lian, J. Lin, Inorg. Chem. 54 (2015) 7992–8002.

[106] P. Li, M. Peng, X. Yin, Z. Ma, G. Dong, Q. Zhang, J. Qiu, Opt. Expr. 21 (2013) 18943.

[107] M. Qu, X. Zhang, X. Mi, Q. Liu, Z. Bai, J. Alloys Compd. 828 (2020) 154398.

[108] C.M. Mehare, G. Mishra, N.S. Dhoble, S.J. Dhoble, J. Mol. Struct. 1264 (2022) 133250.

[109] M. Taywade, A.R. Kadam, N.S. Dhoble, S.J. Dhoble, Results Chem. 6 (2023) 101097.

[110] H. Kaur, M. Jayasimhadri, Ceram. Int. 45 (2019) 15385–15393.

[111] B. V. Ratnam, M. Jayasimhadri, K. Jang, Spectrochim. Acta Part A Mol. Biomol. Spectrosc. 132 (2014) 563–567.

[112] Y. jie Han, S. Wang, H. Liu, L. Shi, S. xia Liu, Y. Zhang, C. Liu, X. fan Shi, Q. Wang, Z. fei Mu, Z. yong Mao, D. jian Wang, Z. wei Zhang, J. Mol. Struct. 1210 (2020) 127998.

[113] G.L. Bhagyalekshmi, D.N. Rajendran, J. Alloys Compd. 850 (2021) 156660.

[114] R. Nagaraj, A. Raja, S. Ranjith, J. Alloys Compd. 827 (2020) 154289.

[115] K.N. Kumar, L. Vijayalakshmi, P. Hwang, A.D. Wadhwani, J. Choi, J. Alloys Compd. 840 (2020) 155589.

[116] G. Jia, D. Dong, C. Song, L. Li, Mater. Lett. 120 (2014) 251–254.

[117] H. Li, Z. Wang, Opt. Mater. 143 (2023) 114158.

[118] G. Wu, J. Xue, X. Li, Q. Bi, M. Sheng, Z. Leng, Ceram. Int. 49 (2023) 10615–10624.

[119] Q. Zhang, X. Wang, X. Ding, Y. Wang, Inorg. Chem. 56 (2017) 6990–6998.

[120] K. Somasundaram, C.K. Rastogi, I. Roy, P.C. Selvin, Mater. Res. Bull. 113 (2019) 133–140.

[121] L. Li, J. Chen, X. Peng, S. Xu, R. Wei, H. Guo, Ceram. Int. 49 (2023) 25806-25814.

[122] H. Wang, X.Y. Chen, L.M. Teng, D.K. Xu, W.P. Chen, R.F. Wei, F.F. Hu, X.Y. Sun, H. Guo, J. Lumin. 206 (2019) 185–191.

[123] M.T. Abbas, N.Z. Khan, J. Mao, L. Qiu, X. Wei, Y. Chen, S.A. Khan, Mater. Today Chem. 24 (2022) 100903.

[124] A. Oudhia, N. Shukla, P. Bose, R. Lalwani, A. Choudhary, Nano Struct. Nano-Obj. 7 (2016) 69–74.

[125] A. Dwivedi, M. Srivastava, A. Srivastava, C. Upadhyay, S.K. Srivastava, Sci. Rep. 12 (2022) 1–15.

[126] S. Pasternak, D. Levy, Y. Paz, B. Pokroy, CrystEngComm 18 (2016) 6464–6470.

[127] S. Mamidi, R. Gundeboina, S. Kurra, R. Velchuri, V. Muga, Comptes Rendus Chimie 21 (2018) 547–552.

[128] D. V. Deyneko, I. V. Nikiforov, D.A. Spassky, P.S. Berdonosov, P.B. Dzhevakov, B.I. Lazoryak, J. Alloys Compd. 887 (2021) 161340.

[129] J. Zhao, F. Zheng, C. Dou, C. Hu, H. Kong, Y. Feng, S. Sun, J. Li, X. Zhang, L. Wang, F. Yang, B. Teng, J. Tang, D. Zhong, J. Phys. Chem. Solids 158 (2021) 1–8.

[130] L. Tian, P. Yang, H. Wu, F. Li, J. Lumin. 130 (2010) 717–721.

[131] B. Zhang, J. Zhang, Y. Guo, J. Wang, J. Xie, X. Li, W. Huang, L. Wang, Q. Zhang, J. Alloys Compd. 787 (2019) 1163–1172.

[132] P. Dixit, V. Chauhan, P. Kumar, P.C. Pandey, Mater. Chem. Phys. 305 (2023) 127913.

[133] V. Chauhan, P.K. Pandey, P. Dixit, P. Deshmukh, S. Satapathy, P.C. Pandey, J. Lumin. 248 (2022) 118994.

[134] A. Raja, G. Annadurai, V. Sivasubramani, K. Ramachandran, R. Kamesh, V. Govindan, P. Vijayakumar, V. Siva, P. Ramasamy, Ceram. Int. 49 (2023) 11393–11401.

[135] A.R. Kadam, S.J. Dhoble, Luminescence 34 (2019) 846–853.

[136] D. Haranath, P. Sharma, H. Chander, J. Appl. D Appl. Phys. 78 (2005) 371.

[137] A.K. Vishwakarma, M. Jayasimhadri, J. Alloys Compd. 683 (2016) 379–386.

[138] Z. Chen, Y. Pan, L. Xi, R. Pang, S. Huang, G. Liu, Inorg. Chem. 55 (2016) 11249–11257.

[139] H. Kaur, M. Jayasimhadri, Opt. Mater. 107 (2020) 110119.

[140] S. Som, S. Das, S. Dutta, H.G. Visser, M.K. Pandey, P. Kumar, R.K. Dubey, S.K. Sharma, RSC Adv. 5 (2015) 70887–70898.

[141] M.K. Sahu, J. Mula, J. Ame. Ceram. Soc. 102 (2019) 6087–6099.

[142] N. Xue, X. Fan, Z. Wang, M. Wang, Mater. Lett. 61 (2007) 1576–1579.

[143] H. Gu, L. Yu, J. Wang, M. Ni, T. Liu, F. Chen, Spectrochim. Acta Part A Mol. Biomol. Spectrosc. 177 (2017) 58–62.

[144] R. Hao, Q. Meng, W. Liu, H. Liu, J. Rare Earths 31 (2013) 864–870.

[145] B. Yan, F. Lei, J. Alloys Compd. 507 (2010) 460–464.

[146] H. Zheng, B. Chen, H. Yu, J. Zhang, J. Sun, X. Li, M. Sun, B. Tian, S. Fu, H. Zhong, B. Dong, R. Hua, H. Xia, J. Colloid Interface Sci. 420 (2014) 27–34.

[147] R. Kamal, M. Saif, Spectrochim. Acta Part A Mol. Biomol. Spectrosc. 229 (2020) 117928.

[148] J. Huang, W. You, G. Gong, G. Liu, P. Liu, B. Wang, Opt. Mater. 88 (2019) 534–539.

[149] A. Boukerika, L. Guerbous, N. Brihi, J. Alloys Compd. 614 (2014) 383–388.

[150] X. He, L. Xiaofang, R. Li, B. Yang, K. Yu, M. Zeng, R. Yu, Sci. Rep. 6 (2016) 1–11.

[151] H. Liu, J. Yuan, W. Shangguan, Y. Teraoka, J. Phys. Chem. C 112 (2008) 8521–8523.

[152] B.P. Singh, A.K. Parchur, R.K. Singh, A.A. Ansari, P. Singh, S.B. Rai, Phys. Chemi. Chem. Phys. 15 (2013) 3480–3489.

[153] A.K. Vishwakarma, K. Jha, M. Jayasimhadri, A.S. Rao, K. Jang, B. Sivaiah, D. Haranath, J. Alloys Compd. 622 (2015) 97–101.

[154] Q. Ma, A. Zhang, M. Lü, Y. Zhou, Z. Qiu, G. Zhou, J. Phys. Chem. B 111 (2007) 12693–12699.

[155] Y.C. Chang, C.H. Liang, S.A. Yan, Y.S. Chang, J. Phys. Chem. C 114 (2010) 3645–3652.

[156] Y. Hua, W. Ran, J.S. Yu, ACS Sustain. Chem. Eng. 9 (2021) 7960–7972.

[157] Y.D. Ma, X.S. Peng, M.Z. Fei, W.N. Zhang, L.M. Teng, F.F. Hu, R.F. Wei, H. Guo, J. Alloys Compd. 846 (2020) 156435.

[158] Y. Zhang, J. Xu, Q. Cui, B. Yang, Sci. Rep. 7 (2017) 1–12.

[159] J. Xiang, J. Yang, N. Luo, J. Zhu, S. Huang, Y. Mao, Results Phys. 13 (2019) 102258.

[160] S. Qi, D. Wei, Y. Huang, S. Il Kim, Y.M. Yu, H.J. Seo, J. Ame. Ceram. Soc. 97 (2014) 501–506.

[161] S. Wang, Q. Sun, B. Devakumar, J. Liang, L. Sun, X. Huang, J. Alloys Compd. 804 (2019) 93–99.

[162] S. Wang, C. Xu, X. Qiao, Ceram. Int. 47 (2021) 1063–1075.

[163] Q. Yu, J. Liu, P. Zhang, S. Hao, C. Zhu, C. Yang, Opt. Mater. 149 (2024) 115068.

[164] Z. Wang, Y. Wang, J. Zhang, Y. Lu, Mater. Res. Bull. 44 (2009) 1183–1187.

[165] V. Sangwan, M. Jayasimhadri, J. Phys. D Appl. Phys. 57 (2024) 195-301.

[166] T. Krishnapriya, R.M. P, A. Jose, J.R. Jose, C. Joseph, P.R. Biju, Mater. Chem. Phys. 280 (2022) 125827.

[167] J. Llanos, D. Espinoza, R. Castillo, RSC Adv. 7 (2017) 14974–14980.

[168] I. V Baklanova, V.N. Krasil, A.P. Tyutyunnik, Y. V Baklanova, J. Phys. Chem. Solids 165 (2022) 110683.

[169] Y. Xiang, Y. Zheng, L. Yang, M. Li, Y. Mao, J. Zhu, J. Alloys Compd. 919 (2022) 165837.

[170] K.N. Kumar, L. Vijayalakshmi, J. Lim, J. Choi, Spectrochim. Acta A: Mol. Biomol. Spectrosc. 278 (2022) 121309.

[171] J. Guo, S. Li, J. Kong, Y. Li, L. Zhou, L. Lou, Q. Lv, R. Tang, L. Zheng, B. Deng, R. Yu, Opt. Laser Technol. 155 (2022) 108347.

[172] A. George, A. Jose, T. Krishnapriya, T. Francis, C. Joseph, P.R. Biju, J. Solid State Chem. 305 (2022) 122625.

[173] J. Liao, B. Qiu, H. Wen, W. You, Y. Xiao, J. Lumi. 130 (2010) 762–766.

[174] R. Luo, Q. Li, J. Wang, Z. Ning, Y. Zhao, M. Liu, X. Lai, C. Zhong, J. Bi, D. Gao, J. Alloys Compd. 828 (2020) 154375.

[175] Y. Tian, X. Qi, X. Wu, R. Hua, B. Chen, J. Phys. Chem. C 113 (2009) 10767–10772.

[176] T. Gavrilović, J. Periša, J. Papan, K. Vuković, K. Smits, D.J. Jovanović, M.D. Dramićanin, J. Lumin. 195 (2018) 420–429.

[177] A.R. Sharits, J.F. Khoury, P.M. Woodward, Inorg. Chem. 55 (2016) 12383–12390.

[178] X. Bai, Y. Cun, Z. Xu, Y. Zi, A.A. Haider, A. Ullah, I. Khan, J. Qiu, Z. Song, Z. Yang, J. Chem. Eng. 429 (2022) 132333.

[179] M. Vasilopoulou, A. Soultati, D.G. Georgiadou, T. Stergiopoulos, L.C. Palilis, S. Kennou, N.A. Stathopoulos, D. Davazoglou, P. Argitis, J. Mater. Chem. A 2 (2014) 1738–1749.

[180] P. Ranjith, S. Sreevalsa, P. Patra, S. Som, A. Menon, K. Jayanthi, K. Annapurna, N.M.A. Krishnan, A.R. Allu, S. Das, Phys. Chem. Chem. Phys. 23 (2021) 15245–15256.

[181] T. Bavani, P. Sasikala, S. Arumugam, A. Malathi, P. Praserthdam, J. Madhavan, Environ. Sci.Pollut. Res. 30 (2023) 34468–34480.

[182] Y.A. Shaban, Method for Electrocatalysis: Advanced Materials and Allied Applications, Switzerland AG, pp. 353, ISBN 978-3-030-27161-9 (2020).

[183] F. Lei, B. Yan, H.H. Chen, J.T. Zhao, J. Ame. Ceram. Soc. 92 (2009) 1262–1267.

[184] J.Y. Park, J.W. Chung, H.K. Yang, Ceram. Int. 45 (2019) 11591–11599.

[185] S. Li, J. Guo, W. Shi, X. Hu, S. Chen, J. Luo, Y. Li, J. Kong, J. Che, H. Wang, B. Deng,

R. Yu, J. Lumi. 244 (2022) 118681.

[186] R. Yu, D.S. Shin, K. Jang, Y. Guo, H.M. Noh, B.K. Moon, B.C. Choi, J.H. Jeong, S.S. Yi, J. Ame. Ceram. Soc. 97 (2014) 2170–2176.

[187] J. Long, F. Chu, Y. Wang, C. Zhao, W. Dong, X. Yuan, C. Ma, Z. Wen, R. Ma, M. Du, Y. Cao, Inorg. Chem. 56 (2017) 10381–10386.

[188] J. Xiao, W. Zhang, T. Wang, J. Zhang, H. Du, Ceram. Int. 47 (2021) 12028–12037.

[189] M. Vikas, D. Jayasimhadri, Haranath, J. Lumin. 266 (2024) 120276.

[190] M. Jayasimhadri, D. Haranath, Int. J. Appl. Glass Sci. 13 (2022) 645–654.

[191] X.Y. Sun, T.T. Han, D.L. Wu, F. Xiao, S.L. Zhou, Q.M. Yang, J.P. Zhong, J. Lumin. 204 (2018) 89–94.

[192] W. Li, Z. Chen, B. Zhang, P. Zhao, Y. Fan, J. Lumin. 246 (2022) 118824.

[193] X. Wu, X. Zhao, Q. Ren, L. Du, M. Pei, O. Hai, Ceram. Int. 48 (2022) 18793–18802.

[194] R. Singh, M. Manhas, A.K. Bedyal, F. Durani, H.C. Swart, V. Kumar, Mater. Chem. Phys. 291 (2022) 126735.

[195] S. Liu, L. Zeng, Z. Zhao, M. Deng, X. Wang, W. Zhang, Ceram. Int. 48 (2022) 36706–36714.

[196] V.R. Bandi, B.K. Grandhe, H.J. Woo, K. Jang, D.S. Shin, S.S. Yi, J.H. Jeong, J Alloys Compd. 538 (2012) 85–90.

[197] A.M. Kłonkowski, W. Wiczk, K. Szczodrowski, D. Wileńska, N. Górecka, M. Szyszkowska, J Alloys Compd. 705 (2017) 539–549.

[198] N. Sarode, Y.R. Parauha, N.S. Dhoble, S.J. Dhoble, Mater. Today Comm. 37 (2023)

107225.

[199] H. Zhang, H. Zhang, Light Sci. Appl. 11 (2022) 10–12.

[200] C. Ronda, Reference Module in Materials Science and Materials Engineering, Elsevier Inc., ISBN 9780128035818 (2017).

[201] V. Sangwan, M. Jayasimhadri, D. Haranath, J. Mol. Struct. 1322 (2025) 140577.

[202] H. Liu, J. Yuan, W. Shangguan, and Y. Teraoka: Visible-light-responding $BiYWO_6$ solid solution for stoichiometric photocatalytic water splitting. J. Phys. Chem. C 112 (23), 8521 (2008).

[203] J. Kaur, Y. Parganiha, V. Dubey, D. Singh, D. Chandrakar, Superlattices Microstruct. 73 (2014) 38–53.

[204] A.K. Vishwakarma, K. Jha, M. Jayasimhadri, A.S. Rao, K. Jang, B. Sivaiah, D. Haranath, J. Alloys Compd. 622 (2015) 97-101.

[205] M. Zhang, M. Jia, T. Liang, Z. Wang, H. Xu, D. Duan, Y. Wei, Z. Fu, J. Colloid Interface Sci. 608 (2022) 758–767.

[206] Y. Zhong, Q. Wang, G. Chen, Int. J. Biolog. Macroml. 164 (2020) 2224–2231.

[207] J. V. Rival, P. Mymoona, R. Vinoth, A.M.V. Mohan, E.S. Shibu, ACS Appl. Mater. Interfaces 13 (2021) 10583–10593.

[208] J.Y. Park, J.W. Chung, H.K. Yang, Ceram. Int. 45 (2019) 11591–11599.

[209] R. Ziniuk, A. Yakovliev, H. Li, G. Chen, J. Qu, fchem. 9 (2021) 1–10.

[210] J. Andres, R.D. Hersch, J.E. Moser, A.S. Chauvin, Adv. Funct. Mater. 24 (2014) 5029–5036.

[211] Y.J. Kim, H.S. Jung, J. Lim, S.J. Ryu, J.K. Lee, Langmuir 32 (2016) 8077–8083.

[212] R.L. Yang, Y.J. Zhu, F.F. Chen, L.Y. Dong, Z.C. Xiong, ACS Appl. Mater. Interfaces 9 (2017) 25455–25464.

[213] S. Wang, J. Lin, Y. He, J. Chen, C. Yang, F. Huang, D. Chen, J. Chem. Eng. 394 (2020) 124889.

[214] N. Katumo, K. Li, B.S. Richards, I.A. Howard, Sci. Rep. 12 (2022) 1–14.

[215] M.K. Sahu, M. Jayasimhadri, J. Lumin. 227 (2020) 117570.

[216] T. Liu, Q. Meng, W. Sun, J. Lumin. 170 (2016) 219–225.

[217] G. Born, A. Hofstaetter, A. Scharmann, G. Schwarz, J. Lumin. 1–2 (1970) 641–650.

[218] Y.A. Tanko, M.R. Sahar, S.K. Ghoshal, Results Phys. 6 (2016) 7–11.

[219] H. Kaur, M. Jayasimhadri, J. Am. Ceram. Soc. 104 (2021) 5764–5775.

[220] Y. Yang, F. Li, Y. Lu, Y. Du, L. Wang, S. Chen, X. Ouyang, Y. Li, L. Zhao, J. Zhao, B. Deng, R. Yu, J. Lumin. 251 (2022) 119234.

[221] A.K. Kunti, N. Patra, S.K. Sharma, H.C. Swart, J. Alloys Compd. 735 (2018) 2410–2422.

[222] K. Li, X. Liu, Y. Zhang, X. Li, H. Lian, J. Lin, Inorg. Chem. 54 (2015) 323–333.

[223] F.B. Xiong, C.Y. Han, H.F. Lin, Y.P. Wang, H.Y. Lin, H.X. Shen, W.Z. Zhu, Ceram. Int. 42 (2016) 13841–13848.

[224] J. Grigorjevaite, E. Ezerskyte, J. Páterek, S. Saitzek, A. Zabiliūtė-Karaliūnė, P. Vitta, D. Enseling, T. Jüstel, A. Katelnikovas, Mater. Adv. 1 (2020) 1427–1438.

[225] Y. Li, C. Li, J. Kong, H. Su, L. Zhou, R. Yang, Y. Shang, C. Wang, J. Lian, G. Zhang,

R. Yu, Ceram. Int. 49 (2023) 17488–17496.

[226] I.E. Kolesnikov, E. V. Golyeva, M.A. Kurochkin, E.Y. Kolesnikov, E. Lähderanta, J. Lumin. 219 (2020).

[227] Z. Zou, T. Wu, H. Lu, Y. Tu, S. Zhao, S. Xie, F. Han, S. Xu, RSC Adv. 8 (2018) 7679–7686.

[228] G.R. Mamatha, B.R. Radha Krushna, J. Malleshappa, B. Subramanian, B. Daruka Prasad, C. Srikanth, H. Nagabhushana, J. Photochem. Photobiol. A Chemi. 439 (2023) 114560.

[229] M.R. Chandana, B.R.R. Krushna, J. Malleshappa, K. Manjunatha, T.E. Hsu, S.Y. Wu, S.C. Sharma, B.D. Prasad, B. Subramanian, H. Nagabhushana, Mater. Today Sustain. 22 (2023) 100397.